UNIVERSITEIT VAN PRETORIA
UNIVERSITY OF PRETORIA
YUNIBESITHI YA PRETORIA

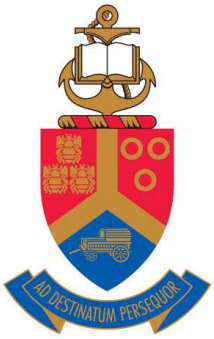

UNIVERSITEIT VAN PRETORIA
UNIVERSITY OF PRETORIA
YUNIBESITHI YA PRETORIA

MIMO CHANNEL MODELLING FOR INDOOR WIRELESS COMMUNICATIONS

BTJ MAHARAJ

2007

UNIVERSITEIT VAN PRETORIA
UNIVERSITY OF PRETORIA
YUNIBESITHI YA PRETORIA

MIMO CHANNEL MODELLING FOR INDOOR WIRELESS COMMUNICATIONS

By

Bodhaswar Tikanath Jugpershad MAHARAJ

Promotor: Professor Dr L.P. Linde (University of Pretoria, South Africa)

Submitted in partial fulfillment of the requirements for the degree

Philosophiae Doctor (Electronic)

in the

Department of Electrical, Electronic & Computer Engineering

in the

School of Engineering

in the

Faculty of Engineering, Built Environment & Information Technology

UNIVERSITY OF PRETORIA

September 2007

UNIVERSITEIT VAN PRETORIA
UNIVERSITY OF PRETORIA
YUNIBESITHI YA PRETORIA

SUMMARY

MIMO CHANNEL MODELLING FOR INDOOR WIRELESS COMMUNICATIONS

by

Bodhaswar Tikanath Jugpershad MAHARAJ

Promotor: Professor Dr L.P. Linde (University of Pretoria, South Africa)

Department of Electrical, Electronic & Computer Engineering

Philosophiae Doctor (Electronic)

This thesis investigates multiple-input-multiple-output (MIMO) channel modelling for a wideband indoor environment. Initially the theoretical basis of geometric modelling for a typical indoor environment is looked at, and a space-time model is formulated. The transmit and receive antenna correlation is then separated and is expressed in terms of antenna element spacing, the scattering parameter, mean angle of arrival and number of antenna elements employed. These parameters are used to analyze their effect on the capacity for this environment. Then the wideband indoor channel operating at center frequencies of 2.4 GHz and 5.2 GHz is investigated. The concept of MIMO frequency scaling is introduced and applied to the data obtained in the measurement campaign undertaken at the University of Pretoria. Issues of frequency scaling of capacity, spatial correlation and the joint RX/TX double direction channel response for this indoor environment are investigated. The maximum entropy (ME) approach to MIMO channel modelling is investigated and a new basis is developed for the determination of the covariance matrix when only the RX/TX covariance is known. Finally, results comparing this model with the established Kronecker model and its application for the joint RX/TX spatial power spectra, using a beamformer, are evaluated. Conclusions are then drawn and future research opportunities are highlighted.

Keywords:

MIMO channel modelling, frequency scaling, capacity, correlation and maximum entropy.

UNIVERSITEIT VAN PRETORIA
UNIVERSITY OF PRETORIA
YUNIBESITHI YA PRETORIA

OPSOMMING

MIMO CHANNEL MODELLING FOR INDOOR WIRELESS COMMUNICATIONS

deur

Bodhaswar Tikanath Jugpershad MAHARAJ

Promotor: Professor Dr L.P. Linde (University of Pretoria, South Africa)

Departement Elektriese, Elektroniese & Rekenaar Ingenieurswese

Philosophiae Doctor (Elektronies)

Veelvuldige-inset-veelvuldige-uitset (VIVU) kanaalmodellering vir ’n wyeband binnemuurse omgewing word in hierdie proefskrif ondersoek. Die teoretiese basis van meetkundige modellering vir ’n tipiese binnemuurse omgewing is aanvanklik ondersoek en ’n ruimte-tyd model is geformuleer. Die stuur- en ontvangsantenna korrelasie is toe geskei en in terme van die antenna elementspasiëring, die verstrooiingsparameter, die gemiddelde aankomshoek en die aantal antennas wat gebruik is, uitgedruk. Hierdie parameters word gebruik om hulle effek op die kapasiteit van die kanaal te bepaal. Die gebruik van 2.4 GHz en 5.2 GHz in die wyeband binnemuurse omgewing is ondersoek. Die konsep van VIVU frekwensieskalering is met behulp van metings by die Universiteit van Pretoria getoets en toegepas. Frekwensieskalering van kapasiteit, ruimtelike korrelasie en die gesamentlike ontvang/stuur dubbelrigtingkanaalrespons is in hierdie omgewing ondersoek. Die maksimum entropie benadering vir VIVU kanaalmodellering is ondersoek en ’n nuwe basis vir die bepaling van die kovariansie matriks wanneer slegs die stuur/ontvang kovariansie bekend is, is ontwikkel. Laastens word resultate van hierdie model met die gevestigde Kronecker model vergelyk. Die toepassing van die gesamentlike stuur/ontvang ruimtelike drywingspektra word met behulp van ’n bundelvormer evalueer. Die studie maak gevolgtrekkings en lig moontlike toekomstige navorsingsgeleenthede uit.

Sleutelwoorde:

VIVU kanaalmodellering, frekwensieskalering, kapasiteit, korrelasie en maksimum entropie.

I dedicate this work to

- The glory of our creator for giving me the intellect, energy and opportunity
- The Jugpershad Jewnath Family - they ventured, struggled and succeed in humility

UNIVERSITEIT VAN PRETORIA
UNIVERSITY OF PRETORIA
YUNIBESITHI YA PRETORIA

ACKNOWLEDGEMENTS

I would like to thank

- Professor Louis P. Linde for his support and encouragement
- Professor Jon W. Wallace for his technical guidance, insight and collaborative support
- The National Research Foundation (NRF), Thuthuka Program
- Professor Michael A. Jensen, Brigham Young University, USA
- My wife Pravina, and children Avikar and Akshay TJ

CONTENTS

LIST OF ABBREVIATIONS

2D	2-Dimensional
A/D	Analogue-to-Digital
AOA	Angle of Arrival
AOD	Angle of Departure
b/s/Hz	Bits per second per Hertz
ccdf	Complementary Cumulative Distribution Function
CIR	Channel Impulse Response
CIRC	Circular Array
COTS	Conventional Off-the-Shelf Components
CSI	Channel State Information
DDCIR	Double Directional Channel Impulse Response
DOA	Direction of Arrival
DOD	Direction of Departure
EVD	Eigenvalue Value Decomposition
EVT1/2	Event 1 or 2
FC	Full Covariance
I/O	Input-Output
IF	Intermediate Frequency
ISM	Industrial Scientific and Medical Bands
KM	Kronecker Model
LIN	Linear Array
LNA	Low Noise Amplifier
LO	Local Oscillator

LOS	Line-Of-Sight
ME	Maximum Entropy
MIMO	Multiple-Input-Multiple-Output
MIO	Multifunction Input-Output
MSE	Mean Square Error
NLOS	Non Line of Sight
PC	Personal Computer
PDF	Probability Distribution Function
RF	Radio Frequency
RX	Receiver
SIMO	Single-Input-Multiple-Output
SISO	Single-Input-Single-Output
SNR	Signal-to-Noise-Ratio
SP8T	Single-Pole-8-Throw
SVD	Singular Value Decomposition
SW	Switch
SYNC	Synchronization Unit
TOA	Time of Arrival
TTL	Transistor-Transistor Logic
TX	Transistor
UCA	Uniform Circular Array
ULA	Uniform Linear Array
UP	University of Pretoria
UPS	Uninterruptible Power Supply
UWB	Ultra-wideband
VIVU	Veelvuldige-Inset-Veelvuldige-Uitset
WB	Wideband

LIST OF FIGURES

LIST OF TABLES

CHAPTER ONE
INTRODUCTION

1.1 BACKGROUND AND MOTIVATION

The rapid growth in the demand for high-speed data rates for both business and residential applications, bandwidth on demand with high spectrum efficiencies and more reconfigurable systems and adaptivity to support multiple standards and multiple frequency bands have accelerated research and development for ”last mile” broadband access technologies. Furthermore with developing countries recognizing the need for such technologies acting as an enabler for improved quality of life and economic revival, the global needs and challenges for broadband wireless access both in fixed and mobile type environments are increasing.

Fixed broadband wireless access systems face the challenges of providing high data rates and high quality wireless access over fading channels at almost wire-line quality as they are often compared to cable modems and asynchronous DSL (xADSL), which operate over fixed wire-line channels. The use of multiple antennas at both the transmitter (TX) and receiver (RX) side of a wireless link is one of the most promising technological means to address the challenges described. This is known as multiple-input-multiple-output (MIMO) antennas and when used in combination with signal processing and coding, it is proving to be a good implementation choice.

The major impairment of a wireless system is fading caused by destructive addition of multi-paths in the propagation medium and interference from other users. The performance improvement gained from MIMO is achieved through array gain, diversity gain, interference

suppression and multiplexing gain. In array gain, multiple antennas can coherently combine signals to increase the signal-to-noise ratio and thus improve coverage. This coherent combination can be employed at both the TX and RX and to be exploited, one needs channel state information (CSI). Since accurate CSI is difficult to obtain at the TX, array gain is more likely to occur at the RX. Spatial diversity through multiple antennas can be used to combat fading and significantly improve link reliability.

Diversity provides the RX with several (ideally independent) replicas of the transmitted signal and is therefore a powerful means to combat fading and interference. Time diversity (due to doppler spread) and frequency diversity (due to delay spread) are the more common forms [1], but in recent years the use of spatial or antenna diversity has received prominence. Diversity gain can be obtained at both the TX and RX end. Space-time codes (that is coding across space $\{$antennas$\}$ and across time) developed in [2] help to realize the transmit diversity gain without knowing the channel at the TX. The idea of separating signal transmissions in a temporal and spatial domain has been previously implemented in systems which use multiple antennas at the RX side and a single antenna at the TX side, referred to as single-input-multiple-output (SIMO) systems [1]. Such systems are known to provide spatial/receiver diversity and together with maximum ratio combining can provide higher capacities. As mentioned above, multi-path fading is seen as one of the major impairments in wireless systems. With the use of multiple antennas in the MIMO systems, the multi-path environment is exploited through spatial multiplexing to achieve enhanced capacities, increasing linearly with N, where N is the minimum number of antennas on the TX and RX side [3–5]. Since the separation of the data streams happens in the spatial domain through the many different propagation paths in the rich scattering environment, one is able to transmit several data streams simultaneously at the same time within the same frequency interval and without increasing the overall transmit power of the system. The deep fades can be eliminated and the signal levels are higher and fluctuates much lesser over time [6, 7].

Interference suppression in multiple antennas can be used to suppress co-channel interference, hence increasing cellular capacity. For a fixed line MIMO system [8], where the channel changes is negligible and have perfect channel state information at the TX, one can use advanced schemes with waterfilling [9], yielding optimal performance of the MIMO system. Where the CSI is imperfect [10], the TX would rely on the average spatial statistics from the

RX, which could result in sub-optimal channel capacity [11]. In the case where the channel may experience fast fading but the average channel statistics do not [12], transmission schemes like eigen-beam forming can be applied. Ivrlač has shown in [13] that it is possible to achieve almost the same capacity as in the case with perfect CSI when average channel information was used.

In the final analysis, achieving the best performance can finally be attributed to having the most reliable channel characteristics. Since the performance of the MIMO system is highly channel dependent, it is essential to accurately characterize the channel by understanding the complex spatial behavior of the wireless MIMO channel [14]. Although statistical analysis [15] and ray tracing [16] are useful for modelling, these tools often do not represent the true channel behavior. Hence this research work is exactly addressing the above-mentioned issues, but with particular reference to the fixed broadband wireless indoor MIMO environment.

1.2 AUTHOR'S CONTRIBUTIONS AND OUTPUTS

1.2.1 Research Contribution

The author's main research contribution can be summarized as follows:

- The author presents a new geometrical model for the indoor environment with separate transmit and receive antenna correlation expressions in a closed form. Using this, the effect of capacity in such a system based on the effects of scattering, antenna element spacing, angular orientation of antenna array and number of antenna elements deployed, is determined. Using the results here as a basis the usefulness of a measurement campaign is suggested.

- Then a unique low cost wideband MIMO channel measurement system, developed in the University of Pretoria (UP) wireless research laboratory, for the measurement campaign undertaken at 2.4 GHz and 5.2 GHz using uniform linear arrays (ULA) and uniform circular arrays (UCA), is presented.

- The different types of metrics which have been determined are presented so as to characterize the channel and describe the channel behavior. The concept of *frequency scaling* in MIMO systems has also been developed. Two new frequency scaling

models, one for capacity using a UCA and the other for spatial correlation for the ULA are contributed.

- Steinbauer's [17] work for the double directional radio channel is extended. New expressions for the double directional response is defined in terms of joint spatial power spectra for two different types of beamformer methods. The *frequency scaling* technique is then applied.

- A new method and the corresponding analysis are presented to determine the maximum entropy estimate of the full joint TX/RX MIMO channel covariance matrix, where knowledge of only the separate TX and RX covariance is assumed. This is then compared to the well known Kronecker model [18].

1.2.2 Journal Publications

The following peer reviewed and accredited journal articles have been published by the author as part of his research activities.

- B.T. Maharaj, J.W. Wallace, L.P. Linde and M.A. Jensen, "Frequency scaling of spatial correlation from co-located 2.4 GHz and 5.2 GHz wideband indoor MIMO channel measurements", *Electronics Letters*, vol. 41, no. 6, pp.336-338, March 2005.

- B.T. Maharaj, J.W. Wallace, L.P. Linde and M.A. Jensen, "Linear dependence of double directional spatial power spectra at 2.4 and 5.2 GHz from indoor MIMO channel measurements", *Electronics Letters*, vol. 41, no. 24, pp. 1138-1340, November 2005.

- B.T. Maharaj and L.P. Linde, "Geometric modelling of a spatially correlated MIMO fading channel", *SAIEE Africa Research Journal*, IEEE/SAIEE-AFRICON '04 Special Issue, vol. 97, no. 2, pp. 191-197, June 2006.

- B.T. Maharaj, J.W. Wallace, L.P. Linde and M.A. Jensen, "A low cost open-hardware wideband MIMO wireless channel sounder", *IEEE Transactions in Instrumentation and Measurement*, completed first review, July 2007.

1.2.3 Conference Proceedings

The author's research work as reflected in this thesis, contributed the following outputs through publications in the following peer reviewed and accredited conference proceedings:

- B.T. Maharaj and L.P. Linde, "Capacity for spatial-temporal correlated MIMO fading channel", *Proceedings of IEEE AFRICON 2004*, vol. 1, pp.269-274, Gaborone, Botswana, September 2004.

- B.T. Maharaj, J.W. Wallace, L.P. Linde and M.A. Jensen, "A cost-effective wideband MIMO channel sounder and initial co-located 2.4 GHz and 5.2 GHz measurements", *in Proc. 2005 IEEE International Conference on Acoustics, Speech and Signal Processing (ICASSP)*, vol. 3, Philadelphia, PA, USA, 18-23 March 2005, pp. 981-984.

- B.T. Maharaj, J.W. Wallace, L.P. Linde and M.A. Jensen, "Co-located indoor 2.4- and 5.2- GHz MIMO channel measurements: frequency scaling of capacity and correlation", *in Proceedings of 2005 IEEE International Conference on Telecommunications (ICT'05)*, Cape Town International Conference Centre, Cape Town, South Africa, May 2005, CD-ROM.

- B.T. Maharaj and L.P. Linde, "Frequency scaling of capacity for a co-located 2.4 GHz and 5.2 GHz wideband indoor MIMO circular array system", *in Proc. IEEE ICTe Africa*, KICC, Nairobi, Kenya, 17-21 May 2006, CD-ROM.

- B.T. Maharaj, J.W. Wallace and L.P. Linde, "MIMO channel modelling: the Kronecker model and maximum entropy", *in Proc.2007 IEEE Wireless Communications and Networking Conference (WCNC)*, Hong Kong, 18-23 March 2007, CD-ROM.

1.2.4 Invited Paper

- B.T. Maharaj, J.W. Wallace and M.A. Jensen, "Comparison of double-directional channel response at 2.4 and 5.2 GHz from indoor co-located wideband MIMO channel measurements", *in Proceedings of General Assembly of International Union of Radio Science (URSI-GA '06)*, URSI - GA'06, New Delhi, India, 23-29 October 2005.

1.2.5 Additional Contributions

These contributions were based on the work related to that done by the author either as work done through supervision or collaboration.

- B.T. Maharaj, J.W. Wallace and M.A. Jensen, "Experimental evaluation of the MIMO wideband channel temporal variation", *in Proceedings of General Assembly of*

International Union of Radio Science (URSI-GA '06), URSI - GA'06, New Delhi, India, 23-29 October 2005.

- B.B. Varghese and B.T. Maharaj, "A spatially correlated model for MIMO fading channels", *in Proceedings of 2005 IEEE International Conference on Telecommunication (ICT '05)*, Cape Town International Conference Centre, Cape Town, May 2005, CD-ROM.

1.3 OUTLINE OF THESIS

Chapter Two gives the reader an overview of the the description of the MIMO system and a brief introduction to MIMO channels. Some of the propagation based developments for geometric models, ray tracing, statistical modelling and measurements based are discussed. The double directional channel case is outlined and then the MIMO capacity for the case where no CSI information at the TX, is presented.

Having developed a geometric model, one needs to establish the accuracy of this model for a real indoor environment. Hence in Chapter Four the University of Pretoria's and Africa's first wideband 8 x 8 MIMO channel sounder is presented. The uniqueness of this system, compared to some of the commercial systems available, lies in the fact that it is largely constructed from off-the-shelf components, hence making it low cost and easily within reach of most research groups' budgets. A description of the system deployed for this research work is outlined and this is followed with the description of the indoor measurement environment where the measurement campaign was undertaken. Finally, an exposé of our data collection and calibration procedure is presented.

Having undertaken the measurement campaign, the data was analyzed and various metrics such as capacity, spatial correlation and joint TX/RX beamforming, which can be used to characterize the channel in Chapter Five, are looked at. Initially some bulk statistics are presented, and then capacity (eigenvalues) for this environment is evaluated at both 2.4 GHz and 5.2 GHz. The analysis for the indoor environment leads to the development of the *frequency scaling* model of capacity for the UCA. Modelling of the separate spatial correlation for the ULA is developed and the new model is analyzed, justifying its accuracy and also

establishing a new *frequency scaling* relationship. Finally, a joint TX/RX beamforming (eigenvectors) model is developed and a closed form expression is derived in order to determine the joint spatial power characteristics in the channel. This is then compared with the conventional Bartlett and the Capon Beamforming techniques both at 2.4 GHz and 5.2 GHz.

Chapter Six describes the mathematical development of a new approach using maximum entropy, where, in order to derive the full joint covariance, only on knowledge of the separate TX and RX covariances is required. This unique model is compared to one of the most popular and well known models, viz. the Kronecker model. This model has some improvement over the Kronecker model and also shows great potential for further research and investigation.

Based on the techniques, analysis and results presented, Chapter Seven summarizes the conclusions and offers opportunities for further research and investigations.

CHAPTER TWO

CHANNEL MODELLING: AN OVERVIEW

2.1 MIMO COMMUNICATION SYSTEM MODEL

A block diagram for a generalized MIMO wireless communication system can be represented as that shown in Figure 2.1, where the system is divided into the space-time coding and signal processing parts and then multiplexed onto the N transmitter elements and finally through the channel. It is assumed that a set of Q independent data streams represented by the symbol vector $\mathbf{b}^{(n)}$ is encoded into N_T discrete-time complex baseband streams $\mathbf{x}^{(n)}$ at the transmitter as described in [19], where n is the time index. These input symbols are then converted into discrete-time samples by coding in space across the N_T outputs and over time through sampling. This is then converted into a continuous-time baseband waveform, $\mathbf{X}(\omega)$, with ω being the frequency. This signal is then up-converted and fed into the N_T antennas after any filtering and amplification. At the receiver the signal is combined from the N_R channels to produce the continuous output vector waveform $\mathbf{Y}(\omega)$, which is then matched-filtered and sampled to produce the discrete-time baseband sample stream $\mathbf{y}^{(n)}$. This $\mathbf{y}^{(n)}$ signal is finally space-time decoded to generate the estimated transmitted symbols, $\hat{\mathbf{b}}^{(n)}$ for the Q independent data streams.

Hence the baseband MIMO input-output relationship can be expressed as

$$\mathbf{y}(t) = \mathbf{H}(t) * \mathbf{x}(t) + \mathbf{n}(t) \tag{2.1}$$

where $\mathbf{n}(t)$ is additive white Gaussian noise (AWGN) and $*$ denotes the convolution. $\mathbf{H}(t)$ is an N$\times$M channel impulse response matrix. Equation (2.1) can also be written in the frequency

domain as

$$\mathbf{Y}(\omega) = \mathbf{H}(\omega)\mathbf{X}(\omega) + \mathbf{n}(\omega). \tag{2.2}$$

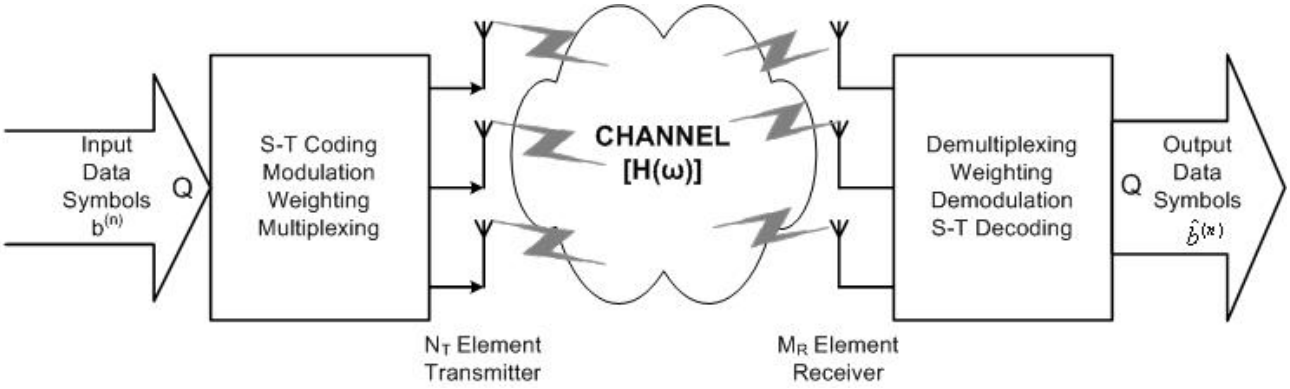

FIGURE 2.1: Block diagram of a generic MIMO wireless system

Each element $H_{ij}(\omega)$ represents the transfer function between the j^th transmit and i^th receive antenna. If the signal bandwidth is sufficiently narrow so that the channel response is constant over the system bandwidth (frequency flat channel), or when the wideband signals can be divided into narrowband frequency bins and processed independently, then equation (2.2) can be written as

$$\mathbf{y} = \mathbf{H}\mathbf{x} + \mathbf{n} \tag{2.3}$$

where $\mathbf{H}$ is the narrowband MIMO channel matrix. In order to study the MIMO channel capacity, the elements of the narrowband MIMO channel matrix is assumed to be independent, identically distributed (iid) and at best, the data streams Q, would be equal to the rank of $\mathbf{H}$. However, in real MIMO systems factors such as antenna impedance matching, antenna element spacing, polarization properties and degree of scattering influence these and affect the system performance.

2.2 MIMO SYSTEM CAPACITY

In the single-input-single-output (SISO) system, the ergodic (mean) capacity of a random channel with N_T = N_R = 1 and an average transmit power constrained by P_T can be written as [20]

$$C = E_H \left\{ \max_{p(x):P \leqslant P_T} I(X;Y) \right\} \tag{2.4}$$

where P is the average power of a single channel codeword transmitted over the channel and E_H denotes the expectation over all channel realizations. The channel is thus defined [20] as the maximum of the mutual information between the input and the output over all statistical distributions on the input, that satisfy the power constraint. If each symbol at the transmitter is denoted by b, the average power constraint can be written as

$$P = E\left[|b|^2\right] \leqslant P_T. \tag{2.5}$$

Using (2.4), the ergodic (mean) capacity of a SISO system $(N_T = N_R = 1)$ with a random complex channel gain h_{11} is given in ([15]) as

$$C = E_H \left\{ \log_2(1 + \rho. \left|h_{11}\right|^2 \right\} \tag{2.6}$$

where ρ is the average signal-to-noise ratio (SNR) at the receiver branch. If $|h_{11}|$ is Rayleigh, $|h_{11}|^2$ follows the chi-squared distribution with two degrees of freedom [21]. Thus equation (2.6) can be written as [15]

$$C = E_H \left\{ \log_2(1 + \rho.\chi_2^2 \right\} \tag{2.7}$$

where χ^2 is a chi-squared distribution random variable with two degrees of freedom.

Thus, using equation (2.7) one can show as in Figure 2.2 the Shannon capacity for a Gaussian channel and the capacity of a Rayleigh fading channel for a SISO channel, where the Rayleigh fading plot is as in [22].

For the MIMO system we can write the capacity of a random channel with power constraint P_T and transmit vector $\mathbf{X}(\omega)$, whose elements are complex Gaussian-distributed random variables, as

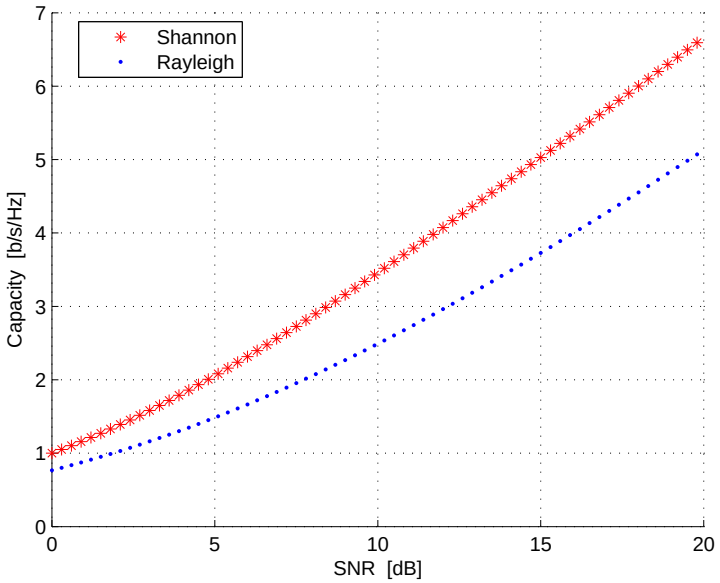

FIGURE 2.2: Ergodic capacity for a SISO channel vs SNR

$$C = E_H \left\{ \max_{p(\mathbf{x}):tr(\mathbf{R}_x)\leqslant P_T} I(\mathbf{x},\mathbf{y}) \right\} \tag{2.8}$$

where $\mathbf{R}_x = E\left\{\mathbf{x}\mathbf{x}^H\right\}$ is the diagonal elements of the transmit covariance representing the transmit power from each antenna, tr(.) denotes the trace, P_T is the total transmit power limited by the constraint $tr(\mathbf{R}) \leq P_T$ and E$\{\cdot\}$ is the expectation.

Now the ergodic (mean) capacity for a complex additive white Gaussian noise (AWGN) MIMO channel can be expressed as [9], [15]

$$C = E_H \left\{ \log_2 \left[\det \left(\mathbf{I}_{N_R} + \frac{P_T}{\sigma^2 N_T} \mathbf{H}\mathbf{H}^H \right) \right] \right\} \tag{2.9}$$

which can also be written as

$$C = E_H \left\{ \log_2 \left[\det \left(\mathbf{I}_{N_R} + \frac{\rho}{N_T} \mathbf{H}\mathbf{H}^H \right) \right] \right\} \tag{2.10}$$

where the average sinal-to-noise ratio (SNR) is $\rho = \frac{P_T}{\sigma^2}$ at each of the receiver branch antenna elements.

The MIMO channel capacity can also be analyzed from equation (2.10) by using the eigenvector decomposition (EVD) [19] or singular value decomposition (SVD). Hence, the

product $\mathbf{H}\mathbf{H}^H = \xi\mathbf{\Lambda}\xi^H$, where ξ is the eigenvector matrix with orthonormal columns and $\mathbf{\Lambda}$ is a diagonal matrix with the eigenvalues on the main diagonal. Thus, equation (2.10) can be re-written as

$$C = E_H\left\{\log_2\left[\det\left(\mathbf{I}_{N_R} + \frac{\rho}{N_T}\xi\mathbf{\Lambda}\xi^H\right)\right]\right\} \tag{2.11}$$

If the SVD is used, then one can write

$$\mathbf{H} = \mathbf{U}\mathbf{S}\mathbf{V}^H \tag{2.12}$$

where $\mathbf{U}$ and $\mathbf{V}$ are unitary matrices and $\mathbf{S}$ is a matrix with singular values on the main diagonal. The number of non-zero singular values, k, on the diagonal of $\mathbf{S}$ gives the rank of the channel matrix, where the rank can be generally expressed as

$$rank\,(\mathbf{H}) = k \leqslant \min\{N_T, N_R\} \tag{2.13}$$

Now one can re-write (2.11) using (2.13) and noting that the determinant of a unitary matrix equals 1, one obtains

$$C = E_H\left\{\sum_{i=1}^{k}\log_2\left(1 + \frac{\rho}{N_T}\lambda_i\right)\right\} \tag{2.14}$$

where λ_i is the eigenvalues of the diagonal matrix $\mathbf{\Lambda}$. The ideal maximum capacity would be attained when each of the N_T transmitted signals is received by the same set of N_R receiver antennas without any interference.

With optimal combining at the RX and only receive diversity (ie.$N_T = 1$), one can write the channel capacity as

$$C = E_H\left\{\log_2\left(1 + \rho.\chi^2_{2N_R}\right)\right\} \tag{2.15}$$

where $\chi^2_{2N_R}$ is a chi-distributed random variable with $2N_R$ degrees of freedom. As in [15], for N_T transmit antennas and optimal combining between the N_R receive antennas, the capacity can be written as

$$C = E_H\left\{N_T\log_2\left[1 + \frac{\rho}{N_T}\chi^2_{2N_R}\right]\right\}. \tag{2.16}$$

Figure 2.3 shows the implementation of equation (2.16), which represents the ergodic capacity upper bound of a Rayleigh fading MIMO channel with $N_T = N_R = 8$, when compared to a SISO channel with the Shannon capacity bound. Although this is a special case, it proves the inherent potential and research imperatives that need to be undertaken so as to exploit this opportunity of improved capacity in wireless communications, for example [2, 23–25].

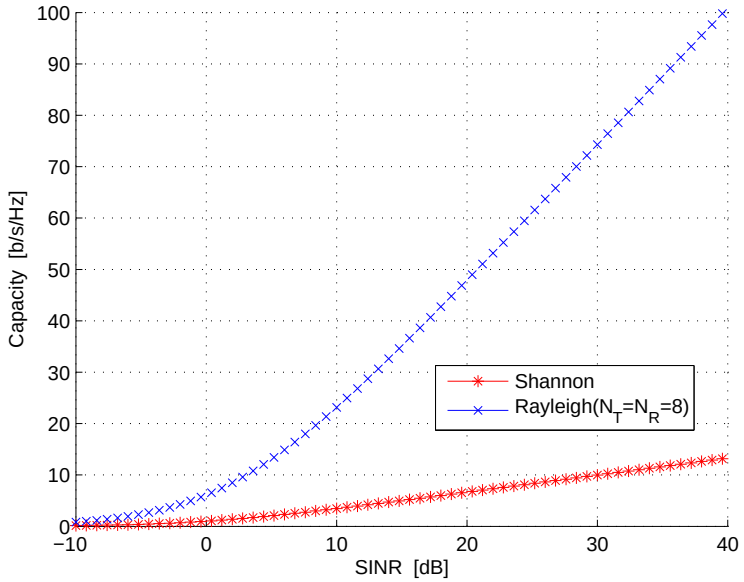

FIGURE 2.3: Comparison of Shannon capacity for SISO and ergodic capacity for Rayleigh fading MIMO Channels.

2.2.1 Water-Filling Capacity

The capacity can be obtained if one can determine the covariance $\mathbf{R_x}$ that will maximize equation (2.8). Having been able to show $\mathbf{H}$ in terms of the SVD as in (2.12), and since $\mathbf{V}$ is unitary, one can write

$$\mathbf{x}' = \mathbf{V}^H \mathbf{x} \tag{2.17}$$

and

$$\mathbf{R}'_x = E\left\{\mathbf{x}'\mathbf{x}'^H\right\} = \mathbf{V}^H \mathbf{R}_x \mathbf{V} \tag{2.18}$$

Using equation (2.18), it is shown in [26] that to maximize equation (2.8), $\mathbf{R}'_x$ must be diagonal.

The capacity expression can then be written as [19]

$$C = \max_{\{R'_x : \sum_i R'_{x,ii} \leqslant P_T\}} \sum_{i=1}^{N_R} \log_2 \left(1 + \frac{S_{ii}^2 R'_{x,ii}}{\sigma^2}\right) \tag{2.19}$$

where $R'_{x,ii}$ represents the optimal transmit power on the i^th un-encoded stream and S_{ii}^2 is the power gain of the i^th eigenchannel. $R'_{x,ii}$ can be maximized in (2.19) by using Lagrange multipliers in order to obtain a waterfilling solution [20, 26–28]. The waterfilling method allocates power proportionally to the high-gain channels and generally would not use the weaker channels. As shown in [29], by using the waterfilling technique, one can have increased capacity by exploiting the improvement in the quality of the channels.

2.2.2 Uninformed Transmitter Capacity

When the transmitter does not have channel state information (that is it does not know $\mathbf{H}$), it would divide the power equally among all the N_T transmitter antennas. This implies that $\mathbf{R}_x = (P_T/N_T)\mathbf{I}$ and substituting this into (2.8) results in the uninformed transmitter capacity [15].

$$C_{UT} = \log_2 \left|\mathbf{I} + \frac{P_T}{N_T \sigma^2} \mathbf{H}\mathbf{H}^H\right| \tag{2.20}$$

2.2.3 Diversity and Spatial Multiplexing

In traditional antenna diversity the TX is used to send duplicate copies of the same information to the RX so as to increase the reliability of detection. With MIMO one would have the capability of exploiting the channel spatial degrees of freedom as it enables one to send distinctly different streams of information through the channel, hence increasing the throughput and spectral efficiency. Depending on the application and quality of service requirement, this combination of diversity and spatial multiplexing can vary as described in [30].

Diversity systems used for reducing branch signal correlation are also applicable to improving MIMO systems' performance. Low correlation is a good indicator for MIMO system performance [31], but need not necessarily be a sufficient condition. The pinhole or keyhole channel could exist as described in [32–35], where there is high correlation but also high capacity. This motivates a case for importance of knowledge of the channel and the

propagation environment having rich scattering.

Low correlation is achieved when each antenna provides a unique weighting to each multipath component based on its direction of departure (DOD) and direction of arrival (DOA). Systems would generally use a combination of the weighting based on the arrival phase due to antenna location (spatial diversity) or on magnitude and phase due to antenna pattern or polarization characteristics.

Generally low correlation would occur for a large set of multipaths with large angular spread created by a rich scattering environment. This could produce a low SNR, which in turn decreases the channel capacity [31, 36]. The effect that antenna spacing (branch correlation) has on capacity has been investigated in [14], where it is shown that a wide antenna spacing resulted in a low correlation for a 2×2 channel and as the antenna spacing decreased due to the adding of more elements across a constant array length, the capacity per antenna dropped due to the higher correlation between adjacent elements. Similar phenomena was also reported in [37–41], where it is shown that the increased signal correlation degrades the MIMO system performance.

2.3 MULTIPATH CHARACTERIZATION

2.3.1 Beamforming

Beamforming and subspace-based methods form part of the spectral-based approach [42]. One 'steers' the array in one direction at a time and measure the output power. The maximum power at each of the steering positions gives the direction of arrival (DOA) estimates. This output can be written as a linear combination given by

$$y(t) = \sum_{l=1}^{L} w_l^* x_l(t) = \mathbf{w}^H \mathbf{x}(t) \tag{2.21}$$

where $\mathbf{x}$ is the array output vector (for example DOA emitter signals) and $\mathbf{w}$ is the weighting vector.

For samples y(1), y(2), ...,y(N); the output power is measured by

$$P(\mathbf{w}) = \frac{1}{N}\sum_{l=1}^{N}|y(t)|^2 = \frac{1}{N}\sum_{l=1}^{N}\mathbf{w}^H\mathbf{x}(t)\mathbf{x}^H(t)\mathbf{w} = \mathbf{w}^H\hat{\mathbf{R}}\mathbf{w} \tag{2.22}$$

where $\hat{\mathbf{R}}$ is the sample covariance matrix and can be written as [42]

$$\hat{\mathbf{R}} = \frac{1}{N}\sum_{t=1}^{N}\mathbf{x}(t)\mathbf{x}^H(t) \tag{2.23}$$

2.3.2 Bartlett Beamformer

The Bartlett or conventional beamformer dates back to World War II and it is an extension of the Fourier-based spectral analysis to spatio-temporally sampled data [43]. For a particular array geometry (for example the UCA) this algorithm maximizes the power of the beamforming output for a given input signal.

If one wishes to maximize the output power from a certain direction θ, then the array output, corrupted with additive noise, can be written in terms of the steering vector, $\mathbf{a}$, and the baseband signal waveform, s(t) as

$$\mathbf{x}(t) = \mathbf{a}(\theta)s(t) + \mathbf{n}(t) \tag{2.24}$$

The maximum output power can be formulated and the weighting vector can be determined [42, 43] as

$$\mathbf{w}_{BF} = \frac{\mathbf{a}(\theta)}{\sqrt{\mathbf{a}^H(\theta)\mathbf{a}(\theta)}} \tag{2.25}$$

This weight vector can be interpreted as a spatial filter, which has been matched to the impinging signal. One can then insert equation (2.25) into equation (2.22) to obtain the spatial power spectrum as [42]

$$P_{BF}(\theta) = \frac{\mathbf{a}^H(\theta)\hat{\mathbf{R}}\mathbf{a}(\theta)}{\mathbf{a}^H(\theta)\mathbf{a}(\theta)} \tag{2.26}$$

For the UCA case the steering vector $\mathbf{a}(\theta)$ can be written as

$$\mathbf{a}_{UCA} = \exp(j2\pi(x\cos\theta + y\sin\theta)) \tag{2.27}$$

where x and y are the resolved co-ordinates for each antenna element as shown in Figure 2.4, thus making it possible to determine the beamforming spectra versus DOA.

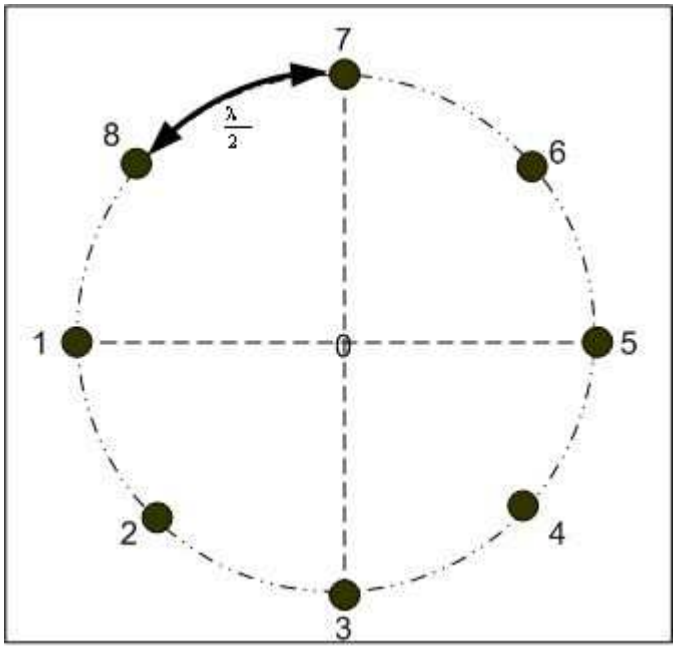

FIGURE 2.4: Uniform circular 8 element antenna array layout

2.3.3 Capon Beamformer

Capon's beamformer attempts to minimize the power contributed by noise and any signals coming from other directions other than θ, while still maintaining a fixed gain in the direction of θ. Capon [44] proposed a different method based on the optimization problem formulated as

$$\min_{\mathbf{w}} P(\mathbf{w}) \quad subject\ to\ \mathbf{w}^H\mathbf{a}(\theta) = 1 \tag{2.28}$$

where $\mathbf{P}$(w) is as defined in equation (2.22). Using the technique of Lagrange multipliers, one can find the optimal $\mathbf{w}$ as [44]

$$\mathbf{w}_{CAP} = \frac{\hat{\mathbf{R}}^{-1}\mathbf{a}(\theta)}{\mathbf{a}^H\hat{\mathbf{R}}^{-1}\mathbf{a}(\theta)} \tag{2.29}$$

and inserting equation (2.29) into equation (2.22) leads to the spatial spectrum

$$P_{CAP}(\theta) = \frac{1}{\mathbf{a}^H(\theta)\hat{\mathbf{R}}^{-1}\mathbf{a}(\theta)} \tag{2.30}$$

Consequently, using equations (2.30) and (2.27) one can determine the spatial power for DOA. The Capon beamformer generally performs better than the Bartlett beamfomer as it uses every available degree of freedom to concentrate the received energy along one direction, since the constraint minimizes $\mathbf{P}(\mathbf{w})$ as compared to the Bartlett beamfomer which maximizes the output power. However the Capon beamfomer can suffer from noise enhancement as a result of $\mathbf{R}^{-1}$ as shown in (2.30) and is also dependent on the SNR and array aperture in resolving the spectral power content.

2.3.4 Double-Directional Channel Model

The double directional concept includes angular information which is defined in terms of paired discrete plane-wave departures and arrivals at both the TX and RX. This is described through the propagation channel approach [45] where the TX and RX antennas can be excluded.

Generally, the local propagation scenario can be represented in a system-related fashion by the multi-dimensional spreading function (MDSF) as [46]

$$s = (\nu, \tau, \varphi_R, \varphi_T) \tag{2.31}$$

where ν is the Doppler shift, τ is the delay, φ_R is the angle of arrival at RX and φ_T is the angle of departure at the TX.

One can express the input-output relationship through convolution of the MDSF in multi-dimensions. The approach used here is to describe the directional case via the time-dependent complex channel impulse response (CIR), as $h(t, \tau, \varphi_R)$ and the non-directional case as $h(t, \tau)$. The RX antenna coherently sums up components from all directions, weights them with the complex antenna pattern $g_R(\varphi_R)$, and thus integrates over the respective angular domain as [46]

$$h(t, \tau, \varphi_R) = \int_{-\pi}^{\pi} h(t, \tau, \varphi_T, \varphi_R) g_T(\varphi_T) d\varphi_T \tag{2.32}$$

$$h(t, \tau) = \int_{-\pi}^{\pi} h(t, \tau, \varphi_R) g_R(\varphi_R) d\varphi_R \tag{2.33}$$

where T and R represent the transmit and receive, respectively.

From the above, one observes that $h(t,\tau)$ is the angle integrated directional channel impulse response $h(t,\tau,\varphi_R)$, while the directional channel impulse response is the angle integrated double directional channel impulse response $h(t,\tau,\varphi_R,\varphi_T)$. Hence, the propagation channel is now described by the double directional channel response.

The double directional channel model [45, 46] separates the radio transmission chain into the TX antenna, double directional channel and the RX antenna. The TX antenna would essentially distribute the RF energy into the respective directions of departure (DOD), while the RX antenna would collect and capture the signal from the different angles of arrival (AOA) by weighted combination. The double directional channel includes all resolvable propagation paths, L, between the TX and RX and can be expressed by the CIR as shown in [46].

Now the wideband MIMO channel response can be computed for any antenna constellation as [46]

$$h(t,\tau,x_R,x_T)=\sum_{i=1}^{L}h(t,\tau,\varphi_{R,i},\varphi_{T,i})g_R(\varphi_{R,i})g_T(\varphi_{T,i})e^{-j\vec{k}^T(\varphi_{R,i})\vec{x}_R}e^{-j\vec{k}^T(\varphi_{T,i})\vec{x}_T} \tag{2.34}$$

where L= is the overall number of multipath components aggregated over all domains, $\vec{x}_R$ and $\vec{x}_T$ are the vectors of the chosen element position measured from an arbitrary but fixed reference point on the corresponding array. The exponential k-terms in (2.34) are defined as:

$$\vec{k}^T(\varphi).\vec{x}=\frac{2\pi}{\lambda}(x\cos\varepsilon\cos\varphi+y\cos\varepsilon\sin\varphi+z\sin\varepsilon) \tag{2.35}$$

When the true channel behavior is represented by the above equations, the multipath parameters may then be measured using conventional beamforming [42], basis matching techniques [47], or parametric estimation algorithms such as ESPRIT [42, 48, 49].

2.3.5 Ray Tracing

Ray tracing is a technique that allows multipath routes to be predicted from positions off walls and other reflecting surfaces through the creation of either two-dimensional (2D) or three-dimensional (3D) models from modelling the electromagnetic excitation in that

environment. This allows not only the signal strengths of the multipath components, but also their angles of arrival and departure from the transmitter and receiver to be estimated, hence allowing one to determine the channel capacity.

The ray tracing approach can be extremely computationally intensive [16], especially if one has to include line-of-sight (LOS), reflected, transmitted, diffracted, scattered and some combined rays. Therefore, generally simple scenarios are considered and have emerged as the most popular technique for the analysis on site-specific scenarios [50–52]. Some of the more commonly used ray tracing methods are the shooting and bouncing ray launching algorithm, the image method and the hybrid acceleration method of ray tracing algorithms [53].

Ray tracing techniques have shown some promise in predicting large scale path loss variation, with the average error standard deviation being 7.2 [53], but preliminary comparisons of ray tracing with MIMO measurements indicated that the simulations tended to underestimate the capacity [54]. However, recent propagation prediction and site planning for an indoor environment yielded an error standard deviation of less than 3dB [55] for a specific case. There have been some promising results for AOA and AOD when compared with measurements which, when combined with the random distribution of the phase [56, 57], can be used to characterize the channel. However, integration of the ray-tracing approach for outdoor/indoor propagation through windows and reflection as well as transmission through complex walls with 3D would be required to improve the accuracy of the technique [58, 59] and enable it to be more generally used.

Although some work using ray tracing to predict MIMO capacity variation with array location and antenna spacing [40, 60] and spatial power signature in the channel [61] have been reported, more opportunity exists for research into the modelling and computational efficiency versus accuracy in this complex arena.

2.3.6 Geometric Models

Geometric models capture the spatial multipath behavior range in complexity and can be represented by various physical properties [62]. For the narrowband case they can be the received signal power and time varying amplitude (fading) distribution, but for wideband

systems properties such as angle of arrival (AOA), angle of departure (AOD), time of arrival (TOA), time delay spread and adaptive array antenna geometries become relevant in order to improve the accuracy of the representation of the physical channel. Some of the models briefly mentioned hereafter will vary in the complexity of the geometry and the scattering mechanisms considered, largely due to computational and numerical limitations in finding closed form solutions.

In the one-ring model [37], the transmitter (TX) is assumed to be elevated and hence, assumed to be unobstructed by local scattering, while the receiver (RX) is surrounded by scatterers. There is also no-line-of-sight component between TX and RX, the scattering is uniformly distributed at the RX across some angle θ, so that each ray is assumed to be reflected only once and all rays reach the receive array with the same power. In [37], they derive an equation for the channel covariance which is in terms of some of the geometrical parameters and can be evaluated by numerical analysis. Similarly the two-ring model [63] is derived where there is a ring of scatterers at both the TX and RX.

In [64, 65] a model is proposed that uses the von Mises angular probability density function (PDF) as the angular PDF at only the RX and also considers the Doppler spread distribution. The von Mises angular PDF is proposed as a versatile model for the representation of the angular PDF as it compared well with measured data [66]. Furthermore it has a scattering parameter κ that can be varied depending on the scattering for that particular environment. In [64] the channel covariance can be written as

$$\begin{aligned} E\left[H_{p,n}(t)H^{H}_{q,m}(t+\tau)\right] = \frac{\exp\left[jc_{pq}\cos(\alpha)\right]}{I_0(\kappa)} I_0(\{\kappa^2 - a^2 - b^2_{nm} - c^2_{pq}\gamma^2\sin^2(\alpha) \\ +2ab_{nm}\cos(\beta-\phi) \\ +2c_{pq}\gamma\sin(\alpha)[a\sin(\phi) - b_{nm}\sin(\beta)] \\ -j2\kappa[a\cos(\mu-\phi) - b_{nm}\cos(\mu-\beta) \\ -c_{pq}\gamma\sin(\alpha)\sin(\mu)]\}^{1/2}) \end{aligned} \tag{2.36}$$

and the von Mises PDF is defined by the angular PDF, $p(\theta)$ as

$$p(\theta) = \frac{\exp[\kappa\cos(\theta-\mu)]}{2\pi I_0(\kappa)} \tag{2.37}$$

where d_{pq} and d_{nm} are the element spacing at the BS and MS respectively, ϕ is the direction of the moving MS, τ is the relative time difference between the two links $H_{p,n}$ and $H_{q,m}$, $f_D = v/\lambda$ is the Doppler shift with v being the speed of the MS, $\theta \in [-\pi, \pi)$, μ is the mean AOA at the MS and $I_0(\cdot)$ is the zero order modified Bessel function.

The above model has a closed form expression and can therefore be used to analytically study the channel covariance and the impact of the various model parameters on the capacity, both for LOS and NLOS scenarios. This model is adapted for an indoor scenario where scattering at both the TX and RX is considered, and is analyzed in Chapter 3.

The distributed scattering model was proposed in [67] to describe outdoor MIMO propagation channels. Here the TX and RX are obstructed by the surrounding scatterers which are located at a distance large enough from the TX and RX so that one can assume the signals as plane waves. Assuming that there are a large number of scatterers (S), having random fading, the MIMO channel transfer function can described by

$$\mathbf{H} = \frac{1}{\sqrt{S}} \mathbf{R}_{\theta_r,d_r}^{1/2} \mathbf{G}_r \mathbf{R}_{\theta_s,2D_r/S}^{1/2} \mathbf{G}_t \mathbf{R}_{\theta_t,d_t}^{T/2} \tag{2.38}$$

where $\frac{1}{\sqrt{S}}$ is the normalization factor, $\mathbf{G}_t$ and $\mathbf{G}_r$ are random matrices with iid zero mean complex Gaussian elements, $\mathbf{R}_{\theta_t,d_t}$, $\mathbf{R}_{\theta_s,2D_r/S}$, $\mathbf{R}_{\theta_r,d_r}$ are the correlation matrices seen from the transmitter, the virtual array and receiver respectively, d is the array element distance and θ_i is the AOA of the i^{th} scatterer.

In [68] a wideband SISO multipath channel model was proposed for the indoor scenario based on an indoor measurement campaign. The multipath components were observed to arrive in groups and therefore the scatterers could be separated into clusters. This Saleh-Valenzuela model was extended for MIMO channels in [69–71], taking into account the statistics of the AOA and AOD, giving the coefficient of the narrowband channel matrix as

$$H_{nm} = \int_{2\pi} \int_{2\pi} W_n^R(\theta^R) h(\theta^R, \theta^T) W_m^T(\theta^T) d\theta^T d\theta^R \tag{2.39}$$

where $W_q^P(\theta) = G_q^P \exp[j\psi_q^P(\theta)]$, with G_q^P being the antenna gain pattern, $\psi_q^P(\theta) = 2\pi[x_q^P \cos(\theta) + y_q^P \sin(\theta)]$, $P \; \epsilon \; (T, R)$ and $q \; \epsilon \; (m, n)$. This model was compared with narrowband indoor channel measurements and reported good accuracy in terms of channel capacity PDF.

A directional channel model developed by the European research initiative COST259 was reported in [72], and can be used to model different MIMO propagation channels. The double directional channel impulse response (DDCIR) was derived as

$$H_{nm}(t,\tau,\theta^R) = \int_{\theta^T} G_m^T(\theta^T) H_{nm}(t,\tau,\theta^R,\theta^T) d\theta^T \tag{2.40}$$

where $G_m^T(\theta^T)$ is the complex antenna pattern for the m^th transmit element, θ_R and θ_T are the corresponding AOA and AOD at the RX and TX respectively and m and n are the number of TX and RX elements respectively.

To simulate the channel as described in [72], a layered approach whereby different environments have been separated into three levels was followed. The top level is the cell type and each cell type includes the second level, namely the number of radio environments. For each of the radio environments, some propagation scenarios have been identified, hence forming the third level. Each of these levels have certain input parameters which are either known, measured or statistically obtained to model the channel.

Other known models are the Virtual Channel Model [73] and EM Scattering model as presented in [74–76], where the properties of the channel and antennas are taken into account. This model has two discs of scatterers for transmit and receive and the scatterers on each side are organized into clusters. The model includes antenna polarization properties through the antenna functions, consequently enabling one to also study depolarization.

Others [77–80] have also modelled the scatterers as discrete objects which can represent specific scatterers in the channel, or they can be defined by some statistical function such as a Poisson process in proximity of either the TX or RX. Assuming a single or double bounce scattering mechanism, the channel response can be determined. In real world channels it may not be possible to completely describe the channel by these limited number of parameters and one may be able to validate the geometric models that describe the radio channel in certain environments. Hence there will always be some limitation (which can be taken into account) to geometric modelling, but they will always form an important aspect to wireless channel characterization [81].

2.4 CONCLUSION

This chapter has presented an overview of some of the modelling techniques one could use to characterize a wireless channel, as well as some of the research activities that have been undertaken, and are still ongoing, aimed at reliably and accurately representing the electromagnetic propagation in the MIMO channel. The collective importance and integration of electromagnetic theory, signal processing and communication theory lends much opportunity for further research into MIMO channel modelling.

CHAPTER THREE
GEOMETRIC MODELLING

3.1 INTRODUCTION

In a traditional macro-cell type wireless communication scheme, the base station would be on some elevated tower and not be surrounded by many close local scatterers, while the receiver would most probably be at ground level, either in a building, automobile or on the street, which would be surrounded by many local scatterers. Investigations in [37, 64, 82] focused on the spatial correlation effects for the above scenario, where the scattering could vary from isotropic to highly non-isotropic scattering.

With the opportunity for wireless local area networks achieving very high data rates for multiple users, the space-time correlation of such channels needs to be investigated [82] so that adequate and appropriate channel models can be adopted. The geometrically based modelling approach used in [64, 83, 84] is considered, but applied specifically for an indoor fixed wireless environment [85] with different scattering PDF configurations at the transmitter and receiver, with the derivation of space-time correlation function. For the fixed wireless scenario considered herein, isotropic scattering at the transmitter end is considered, while the angular distribution of the scatterers at the receiver follows the von Mises probability distribution function (PDF) [64]. The approach used here is to derive the joint space-time correlation function and then separate the transmit antenna and receive antenna correlation. Consequently one derives expressions for the transmit antenna correlation in terms of antenna element spacing and the receive antenna correlation in terms of the scattering parameter k, antenna element spacing $d_{pn},\ d_{mn}$ and mean direction of angle of arrival (AOA), ϕ_R. The

closed form solutions herein presented enables one to determine the effect on the capacity in such a system based on the effects of scattering, antenna element spacing, angular orientation of antenna array and number of antenna elements employed.

3.2 MODEL DESCRIPTION

The new geometric MIMO channel model was initially described after which the mathematical analysis was developed. The new antenna cross correlation function is derived from the mathematical analysis and is based on the below mentioned assumptions.

The new geometric model for a two element transmit antenna and a two element receive antenna (referred here-in as a 2 x 2 MIMO channel, shown in Figure 3.1) is developed by using the multi-element antenna system in [64] as a basis. The fixed receiver/user has a multi-element antenna system with receiver elements RE_m, $RE_n, ...RE_x$; where $x = 2$ here. In this case the 2 x 2 MIMO channel antenna elements form a uniform linear array (ULA) of monopoles that radiate omni-directionally. From the scatterers at TS_l, from the transmitter there is a very narrow dominant beamwidth and the receiver obtains the signal from a large number of surrounding local scatterers, that need not necessarily be isotropic, but the scatterers impinge at point RS_i, as shown in Figure 3.1. It is also assumed that the i^{th} scatterer is planar and could be the sum of different coherent scatterers, which can be of distance R from the center O_R of the RX antenna array.

D is the distance between the transmitter and the receiver and the angles α_{pq} and β_{mn} are the angles the antenna arrays form with the horizontal axis at the transmitter and receiver, respectively. The planar wave formed by the scattering around the receiver can be represented as the angle from the point ϕ_R to the point RS_i. Similarly there are l omnidirectional scatterers at the TX and they lie on a ring of radius L. The l^{th} scatterer at the TX is denoted by TS_l, and θ_T is the angle from the horizontal axis of the antenna array and this scatterer. It is assumed that in this indoor environment the local scattering at the TX is omni-directional and the radius of scatters is very small, that is $L \ll D$ and $L < R$. It is also assumed that the angle of the arc that O_T would form on the circumference of circle O_R is small (typically less than 15^0) [86], for $D \gg R$, that is the angle formed between TS_l and RS_i is small. In this model the line of sight (LOS) component is not considered, but a Rayleigh PDF in a picocell type environment is

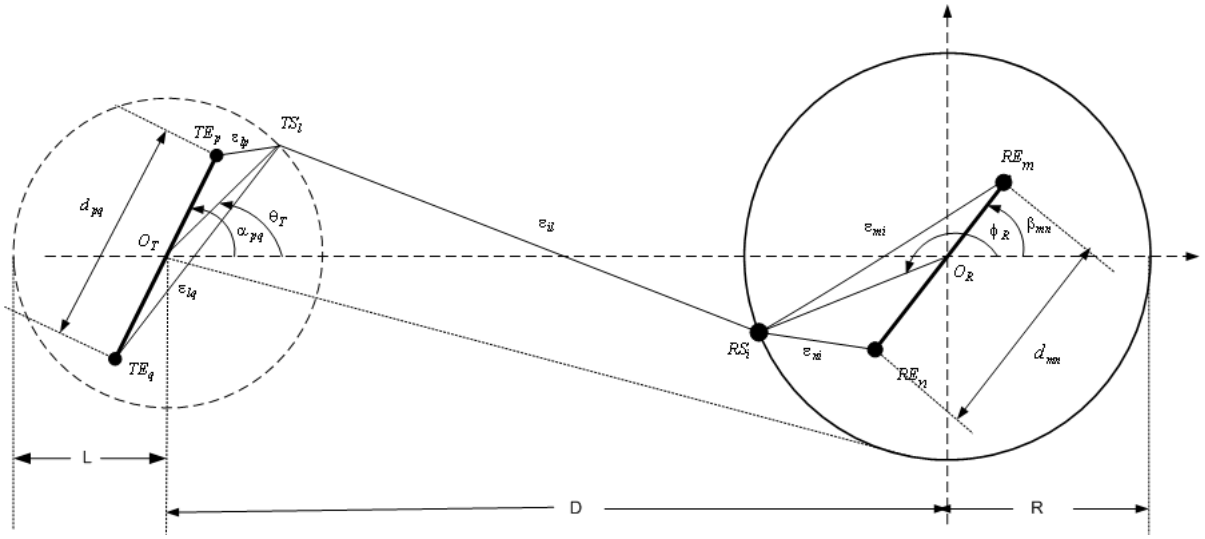

FIGURE 3.1: Geometric Model for a 2x2 MIMO channel

assumed. This MIMO system can be written using the complex baseband notation as

$$\mathbf{y}(t) = \mathbf{H}(t) * \mathbf{x}(t) + \mathbf{n}(t) \tag{3.1}$$

where $\mathbf{H}(t)$ is the channel matrix of complex path gains $h_{ij}(t)$ between TX_j and RX_i, $\mathbf{n}(t)$ is the complete envelope of the AWGN with zero mean from each receive element, $\mathbf{x}(t)$ is the transmit vector made up of the signal transmitted from each TX, $n_t \times 1$ antenna element and $\mathbf{y}(t)$ is the receive vector made up of the signal from each point RS_i.

It is assumed that any gain and phase shift introduced by a scatterer at the transmitter is different to that received at point RS_i. Also, the scatterers at point RS_i are of approximately the same angle, implying that the gain and phase shift is the same at point RS_i and the scatterers do not change with time (that is fixed) in this case. It is also assumed that

$$\lim_{L,N\to\infty} \frac{1}{L}\frac{1}{N} \sum_{i=1}^{L}\sum_{i=1}^{N} E[g_{il}^2] = 1 \tag{3.2}$$

where g_{il} is the amplitude of the wave that comprises of the joint gain of scatterers TS_l and RS_i and L, N are the number of independent scatterers TS_l around the TX, and RS_i around the RX, respectively.

Based on the statistical properties of the described channel, the central limit theorem implies that h_{mp} is a low pass, zero mean, complex Gaussian random process. This means that the envelope $|h_{mp}(t)|$ is a Rayleigh (fading) process. Hence, for the above no line of sight (NLOS),

frequency non-selective, MIMO fading channel propagation scenario, the channel gain, $h_{mp}(t)$, for the link $TE_p - RE_m$ as shown in Figure 3.1, can be written as

$$h_{mp}(t) = \sqrt{\Omega_{mp}} \lim_{L,N\to\infty} \frac{1}{\sqrt{LN}} \sum_{l=1}^{L} \sum_{i=1}^{N} g_{il} \times \exp\left\{ j\psi_{il} - \frac{j2\pi}{\lambda} \left[\varepsilon_{lp} + \varepsilon_{il} + \varepsilon_{mi}\right] \right\} \tag{3.3}$$

where $\psi_i l$ is the joint phase shift introduced by the l_{th} scatterer at TS_l and the i^{th} scatterer at RS_i, $\{\psi_{il}\}_{i,l=1}^{\infty}$ is the iid random process with uniform distribution over the interval $[-\pi, \pi]$, ϵ_{lp}, ϵ_{il} and ϵ_{mi} are the distances as shown in Figure 3.1 which are functions of the angle of departure (AOD) and angle of arrival (AOA), Ω_{mp} is the power transferred through the link from transmit antenna p, through to receive antenna m and λ is the wavelength of the carrier RF signal.

The transpose of the channel gain, $h_{nq}(t)$, for the link $TE_q - RE_n$ shown in Figure 3.1 is

$$h^*_{nq}(t) = \sqrt{\Omega_{nq}} \lim_{L,N\to\infty} \frac{1}{\sqrt{LN}} \sum_{l=1}^{L} \sum_{i=1}^{N} g_{il} \times \exp\left\{ -j\psi_{il} + \frac{j2\pi}{\lambda} \left[\varepsilon_{lq} + \varepsilon_{il} + \varepsilon_{ni}\right] \right\} \tag{3.4}$$

where Ω_{np} is the power transferred through the link from TX antenna q, through to RX antenna n.

3.3 MODEL ANALYSIS

Using the geometric model described in the previous section as a basis, a joint space-time cross correlation function is derived.

The space-time correlation between the two links, $TE_p - RE_m$ and $TE_q - RE_n$, as shown in Figure 3.1, can be defined as

$$\rho_{mp,nq}(\tau) = E[h_{mp}(t).h^*_{nq}(t+\tau)/\sqrt{\Omega_{mp}\Omega_{nq}}] \tag{3.5}$$

where τ is an arbitrary time delay, $*$ indicates the complex conjugate and $\Omega_{mp,nq}$ is the power transfer through $TE - RE$ in a specific $TE_{p,q} - RE_{m,n}$ antenna link element.

The cross correlation function for the scenario in Figure 3.1 can be represented independently of D accordingly as

$$\rho_{mp,nq}(\tau) = \lim_{L,N\to\infty} \frac{1}{L}\frac{1}{N} \sum_{l=1}^{L} \sum_{i=1}^{N} E[g_{il}^2] \times \exp\left\{ \frac{-j2\pi}{\lambda} \left[\varepsilon_{lp} - \varepsilon_{lq} + \varepsilon_{mi} - \varepsilon_{ni}\right] \right\} \tag{3.6}$$

For large number of scatterers L and N and considering the fact the channel is in a quasi-static state, with the receiver at a fixed position, one can write

$$\rho_{mp,nq}(\tau, t) = \rho_{mp,nq}(\tau) = \rho_{mp,nq} \tag{3.7}$$

and hence re-write (3.6) as an integral form of

$$\rho_{mp,nq} = \int_{-\pi}^{\pi} \int_{-\pi}^{\pi} \exp\left\{ \frac{-2\pi j}{\lambda} \left[\varepsilon_{lp} - \varepsilon_{lq} + \varepsilon_{mi} - \varepsilon_{ni}\right] \right\} \times p(\theta_T) p(\phi_R) d\theta_T d\phi_R \tag{3.8}$$

where $p(\theta_T)$ is the probability distribution function of the uniform scatterers at the TX and $p(\theta_R)$ is the probability distribution function of the scatterers at the RX respectively.

Equation (3.8) can now be written in terms of the scatterer angles shown in Figure 3.1 as

$$\rho_{mp,nq} = \int_{-\pi}^{\pi} \int_{-\pi}^{\pi} \exp\left\{ \frac{-2\pi j}{\lambda} \left[\varepsilon_{\theta p} - \varepsilon_{\theta q} + \varepsilon_{m\phi} - \varepsilon_{n\phi}\right] \right\} \times p(\theta_T) p(\phi_R) d\theta_T d\phi_R \tag{3.9}$$

where $\varepsilon_{\theta p,q}$ is the distance from $TE_{p,q}$ to the ring of scatterers TS_l at an angle θ_T from the scattering center, O_T, and $\varepsilon_{\phi m,n}$ is the distance from $RE_{m,n}$ to the ring of scatterers RS_i at an angle ϕ_R from the scattering center O_R.

Using Figure 3.1 one can write the distances in (3.9) for the TX and RX side using the Cosine Law as

$$\varepsilon_{lp}^2 = L^2 + \frac{d_{pq}^2}{4} - d_{pq} L \cos(\alpha_{pq} - \theta_T) \tag{3.10}$$

$$\varepsilon_{\theta p}^2 = L^2 + \frac{d_{pq}^2}{4} - d_{pq} L \cos(\alpha_{pq} - \theta_T) \tag{3.11}$$

$$\varepsilon_{lq}^2 = L^2 + \frac{d_{pq}^2}{4} + d_{pq} L \cos(\alpha_{pq} - \theta_T) \tag{3.12}$$

$$\varepsilon_{\theta q}^2 = L^2 + \frac{d_{pq}^2}{4} + d_{pq} L \cos(\alpha_{pq} - \theta_T) \tag{3.13}$$

$$\varepsilon_{mi}^2 = R^2 + \frac{d_{mn}^2}{4} - d_{mn} R \cos(\phi - \beta_{mn}) \tag{3.14}$$

$$\varepsilon_{m\phi}^2 = R^2 + \frac{d_{mn}^2}{4} - d_{mn}R\cos(\phi - \beta_{mn}) \tag{3.15}$$

$$\varepsilon_{ni}^2 = R^2 + \frac{d_{mn}^2}{4} + d_{mn}R\cos(\phi - \beta_{mn}) \tag{3.16}$$

$$\varepsilon_{n\phi}^2 = R^2 + \frac{d_{mn}^2}{4} + d_{mn}R\cos(\phi + \beta_{mn}) \tag{3.17}$$

Assuming that $R > L$, $L \gg d_{pq}, d_{mn}$ and $R \gg d_{pq}, d_{mn}$, such that $\frac{d_{pq}^2}{4}$ is negligible with respect to the other terms, one can re-write equations (3.11), (3.13), (3.15), (3.17) as

$$\frac{\varepsilon_{\theta p}^2}{L^2} = 1 - \frac{d_{pq}\cos(\alpha_{pq} - \theta_T)}{L} \tag{3.18}$$

$$\frac{\varepsilon_{\theta q}^2}{L^2} = 1 + \frac{d_{pq}\cos(\alpha_{pq} - \theta_T)}{L} \tag{3.19}$$

$$\frac{\varepsilon_{m\phi}^2}{R^2} = 1 - \frac{d_{mn}\cos(\phi - \beta_{mn})}{R} \tag{3.20}$$

$$\frac{\varepsilon_{n\phi}^2}{R^2} = 1 + \frac{d_{mn}\cos(\phi + \beta_{mn})}{R} \tag{3.21}$$

Now using the relation $\sqrt{1+x} \approx 1 + \frac{x}{2}$ for $|x| \ll 1$, the above equations (3.18) – (3.21) can be simplified to

$$\varepsilon_{\theta p} \approx L - \frac{d_{pq}}{2}\cos(\alpha_{pq} - \theta) \tag{3.22}$$

$$\varepsilon_{\theta q} \approx L + \frac{d_{pq}}{2}\cos(\alpha_{pq} - \theta) \tag{3.23}$$

$$\varepsilon_{m\phi} \approx R - \frac{d_{mn}}{2}\cos(\phi - \beta_{mn}) \tag{3.24}$$

$$\varepsilon_{n\phi} \approx R + \frac{d_{mn}}{2}\cos(\phi - \beta_{mn}) \tag{3.25}$$

One can write the joint correlation in (3.7) as an approximate product of transmit antenna and receiver antenna correlation [1, 64, 71].

$$\rho_{mp,nq} = \rho_{pq}^{TX} \rho_{mn}^{RX} \tag{3.26}$$

Hence

$$\rho_{pq}^{TX} = \int_{-\pi}^{\pi} \exp\left\{\frac{-j2\pi}{\lambda}\left[\varepsilon_{\theta p} - \varepsilon_{\theta q}\right]\right\} p(\theta_T) d\theta_T \tag{3.27}$$

and

$$\rho_{mn}^{RX} = \int_{-\pi}^{\pi} \exp\left\{\frac{-j2\pi}{\lambda}\left[\varepsilon_{m\phi} - \varepsilon_{n\phi}\right]\right\} p(\phi_R) d\phi_R \tag{3.28}$$

It is assumed that this TX could be for example in a wide-open hallway, where there is uniform (isotropic) scattering around the close proximity of L for this uniform linear array. This will herein be represented by a PDF [37], $p(\theta_T) = \frac{1}{2\pi}$. Substituting (3.22) and (3.23) and for $p(\theta_T)$ into (3.27), one can re-write (3.27) as

$$\rho_{pq}^{TX} = \int_{-\pi}^{\pi} \exp\left\{\frac{-j2\pi}{\lambda}\left[-d_{pq}\cos(\alpha_{pq} - \theta_T)\right]\right\} \frac{1}{2\pi} d\theta_T \tag{3.29}$$

By applying the trigonometric functions in [87], one can reduce (3.29) to

$$\rho_{pq}^{TX} = \frac{1}{2\pi} \int_{-\pi}^{\pi} \exp jc_{pq}\left[\sin\alpha_{pq}\sin\theta_T + \cos\alpha_{pq}\cos\theta_T\right] d\theta_T \tag{3.30}$$

where $c_{pq} = \frac{2\pi d_{pq}}{\lambda}$

Assuming that the scattering distribution at the RX side follows the von Mises PDF [64] given as:

$$p(\phi) = \frac{\exp\left[k\cos(\phi - \mu)\right]}{2\pi I_0(k)} \tag{3.31}$$

where $I_0(\cdot)$ is the zero-order modified Bessel function, $\phi \in [-\pi, \pi)$, $\mu \in [-\pi, \pi)$ is the mean direction of the AOA seen by the user, and k is the isotropic scattering parameter.

Substituting (3.31) into (3.28), one can re-write (3.28) as

$$\rho_{mn}^{RX} = \frac{1}{2\pi I_o(k)} \int_{-\pi}^{\pi} \exp\left\{\frac{j2\pi d_{mn}}{\lambda}\cos(\phi_R - \beta_{mn}\right\} \exp\left\{k\cos(\phi_R - \mu)d\phi_R\right\} \tag{3.32}$$

Setting $b_{mn} = \frac{2\pi d_{mn}}{\lambda}$, (3.32) can be written as

$$\rho_{mn}^{RX} = \frac{1}{2\pi I_o(k)} \int_{-\pi}^{\pi} \exp\left\{jb_{mn}\cos(\phi_R - \beta_{mn}) + k\cos(\phi_R - \mu)\right\} d\phi_R \tag{3.33}$$

Using the trigonometric functions in [87], (3.33) can be reduced to

$$\rho_{mn}^{RX} = \frac{1}{2\pi I_o(k)} \int_{-\pi}^{\pi} \exp\left\{\sin\phi_R\left[jb_{mn}\sin\beta_{mn} + \sin\mu\right]\right\} \times \exp\left\{\cos\phi_R\left[jb_{mn}\cos\beta_{mn} + k\cos\mu\right]\right\} d\phi_R \tag{3.34}$$

Using the integration rule in [87], equation $3.338 - 4$, page 336 is given as

$$\int_{-\pi}^{\pi} \exp(y\sin x + z\cos x).dx = 2\pi I_0(\gamma) \tag{3.35}$$

where $\gamma = \sqrt{y^2 + z^2}$.

Hence one can express (3.30) as

$$\rho_{pq}^{TX} = I_0(jc_{pq}) \tag{3.36}$$

Similarly (3.35) can be applied to (3.34) to give

$$\rho_{mn}^{RX} = \frac{1}{2\pi I_0(k)} \int_{-\pi}^{\pi} \exp\left\{(jb_{mn}\cos(\phi_R - \beta_{mn})) + k\cos(\phi_R - \mu)\right\} d\phi_R \tag{3.37}$$

which is reduced to

$$\rho_{mn}^{RX} = \frac{1}{I_0(k)} I_0((jb_{mn}\sin\beta_{mn} + k\sin\mu)^2 + (jb_{mn}\cos\beta_{mn} + k\cos\mu)^2)^{1/2} \tag{3.38}$$

Applying the basic trigonometric identities to (3.38) and simplifying it gives

$$\rho_{mn}^{RX} = \frac{1}{I_0(k)} I_0\left(k^2 - b_{mn}^2 + j2kb_{mn}\cos(\mu - \beta_{mn})\right)^{1/2} \tag{3.39}$$

where $b_{mn} = \frac{2\pi d_{mn}}{\lambda}$.

The closed form expressions for the antenna correlations are represented in equations (3.36) and (3.39) for the TX and RX respectively. This allows one to solve these expressions analytically in order to determine some of the model characteristics and its impact on the capacity of the MIMO system.

3.4 RESULTS

The spatially and temporally correlated variates are generated by generating an $n_R \times n_T$ matrix $\mathbf{U}$, of random, independent and zero mean complex Gaussian variates with unit variance. Using $\mathbf{X} = \mathbf{U}\sqrt{\mathbf{R}_T}$, the $n_R \times n_T$ with the desired transmit antenna correlation is calculated. $\mathbf{R}_T$ is the $n_T \times n_T$ matrix of the transmit antenna correlation, with matrix elements ρ_{pq}^{TX} calculated from (3.39). Matrix $\mathbf{H}$ is then calculated using $\mathbf{X}$ as the input vector with the desired correlation matrix elements calculated from (3.39).

The normalized MIMO channel capacity, C, in b/s/Hz for a particular realization $\mathbf{H}$ can be expressed [9, 15] as

$$C = \log_2 \det\left(I_{n_R} + \frac{\rho}{n_T}\mathbf{H}\mathbf{H}^H\right) \tag{3.40}$$

where $\mathbf{H}^H$ is the conjugate transpose, det is the determinant of the matrix, I_{n_R} is a $n_R \times n_T$ identity matrix, and, ρ is the average SISO SNR at each of the n_R elements.

Many different random channel realizations were considered and the capacity for each of these realizations were computed and then statistically distributed. From this, the cumulative distribution function (cdf) for the capacity was calculated by taking into account the effects of the various parameters derived in the model.

Uniform linear arrays (ULA's) were considered in this case with the following general parameters applied to this model.

SNR = ρ = 20 dB
TX carrier frequency = 2.4 GHz
$\alpha_{pq} = \beta_{mn} = \pi/2$
k = 0.25
D = 20 metres
R = 0.2 metres

Figure 3.2 shows the complimentary cumulative distribution function (ccdf) versus capacity for varying number of TX, n_T, and receiver, n_R, antenna elements. Here $\mu = \pi$, $\lambda = 0.125$,

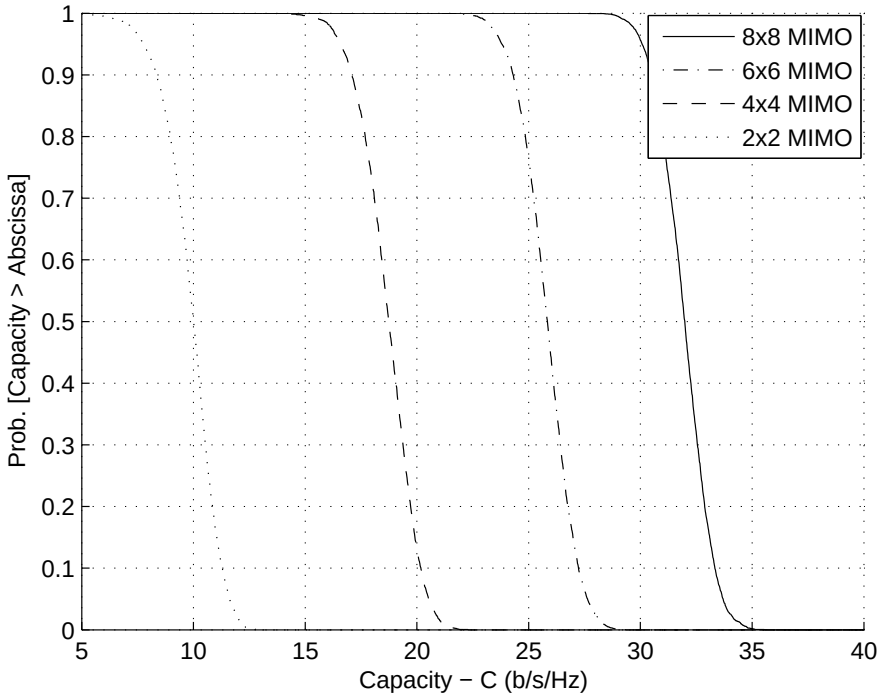

FIGURE 3.2: ccdf versus capacity for varying antenna elements, $n_T = n_R$

$d_{mn} = d_{pq} = 0.5\lambda$, ρ = 20 dB and $k = 25$. One observes [37] that the capacity increases as the number of antenna elements in the MIMO system increases from two to eight elements for some fixed outage probability. Increasing the number of antenna elements, both at the transmitter and receiver ends, makes the greatest impact on the channel capacity when compared to the other parameters. Based on the indoor MIMO measurement campaign undertaken and described herein and in [88], it was observed that for $n_R = n_T = 8$, with SNR = 20 dB, the capacity was 95% accurate for an outage probability greater than 90% for location 2 [89], having characteristics almost identical to the described model.

Figure 3.3 indicates the ccdf for the case where the antenna element spacing d_{mn} is varied from 0.25λ up to 4λ, referred to as d in Figure 3.3. The SNR=20 dB, $k = 25$, $\mu = \pi$, $d_{pq} = 0.5\lambda$ and $n_R = n_T = 2$ were used in the computation.

For the above chosen parameters, one observes that for an outage probability of greater than 95%, the capacity can vary by approximately 2b/s/Hz for $0.25\lambda \leqslant d \leqslant 4.0\lambda$. The RX antenna array element spacing of $d_{mn} > 4.0\lambda$ and for $d_{mn} < 0.25\lambda$ resulted in a negligible effect on

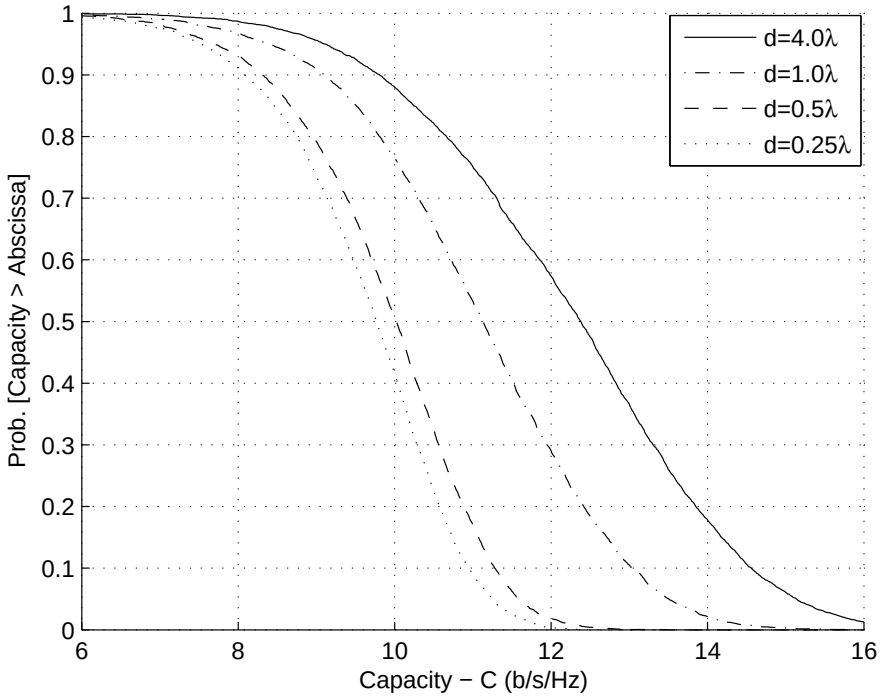

FIGURE 3.3: ccdf versus capacity for varying antenna spacing, d=d_{mn}

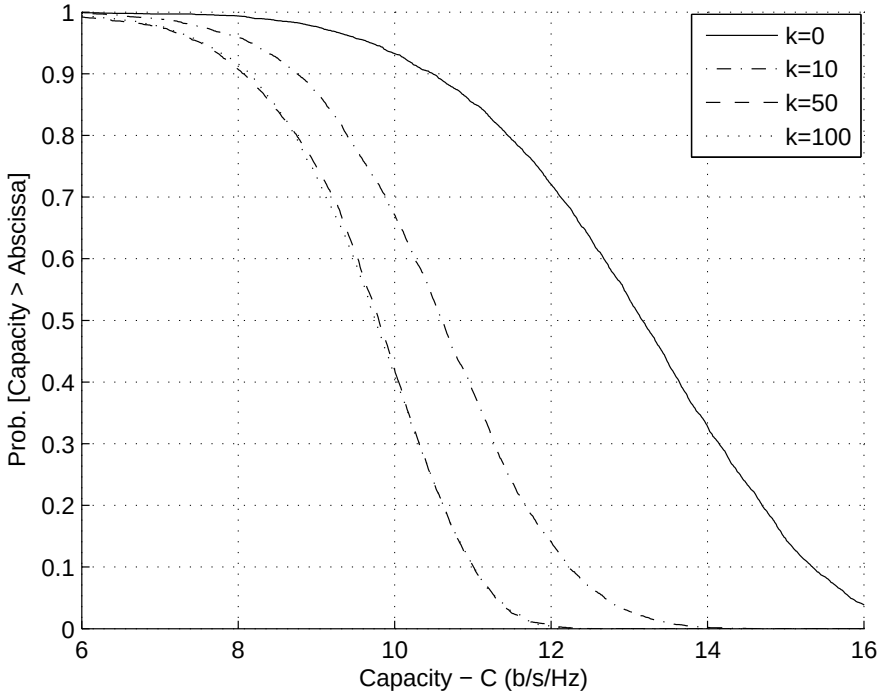

FIGURE 3.4: ccdf versus capacity for varying scattering parameter, k

the capacity for a specific outage probability. As expected, increasing the element spacing d_{pq} resulted in a trend similar to that in Figure 3.3, except that it occurred at a higher capacity.

Figure 3.4 shows the effect of the scattering parameter k on the capacity of the 2×2 MIMO system where the SNR=20 dB and $d_{mn} = d_{pq} = 0.5\lambda$. From the isotropic scattering $(k = 0)$ case to the highly non-isotropic scattering at the RX, the capacity could decrease by less than 2.5 b/s/Hz for an outage probability beyond 95%. One observes that for $k > 50$ the capacity does not vary significantly for some fixed high outage probability. This implies that in an indoor environment where there are significantly large number of local scatterers, using a k value of greater than 50 should not have any significant impact upon the degradation in channel capacity.

For $k = 25$, $n_R = n_T = 2$, $d_{mn} = d_{pq} = \lambda$ and $\rho = 20$ dB the plot of capacity outage probability for the variation in RX antenna array orientation, β_{mn} was determined as shown in Figure 3.5. For the antenna orientation variation from $\pi/2$ to 0 radians, the capacity could decrease by less than 3.0 b/s/Hz for an outage probability of greater than 95%. As expected from a uniform linear antenna array, rotating the RX antenna array between π and $\pi/2$ radians has a similar effect to that as shown in Figure 3.5.

Figure 3.6 validates the developed model behavioral characteristics and confirms the effect of SNR on the channel capacity as proposed in [9]. This was simulated for the parametric settings of $d_{mn} = d_{pq} = 0.5\lambda$, $n_R = n_T = 2$ and $k = 25$. One also observes, as expected, that for an increase of SNR by 3dB the capacity maximally increased by approximately 1 b/s/Hz for an outage probability beyond 90%.

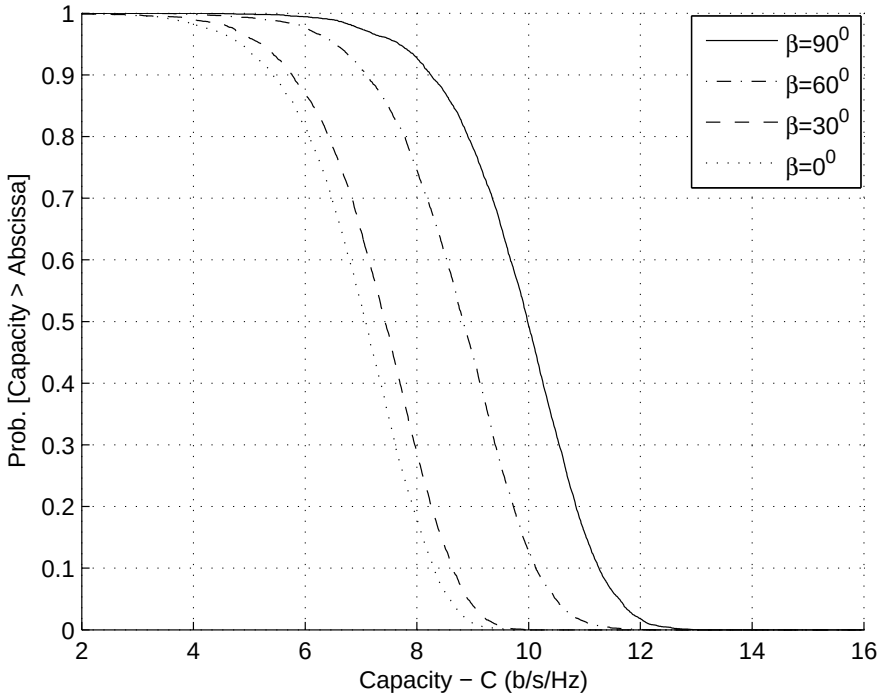

FIGURE 3.5: ccdf versus capacity for varying RX antenna orientation, β

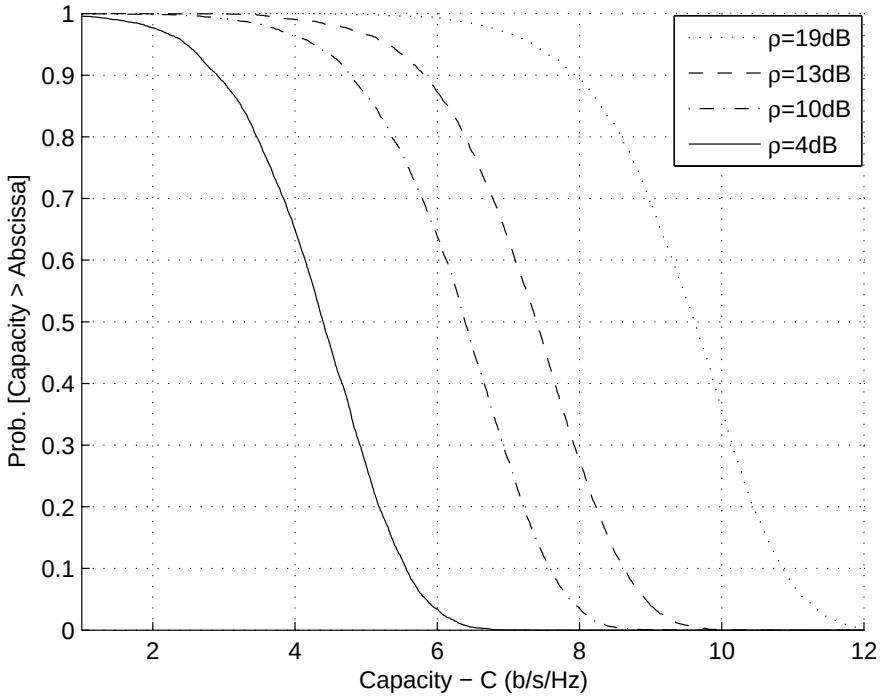

FIGURE 3.6: ccdf versus capacity for varying SNR(ρ) in dB

3.5 CONCLUSION

Performance gains of MIMO systems have been explored by theoretical studies involving stochastic channel models, ray tracing techniques and direct channel measurements. Arguably geometric modelling could be the most cost effective and time efficient technique. A geometrically based model as a way to characterize a MIMO channel in a fixed wireless indoor environment has successfully been derived. The geometric model that was presented led to the derivation of the joint correlation function as well as the receiver and transmitter antenna correlation functions in a neat, compact and closed form. The model incorporates key characteristics such as the type of antennas, configuration of the antenna array, the number of antenna elements, antenna element spacing, degree of scattering at the receive antenna and antenna orientation so as to exploit the MIMO channel performance gains. In comparison to all the described parameters, the increase in the number of antenna elements made the greatest impact and contribution to the increase in channel capacity while antenna spacing affecting the spatial correlation was another significant contributor.

CHAPTER FOUR

WIDEBAND MIMO MEASUREMENT SYSTEM

4.1 INTRODUCTION

For many realistic environments and systems, limited multipath or compact arrays lead to channels with non-Rayleigh iid statistics. Research in MIMO channel characterization and modelling [90, 91] indicates that MIMO channels have very complicated behavior that is only captured by direct measurement (see [19] and references therein). Although theoretical channel capacity may be insensitive to the exact structure of the channel, realistic system design may depend heavily on this structure. For example, double-directional clustering observed in measured channels suggests the advantage of directional elements [47]. Space-time codes designed with an understanding of the channel structure can outperform codes designed with the iid assumption [7]. Furthermore, performance in realistic scenarios with multiple users may depend more heavily on channel structure than the single-user channel [92]. Since a detailed understanding of the channel behavior is required for optimal system design and accurate performance assessment, direct measurement of MIMO channels continues to be important. To partially fill the gap between the high cost of commercial channel sounders and the long time associated with in-house development, a new low-cost wideband MIMO channel sounder has been developed. It is operationally similar to commercial sounders [93], and can be constructed at moderate cost by leveraging conventional off-the-shelf components (COTS), instruments and modules. The purpose of developing this low-cost channel sounder was to obtain indoor channel data for modelling research presented in this thesis. The objective of this chapter is to give the reader an overview of the developed and deployed system. The reader can refer to other sources

such as [88, 94, 95] for more detail should anyone wish to develop such a system.

4.2 SYSTEM OVERVIEW

The design goals that were envisioned with the channel sounder at the University of Pretoria are:

- *Rapid Development*

The idea was that measurement equipment, instruments and mainly off-the-shelf components should be used so that the system development time and risk are reduced. With the experience and expertise available such a system can be deployed within six to eight months.

- *Affordability*

Considering the financial constraints, the implemented system should be affordable to build and integrate.

- *Antenna Arrays*

The system should be capable of supporting up to a maximum of eight transmitters and receivers and the system should be flexible so that one could change the orientation of the antennas without much difficulty.

- *System Flexibility*

The components in the system should be flexible and modular, allowing easy reconfiguration for different measurement scenarios. It should be easily modified to accommodate outdoors and mobile measurement scenarios.

- *Frequency Range*

It was envisaged that one should be able to undertake measurements in the 2-8 GHz band as this seemed to be a band with greater focus of attention and relevance. However, measurements were taken at 2.4 GHz and 5.2 GHz carrier frequencies since these were in the ISM band and did not require any permission from the regulator to use them in South Africa. These two frequencies also provided a reasonable separation to base any of the frequency scaling issues discussed.

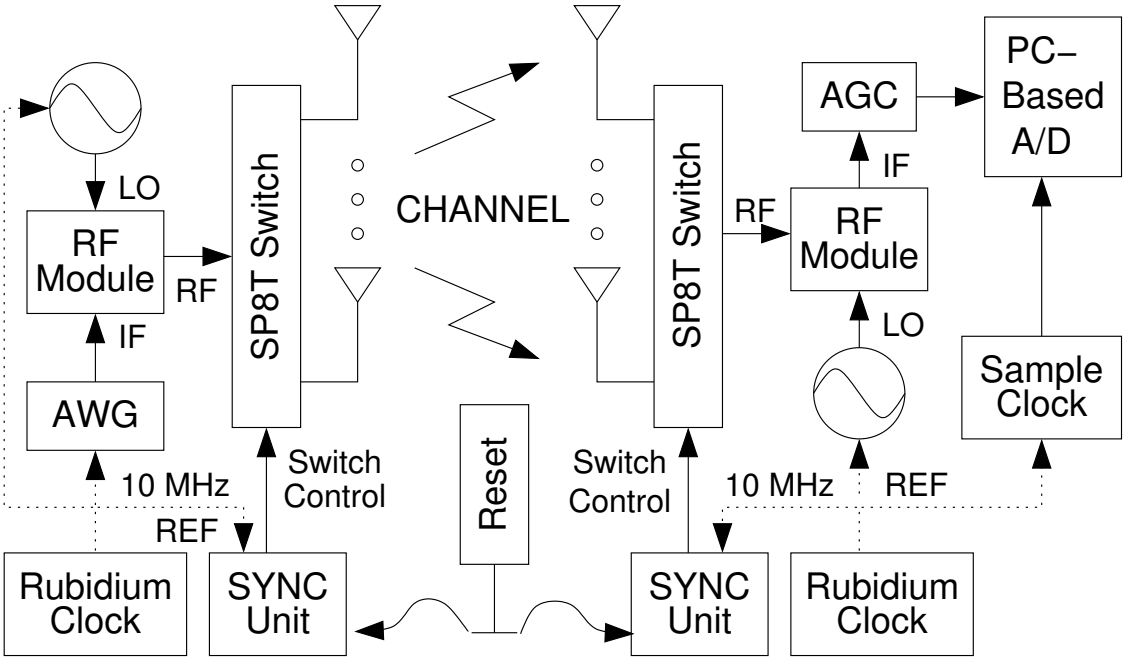

FIGURE 4.1: High level diagram of the wideband MIMO channel sounder

- *Bandwidth*

The intention was to be probing bandwidths in excess of 120 MHz but the instrumentation allowed only 80 MHz of instantaneous bandwidth. However this was considered sufficient in this study of current realistic wideband MIMO system communication signalling.

The system implemented is shown in Figure 4.1 with the popular ”switched array” architecture being employed where various antenna elements are connected to the TX and RX via high speed absorptive microwave switches. ”True array” techniques that measure multiple TX/RX channels simultaneously can also be employed but these tend to be expensive, they require longer development time and can complicate maintenance. With the availability of high speed absorptive microwave switches with switching times in the order of 25 ns, as well as having an off-time to take care of transients, the non-ideal response induced by the ”switched array” is negligible.

At the TX in the system shown in Figure 4.1, a radio frequency (RF) module mixes the wideband signal from the arbitrary generator (AWG) with the local oscillator (LO) to up-convert to the desired microwave carrier. This signal is fed into an RF power amplifier and then into a single pole eight-throw (SP8T) microwave switch to one of the eight TX antennas. At the

RX, the signals on the antennas are routed via another SP8T switch to an RF block, consisting of a low noise amplifier (LNA), a single stage down-conversion to an intermediate frequency (IF) and then through a low-pass filter (LPF). This IF signal is amplified by an automatic gain control (AGC) circuit and stored onto a computer hard disk drive using a high-speed PC-based A/D card (example GaGe). The accurate co-ordination of the switching of TX and RX arrays is accomplished by a custom-designed synchronization (SYNC) unit [94]. Timing in the system is referenced by highly stable 10MHz rubidium time/frequency oscillators, ensuring proper timing and phase coherence throughout the system.

4.3 SYSTEM COMPONENTS

This section outlines the respective hardware components used in the wideband MIMO channel sounder.

4.3.1 Transmitter Subsystem

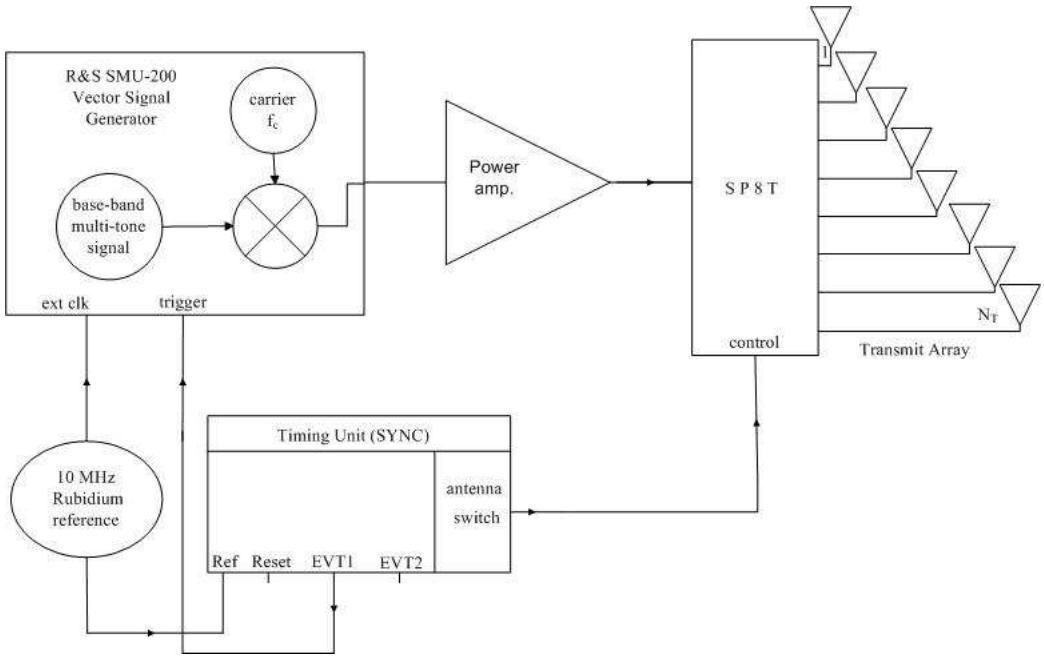

FIGURE 4.2: High level block diagram of the TX subsystem

The TX subsystem implemented at the University of Pretoria (UP) is shown in Figure. 4.2. This system is essentially used to sequentially excite the wireless channel across an instantaneous bandwidth of 80MHz for each of the N_T antennas. After generating a baseband

probing signal on the AWG, an RF module mixes this signal to the LO to up-convert to the microwave switch to one of eight outputs. In this implementation the Rohde & Schwarz SMU200 vector signal generator is used to generate the base-band signal and up-converts it to the desired microwave center frequency. This signal is then amplified by a high power RF amplifier and then fed into the SP8T microwave switch. Each of the eight antennas are connected to the SP8T. The SYNC unit supplies transistor-transistor-logic (TTL) enabled lines to the microwave switch and an event trigger releases timing bursts to the AWG located in the SMU200 unit.

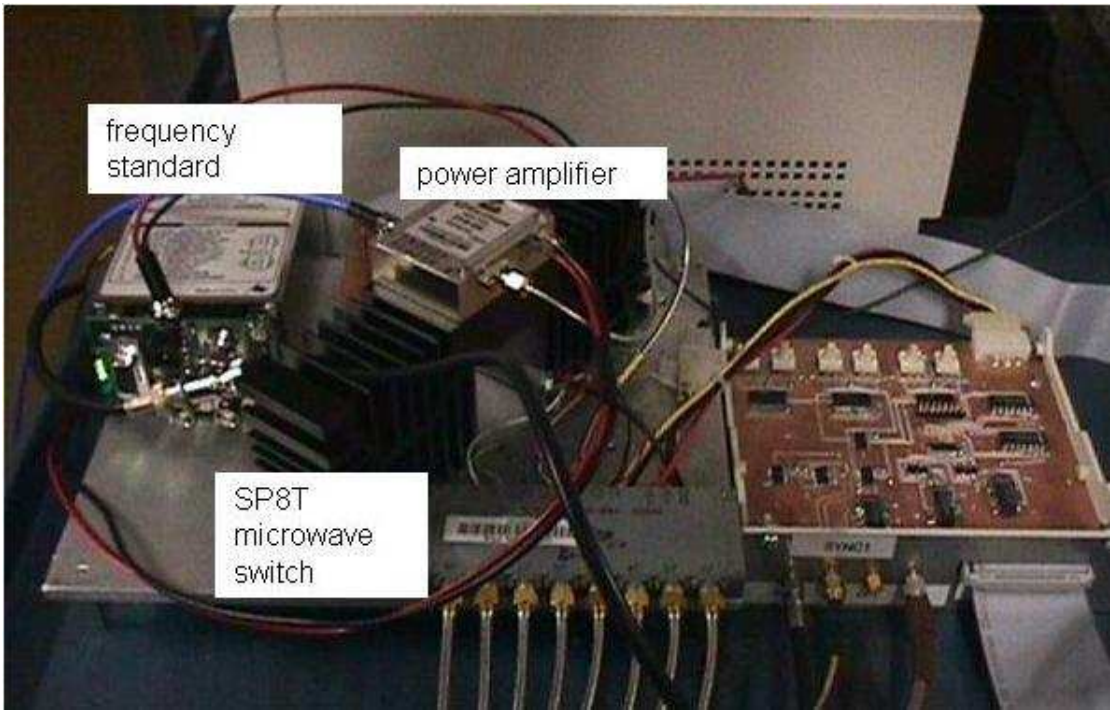

FIGURE 4.3: Transmit RF module

The RF module as shown in Figure 4.3 houses primarily the microwave components required for the up-conversion of the base-band probing signal to the microwave carrier and routing of the signal to the proper output antenna via the SP8T microwave switch.

4.3.2 Receiver Subsystem

Figures 4.4 and 4.5 show a block diagram of the RX subsystem, whose purpose is to sample the received wideband signal for $N_T \times N_R$ antenna combinations. For each combination, the RX-RF module routes the signal from one of the N_R RX antennas to a broadband 40 dB gain

LNA, followed by a mixer for a single-stage down conversion to an intermediate

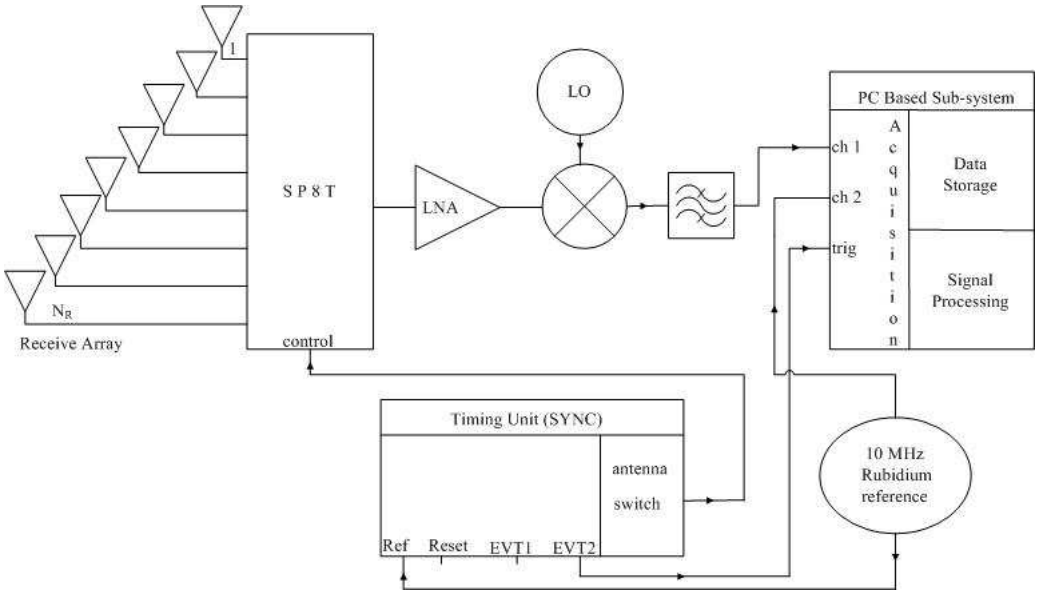

FIGURE 4.4: High level block diagram of the RX subsystem

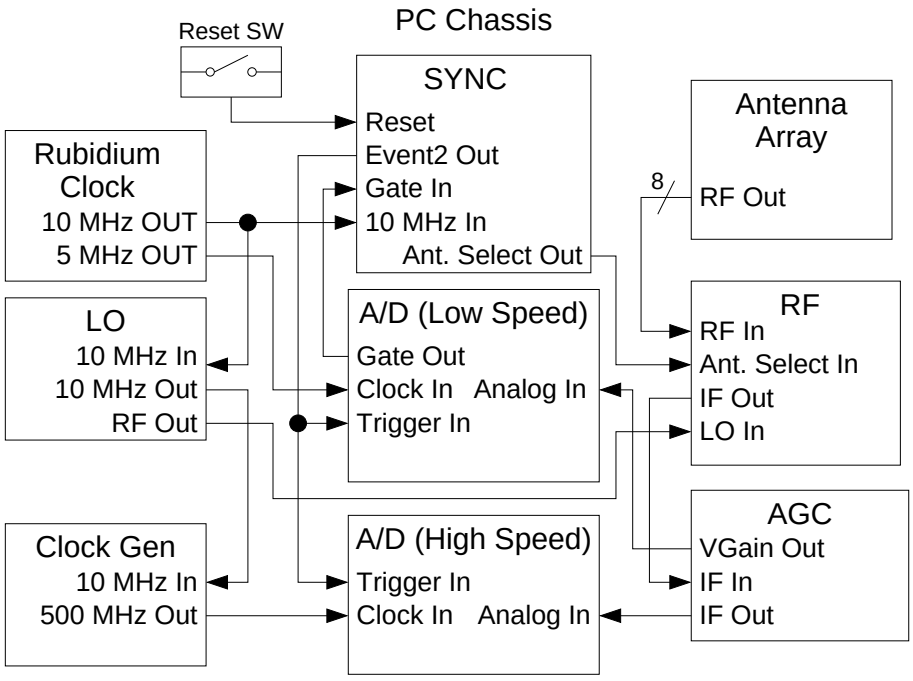

FIGURE 4.5: Block Diagram of the RX subsystem connections

frequency (IF) of 100 MHz. The IF signal is low-passed filtered, fed to the AGC module with 0-40 dB of IF gain, and sampled on a high speed 500 MSa/s analog-to-digital (A/D) card. The voltage gain signal of the AGC is a power detector output whose voltage is proportional to the signal in dB, and this signal is sampled by an inexpensive low-speed multifunction

input-output (I/O) (MIO) board.

The rate of switching on the SYNC unit is $1/N_T$ relative to the TX subsystem so as to allow the channel from all N_T transmitters to be measured for each of the N_R receivers. The high- and low- speed A/D boards (for measuring the wideband IF waveform and gain level respectively) are triggered simultaneously by the EVT1 (event1) signal, which is asserted for each complete scan of the N_R antennas.

The use of two A/D boards can create potential problems for triggering, since the software must sequentially arm the two boards, thus creating a critical section where one board can trigger while the other is not ready. To avoid this potential hazard, the SYNC unit has an additional Gate input, which, when negated, inhibits event outputs. Thus, Gate is first negated (using a digital output of the MIO board), the two cards are sequentially armed, and finally Gate is asserted. Subsequent event signals then trigger both boards simultaneously.

Although most instruments use the 10 MHz rubidium clock directly, the A/D boards require direct input of an external sample clock. A function (or clock) generator provides a 500 MHz sine wave signal to the high-speed A/D board, and an auxiliary 5 MHz square wave output on the rubidium oscillator drives the low-speed A/D board clock. A large change in the RX power level with movement or time is possible due to multipath fading and shadowing in a communications environment. In order to capture this, measurement sensitivity using an AGC circuit was implemented using a simple AD8367 based circuit that provides 0-40 dB of IF gain. The time constant of the AGC loop is approximately 5 μs, so that the gain can adapt for each new TX/RX pair. A fairly low-speed (1MS/s) A/D board samples the output voltage of the AGC loop, from which the gain can be computed and the true waveform recovered.

4.3.3 Synchronization Module

The key to the operation of the switched array technique in MIMO wideband channel sounding is the synchronization. There needs to be co-ordinated switching as at the TX the signal bursts and at the RX data acquisition needs to take place within a set time window. These tasks are accomplished by a synchronization unit (SYNC) as shown in Figure 4.7. This SYNC

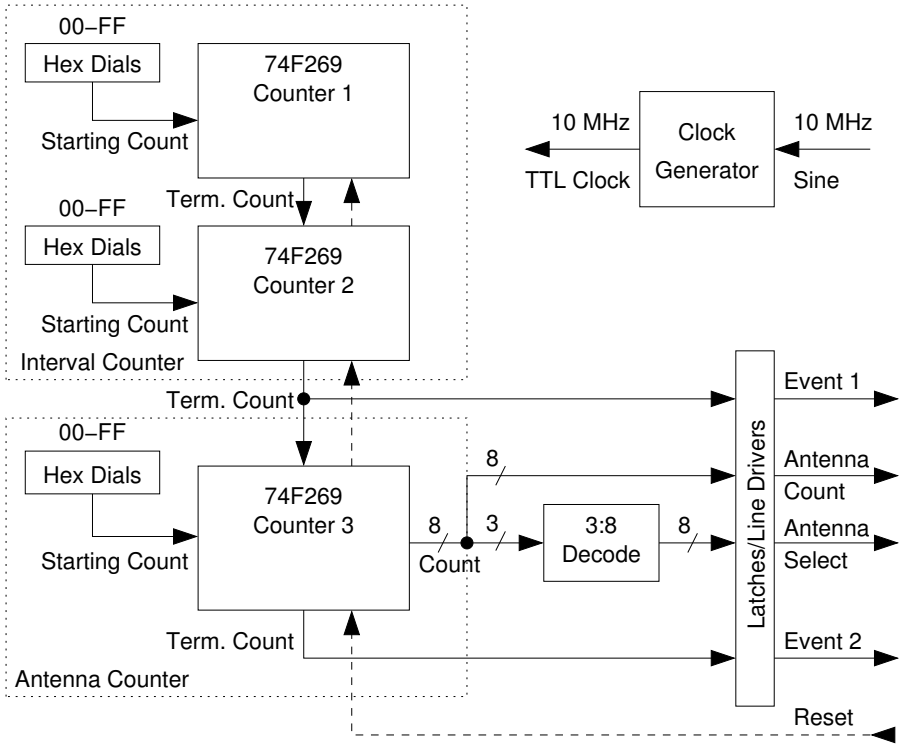

FIGURE 4.6: Simplified schematic of the SYNC unit

unit which was custom designed by Wallace [94] as no affordable COTS solution was then available, consists of counters operating at a rate of 10 MHz.

The unit provides antenna selection signals and event outputs required for antenna switching, namely the AWG and A/D triggering. Figure 4.6 shows a simplified schematic diagram of the synchronization module, which is driven by a single stable, high quality 10 MHz input derived from a Rubidium source as shown in Figure 4.10. The board assumes that the input signal is a 10 MHz sine wave, and the ”clock source” circuit converts this input to a 5 V TTL signal with a comparator. The inputs of the comparator are set to a quiescent level of 2.5 V with resistive voltage dividers. The positive comparator input is then capacitively coupled to the 10 MHz reference. Thus, positive and negative input levels correspond to 5 V and 0 V TTL outputs respectively. Note that the 10MHz input is left unterminated, thus presenting a high impedance and allowing another reference input to be connected in tandem.

As depicted, the SYNC board consists of three 8-bit counters (74F269) operating at 10 MHz. The three counters are arranged into a 16-bit “interval counter” that controls the dwell time on each antenna and an 8-bit “antenna counter” that cycles through the antennas. Thus,

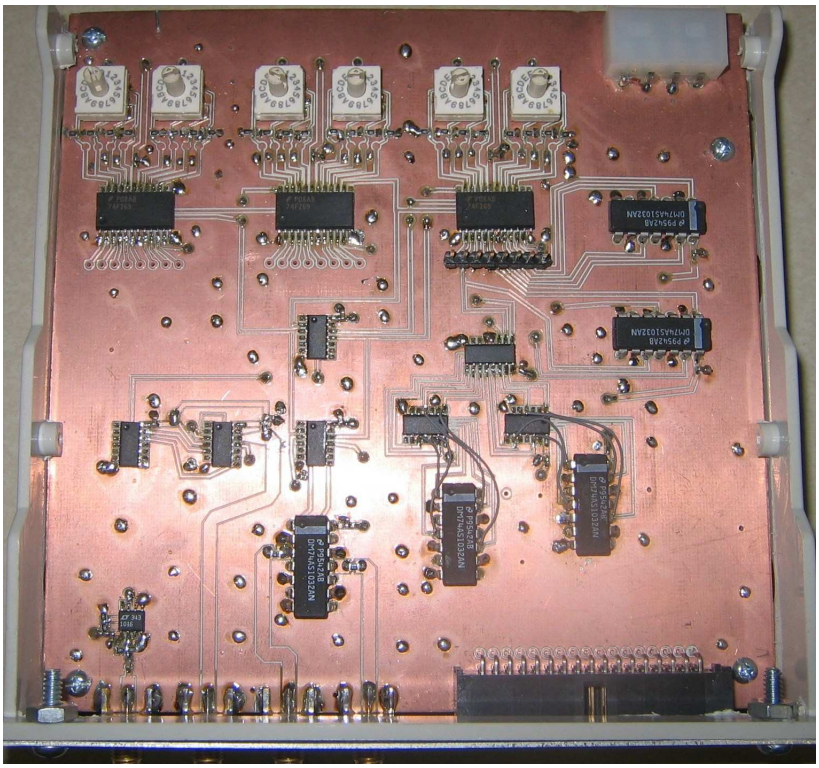

FIGURE 4.7: Top view of SYNC Unit

dwell times from 100 ns to 6.5 ms and antenna counts from 1 to 256 can be accommodated. The interval counter decrements on each clock cycle, and upon reaching the terminal count of zero, performs a parallel reload of its starting value, enables the antenna counter to decrement and asserts the terminal count (∼TC2) signal of counter 1. When both the interval and antenna counters simultaneously reach their terminal count, the antenna counter is also reloaded and the terminal count (∼TC3) signal from counter 2 is asserted. The initial values of both counters are currently set by hexadecimal dials, which should be set to the desired interval *minus one*. The dials are single-throw switches, and the outputs must be pulled down with 1 kΩ resistors on the board.

The 8-bit antenna counter value is fed via high-speed line drivers with a 100 Ω source termination to a ribbon cable connector. Since many commercial packaged PIN-diode switches have separate negative-logic enabled lines for each port, a 74F138 device decodes the three least-significant bits and provides the negative-logic strobe signals for the switches via line drivers to the ribbon cable interface. In this circuit, faster logic families, such as 74F and 74AS have been used to minimize propagation time and ensure smooth operation at 10 MHz. In order

to simplify triggering of AWG bursts and A/D conversion, event signals are also provided. The EVT1 signal is a synchronous and inverted version of the ∼TC2, thus asserting a pulse each time the interval counter resets. Likewise, the EVT2 signal, which is also shown in Figure 4.9, is derived from the ∼TC3 signal, providing a pulse when the antenna counter resets. The event signals are delivered by 50 Ω source-terminated line drivers fed to SMA type connectors.

Because the antenna counter counts in reverse order, the antenna outputs will be excited in descending order (for example for a 4-antenna measurement, the port excitation order is J4, J3, J2, J1). The reverse order must be accounted for either by reversing the order of connection to the array or by reversing the rows and columns of measured channel matrices during data processing.

The SYNC board is initially reset by an external reset switch connected to the reset (RST_SW) input. A temporary low signal on the RST_SW input creates a single reset pulse that causes the two counters to be loaded with their initial values. Figure 4.8 depicts a reset switch used to trigger two SYNC boards simultaneously. This very simple unit consists of a momentary switch that simultaneously shorts the two SMA cables to ground when the button is pressed. When the two cables are connected to two SYNC boards, this action causes the boards to begin counting at the same time.

Figures 4.7 and 4.9 show the top and front views of the completed SYNC module respectively. Here, the board has been mounted inside a 3.5” to 5.25” drive converter, which also gives one the option to conveniently integrate the unit into a computer chassis. One notices that the 10 MHz reference signal will be input and at the TX one will use EVT1 output for triggering, while at the RX one would use the EVT2 output for triggering while the microwave switches will be controlled by the outputs from ANTENNA SW so that respective switching configuration from TX-to-RX is active.

4.3.4 Monopole Antennas

The simple monopole antenna shown in Figure 4.11 and Figure 4.14 was used in the measurement system. It was mounted onto the grid plate shown in Figure 4.13 so as to produce reconfigurable antenna arrays.

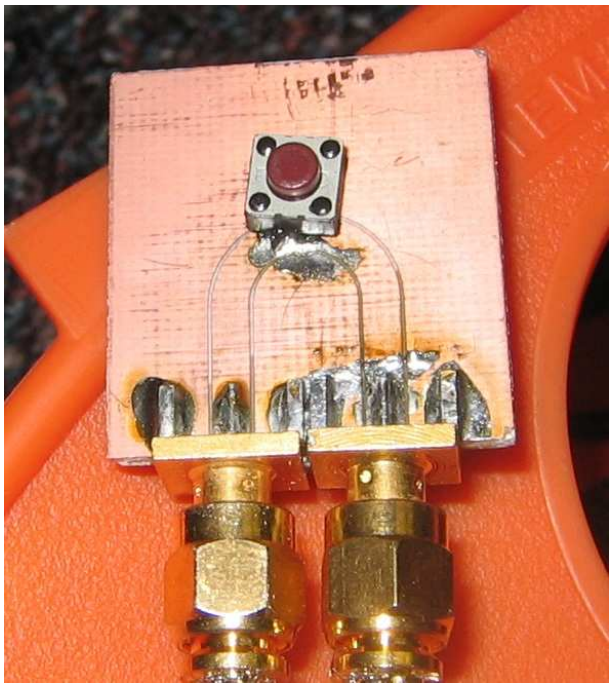

FIGURE 4.8: Reset/Trigger switch allowing simultaneous reset of two SYNC units

The design, layout and analysis of the single monopole antenna used in this system implementation is given in [96]. It was manufactured as shown in Figure 4.11, by soldering a copper whip to the center of a standard SMA bulkhead connector (Johnson part number 142-0901-401). A good 50Ω match was provisioned by providing an adequate length of the coaxial feed above the ground plane. The antennas were constructed for 2.4 GHz and 5.2 GHz center frequencies and the plots in [96] demonstrate that the antennas characteristics were adequate for implementation in this system.

The antennas were mounted on the grid plate shown in Figure 4.17, which also provided a very good ground plane. This novel method of implementation allowed for the flexibility in varying the element spacing as well as antenna array configuration for up to at least eight antenna elements as shown in example Figure 4.16. The spacing for the eight element circular array is $\lambda/2$ for both the 2.4 GHz and 5.2 GHz measurement campaign as shown in Figures 4.13 and 4.16 respectively. The linear array configuration shown in Figures 4.12 and 4.15 are for the implementation of the 2.4 GHz and 5.2 GHz respectively. Since the grid array was limited in physical size, an inter-element spacing of $\lambda/3$ was implemented for the eight element linear array at 2.4 GHz.

FIGURE 4.9: Front view of SYNC Unit

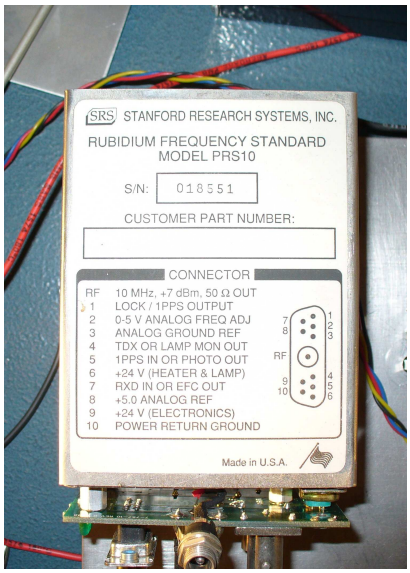

FIGURE 4.10: Rubidium frequency standard

4.4 SYSTEM DEPLOYMENT

4.4.1 Wideband Probing

In order to estimate the channel response at more than a single frequency, the measurement signal must have sufficient bandwidth. Possible choices of wideband excitations include pseudonoise (PN), chirp and multitone signals. The technique typically used in commercial sounders, as well as this current implementation, is the multitone signal, where the number and

FIGURE 4.11: A 2.4 GHz Monopole antenna

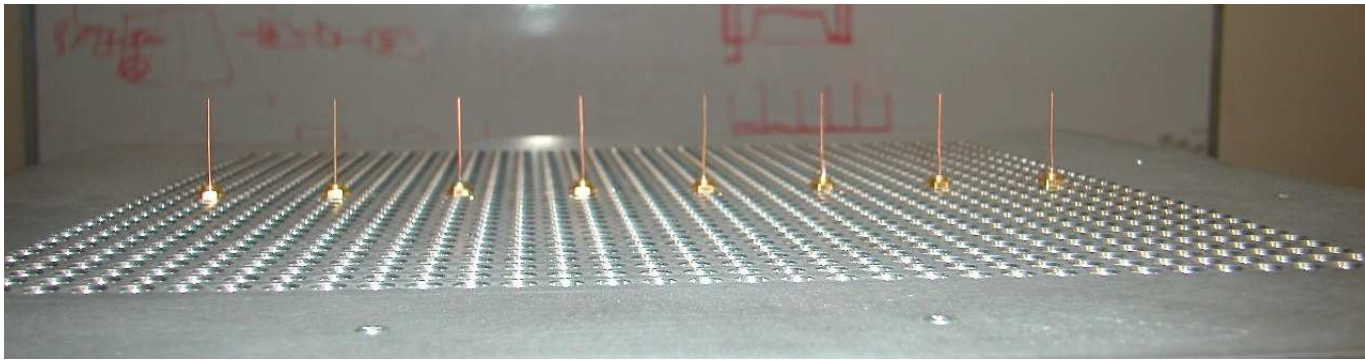

FIGURE 4.12: 2.4 GHz Linear eight element array

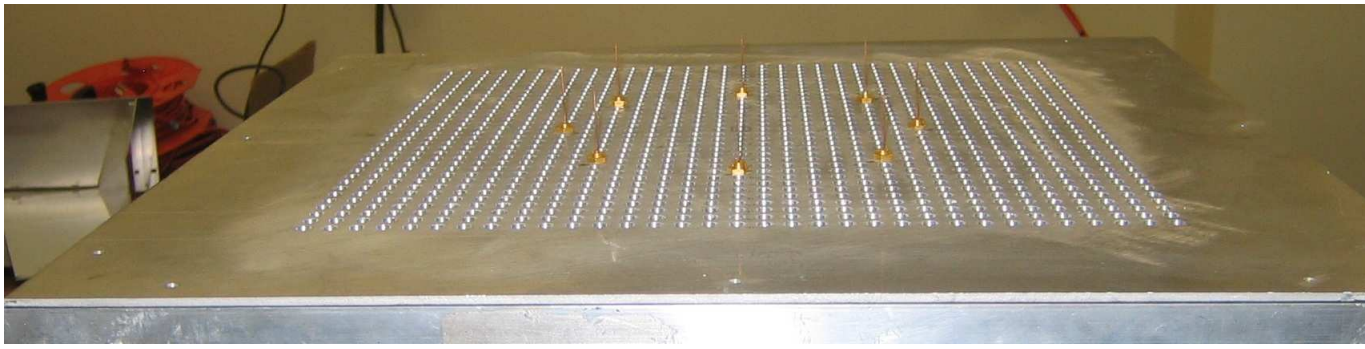

FIGURE 4.13: 2.4 GHz Circular eight element array

FIGURE 4.14: A 5.2 GHz Monopole antenna

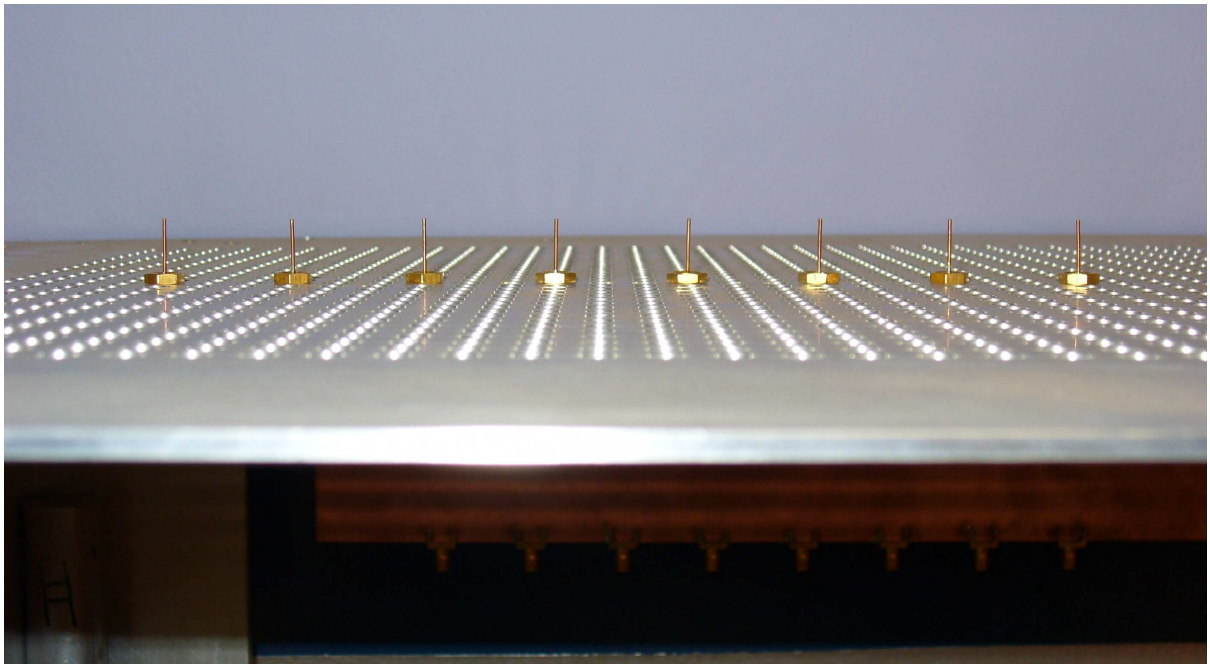

FIGURE 4.15: 5.2 GHz Linear eight element array

FIGURE 4.16: 5.2 GHz Circular eight element array

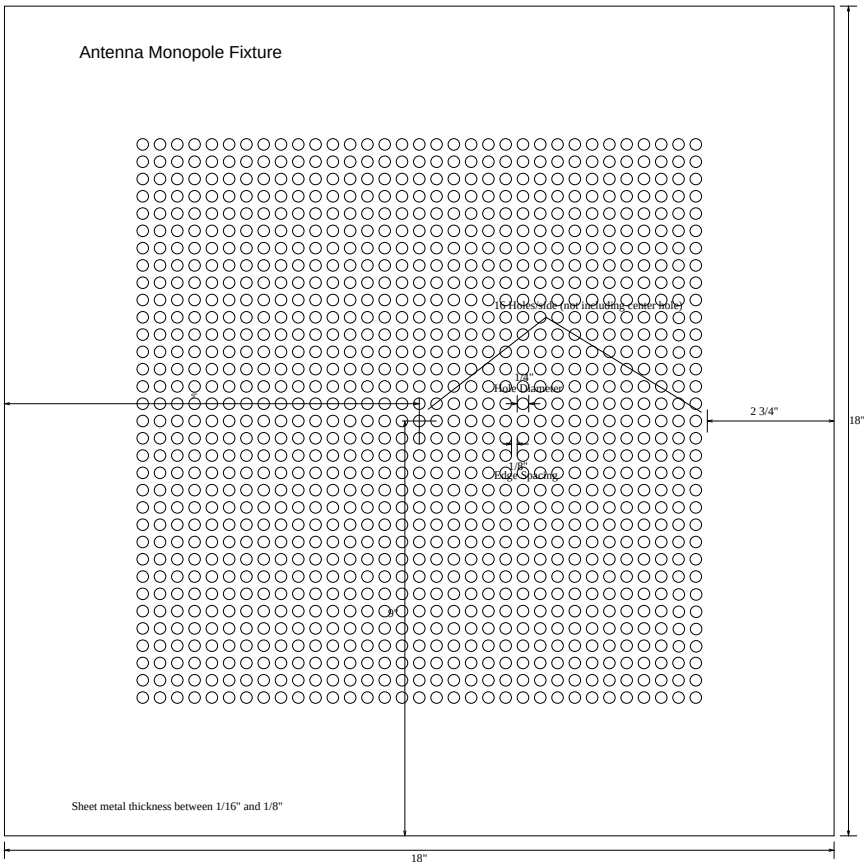

FIGURE 4.17: Grid plate layout for fixing monopole antenna array

spacing of tones can be controlled. In this work, a baseband multitone signal of the form

$$x(t) = \sum_{i=0}^{N_F-1} \cos(2\pi f_i t + \phi_i) \tag{4.1}$$

is used, where f_i and ϕ_i are the frequency and phase of the ith tone, respectively, and for equally spaced tones, $f_i = (i + 0.5)\Delta f$. Note that for each term in (4.1), two tones are created symmetrically about zero frequency, and both tones are present when the signal is up-converted to the microwave carrier. Thus, (4.1) produces $2N_F$ tones with a total probing bandwidth of $(2N_F - 1)\Delta f$. Post processing is simplified if each tone corresponds to a single FFT bin, which is guaranteed when $\Delta f = 2kf_s/N$, where f_s is the sample rate, N is the number of samples in each record and k is an integer.

An obvious advantage of multitone signalling is that the channel response is obtained directly by selecting the appropriate bins of the FFT. One of the drawbacks, however, is that the envelope is not constant, and care must be taken to ensure that the linearity of TX power amplifiers and switches is sufficient to avoid corruption of the measurements. Usually, one

TABLE 4.1: Parameters of the example multitone signal

Parm.	N_F	Δf	T_1	T_2	σ	f_s	N
Value	4	1 MHz	6 μs	7 μs	0.3 μs	400 MS/s	20,000

minimizes the signal's peak-to-average ratio by adjusting the phases of the tones. Here, the phases were optimized by simply selecting a set of random phases uniformly on $[0, 2\pi]$ and retaining the signal with the lowest peak-to-average ratio over many independent realizations.

One consideration with switched measurements is that most PIN-diode switches are not designed for *hot switching*, where high signal level exists during a switching operation. Furthermore, channel estimation is simpler if the acquired signals for the different antenna combinations have no temporal overlap. To avoid hot switching and create separate data records, the multitone signal is multiplied by a Gaussian window of the form

$$w(t) = \begin{cases} e^{-(T_1-t)^2/(2\sigma^2)}, & 0 \leq t < T_1 \\ e^{-(T_2-t)^2/(2\sigma^2)}, & T_2 \leq t \leq T \\ 1, & \text{otherwise}, \end{cases} \tag{4.2}$$

where T_1 and T_2 are the limits of the window, and the standard deviation σ controls the rise and fall time of the window. Typically, the guard time $T_1 + T_2$ is chosen to be much larger than the delay spread of the channel. Guard time also allows the AGC to adapt between switch events.

A simple 8 MHz multitone signal used for outdoor channel probing is depicted in Figure 4.18, with the important parameters listed in Table 4.1. The window spreads the tones slightly, which is unavoidable for a finite-length signal. The active portion of the time-domain signal has a peak-to-average ratio of 1.74, which is close to that of a constant sine wave ($\pi/2 \approx 1.57$).

4.4.2 Calibration Procedure

Since the RF components in the system are not ideal, raw measurements include both the channel and system response. In addition, microwave switches are often constructed with unequal length transmission lines on the various ports, leading to phase errors. These effects can be removed by a careful calibration method.

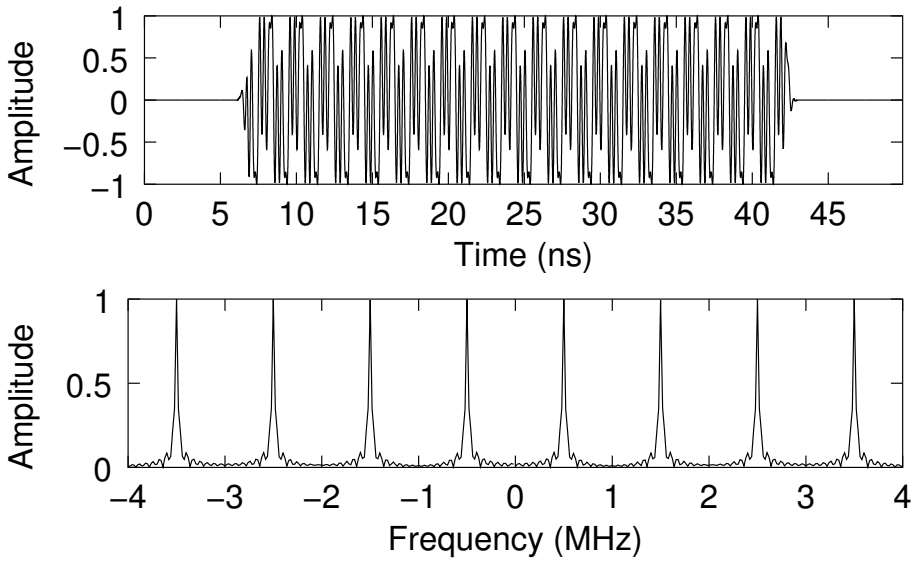

FIGURE 4.18: Example of multitone signal plotted versus time and frequency

Figure 4.19a depicts the measurement setup, where the ideal channel response from the nth TX antenna to the mth RX antenna at baseband frequency f_k is $h_{k,mn}$. One way to accomplish system calibration is to connect TX to RX as depicted in Figure 4.19b, where the switches and antennas have been replaced with a single attenuator with loss L dB. This measurement yields y_k^{cal}, which is the value of the FFT bin corresponding to the baseband tone at frequency f_k. The response of the switches is measured on a network analyzer giving broadband S-parameters $S_{n0}^{\{\text{TX,RX}\}}(f)$, where 0 and n refer to the indices of common and switched ports respectively, and f is the frequency.

Assuming near-linear response from the RX subsystem, a measurement taken with the setup in Figure 4.19a results in

$$y_{k,mn} = L y_k^{\text{cal}} h_{k,mn} S_{0n}^{\text{TX}}(f_k + f_c) S_{0m}^{\text{RX}}(f_k + f_c), \tag{4.3}$$

where k, m, and n are the frequency, RX and TX are indices, and f_c is the carrier frequency. The ideal (or calibrated) channel response h is then obtained from

$$h_{k,mn} = \frac{y_{k,mn}}{L y_k^{\text{cal}} S_{0n}^{\text{TX}}(f_k + f_c) S_{0m}^{\text{RX}}(f_k + f_c)}. \tag{4.4}$$

Another calibration method involves the connection strategy in Figure 4.19c. In this case, the switches remain and the TX and RX are connected via an N_T- and N_R-way power divider and combiner, with measured S-parameters $S_{n0}^{\{\text{TX,RX}\}}(f)$. To avoid RX saturation, a loss of L

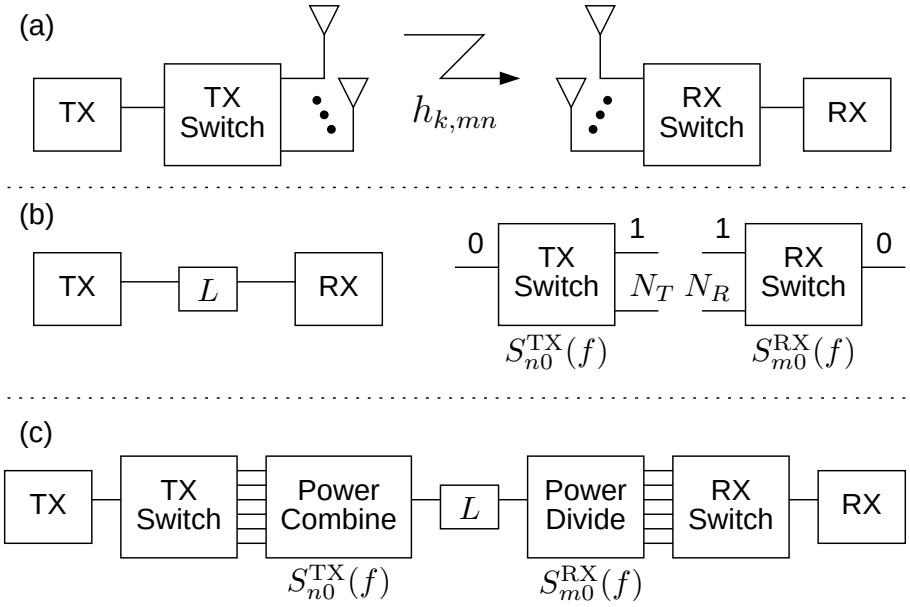

FIGURE 4.19: Procedures for system calibration: (a) original measurement setup, (b) single-channel calibration, and (c) direct matrix calibration

may also be inserted. Measurement of all TX and RX combinations yields $y_{k,mn}^{\mathrm{cal}}$. Similar to the first approach, the ideal channel response is computed as

$$h_{k,mn} = \frac{y_{k,mn} S_{0n}^{\mathrm{TX}}(f_k + f_c) S_{0m}^{\mathrm{RX}}(f_k + f_c)}{L y_k^{\mathrm{cal}}}. \tag{4.5}$$

Note that the position of the S-parameters has changed, since the divider and combiner are present in the calibration, but not the measurement, whereas before the switches were present in the measurement but not the calibration.

The quantity of required calibration information for this procedure can be reduced by noting that the matrix $\mathbf{Y}_k^{cal}$ is rank one, so that $y_{k,mn}^{\mathrm{cal}} = s_k u_{k,m} v_{k,n}^*$, where $\mathbf{u}_k$ and $\mathbf{v}_k$ are the left and right singular vectors associated with the single nonzero singular value s_k for frequency bin k. This rank-one approximation may also improve the calibration accuracy, since information from multiple antennas is averaged.

4.4.3 Measurement Environment

Figure 4.20 depicts the UP system. At the TX side, the antenna array on the grid plate is supported by a pillar which is bolted onto the cart. This provides a good ground plane for the entire system as well. The AWG/microwave source is connected to the RF module which

then feeds the antennas via the SP8T. The rechargeable lead-acid batteries provide 12/24 V so that the rubidium frequency standard, SYNC unit, microwave switches and RF components are continuously powered from a very stable DC source.

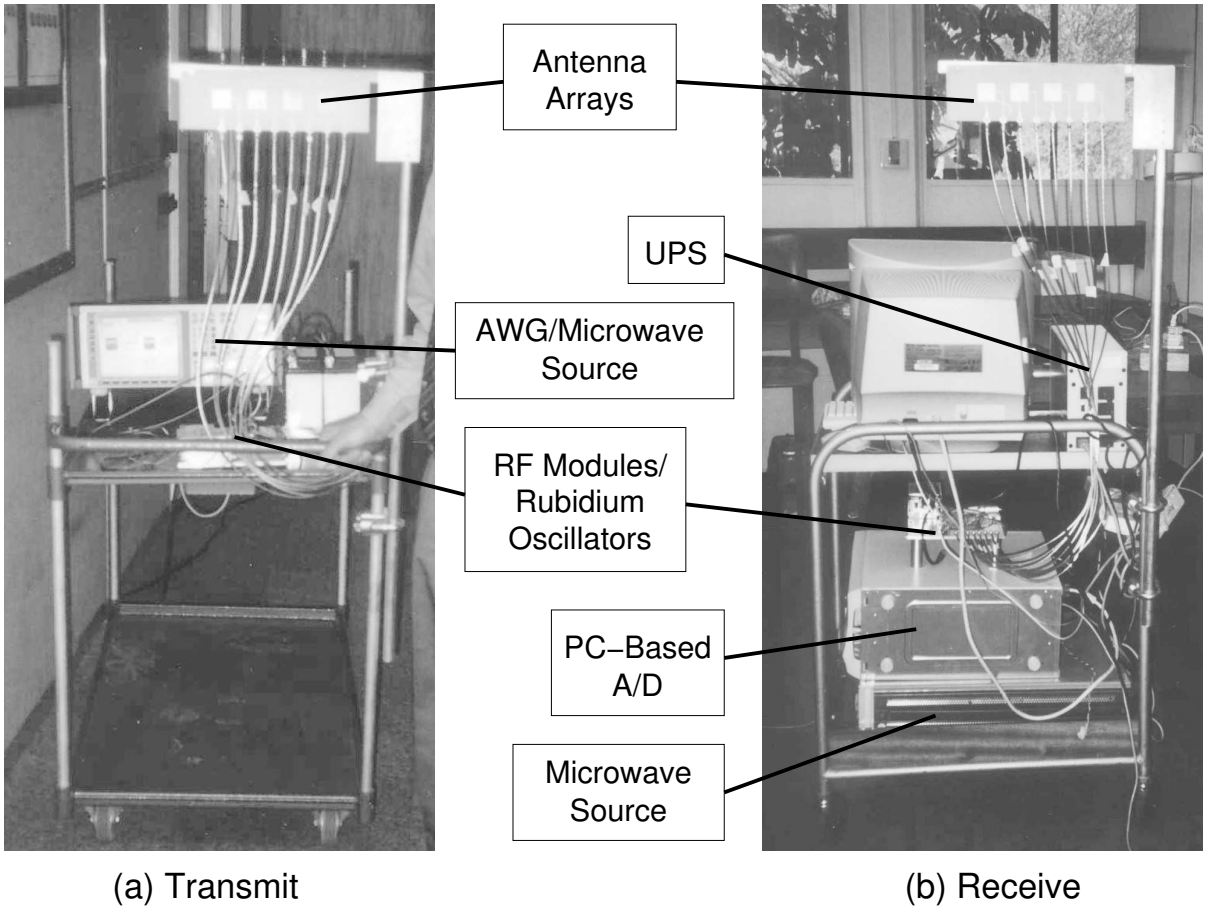

FIGURE 4.20: System constructed and deployed at the University of Pretoria (UP)

At the RX end, an uninterruptible power supply (UPS) provides temporary backup to the PC when the system must be unplugged from the mains for relocation. Here again, the rubidium oscillator and RF module are powered via the 12/24 V rechargeable batteries while the SYNC unit is inside the PC and is powered from the PC power supply.

The measurement campaign performed for this study was done as shown in Figure 4.21 on the first floor in the Carl and Emily Fuchs Institute for Microelectronics (CEFIM) building located on the University of Pretoria (UP) main campus. The TX was fixed at a single position on the central corridor as shown in Fig. 4.21 while the RX was placed at 11 different locations so as to give a good representation of the physical location and its geometry. The TX antennas were

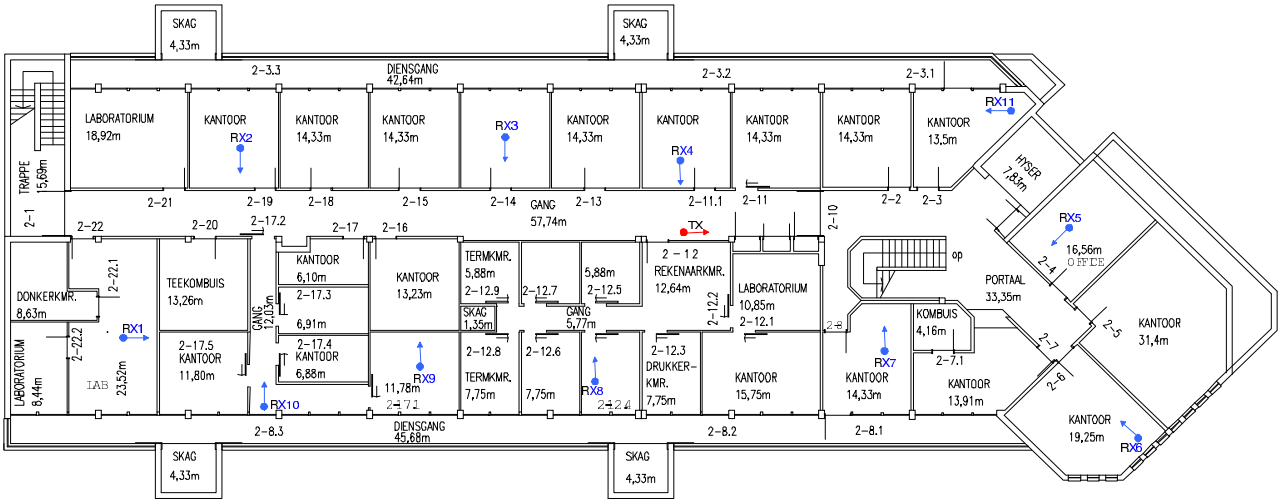

FIGURE 4.21: Measurement scenario in CEFIM at UP

fixed at a height of approximately 1.85 metres and the antenna RX height was approximately 1.5 metres. Co-located MIMO measurements were performed at both 2.4 GHz and 5.2 GHz, meaning that both the TX and RX were at exactly the same geographical position, height and orientation for the 2.4 GHz and 5.2 GHz measurement campaign. This would enable the research, amongst others things, to compare the effect of center frequency on capacity, element correlation, spatial power spectra and other channel modelling characteristics.

4.4.4 Data Collection

In Figure 4.1 the wideband RF signal is routed through the respective port on the SP8T into each of the TX antenna array elements, thus exciting each TX antenna for a total of 20 μs, which consists of 15 μs on time and 5 μs off time. As shown in Figure 4.22, at the receiver another matched SP8T switch, controlled by a SYNC unit synchronized to the one at the TX, routes the incoming RF signal from each of the RX antennas to a common RF receiver. Each RX antenna is connected via the switch for a complete scan of all eight TX antennas, or a total of 160 μs. Thus, a complete scan of the MIMO channel as shown in Figure 4.22 takes 1.28 ms. Since the data acquisition card had limited memory size, approximately 198 ms was allocated for this data to be written onto the hard disk drive of the RX, resulting in a time of 200 ms for one complete 8×8 scan for all TX and RX antennas. In order to improve the accuracy of the results and any variation that may have occurred in the fixed wireless channel, 20 snapshots of the measurement were repeated at each of the 11 locations shown in Figure 4.21, giving us an acquisition time of 4 s. To have a good representation of the channel as well as

sufficient data to capture any impulsive changes at each location, the complete measurement was done twice so that there were at least two snapshots of the complete measurement of the channel at each of the locations. This resulted in the total measurement time of 8 s per location.

Once the raw channel data was captured, the wideband MIMO channel response $\mathbf{H}(\omega)$ for the j^th TX and the i^{th} RX is computed at K=80 discrete frequency bins by dividing the FFT of the captured signal on the j^{th} TX and the i^{th} RX timeslot by the FFT of a calibration signal and selecting bins corresponding to the 80 TX tones. The calibration signal was obtained by connecting the TX and RX through fixed attenuators and performing the measurement as described under the subsection *'Calibration Procedure'*.

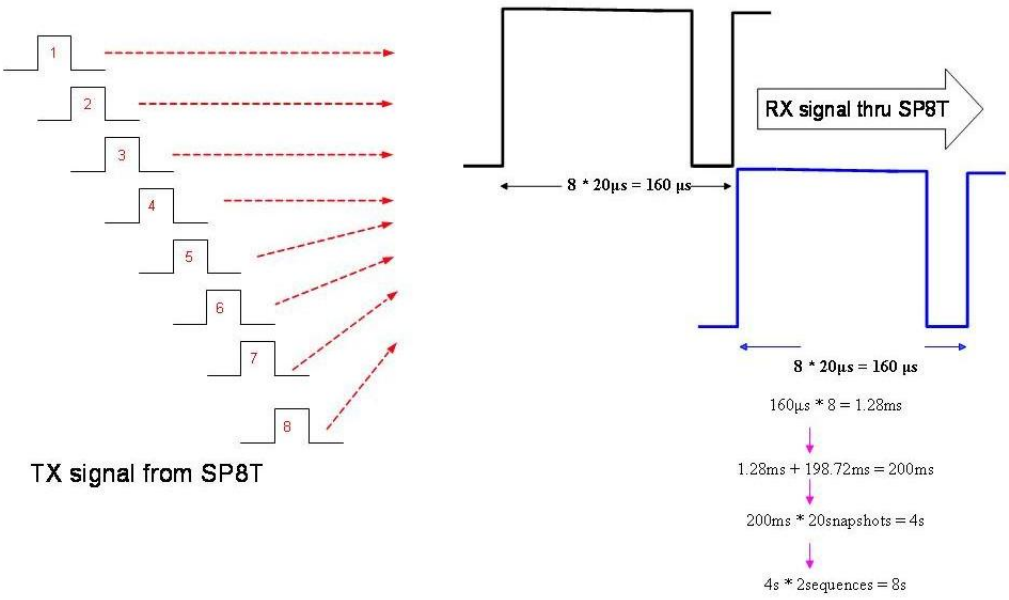

FIGURE 4.22: Switching sequence for measurements at each location

```
H(f,rx,tx,s,ss):
   (f=freq bins,
      rx=RX antennas,
         tx=TX antennas,
            s=sequence no.,
               ss=snapshots)
```

FIGURE 4.23: Channel matrix representation

The channel transfer matrix, **H**, for the channel data is hence formatted in a five dimensional

matrix as shown in Figure 4.23, where the five dimensions are the 80 frequency bins, 8 RX antenna elements, 8 TX antenna elements, 20 sequences of measured data and the 2 snapshots across which all the measurements were acquired respectively. To remove the effect of path loss in all the computations, the channel matrices were normalized according to

$$\tilde{\mathbf{H}}^{(n)} = \left(\frac{1}{N_R N_T N_S} \sum_{m=1}^{N_S} \left\| \mathbf{H}^{(m)} \right\|_F^2 \right)^{-1/2} \mathbf{H}^{(n)} \tag{4.6}$$

where $\tilde{\mathbf{H}}^{(n)}$ and $\mathbf{H}^{(n)}$ are the n^{th} normalized and un-normalized channel matrices respectively. N_s is the number of channel measurements (snapshots and frequency bins) at a single location and $\|\cdot\|_F$ is the Frobenius norm.

4.5 CONCLUSION

Understanding the true channel behavior requires a system capable of direct measurement of the channel. This chapter has introduced the wideband ”switched array” MIMO wireless measurement system as a method of capturing real-world indoor fixed channel behavior, across the 2-6 GHz center frequency band. This chapter presented the hardware and the software techniques for a flexible 8 x 8 MIMO channel measurement system that can probe indoor channels reliably and with accurate repeatability.

CHAPTER FIVE

DATA ANALYSIS AND MODEL ASSESSMENT

Initially, the effect of the antenna array configuration on the capacity is demonstrated. Figure 5.1 shows the capacity PDF at 2.4 GHz while Figure 5.2 depicts the capacity PDF at 5.2 GHz for the 8×8 MIMO system in the same indoor location. The plots demonstrate

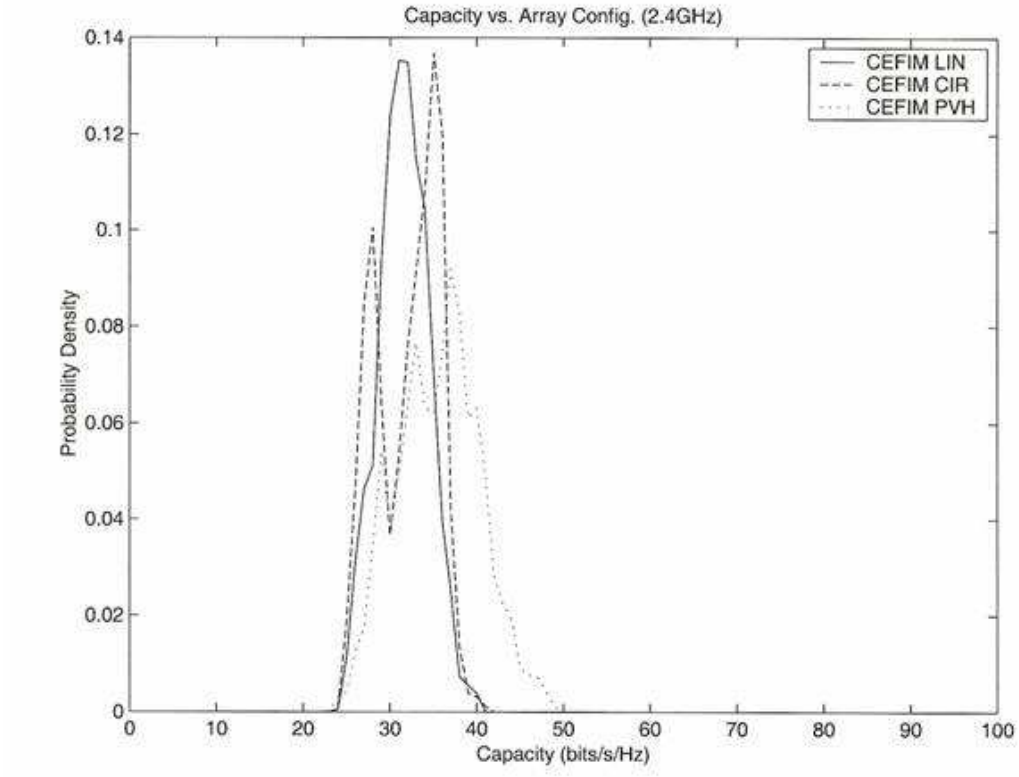

FIGURE 5.1: Capacity PDF for the MIMO system at 2.4 GHz with different array configurations

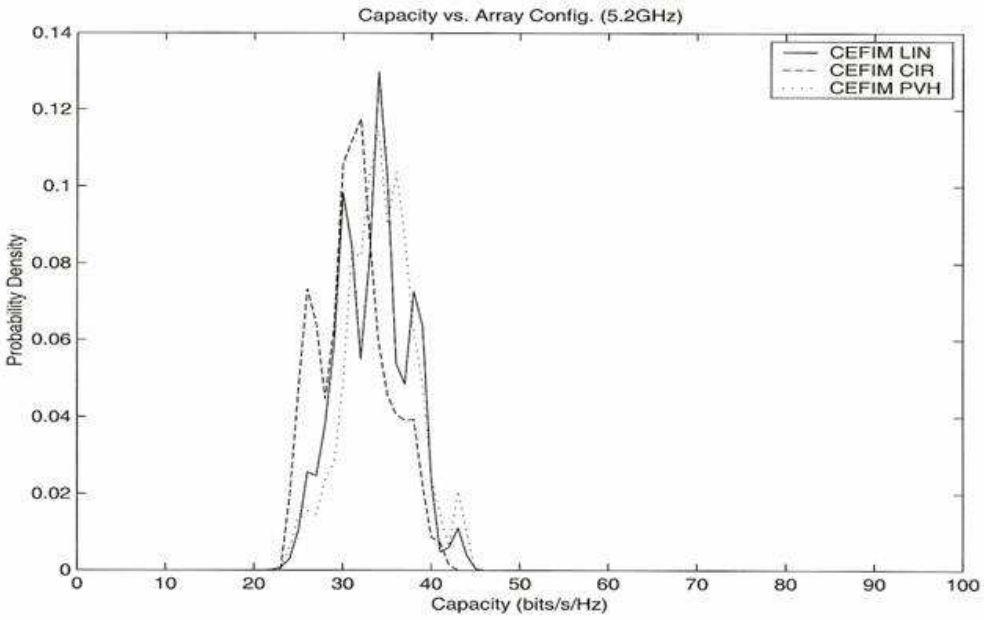

FIGURE 5.2: Capacity PDF for the MIMO system at 5.2 GHz with different array configurations

that the bulk average capacity is only weakly affected by the array configuration and that the capacity using the geometric modelling technique in Chapter 3 provides, on average, a good estimate for the indoor location.

Since the complexity of the algorithms for MIMO systems will depend on the channel rank available, it is of interest to know how much this rank depends on the target center frequency and array configuration. This dependence is investigated by plotting the cumulative distribution function (CDFs) of the channel eigenvalues over all frequency bins and all measurement locations. In Figure 5.3 the distribution at 2.4 GHz is compared with those at 5.2 GHz for the 8×8 linear monopole arrays and in Figure 5.4 they are compared for the eight element circular array across all the physical locations. Overall, these plots show fairly weak dependence on the eigenvalue distributions on the carrier frequency, especially for the dominant eigenvalues for both the array configurations. Thus from a system standpoint, the same MIMO coding techniques will be equally applicable at the 2.4 GHz and 5.2 GHz. This result also suggests that statistical channel models that match bulk eigenvalue behavior data at 2.4 GHz can be used at 5.2 GHz.

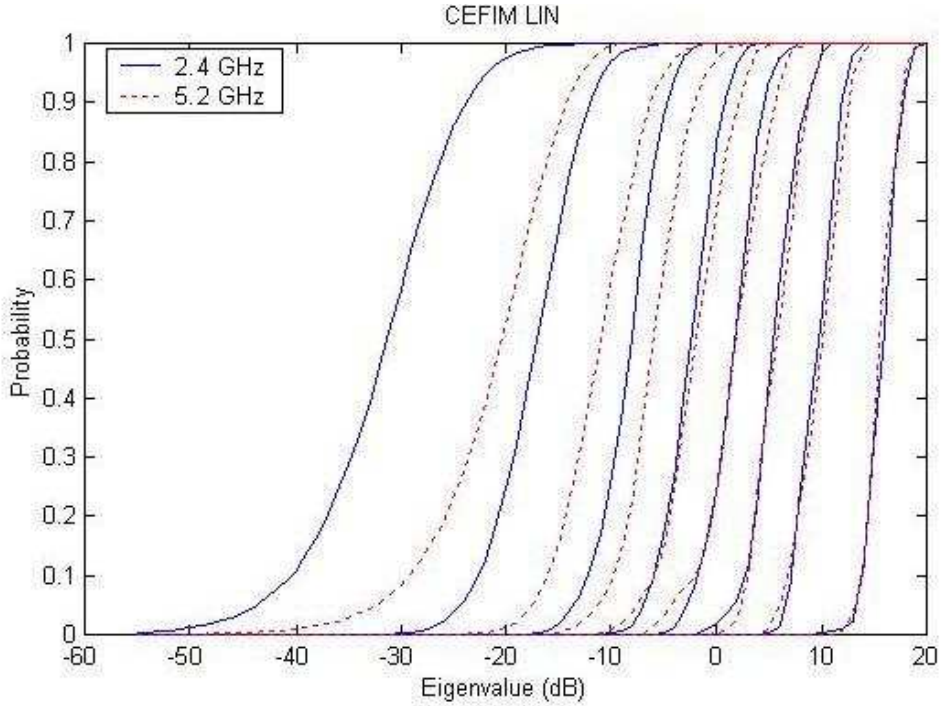

FIGURE 5.3: Eigenvalue CDFs for linear arrays at 2.4 GHz and 5.2 GHz

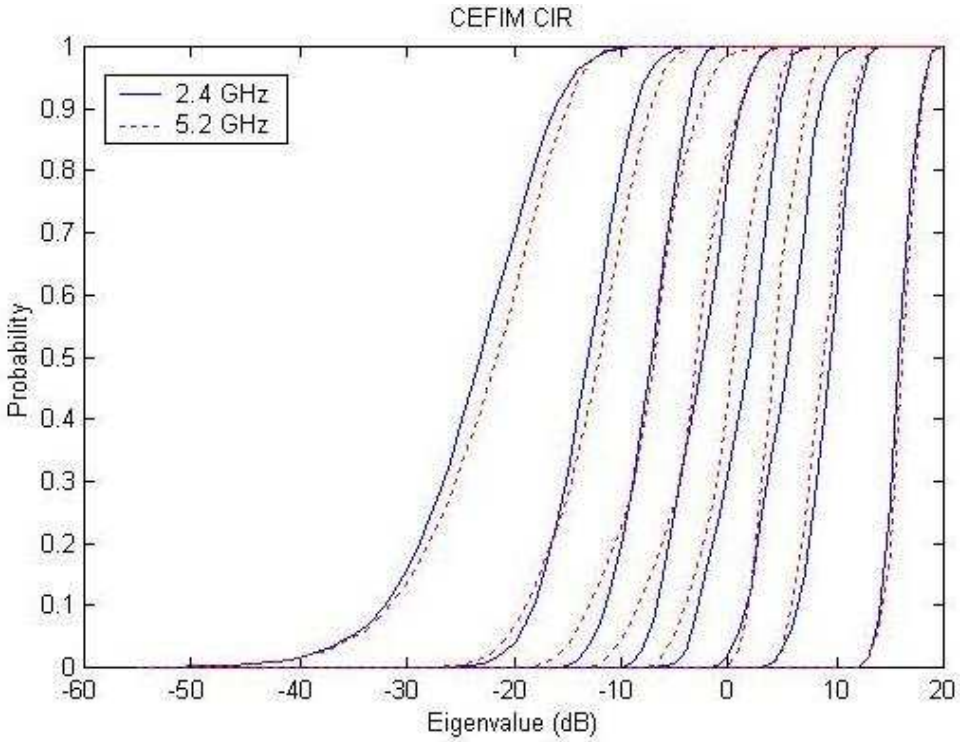

FIGURE 5.4: Eigenvalue CDFs for circular arrays at 2.4 GHz and 5.2 GHz

5.1 CAPACITY MODELLING

5.1.1 Introduction

In this section, the ability of measurements at a center frequency of 2.4 GHz is explored to predict channel behavior at a much higher center frequency of 5.2 GHz, which is referred to as frequency scaling in a MIMO system. In theory, the cost of channel measurements can be greatly reduced when such predictions are possible. Furthermore, frequency scaling suggests that MIMO techniques employed in a system with one center frequency will be directly applicable to systems operating at other frequencies, possibly decreasing the development time of MIMO systems, network planning, et cetra. The validity of frequency scaling will obviously depend on the similarity of the multi-path present at the two different frequencies. To study this idea, measurements were taken at both 2.4 GHz and 5.2 GHz at 11 site-specific measurement positions using a circular antenna array configuration. Capacities were then computed at each position for the two different center frequencies. An average pair-wise correlation measure was also applied to explain the results.

5.1.2 Model Description

The measurements were taken at each of the 11 locations as shown in Figure 4.21. At each of the 11 locations, 20 snapshots were recorded with 200 ms of time between snapshots. This results in a 4 s acquisition time, and since the channel sounding was for a fixed T and RX case, negligible channel variation was observed across this duration.

To remove the effect of path loss in our computations, channel matrices were normalized according to

$$\tilde{\mathbf{H}}^{(n)} = \left(\frac{1}{N_R N_T N_S} \sum_{m=1}^{N_S} \left\| \mathbf{H}^{(m)} \right\|_F^2 \right)^{-1/2} \mathbf{H}^{(n)} \tag{5.1}$$

where $\tilde{\mathbf{H}}^{(n)}$ and $\mathbf{H}^{(n)}$ are the n^th normalized and un-normalized channel matrices respectively. N_s is the number of channel measurements (snapshots and frequency bins) at a single location and $\|\cdot\|_F$ is the Frobenius norm.

The channel capacity is computed according to the uninformed transmit capacity from [15]

as

$$C = \log_2 \det(I + \frac{\rho}{N_T}\tilde{\mathbf{H}}\tilde{\mathbf{H}}^H), \tag{5.2}$$

where I is the 8x8 identity matrix, ρ is an assumed average SISO signal to noise ratio (SNR), N_T is the number of TX antennas, $\tilde{\mathbf{H}}$ is the normalized channel matrix and $(\cdot)^H$ is the conjugate matrix transpose.

Across the 80 MHz excitation bandwidth for each location (loc), the average channel capacity, $\overline{C}_{loc}$, is determined by

$$\bar{C}_{loc} = \left(\sum_{k=1}^{K} C_k\right) \Big/ K, \tag{5.3}$$

where K=80 is the number of discrete frequency bins and locations, loc = 1.....11.

For uniform linear arrays and far-field scattering, the correlation coefficient is shift invariant, allowing the correlation of the signals on two antennas to be presented simply as a function of the distance between elements, rather than a function of the two absolute positions of the elements. Hence in this case, the shift-invariant correlation coefficient at the RX with an element displacement of l is given as:

$$\rho_\ell = \frac{\left[\sum_{k=1}^{N_S}\sum_{j=1}^{N_T}\sum_{i=1}^{N_R-\ell} H_{i,j}^{(k)} H_{i+\ell,j}^{(k)*}\right]}{\left[\left(\sum_{k=1}^{N_S}\sum_{j=1}^{N_T}\sum_{i=1}^{N_R-\ell}\left|H_{i,j}^{(k)}\right|^2\right)\left(\sum_{k=1}^{N_S}\sum_{j=1}^{N_T}\sum_{i=1}^{N_R-\ell}\left|H_{i+\ell,j}^{(k)}\right|^2\right)\right]^{1/2}}, \tag{5.4}$$

where N_s=20*80 is the number of snapshots taken across all the frequency bins and observations, N_T=8 and N_R=8 are the number of transmit and receiver antenna respectively, and $H_{i,j}^{(k)}$ is the k^th channel snapshot from the j^th TX to the i^th RX antenna. Similarly, the shift invariant TX correlation is computed by interchanging roles of TX and RX in equation (5.4).

For the circular array no shift invariance exists, so to allow the correlation to be given in terms of a single displacement variable, the RX pairwise average absolute correlation with a displacement of l is defined as

$$\rho_l = \frac{\left\{\sum_{i=1}^{N_R}\left|\sum_{k=1}^{N_S}\sum_{j=1}^{N_T} H(k,i,j)H^*(k,i+\ell,j)\right|\right\}}{\left[\left\{\sum_{i}^{N_R}\left|\sum_{k=1}^{N_S}\sum_{j=1}^{N_T}|H(k,i,j)|^2\right|\right\}^{1/2}\left\{\sum_{i}^{N_R}\left|\sum_{k=1}^{N_S}\sum_{j=1}^{N_T}|H(k,i+\ell,j)|^2\right|\right\}^{1/2}\right]}. \quad (5.5)$$

In equation (5.5), the number of RX antennas, N_R=8, and number of TX antennas, N_T=8. The pairwise correlation for the TX can be computed by interchanging the roles RX and TX in equation (5.5). The only difference between this quantity and a standard correlation coefficient is the absolute value under the summation, avoiding an artificially low correlation value resulting from phase de-correlation as one moves around the array and the relative angle pair of elements rotates.

5.1.3 Results

Using (5.2), and for the SNR=20 dB, the ULA capacity across the 80 MHz of excitation bandwidth for each of the 11 locations shown in Figure 4.21 was calculated. From (5.4) one can also calculate the TX and RX correlation as shown in Table 5.1.

Figure 5.5 shows the capacity at location 7 both at the center frequencies of 2.4 GHz and 5.2 GHz. The model fit for the capacity at each of the center frequencies, using (5.3) is also shown in Figure 5.5. At Location 7 shown in Figure 5.5 the capacity at 5.2 GHz was found to be greater than that at 2.4 GHz, which is consistent with the correlation obtained in Table 5.1 and [97]. However, comparing this to that shown in Figure 5.6, one observes that the capacity at 2.4 GHz is greater than that at 5.2 GHz. This is consistent as seen in Table 5.1, where the correlation at 2.4 GHz is lesser than that at 5.2 GHz, both for the TX and RX cases. Except for locations 6 and 9, the average capacity across the excitation bandwidth of 80 MHz was greater at 5.2 GHz than that at 2.4 GHz, as shown in Figure 5.7 for all the 11 measured locations. At location 4 this is very marginal, and the discrepancies could be due to experimental error or not exactly positioning the RX ULA at each of these locations for each of the two center frequencies.

For the uniform circular array (UCA) configuration, using a SNR of 20 dB and using (5.2),

TABLE 5.1: TX/RX Pairwise Average Correlation of Capacity for ULA

Locations	Average Correlation (ρ_{av})			
	2.4 GHz		5.2 GHz	
	TX	RX	TX	RX
1	0.3855	0.3600	0.2853	0.3400
2	0.3834	0.5339	0.2655	0.3271
3	0.4265	0.5301	0.2924	0.3764
4	0.0833	0.1089	0.1283	0.1520
5	0.3854	0.3740	0.2484	0.3301
6	0.3190	0.1710	0.2040	0.1364
7	0.5808	0.4041	0.3804	0.2944
8	0.1197	0.2839	0.1291	0.1257
9	0.1765	0.1721	0.5010	0.3613
10	0.3868	0.4886	0.4737	0.3743
11	0.3779	0.8617	0.3139	0.4664

the capacity across the channel excitation bandwidth can be obtained. Figure 5.9 shows the capacity at Location 9 for the 2.4 GHz and 5.2 GHz cases. The average capacity at 2.4 GHz and 5.2 GHz is obtained using (5.3) and plotted as the straight lines shown in Figure 5.9. One observes that the average capacity at 2.4 GHz is greater than that at 5.2 GHz.

The capacity for each of the 11 locations was calculated and averaged across frequency to obtain the capacities shown in Figure 5.10. One observes that in most cases the capacity at 2.4 GHz is larger than that at 5.2 GHz, most likely due to more scattering and less path loss at the lower frequency. As in [97], one should observe a lower correlation coefficient ρ for a relatively greater capacity, as verified in Tables 5.2 and 5.3. The relatively lower capacity at Locations 7 and 8 can also be explained in terms of the pairwise average correlation calculated using equation 5.5. At these locations, the correlation shown in Tables 5.2 and 5.3 for both the RX and TX antenna elements respectively, was found to be larger at 2.4 GHz than at 5.2 GHz. Furthermore Tables 5.3 and 5.2 also show that the percentage error in the determination of this pairwise correlation was a maximum of 0.5% at the RX and 2.0% at the TX, respectively, indicating that this is a reasonably reliable metric.

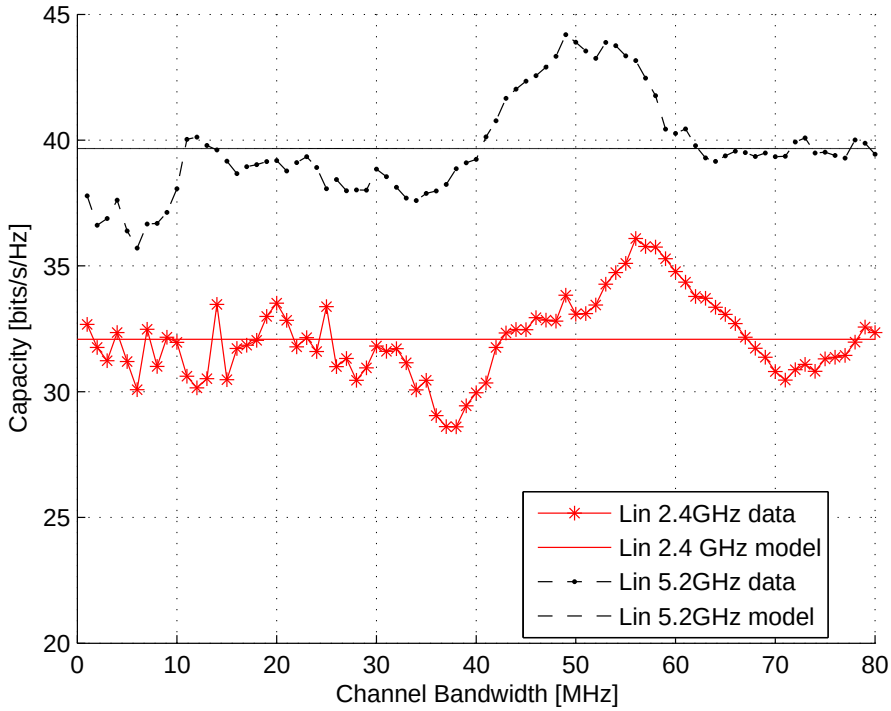

FIGURE 5.5: Capacity versus excitation bandwidth at location 7 for ULA

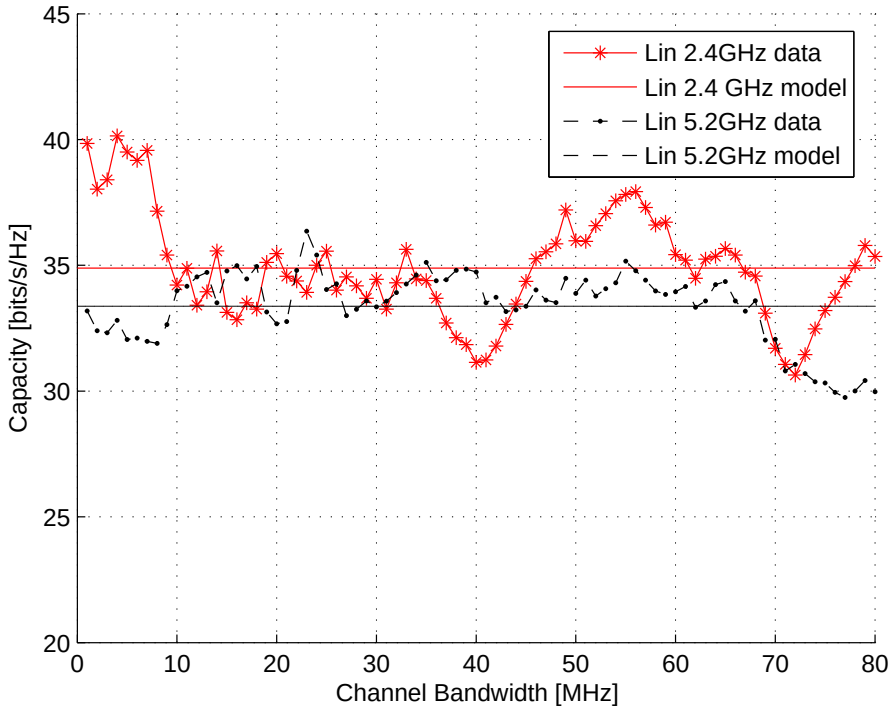

FIGURE 5.6: Capacity versus excitation bandwidth at location 9 for ULA

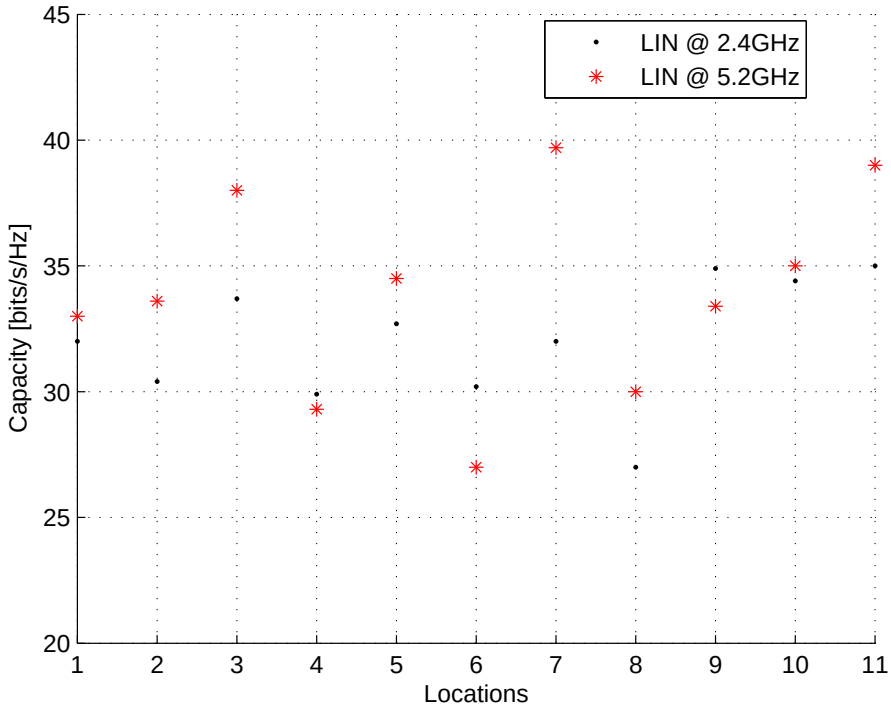

FIGURE 5.7: Average capacity at each of the measurement locations using ULA

To test the correlation of the channel capacity at the two different frequencies, Figure 5.11 presents a scatter plot of the capacities across the 11 locations at 2.4 GHz and 5.2 GHz. The solid line in the figure shows the best-fit linear dependence, obtained with the least-squares approximation. Using all the locations plotted in Figure 5.11 the straight line equation is determined to be

$$\text{cap}_{5.2} = 0.899 \times \text{cap}_{2.4} + 2.367, \tag{5.6}$$

where $\text{cap}_{5.2}$ is the capacity at 5.2 GHz and $\text{cap}_{2.4}$ is the capacity at 2.4 GHz respectively. The linear fit model, when all locations are considered and when Location 7 is taken as an outlier result in a variance of 3.427 and 1.905 respectively, indicating a high degree of correlation in the capacities at the two center frequencies.

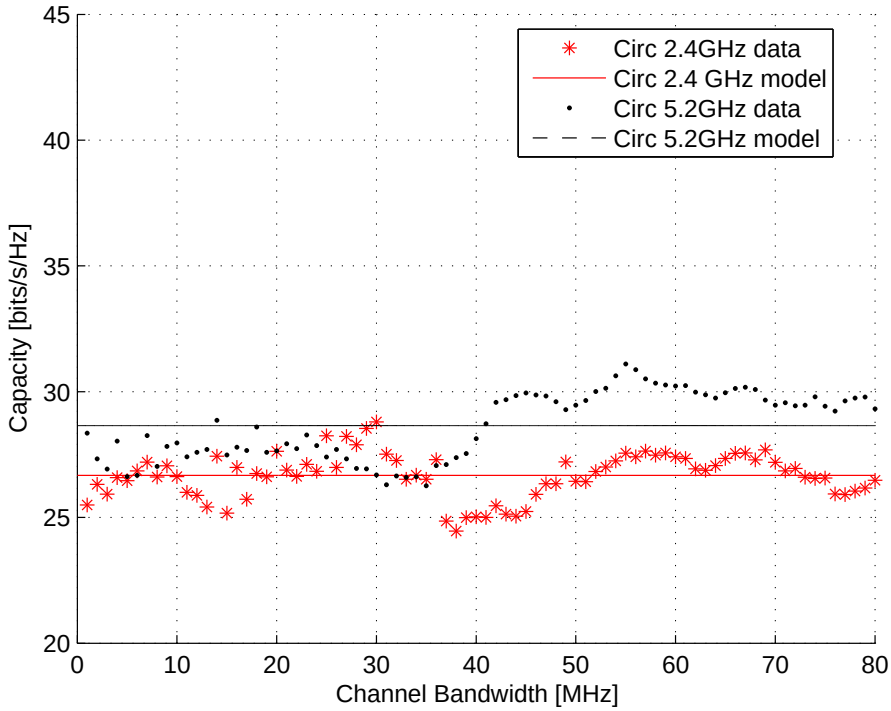

FIGURE 5.8: Capacity versus excitation bandwidth at location 8 for circular array

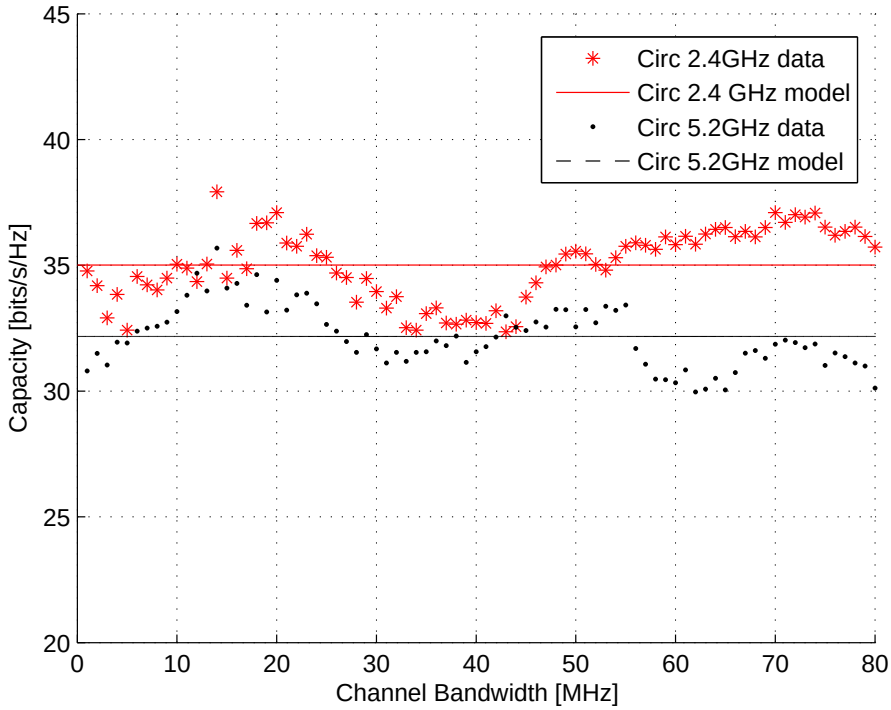

FIGURE 5.9: Capacity versus excitation bandwidth at location 9 for circular array

TABLE 5.2: TX Pairwise Average Correlation of Capacity for UCA

Locations	Transmitter (TX)			
	2.4 GHz		5.2 GHz	
	ρ_{av}	error(%)	ρ_{av}	error(%)
1	0.1646	0.95	0.1553	0.10
2	0.1510	0.83	0.1535	0.40
3	0.2126	0.63	0.2330	0.37
4	0.1449	0.98	0.1692	0.07
5	0.1767	0.64	0.1774	0.05
6	0.2191	1.92	0.2335	1.02
7	0.2292	0.46	0.1897	1.00
8	0.2306	1.46	0.2010	0.57
9	0.1922	0.21	0.1964	0.38
10	0.1545	0.77	0.1547	0.08
11	0.1910	0.66	0.1949	0.05

TABLE 5.3: RX Pairwise Average Correlation of Capacity for UCA

Locations	Receiver (RX)			
	2.4 GHz		5.2 GHz	
	ρ_{av}	error(%)	ρ_{av}	error(%)
1	0.3292	0.53	0.4824	0.22
2	0.4927	0.27	0.4531	0.04
3	0.4035	0.09	0.4505	0.14
4	0.6371	0.26	0.7174	0.14
5	0.5112	0.12	0.5797	0.41
6	0.6954	0.08	0.5887	0.32
7	0.4196	0.05	0.3758	0.33
8	0.7413	0.24	0.6349	0.18
9	0.3896	0.12	0.5357	0.37
10	0.3609	0.09	0.3635	0.53
11	0.3670	0.16	0.4561	0.02

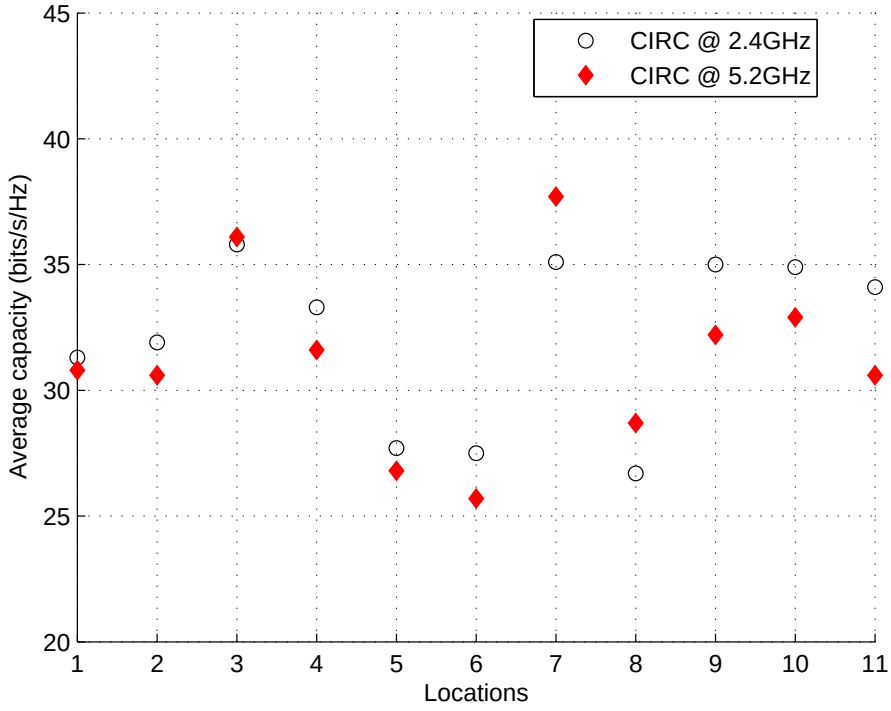

FIGURE 5.10: Average capacity at each of the measurement locations in CEFIM

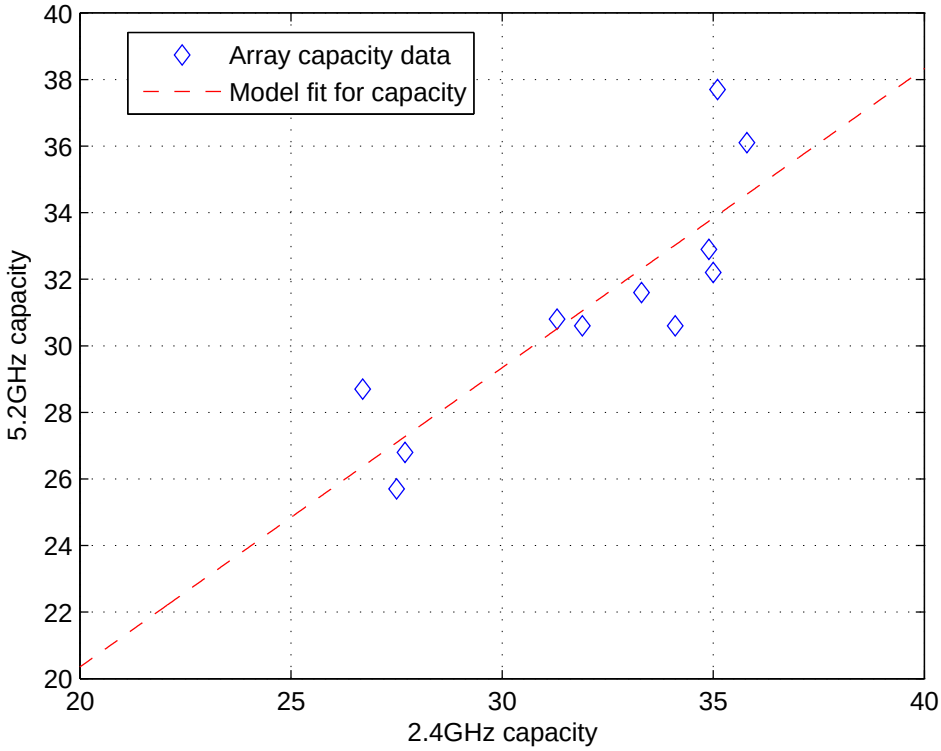

FIGURE 5.11: Frequency scaling relationship of capacities in WB indoor environment

5.2 MODELLING SPATIAL CORRELATION

5.2.1 Introduction

In this section, spatial correlation is explored at a center frequency of 2.4 GHz to predict measurements at a much higher center frequency of 5.2 GHz, which has been referred to as frequency scaling. In theory, the cost of channel measurements can be greatly reduced when such predictions are possible. Furthermore, frequency scaling suggests that MIMO techniques employed in a system with one center frequency will be directly applicable to systems operating at other frequencies, possibly decreasing the development time of MIMO systems and network planning. Obviously, the validity of frequency scaling depends on the similarity of the multipath at the two different frequencies. The modelling approach, parameter determination and the results when frequency scaling is employed using uniform linear arrays (ULA) across all the 11 measured locations are described.

5.2.2 Model Description

At each of the 11 locations shown in Figure 4.21, 20 channel snapshots were recorded with 200 ms between snapshots. This resulted in a 4 s acquisition time, and since the channel sounding was for a fixed TX and RX case, negligible channel variation was observed across this duration.

To remove the effect of path loss in our computations, channel matrices were normalized according to

$$\tilde{\mathbf{H}}^{(n)} = \left(\frac{1}{N_R N_T N_S} \sum_{m=1}^{N_S} \left\| \mathbf{H}^{(m)} \right\|_F^2 \right)^{-1/2} \mathbf{H}^{(n)}, \tag{5.7}$$

where $\tilde{\mathbf{H}}^{(n)}$ and $\mathbf{H}^{(n)}$ are the n^th normalized and un-normalized channel matrices respectively. N_s is the number of channel measurements (snapshots and frequency bins) at a single location and $\|\cdot\|_F$ is the Frobenius norm.

The ULA measurements are well suited to correlation studies since the ULA has a shift-invariant correlation structure under the assumption of far-field scattering. Also in a rich multipath environment, the correlation of the ULA will depend mainly on the relative orientation of the array and the multi-path, allowing the directional signature of the multi-path

to be investigated.

For the ULA, far-field scattering produces a shift-invariant correlation structure, allowing the transmit or receive correlation to be written as a function of just the offset between elements, instead of a function of both indices. In this case, the shift-invariant correlation coefficient at the RX with an element displacement of l is

$$\rho_\ell = \frac{\left[\sum_{k=1}^{N_S}\sum_{j=1}^{N_T}\sum_{i=1}^{N_R-\ell} H_{i,j}^{(k)} H_{i+\ell,j}^{(k)*}\right]}{\left[\left(\sum_{k=1}^{N_S}\sum_{j=1}^{N_T}\sum_{i=1}^{N_R-\ell}\left|H_{i,j}^{(k)}\right|^2\right)\left(\sum_{k=1}^{N_S}\sum_{j=1}^{N_T}\sum_{i=1}^{N_R-\ell}\left|H_{i+\ell,j}^{(k)}\right|^2\right)\right]^{1/2}}, \tag{5.8}$$

where $N_s = 20 \times 80$ is the number of snapshots taken across all frequency bins and observations, $H_T = 8$ and $N_R = 8$ are the number of transmit and receive antenna, respectively, and $H_{i,j}^{(k)}$ is the k^th channel snapshot from the j^th TX to the i^th RX antenna. The shift-invariant TX correlation is computed by interchanging the roles of TX and RX in equation (5.8) above.

To simplify the analysis of correlation, the magnitude of ρ_l was modelled with the exponential function as

$$y_\ell = e^{-b\ell\Delta x} \tag{5.9}$$

where Δx is the element separation in wavelengths and b is the estimated *decorrelation* parameter, which is chosen to minimize the average mean square error (MSE), $\bar{d}$ at TX and RX, where

$$\bar{d} = \frac{1}{\{N_T, N_R\}} \sum_{\ell=0}^{\{N_T,N_R\}-1} (|\rho_\ell| - y_\ell)^2, \tag{5.10}$$

and separate values of *b* are estimated at the TX and RX for each frequency.

Frequency scaling of the spatial correlation was tested by applying the linear regression technique to the decorrelation at the two frequencies, or

$$q_{5.2} = a_1 + a_2 q_{2.4}, \tag{5.11}$$

where $q_{5.2,2.4}$ is the decorrelation at 5.2 GHz and 2.4 GHz respectively, and a_1 and a_2 are obtained with the minimum mean square error (MSE) curve fit.

5.2.3 Results

Figure 5.12 plots the shift-invariant correlation coefficient at the RX for location 4 versus antenna element displacement (in wavelengths) for both 2.4 GHz and 5.2 GHz, whilst Figure 5.14 shows the plot at the TX. The symbols and smooth lines in both plots refer to the data points and the best-fit exponential model respectively.

At location 7, where the capacities were higher in relative terms and the differential in capacity between 2.4 GHz and 5.2 GHz was greatest, one observes in Figure 5.13 that the de-correlation parameter was also correspondingly greater. Similarly, Figure 5.15 shows that the de-correlation parameter is very low at location 8, where the capacity is also lower. It was also found that one cannot use the absolute value, but the relative can be used for comparative and analytical purposes.

The RX decorrelation parameter *b*, as well as the MSE of the model fit to the data points for all 11 locations is computed in Table 5.4 for both the 2.4 GHz and 5.2 GHz channel data. Typical MSE of the model is between 0.2% and 3.3% with only about 20% of the locations having an error above 4%. Average error for the 2.4GHz and 5.2GHz sets are 2.34% and 2.26% respectively, indicating a remarkable good fit for the chosen model.

Following the same procedure for the TX correlation, results obtained from the decorrelation parameter values are listed in Table 5.5. Typical MSE of the model is between 0.2% and 2.9%. The average error for the 2.4 GHz and 5.2 GHz sets is 1.9% and 1.4%, again indicating a good fit for the model.

To establish the effect of frequency scaling on the decorrelation, Figure 5.16 plots the RX parameter $b_{5.2}$ versus $b_{2.4}$ using the data from Table 5.4. One observes that there is very high dependence present with the exception of location 9 having (0.34442, 1.2042). The broken and solid lines in Figure 5.16 show the linear regression of the data when all data points are considered and when location 9 is discarded as an outlier respectively. MSE values for these two cases are 0.109 and 0.012 respectively. Performing a linear regression of the decorrelation parameter using the data in Table 5.5 at TX as shown in Figure 5.17 results in MSE values of 0.136 and 0.034 when again location 9 is included and discarded as an outlier, respectively.

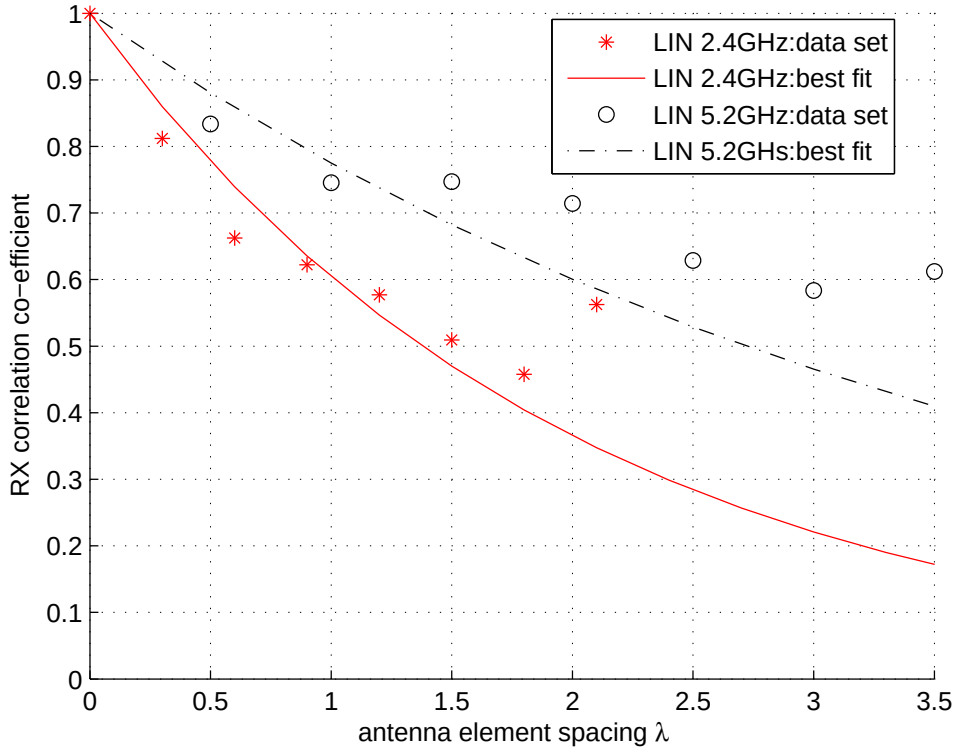

FIGURE 5.12: Calculated relative correlation coefficients with curve fit for RX location 4

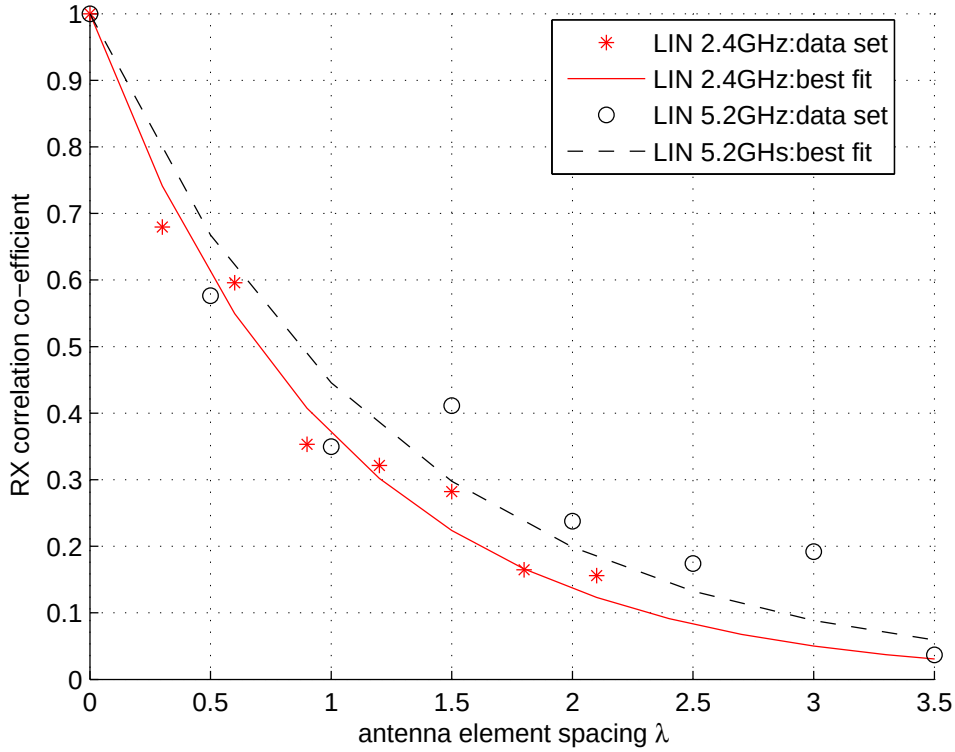

FIGURE 5.13: Calculated relative correlation coefficients with curve fit for RX location 7

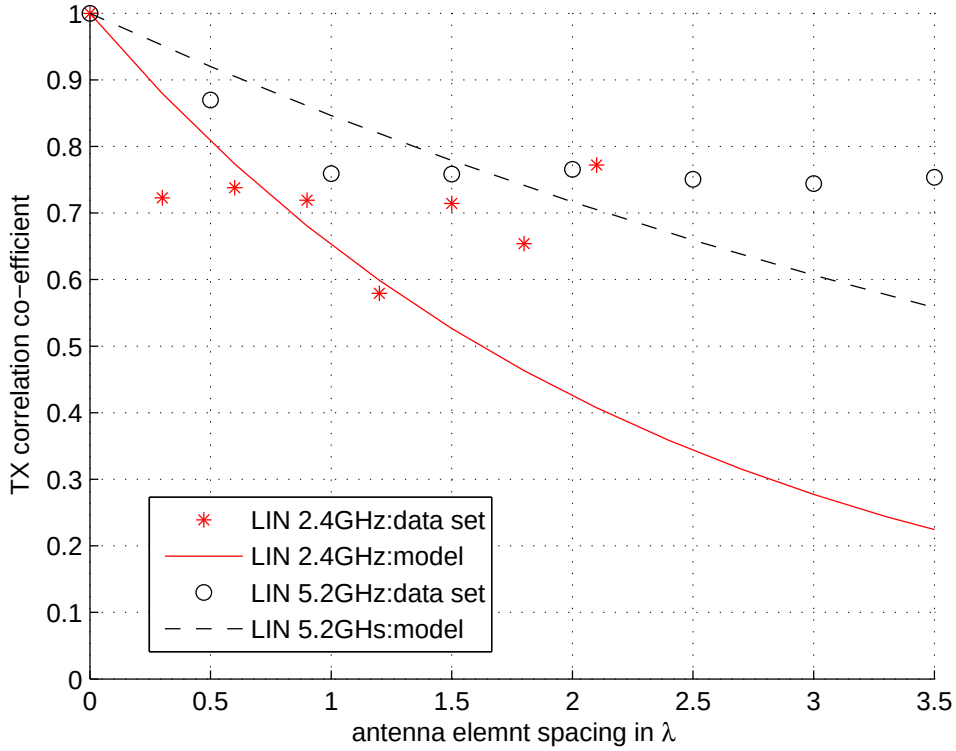

FIGURE 5.14: Calculated relative correlation coefficients with curve fit for TX location 4

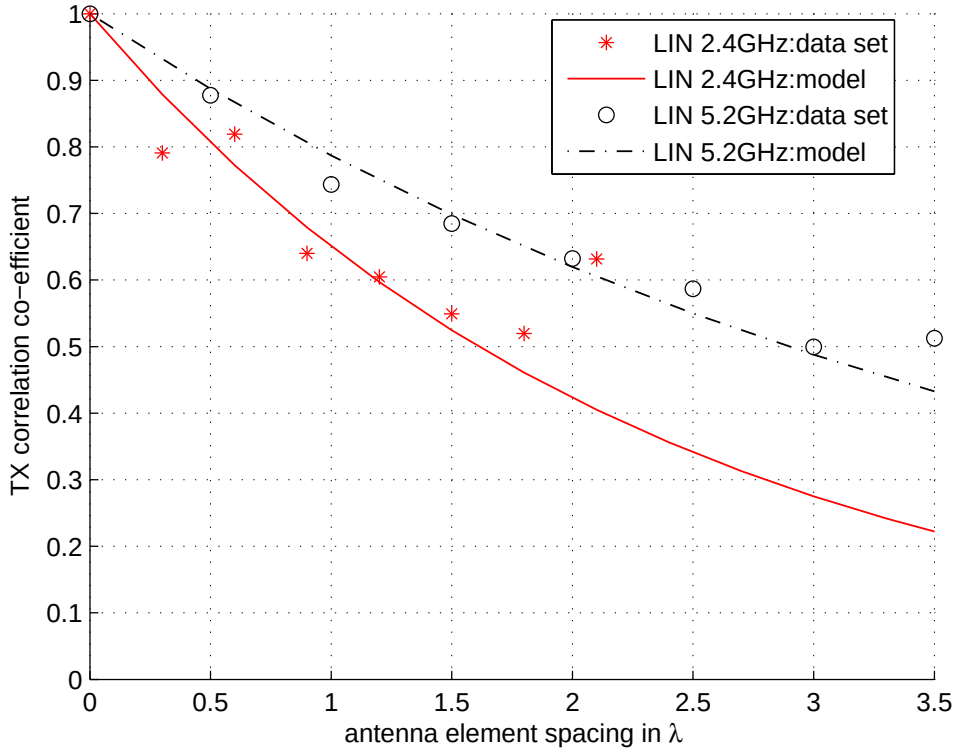

FIGURE 5.15: Calculated relative correlation coefficients with curve fit for TX location 8

TABLE 5.4: Decorrelation Parameter (b) and Error wrt Wavelength (λ) at RX

Locations	2.4 GHz		5.2 GHz	
	b	error(%)	b	error(%)
1	0.8960	4.76	0.8702	3.27
2	1.0903	4.48	1.2795	1.76
3	1.2546	2.00	1.5591	5.64
4	0.4080	0.75	0.2550	1.06
5	0.8799	3.49	1.0536	2.57
6	0.3182	1.15	0.3432	0.98
7	0.9978	0.17	0.9071	0.72
8	0.4190	0.35	0.4883	1.46
9	1.2042	1.18	0.3442	0.45
10	0.9980	2.90	1.0403	2.40
11	1.5548	3.65	1.9721	5.41

TABLE 5.5: Decorrelation Parameter (b) and Error wrt Wavelength (λ) at TX

Locations	2.4 GHz		5.2 GHz	
	b	error(%)	b	error(%)
1	0.9511	0.18	0.9769	1.54
2	0.8849	1.69	1.0189	2.66
3	1.0666	2.34	1.2988	1.68
4	0.4270	2.90	0.2400	2.96
5	0.8325	0.06	0.8746	2.08
6	0.6833	0.56	0.7402	5.84
7	1.2678	1.38	1.4634	1.13
8	0.4302	0.84	0.2845	0.51
9	1.6701	0.96	0.3530	1.03
10	1.4210	3.15	1.0134	0.75
11	1.0462	0.76	0.9514	0.49

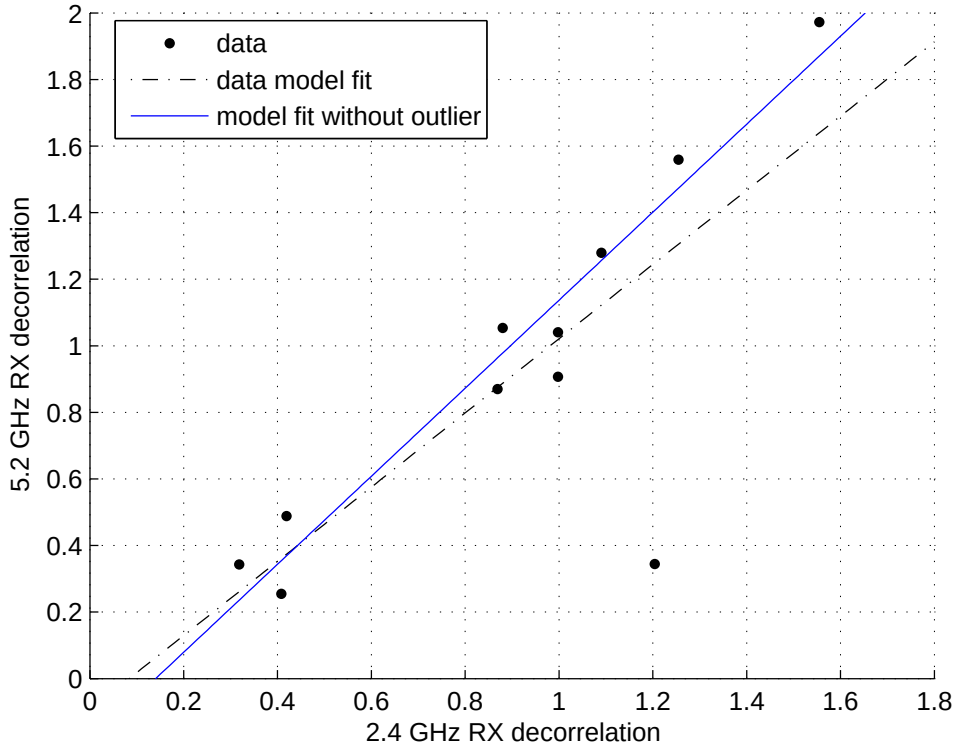

FIGURE 5.16: Relationship of RX decorrelation with respect to frequency scaling

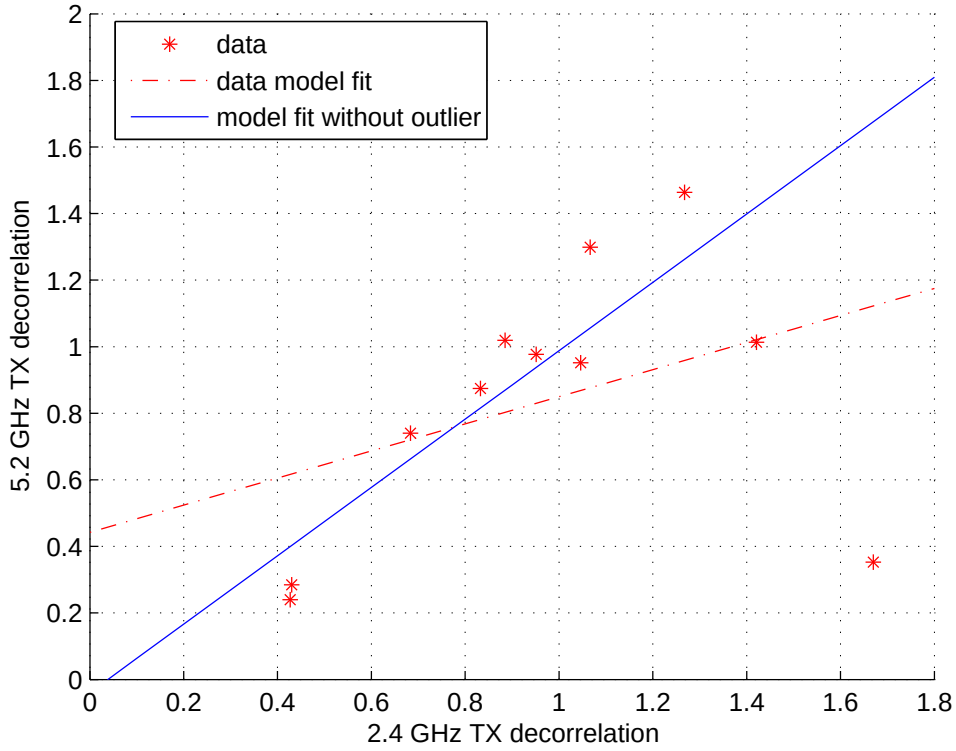

FIGURE 5.17: Relationship of TX decorrelation with respect to frequency scaling

These results show that the correlation at the two frequencies exhibits a strong dependence, suggesting that not only the level of multipath at the frequencies are similar, but also that the directional signature is related as is seen in section5.3.

5.3 DOUBLE DIRECTIONAL CHANNEL MODELLING

5.3.1 Introduction

Since initial research in multiple-input-multiple-output (MIMO) wireless systems [9], the opportunities and demands of higher spectral efficiency, quality of service and data rates in wireless systems have stimulated ongoing research in this area. MIMO architectures are potentially good candidates for future wireless systems, since they employ multiple antennas at both the transmitter (TX) and the receiver (RX) to significantly increase channel capacity in a multipath environment, without increasing the system bandwidth or transmit power.

Accurate characterization of the propagation channel is essential in order to assess the potential benefit of employing sophisticated coding, modulation, and antenna arrays in MIMO systems. This is accomplished either by statistical or geometrical modelling, advanced modelling strategies (such as ray tracing) and direct measurement [19]. Modelling approaches have the advantage of inexpensive implementation on a computer, but may lack sufficient accuracy in representing real-world channels. Direct channel measurement provides accurate characterization, but can be time-consuming and expensive, allowing only a small set of communications channels to be investigated. With the advent of technologies such as ultra-wideband (UWB) communications, and the allocation of new RF spectra, channel characterization becomes necessary not only for several different scenarios, but also for many different communication bands.

This chapter explores the effect of center frequency on the MIMO channel response in an indoor environment, showing that in certain cases the double-directional response of the channel at 2.4 GHz is remarkably similar to that at 5.2 GHz, indicating that propagation mechanisms at the two frequencies may also be very similar. Employing measurements at one frequency to predict channel behavior at a different frequency is referred to herein as *frequency scaling*. In theory, this technique can drastically reduce the cost of MIMO channel measurement campaigns

and decrease development time of MIMO systems.

5.3.2 Model Description

The antenna arrays employed in this measurement were uniform circular arrays (UCAs) with 0.5λ spacing at both 2.4 GHz and 5.2 GHz, where λ is the free-space wavelength. As depicted in Figure 4.21, the RX was placed at 11 different office and laboratory locations, while the TX was placed at a single fixed position in the corridor of CEFIM at the University of Pretoria, South Africa. The RX was set at exactly the same position, height, configuration and direction for both the 2.4 GHz and 5.2 GHz measurements.

At each location, 20 channel snapshots were recorded with 200 ms between snapshots. Since negligible channel variation was observed for each stationary measurement, only a single snapshot from each location was considered. Here, a channel snapshot is defined as $H_{ij}^{(k)}$, where k is a frequency bin index, and i and j are the receive and transmit antenna indices respectively. To remove the effect of path loss in our computations, channel matrices were normalized to have average unit SISO gain, as indicated in [95].

Previous channel modelling efforts have defined the double-directional channel [17] in terms of paired discrete plane-wave departures and arrivals at the TX and RX. In indoor environments, where multipath scattering is severe, extracting individual plane-wave arrivals can be very difficult. It was therefore decided to define the double-directional response in terms of spatial power spectra, obtained with either joint TX/RX Bartlett or Capon beamformers [42]. The joint Capon beamformer can now therefore be defined as

$$P_{\text{CAP}}(\nu_T, \nu_R) = \frac{1}{\mathbf{a}(\nu_T, \nu_R)^H \hat{\mathbf{R}}^{-1} \mathbf{a}(\nu_T, \nu_R)}, \tag{5.12}$$

where $\{\cdot\}^H$ is complex conjugate transpose, ν_T and ν_R are azimuth angles at the TX and RX, and $\hat{\mathbf{R}}$ is the sample covariance matrix. The joint steering vector $\mathbf{a}(\nu_T, \nu_R)$ is defined as

$$\mathbf{a}(\nu_T, \nu_R) = \mathbf{a}_T(\nu_T) \otimes \mathbf{a}_R(\nu_R), \tag{5.13}$$

where $\mathbf{a}_{\{T,R\}}$ are the usual separate array steering vectors for the TX and RX, and $\otimes$ is the Kronecker product. The sample covariance matrix is computed as

$$\hat{\mathbf{R}} = \frac{1}{K}\sum_{k} \mathbf{h}^{(k)}\mathbf{h}^{(k)H}, \tag{5.14}$$

where K is the total number of frequency bins, $\mathbf{h}^{(k)} = \mathrm{Vec}\left\{\mathbf{H}^{(k)}\right\}$, and the vector operation $\mathrm{Vec}\left\{\cdot\right\}$ stacks a matrix into a vector.

Likewise, the joint Bartlett beamformer is defined as

$$P_{\mathrm{BF}}(\nu_T, \nu_R) = \frac{\mathbf{a}(\nu_T, \nu_R)^H \hat{\mathbf{R}} \mathbf{a}(\nu_T, \nu_R)}{\mathbf{a}(\nu_T, \nu_R)^H \mathbf{a}(\nu_T, \nu_R)} \tag{5.15}$$

The similarity of the spectra at 2.4 GHz and 5.2 GHz is evaluated by computing the correlation coefficient on the double-directional spectra at the two different frequencies using either the Capon or Bartlett beamformer. The correlation coefficient is computed as

$$\rho = \frac{\sum_{j=0}^{N}\sum_{i=0}^{N}(P_{2.4,ij} - \overline{P}_{2.4})(P_{5.2,ij} - \overline{P}_{5.2})}{\sqrt{\left[\sum_{i=0}^{N}\sum_{j=0}^{N}(P_{2.4,ij} - \overline{P}_{2.4})^2\right]\left[\sum_{i=0}^{N}\sum_{j=0}^{N}(P_{5.2,ij} - \overline{P}_{5.2})^2\right]}}, \tag{5.16}$$

where N is the number of discretization points, $P_{f,ij} = P_{\{CAP,BF\}}(\nu_{T,i}, \nu_{R,j})$, f is the center frequency in GHz, $\nu_{T,i} = \nu_{R,i} = 2\pi i/N$, and $\overline{P}_f = (1/N^2)\sum_i \sum_j P_{f,ij}$.

5.3.3 Results

Figures 5.18 and 5.19 shows the joint spatial power spectra at Location 4 for the Bartlett and Capon beamformers.

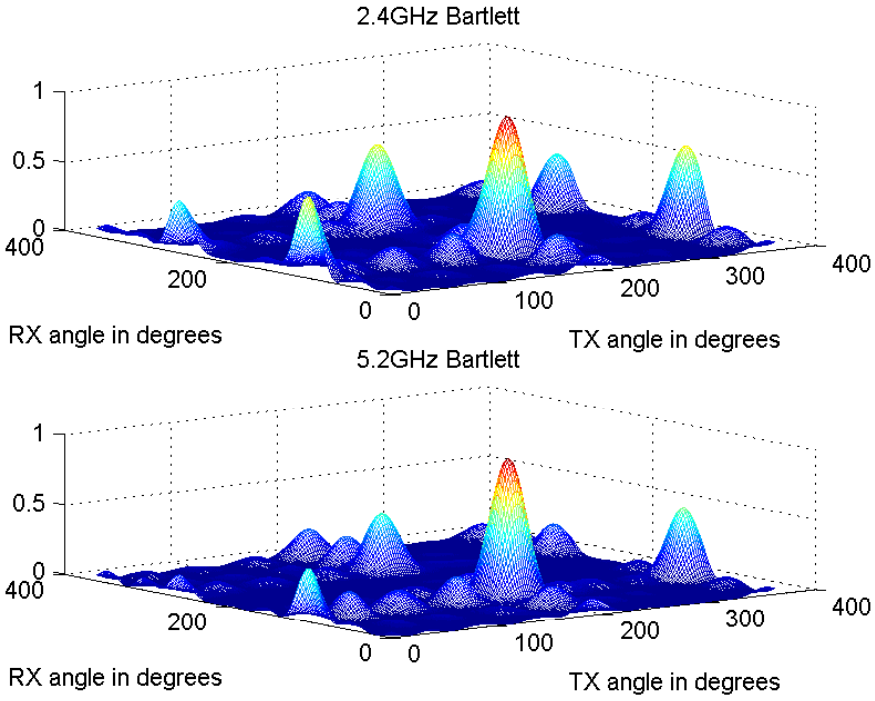

FIGURE 5.18: Spatial spectra for Location 4 employing the Bartlett Beamformer

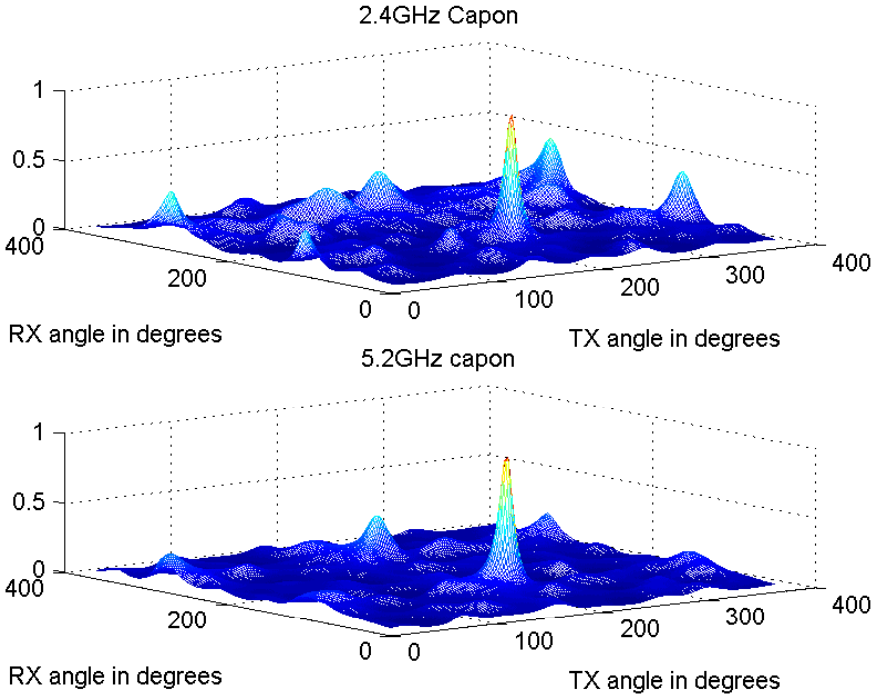

FIGURE 5.19: Spatial spectra for Location 4 employing the Capon Beamformer

TABLE 5.6: Correlation coefficient of 2.4 GHz and 5.2 GHz spectra

Locations	Bartlett Beamformer	Capon Beamformer
	ρ_{BF}	ρ_{CAP}
1	0.37	0.73
2	0.56	0.77
3	0.43	0.72
4	0.56	0.94
5	0.62	0.59
6	0.58	0.47
7	0.35	0.56
8	0.51	0.76
9	0.33	0.56
10	0.25	0.16
11	0.41	0.63

One observes that there is a similarity in the spatial structure of the electromagnetic waves for both beamforming techniques. An alternate approach shown in Figures 5.20 and 5.21 shows the contour mapping of the power spectra also for Location 4 at 2.4 GHz and 5.2 GHz respectively. This is verified by the respective correlation coefficient of 0.56 (Bartlett) and 0.94 (Capon) shown in Table 5.6. Where the joint correlation coefficient shown in Table 5.6, is relatively lower (such as Location 7), one would expect the geometry of the power spectra to be different. This is the case as observed in Figures 5.22 and 5.23, where the angular positions may be somewhat similar, but the amplitudes differ. The plots also indicate that the Bartlett beamformer performs better in terms of spatial similarity, and this is congruent with the higher correlation coefficient computed.

As depicted in Figures 5.24 and 5.25, Location 11 has more scattering but still exhibits a high degree of correlation in the spectra for either beamforming technique. Table 5.6 indicates that the Capon beamformer usually produces a higher correlation coefficient than the Bartlett beamformer, with the exception of Locations 6 and 10. This result might be expected, since the Bartlett beamformer tends to produce complicated interference patterns between major scattering directions, but the Capon beamformer often suppresses this effect. Thus, although

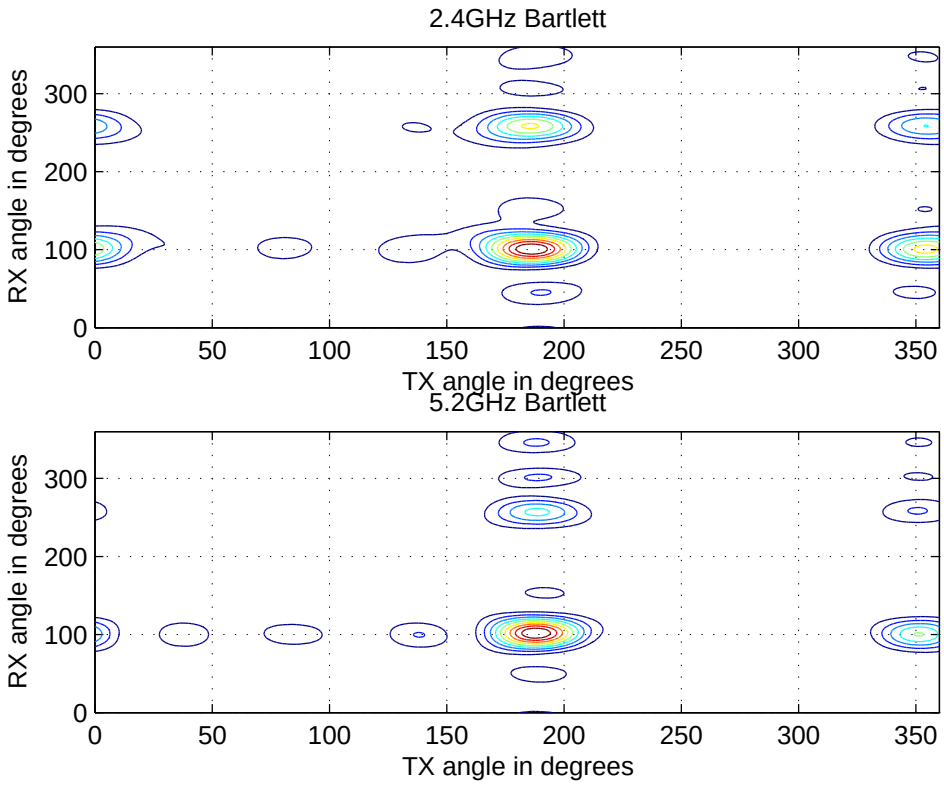

FIGURE 5.20: Spectral contour for Location 4 employing the Bartlett Beamformer

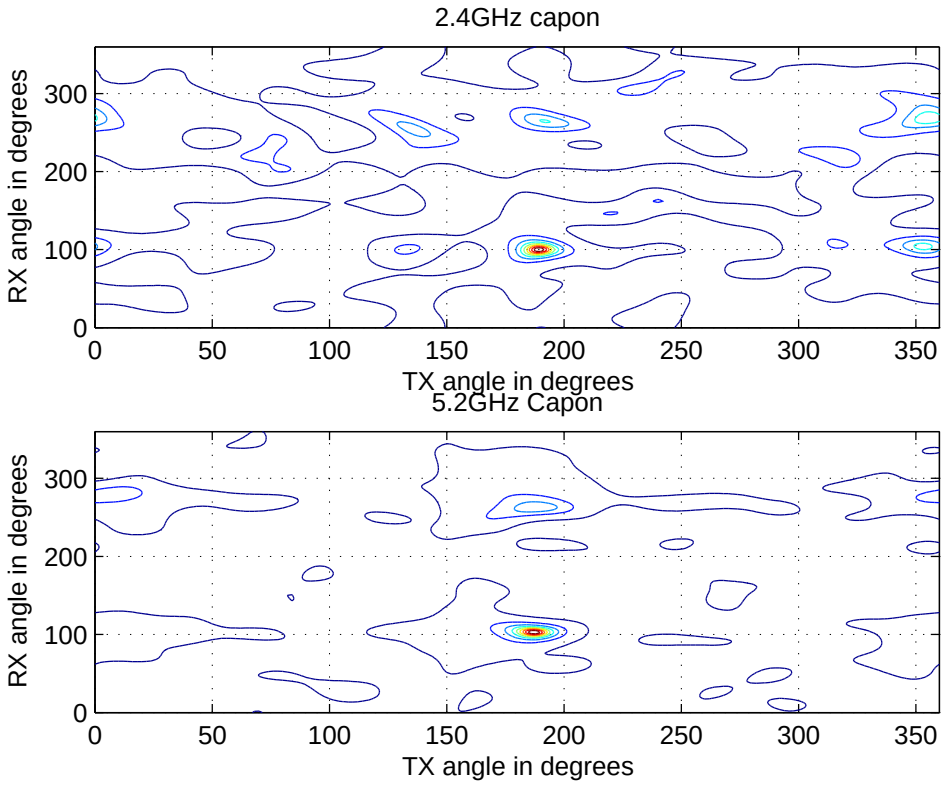

FIGURE 5.21: Spectral contour for Location 4 employing the Capon Beamformer

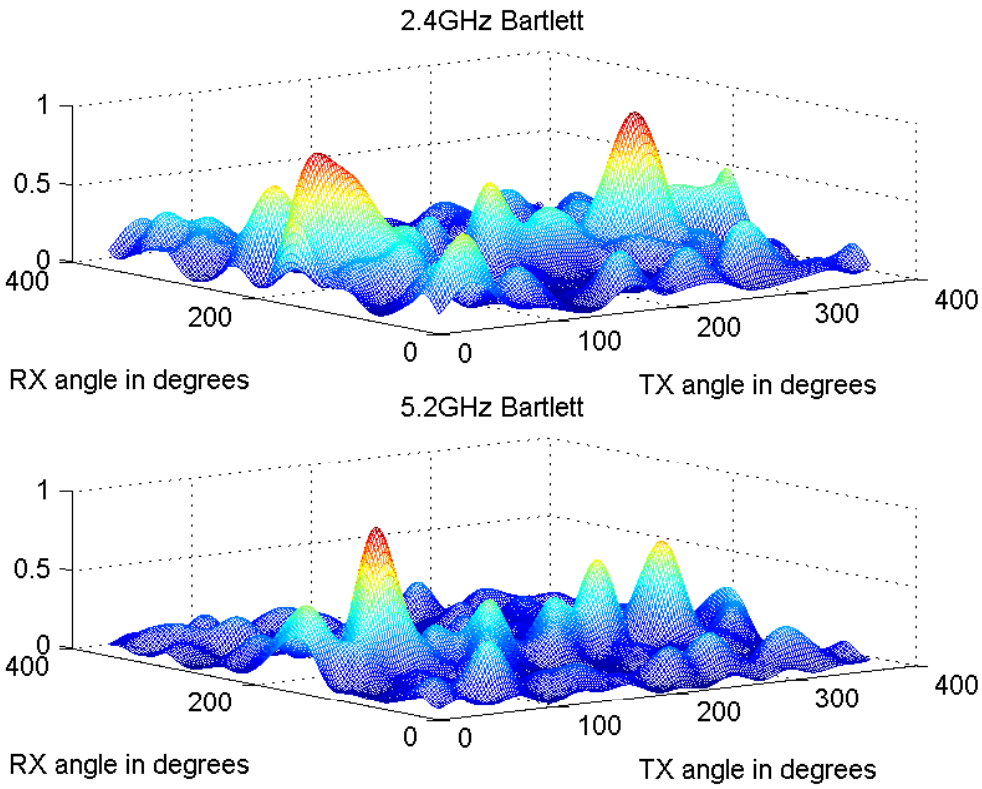

FIGURE 5.22: Spatial spectra for Location 7 employing the Bartlett Beamformer

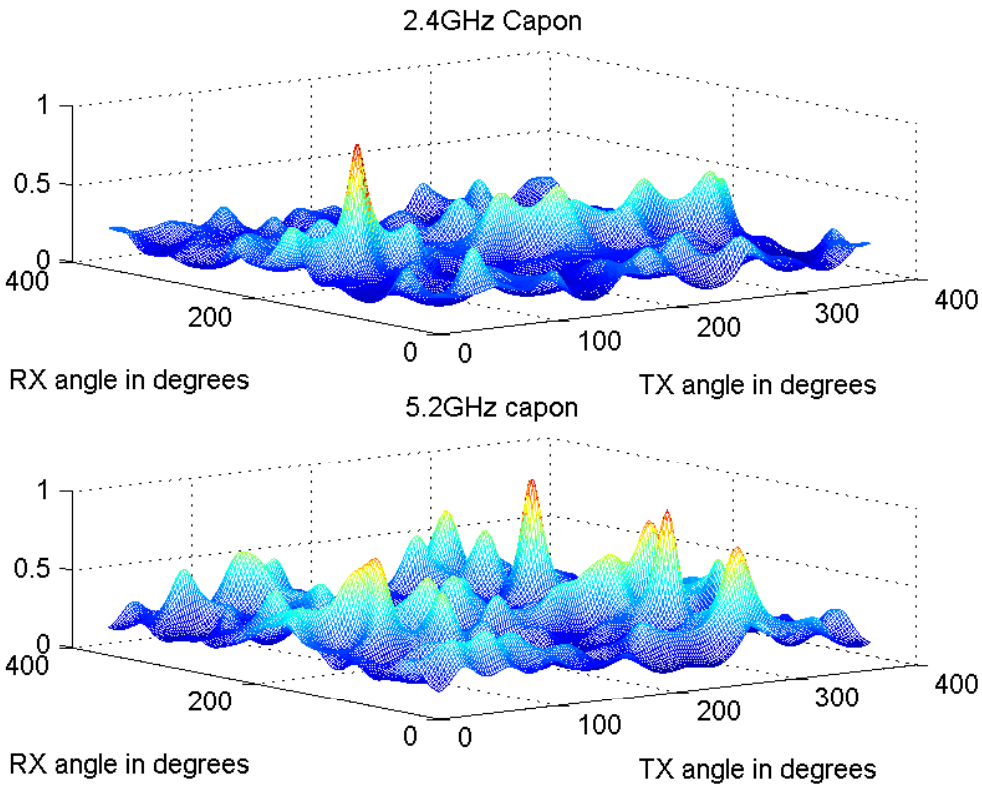

FIGURE 5.23: Spatial spectra for Location 7 employing the Capon Beamformer

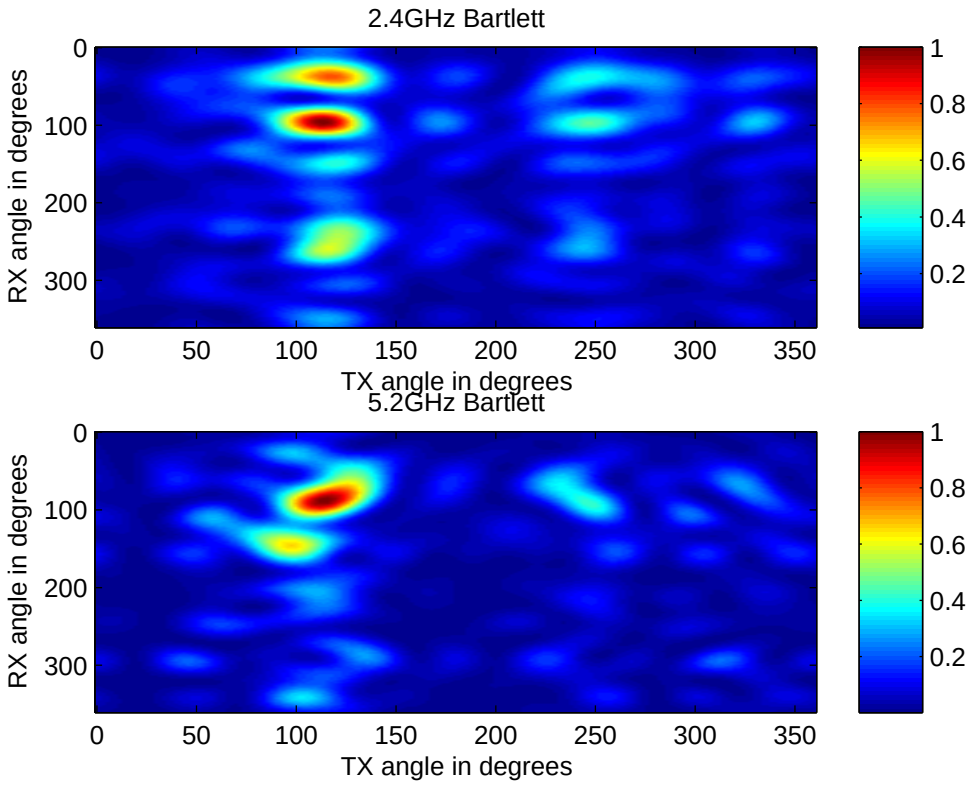

FIGURE 5.24: Spatial spectra for Location 11 employing the Bartlett Beamformer

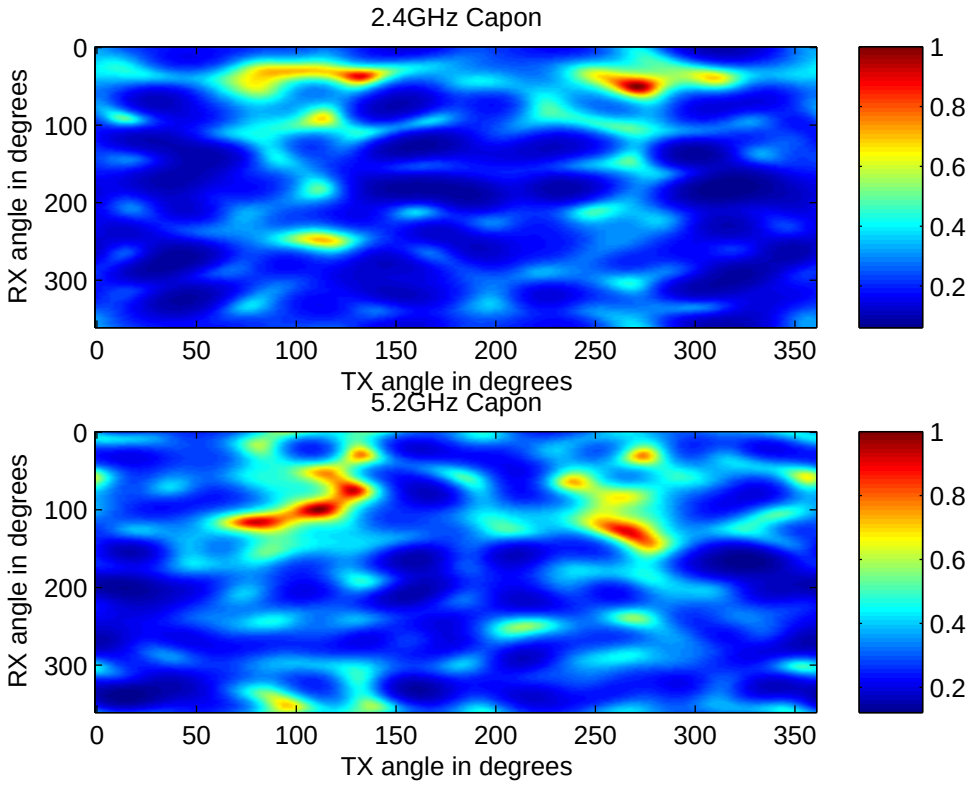

FIGURE 5.25: Spatial spectra for Location 11 employing the Capon Beamformer

the Bartlett beamformer may be a more sensitive metric for comparison of joint spatial power spectra, the Capon beamformer will focus on comparing the principal directions of arrival and departure.

5.4 CONCLUSION

5.4.1 Capacity Modelling

A study on the effect of frequency scaling on capacity in indoor MIMO wireless systems has been presented. The results for the circular antenna array configuration suggest that one can predict the capacity in a MIMO system at another center frequency through a linear dependence relationship. The pairwise correlation coefficient presented can also be reliably used as a metric to explain the differences in measured capacities at the various locations.

5.4.2 Spatial Correlation

Through the study of the spatial correlation for a ULA at both 2.4 GHz and 5.2 GHz it has been shown that for an indoor office type environment there can be exploitation of the relationship of the correlation in MIMO wireless systems. Furthermore, the model determined through the measurement campaign confirmed the model that is sometimes used in the literature [98]. Measured capacity for the ULA at 2.4 GHz and 5.2 GHz suggests that one can predict the correlation through a linear dependence relationship. This suggests that there is high correlation in the directional signature of the multipath propagation. These results suggest that propagation mechanisms in the indoor environment at these two distinct carrier frequencies may be very similar, leading to cost savings in channel measurement campaigns, network planning and MIMO system development.

5.4.3 Double Directional Channel

The idea of frequency scaling in the double-directional joint TX/RX case, or using measured channel characteristics at one center frequency to predict behavior at another frequency, have been proposed. This could save time and cost of channel characterization and network planning. The ability to perform frequency scaling was investigated by comparing the double-directional spectra of measured indoor channels at 2.4 GHz and 5.2 GHz. Comparison of the spatial spectra

at the two center frequencies showed a high degree of similarity, suggesting that the multipath propagation at the two frequencies is mainly due to specular reflections. These results are promising, since it suggests that models may be developed that predict channel behavior at many different bands given measurements at only a single center frequency.

CHAPTER SIX

MAXIMUM ENTROPY MODELLING

6.1 INTRODUCTION

It is well established that multiple-input-multiple-output (MIMO) wireless systems have the potential to meet demands for higher data rates, improved spectral efficiency and better quality of service in wireless systems [15]. Correct assessment of MIMO systems depends on accurate characterization of the propagation channel, which has resulted in numerous measurement campaigns [89, 99–101] as well as modelling strategies [17, 19].

One of the most popular MIMO modelling strategies to date is the Kronecker model [18], which allows the full joint transmit/receive covariance matrix to be synthesized from only the separate transmit and receive covariance matrices. Although the model is preferred due to its simplicity, application of the model to measured channels indicates marginal discrepancies in the modelled capacity and more substantial error in the modelled joint spatial spectra (eigenvalues) [97]. Improvements to the Kronecker model have been proposed by combining the separate transmit/receive covariance information with partial information from the full covariance [102].

A modelling approach based on information theoretic considerations has appeared [103], which applies the principle of maximum entropy (ME) to MIMO channels. Given a set of known channel parameters, the ME estimate of any unknown parameters is that which imposes the least structure on the channel model. Thus, by not imposing "artificial structure" on the channel, the ME principle should allow for more consistent (and possibly more accurate)

modelling, based on only the channel knowledge at hand.

The purpose of the present work is to apply the principle of ME to the problem of deriving the full joint covariance, based only on knowledge of the separate transmit/receive covariances. The main goal is to see if ME offers any modelling improvement by avoiding the artificial structure apparently present in the Kronecker model [97].

6.2 MODEL DESCRIPTION

Suppose the respective transmit and receive covariances $\mathbf{R}_T$ and $\mathbf{R}_R$ are known, respectively, so then the statistics of the channel matrices are constrained by

$$\mathrm{E}\left\{\mathbf{H}\mathbf{H}^H\right\} = \mathbf{R}_R \quad \mathrm{E}\left\{\sum_k H_{ik}H_{jk}^*\right\} = R_{R,ij} \tag{6.1}$$

$$\mathrm{E}\left\{\mathbf{H}^H\mathbf{H}\right\} = \mathbf{R}_T^T \quad \mathrm{E}\left\{\sum_k H_{ki}H_{kj}^*\right\} = R_{T,ij} \tag{6.2}$$

$$p(\mathbf{H}) \geq 0 \tag{6.3}$$

$$\int p(\mathbf{H})d\mathbf{H} = 1, \tag{6.4}$$

where $\{\cdot\}^H$ is complex conjugate transpose, $p(\mathbf{H})$ is the joint probability density function (PDF) of the elements of the channel matrix $\mathbf{H}$, and $\mathrm{E}\{\cdot\}$ is expectation. Assuming we want to maximize the entropy or

$$\int p(\mathbf{H}) \log p(\mathbf{H})d\mathbf{H} \tag{6.5}$$

with respect to the above constraints, one can write the Lagrangian and set the derivative equal to zero to get the form of the PDF

$$\begin{aligned} & p(\mathbf{H}) \\ &= \exp(\lambda_0 + \sum_{ij}\mu_{R,ij}\sum_k H_{ik}H_{jk}^* + \sum_{ij}\mu_{T,ij}\sum_k H_{ki}H_{kj}^*) \\ &= c_0 \exp(\sum_{ijk\ell}\mu_{R,ik}H_{ij}H_{k\ell}^*\delta_{j\ell} + \sum_{ijk\ell}\mu_{T,j\ell}H_{ij}H_{k\ell}^*\delta_{ik}), \end{aligned} \tag{6.6}$$

where $c_0 = \exp(\lambda_0)$. Combining the two equations leads to

$$p(\mathbf{H}) = c_0 \exp\left[\sum_{ijkl} H_{ij}H_{k\ell}^*(\underbrace{\mu_{R,ik}\delta_{j\ell} + \mu_{T,j\ell}\delta_{ik}}_{-R_{ij,k\ell}^{-1}})\right], \tag{6.7}$$

which is the form of the standard multivariate complex normal PDF with a covariance matrix indexed by the stacked receive and transmit indices. This can be expressed with the Kronecker product as

$$\mathbf{R} = -\underbrace{(\mathbf{I}_T \otimes \boldsymbol{\mu}_R + \boldsymbol{\mu}_T \otimes \mathbf{I}_R)}_{\mathbf{A}}^{-1} \tag{6.8}$$

One observes that (6.8) is different from the Kronecker model [18] which has the simpler form

$$\mathbf{R} = \mathbf{R}_T \otimes \mathbf{R}_R. \tag{6.9}$$

Taking the eigenvalue decomposition (EVD) of $\boldsymbol{\mu}_T$ and $\boldsymbol{\mu}_R$, ie.,

$$\boldsymbol{\mu}_T = \boldsymbol{\xi}_T \boldsymbol{\Lambda}_T \boldsymbol{\xi}_T^H, \quad \boldsymbol{\mu}_R = \boldsymbol{\xi}_R \boldsymbol{\Lambda}_R \boldsymbol{\xi}_R^H, \tag{6.10}$$

allows (6.8) to be expanded as

$$\mathbf{R}^{-1} = -\underbrace{(\boldsymbol{\xi}_T \otimes \boldsymbol{\xi}_R)}_{\boldsymbol{\xi}} \underbrace{(\mathbf{I}_T \otimes \boldsymbol{\Lambda}_R + \boldsymbol{\Lambda}_T \otimes \mathbf{I}_R)}_{\boldsymbol{\Lambda}} \underbrace{(\boldsymbol{\xi}_T \otimes \boldsymbol{\xi}_R)^H}_{\boldsymbol{\xi}^H}, \tag{6.11}$$

so that $\mathbf{R} = -\boldsymbol{\xi}\boldsymbol{\Lambda}^{-1}\boldsymbol{\xi}^H$. The matrix $\boldsymbol{\Lambda}$ involves Kronecker products and sums of diagonal matrices, which will also be diagonal, or

$$\begin{aligned} \Lambda_{ij,k\ell} &= \delta_{j\ell}\delta_{ik}\lambda_{R,i} + \delta_{j\ell}\delta_{ik}\lambda_{T,j} \\ &= \delta_{j\ell}\delta_{ik}\left[\lambda_{R,i} + \lambda_{T,j}\right] \qquad (6.12) \\ \Lambda^{-1}_{ij,k\ell} &= \delta_{j\ell}\delta_{ik}\frac{1}{\lambda_{R,i} + \lambda_{T,j}} \qquad (6.13) \end{aligned}$$

Therefore one has the form of the full covariance matrix. The eigenvectors are just the Kronecker product of the separate transmit and receive eigenvectors. The eigenvalues, however, must be found by substituting $\mathbf{R}$ back into the original constraints. Although the constraints (6.1) and (6.2) depend on expectations of $\mathbf{H}$, they can be re-written in terms of the full covariance as

$$R_{R,ik} = \sum_j R_{ij,kj}, \quad R_{T,j\ell} = \sum_i R_{ij,i\ell} \tag{6.14}$$

The covariance matrix from (6.11) can be written in component form as

$$R_{ij,k\ell} = \left\{-\mathbf{A}^{-1}\right\}_{ij,k\ell} = -\sum_{mn} \xi_{ij,mn}\Lambda^{-1}_{mn,mn}\xi^*_{k\ell,mn} \tag{6.15}$$

Substituting (6.15) into (6.14) results in

$$\{-\mathbf{R}_T\}_{jl} = \sum_{mn}\sum_{i} \xi_{ij,mn}\Lambda^{-1}_{mn,mn}\xi^*_{i\ell,mn} \tag{6.16}$$

$$= \sum_{mn} \xi_{T,jn}\xi^*_{T,\ell n}\Lambda^{-1}_{mn,mn} \underbrace{\sum_{i} \xi_{R,im}\xi^*_{R,im}}_{=1} \tag{6.17}$$

$$= \sum_{n} \xi_{T,jn}\xi^*_{T,\ell n} \underbrace{\sum_{m} \Lambda^{-1}_{mn,mn}}_{-D_{T,nn}}, \tag{6.18}$$

Similarly, one can expand the receive covariance constraint as

$$\{-\mathbf{R}_R\}_{ik} = \sum_{m} \xi_{R,im}\xi^*_{R,km} \underbrace{\sum_{n} \Lambda^{-1}_{mn,mn}}_{-D_{R,mm}} \tag{6.19}$$

Equations (6.18) and (6.19) can be recognized as just the eigenvalue decompositions of the transmit and receive covariances

$$\mathbf{R}_T = \boldsymbol{\xi}_T\mathbf{D}_T\boldsymbol{\xi}_T^H \tag{6.20}$$

$$\mathbf{R}_R = \boldsymbol{\xi}_R\mathbf{D}_R\boldsymbol{\xi}_R^H. \tag{6.21}$$

To solve for the full covariance, the system of equations

$$D_{T,nn} = d_{T,n} = -\sum_{m} \frac{1}{\lambda_{R,m} + \lambda_{T,n}} \tag{6.22}$$

$$D_{R,mm} = d_{R,m} = -\sum_{n} \frac{1}{\lambda_{R,m} + \lambda_{T,n}} \tag{6.23}$$

must be solved, but a direct solution can be problematic since one would have to find the roots of multivariate large order polynomials. An indirect approach is possible by noticing that since $\mathbf{H}$ is a Gaussian process, maximum entropy maximizes $det(\mathbf{R})$. Since the eigenvectors are already known, one only needs to find $\boldsymbol{\Lambda}$, such that $\det\left(-\boldsymbol{\Lambda}^{-1}\right)$ is maximized. Letting

$$f_{mn} = -\Lambda^{-1}_{mn,mn}, \tag{6.24}$$

one must find the maximum of $\det(\mathbf{R}) = \prod_{ij} f_{ij}$, subject to the constraints

$$d_{T,j} = \sum_i f_{ij} \tag{6.25}$$

$$d_{R,i} = \sum_j f_{ij} \tag{6.26}$$

$$f_{ij} \geq 0 \tag{6.27}$$

Since the constraints are linear and $-\prod_{ij} f_{ij}$ is convex, there is a simple convex optimization problem that can be solved with conventional techniques. In this research, the solution is obtained by finding an admissible initial guess for the f_{ij} using linear programming and then moving to the optimum with gradient descent method.

6.3 DATA PROCESSING

The data is processed as follows: At each location, 20 channel snapshots were recorded with 200 ms between snapshots. Since negligible channel variation was observed for each stationary measurement, only a single snapshot from each location was considered. Here, a channel snapshot is defined as $H_{ij}^{(k)}$, where k is a frequency bin index, and i and j are the receive and transmit antenna indices respectively. To remove the effect of path loss in the computations, channel matrices were normalized to have average unit SISO gain [95].

Previous channel modelling efforts have defined the double-directional channel [17] in terms of paired discrete plane-wave departures and arrivals at the TX and RX. In indoor environments, where multipath scattering is severe, extracting individual plane-wave arrivals can be very difficult. It was therefore decided to define the double-directional response in terms of spatial power spectra, obtained with joint TX/RX Bartlett beamformers. The joint Bartlett beamformer [42] is given by

$$P(\nu_T, \nu_R) = \frac{\mathbf{a}(\nu_T, \nu_R)^H \hat{\mathbf{R}} \mathbf{a}(\nu_T, \nu_R)}{\mathbf{a}(\nu_T, \nu_R)^H \mathbf{a}(\nu_T, \nu_R)} \tag{6.28}$$

where ν_T and ν_R are azimuth angles at the TX and RX, and $\hat{\mathbf{R}}$ is the sample covariance matrix. The joint steering vector $\mathbf{a}(\nu_T, \nu_R)$ is defined as

$$\mathbf{a}(\nu_T, \nu_R) = \mathbf{a}_T(\nu_T) \otimes \mathbf{a}_R(\nu_R), \tag{6.29}$$

where $\mathbf{a}_{\{T,R\}}$ is the usual separate array steering vectors for the TX and RX, and $\otimes$ is the Kronecker product. The sample covariance matrix is computed as

$$\hat{\mathbf{R}} = \frac{1}{K}\sum_{k} \mathbf{h}^{(k)}\mathbf{h}^{(k)H}, \tag{6.30}$$

where K is the total number of frequency bins, $h^{(k)} = \mathrm{Vec}\left\{H^{(k)}\right\}$, and the vector operation $\mathrm{Vec}\{\cdot\}$ stacks a matrix into a vector.

The similarity of the joint spectra at 2.4 GHz is evaluated by computing the correlation coefficient between spectra A and B as

$$\rho_{A,B} = \frac{\sum_{j=0}^{N}\sum_{i=0}^{N}(P_{A,ij} - \bar{P}_A)(P_{B,ij} - \bar{P}_B)}{\sqrt{\left[\sum_{i=0}^{N}\sum_{j=0}^{N}(P_{A,ij} - \bar{P}_A)^2\right]\left[\sum_{i=0}^{N}\sum_{j=0}^{N}(P_{B,ij} - \bar{P}_B)^2\right]}}, \tag{6.31}$$

where N is the number of discretization points, $P_{ij} = P(\nu_{T,i}, \nu_{R,j})$, A and B represent FC for full covariance extracted from the data, KM for the Kronecker model, and ME for maximum entropy, $\nu_{T,i} = \nu_{R,i} = 2\pi i/N$, and $\bar{P} = \left(\frac{1}{N^2}\right)\sum_i\sum_j P_{ij}$.

6.4 RESULTS

Figures 6.1and 6.2 display the significant eigenvalues for the full covariance (FC), maximum entropy (ME), and the Kronecker model (KM) cases, at Locations 3 and 7 at the carrier frequency of 2.4 GHz for the indoor environment in Figure 4.21. Figures 6.3 and 6.4 display the significant eigenvalues for the same physical locations, but at the carrier frequency of 5.2 GHz. All these cases indicate that the maximum entropy approach only provides a marginal improvement in the eigenvalues (approximately 5%) compared to the Kronecker model. The other nine locations were very similar, except that only the number of dominant eigenvalues varied from around a minimum of two to a maximum of four.

Figure 6.5 plots the spatial spectra for the full covariance (top) and maximum entropy (bottom). The spatial spectrum for the Kronecker model (not plotted) is visibly indistinguishable from that for the maximum entropy. Tables 6.1 and 6.2 give the correlation coefficient $\rho_{FC,ME}$ and $\rho_{FC,KM}$ in columns 2 and 3 for the center frequencies of 2.4 GHz and 5.2 GHz respectively.

TABLE 6.1: Correlation coefficient of spatial power spectra at 2.4 GHz

Locations	Bartlett beamforming at 2.4 GHz	
	$\rho_{FC,ME}$	$\rho_{FC,KM}$
1	0.9387	0.9377
2	0.9258	0.9088
3	0.9470	0.9264
4	0.9927	0.9887
5	0.9716	0.9615
6	0.9818	0.9798
7	0.8850	0.8819
8	0.9872	0.9845
9	0.9028	0.8966
10	0.9007	0.8985
11	0.9261	0.9229

TABLE 6.2: Correlation coefficient of spatial power spectra at 5.2 GHz

Locations	Bartlett beamforming at 5.2 GHz	
	$\rho_{FC,ME}$	$\rho_{FC,KM}$
1	0.9701	0.9764
2	0.9675	0.9664
3	0.9109	0.9064
4	0.9945	0.9907
5	0.9717	0.9680
6	0.9694	0.9691
7	0.8411	0.8403
8	0.9936	0.9921
9	0.9637	0.9584
10	0.9363	0.9259
11	0.8339	0.8372

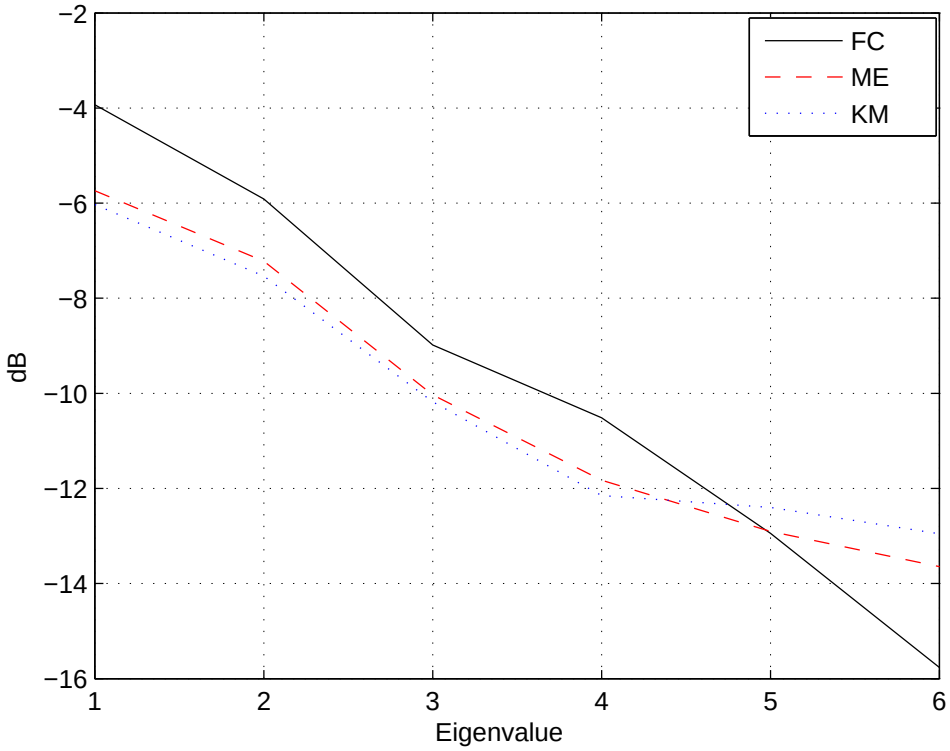

FIGURE 6.1: Dominant singular eigenvalues for Location 3 at 2.4 GHz carrier frequency

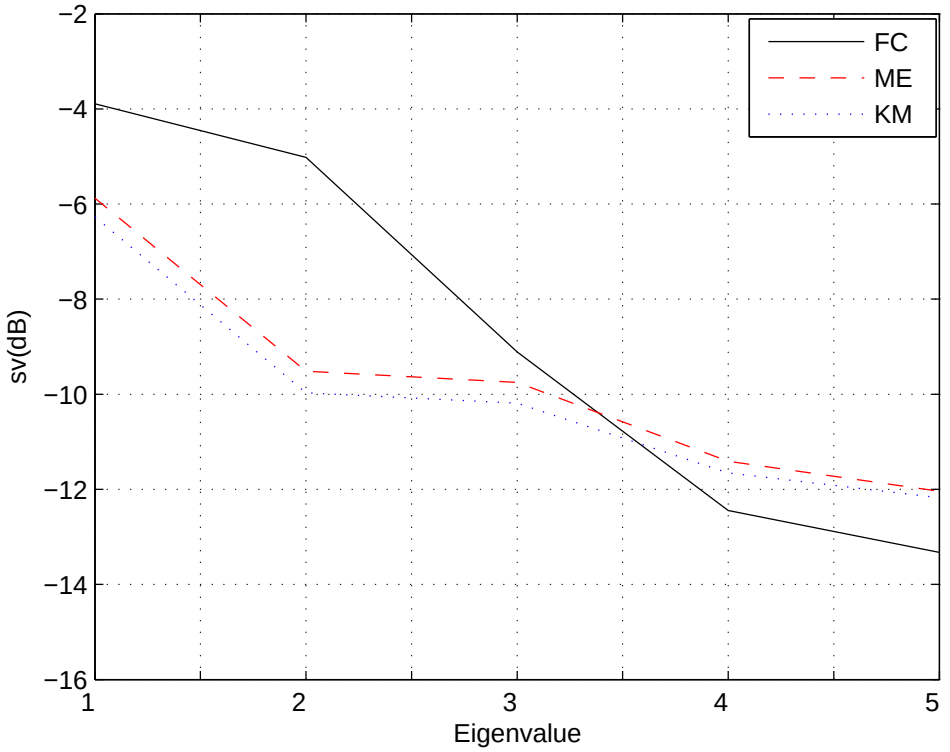

FIGURE 6.2: Dominant singular eigenvalues for Location 7 at 2.4 GHz carrier frequency

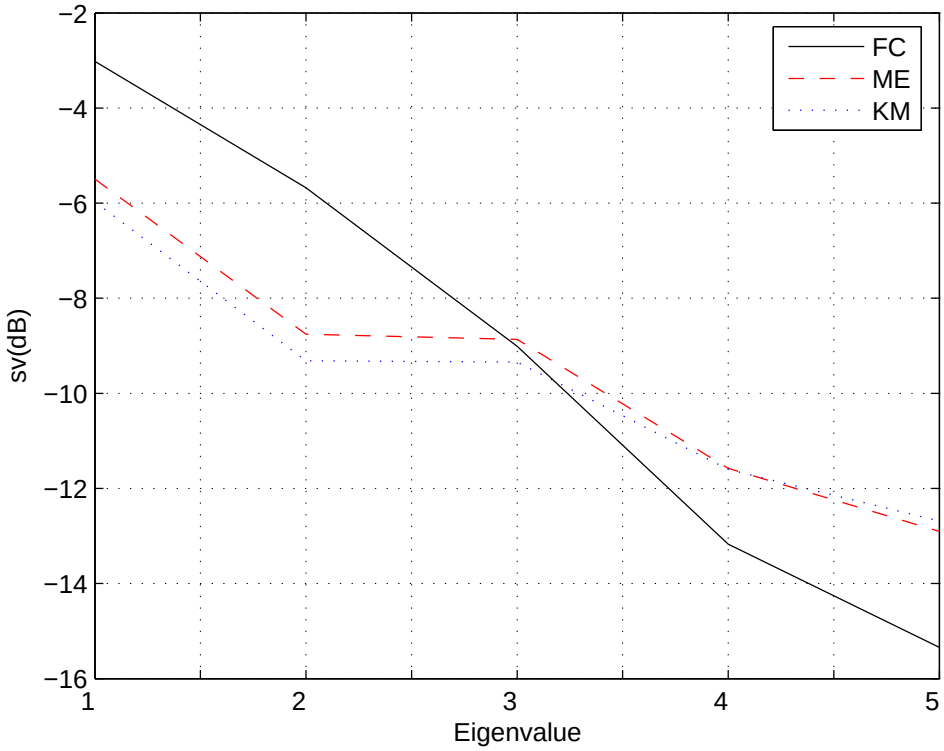

FIGURE 6.3: Dominant singular eigenvalues for Location 3 at 5.2 GHz carrier frequency

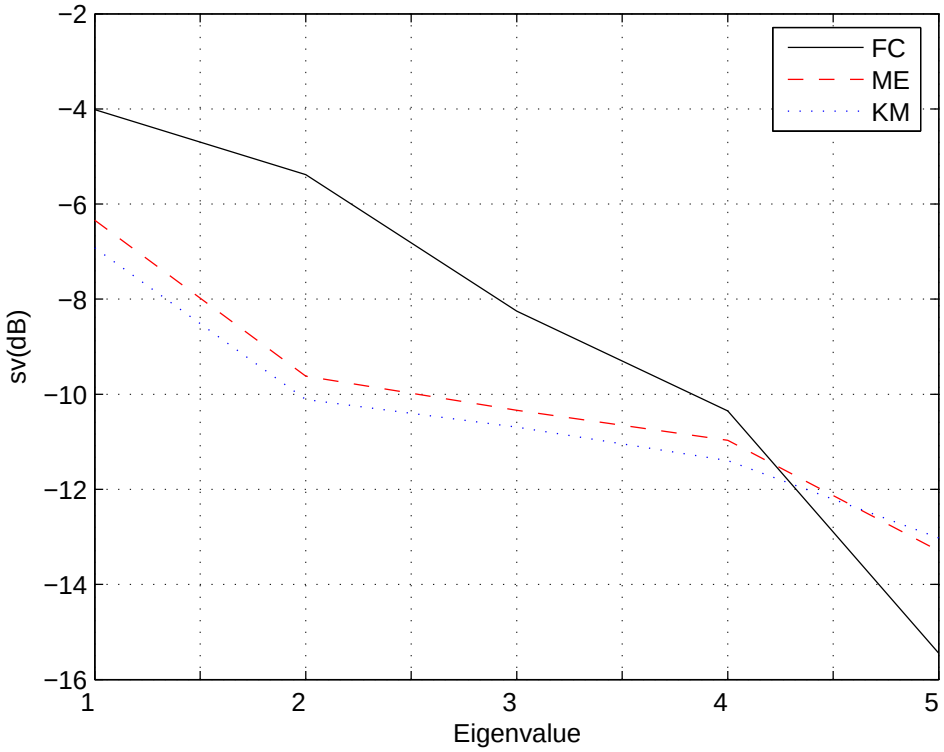

FIGURE 6.4: Dominant singular eigenvalues for Location 7 at 5.2 GHz carrier frequency

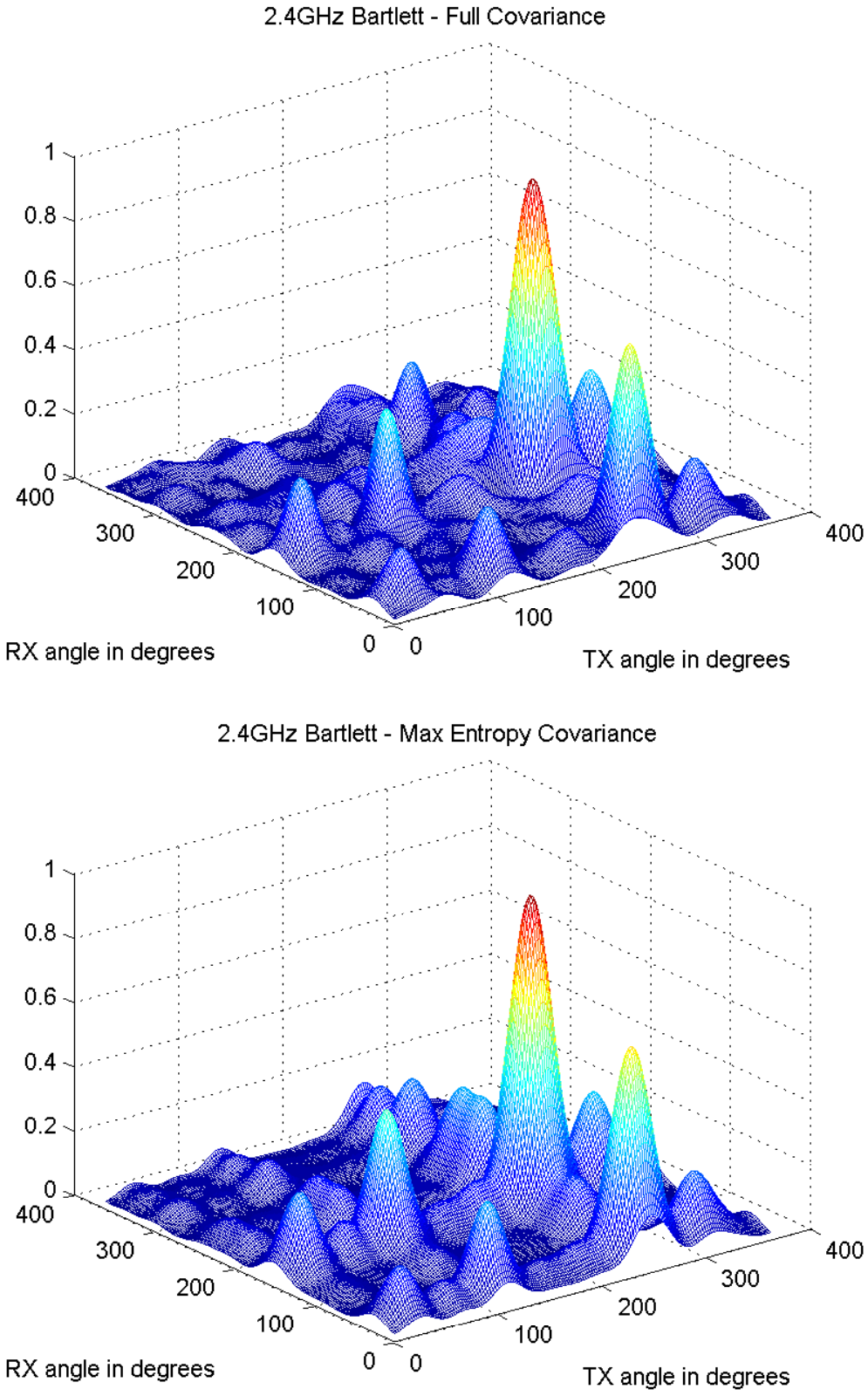

FIGURE 6.5: Spatial power spectra for FC and ME at 2.4 GHz at Location 3

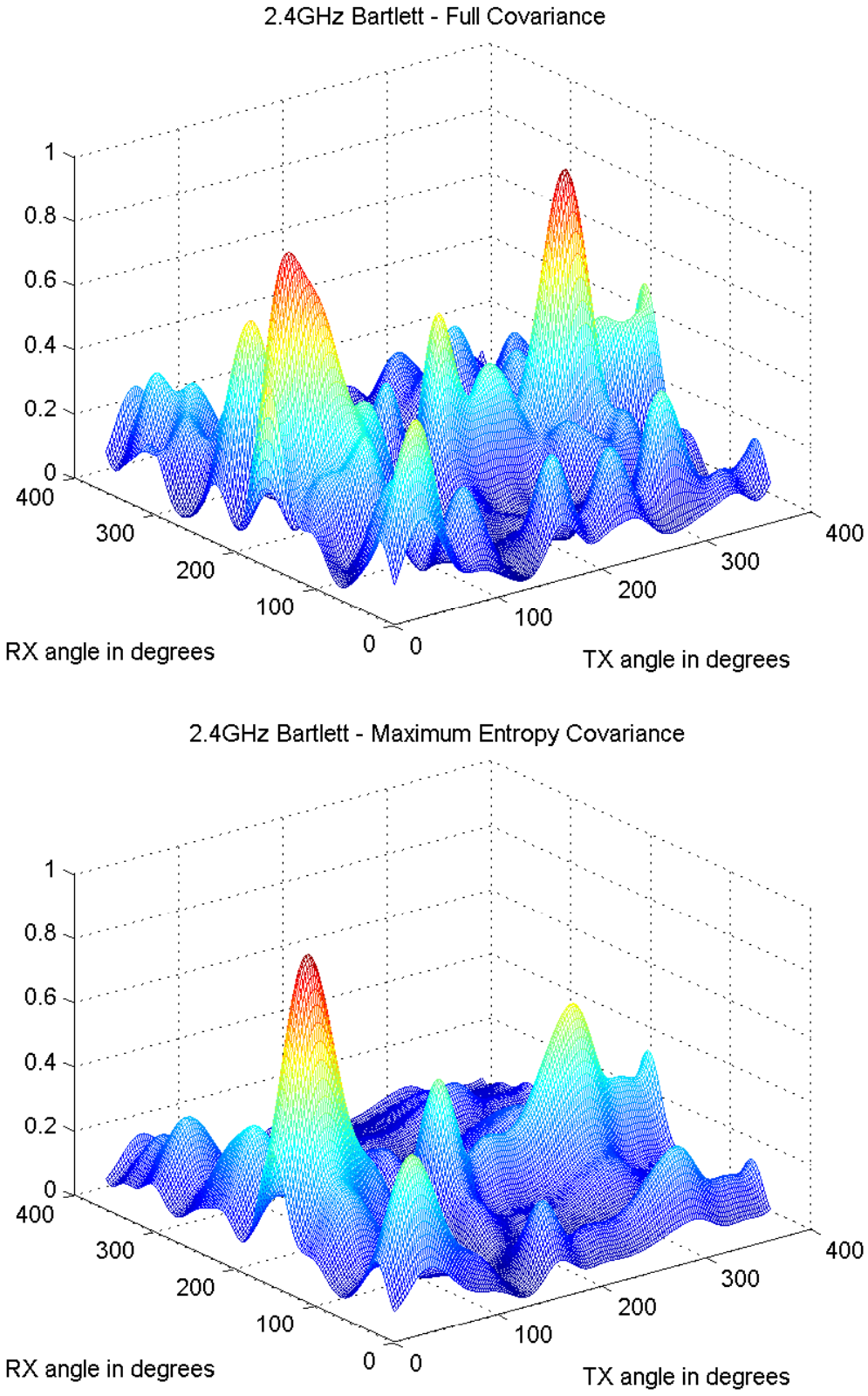

FIGURE 6.6: Spatial power spectra for FC and ME at 2.4 GHz at Location 7

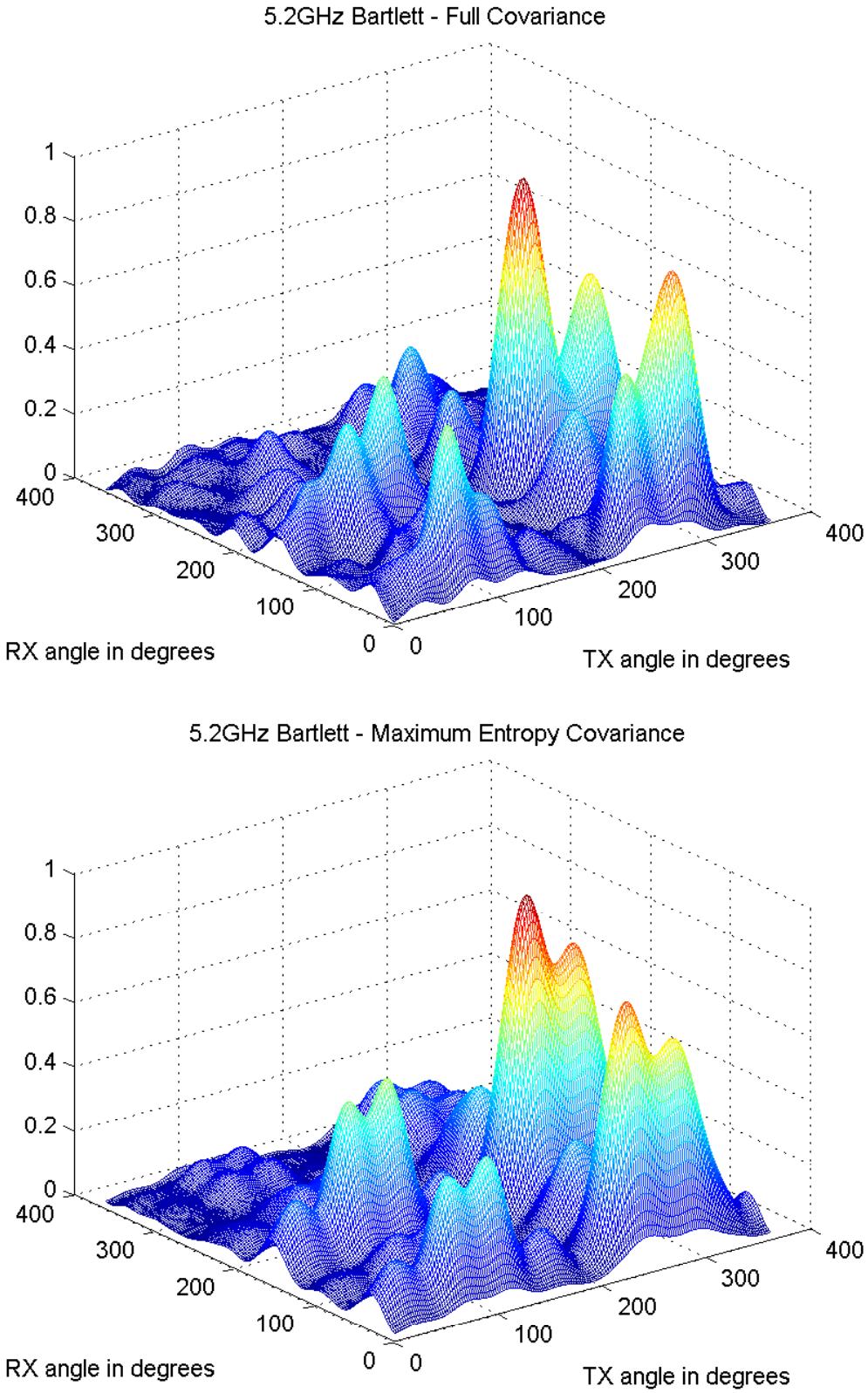

FIGURE 6.7: Spatial power spectra for FC and ME at 5.2 GHz at Location 3

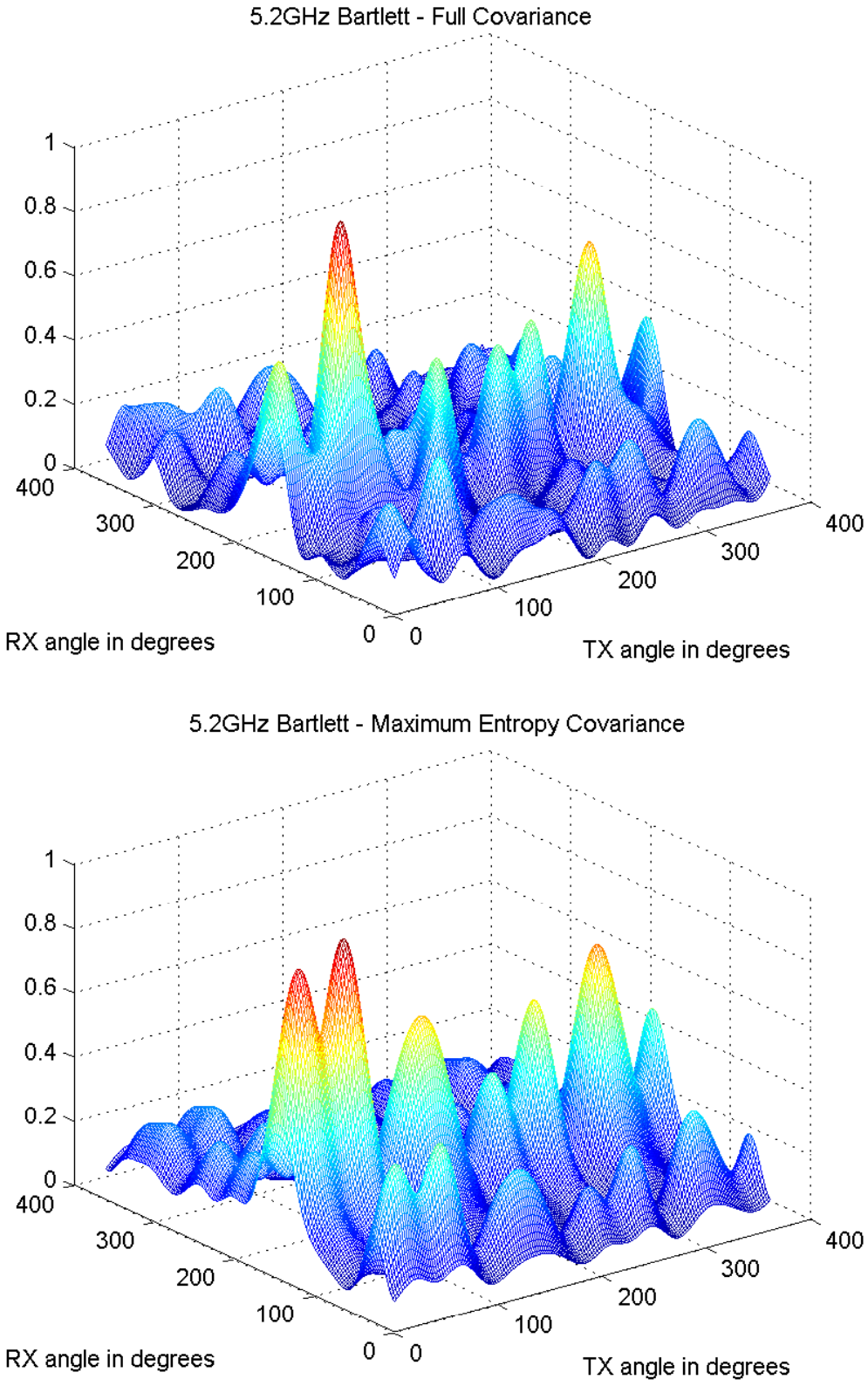

FIGURE 6.8: Spatial power spectra for FC and ME at 5.2 GHz at location 7

As with the eigenvalues, the maximum entropy approach only yields a marginal improvement, yet is distinct from the Kronecker model.

6.5 CONCLUSION

A maximum entropy approach has been presented for obtaining the full channel covariance when only the separate transmit and receive covariances are known. The method indicates that the eigenvectors of the full covariance are the Kronecker product of the separate transmit and receive eigenvectors, which are identical to that of the Kronecker model. The eigenvalues of the full covariance, however, do not strictly match those of the Kronecker model. Application of the new method to measured indoor MIMO channels at 2.4 GHz indicated that the Kronecker model and maximum entropy method gave numerical results that are fairly close to each other. Thus, even though the Kronecker model imposes "structure" on the full covariance, the modelled channel matrices are nearly as unstructured as can be and they almost attain the maximum possible entropy. This result suggests that the inaccuracy of the Kronecker model represents a fundamental limit, which resulted from having no joint transmit/receive channel information, rather than resulting from the incorrect application of knowledge of the separate transmit and receive covariances.

CHAPTER SEVEN
CONCLUSION

7.1 SUMMARY

From the work described herein, one can conclude:

- Geometric modelling

  Chapter 3 chartered the development of a geometric model for the MIMO indoor wireless channel with isotropic scattering PDF at the TX and the von Mises scattering PDF applied to one RX end, while a uniform scattering PDF was applied at the other. The effects of antenna element spacing, angular orientation of antenna array and number of antenna elements employed were shown. It was also found that the number of antenna elements had the greatest impact on the capacity when compared to the other parameters. Although geometric modelling is a useful tool and gives the wireless engineer much insight into the performance of the MIMO channel, it was also shown that, based on the measurement campaign, the results from the geometrical modelling technique did not prove to be able to accurately represent the real world channel in this case.

- Wideband measurement system

  Chapter 4 showed a successful development and implementation of a low cost wideband 8 x 8 MIMO measurement system capable of 80 MHz of instantaneous excitation bandwidth operating across the 2-8 GHz range. The system shows innovation in its implementation of the sub-components and data was obtained for 11 different indoor locations both at 2.4 GHz and 5.2 GHz, using the ULA and UCA antenna configurations

in co-located positions. This measurement system is largely based on off-the-shelf components, making it affordable for empirical research to be undertaken.

- Metrics in data analysis

  In Chapter 5, the data was analyzed in terms of eigenvalue CDFs, capacities and spatial correlation for the specific antenna array configuration at the two carrier frequencies. The concept of *frequency scaling* in MIMO systems was introduced and two new different models were developed where it was shown that a linear relationship existed both for the capacity frequency scaling and spatial correlation frequency scaling. When the fixtures and fittings becomes electrically comparable to the wavelength of frequency in use, this *frequency scaling* approach could not hold. Hence, one should use these models taking careful cognisance of the center frequency in use.

  It was also shown that the capacity at 2.4 GHz was greater than that at 5.2 GHz for the UCA, which could be attributed to more scattering and lesser path loss. Furthermore one can observe that the capacity for the ULA was more clustered, which could be due to the positioning of the antenna array, indicating that indoor channels are more affected by the array orientation than the position of the system. The joint TX/RX beamforming (eigenvectors) were determined and it was shown that the spatial power characteristics at both carrier frequencies showed a high degree of similarity, suggesting that the multi-path propagation at the two frequencies could be mainly due to specular reflections.

- Maximum entropy approach

  Using the principle of maximum entropy, a new approach in Chapter 6 showed that the eigenvalues of the full covariance matrix is different from the Kronecker model and that there is difference (approximately 5%) in the dominant eigenvalues. Although when comparing the spatial power spectra results (using the ME synthetic full covariance and full covariance matrix of the measured channel), they were close to that using the Kronecker model. The correlation coefficient metric clearly indicated that the the ME model performed better. The study also indicates that the joint RX/TX spatial power spectra at 2.4 GHz and 5.2 GHz are similar, indicating that specular reflections at both the carrier frequencies are similar, hence validating the results obtained for the double directional model in Section 5.3.

7.2 FUTURE RECOMMENDATIONS

Some recommendations to the extension of this work could be:

- Enhanced geometric channel model and joint correlation matrix

  One could extend the work on geometric modelling and incorporate more complex PDFs at the TX and RX. A non-trivial approach would be to reduce the approximations and use numerical techniques to analyze the space-time correlation equations, so that there could be a more accurate representation of the channel. The metrics can then be compared to determine the level of computational complexity versus accuracy. One could also include three dimensional models at the TX and/or RX and extend on the models in the recent work by [104, 105] and compare this with other measured wideband channels.

- Wideband measurement system and analysis

  The present wideband channel sounder could be improved, especially the synchronization system. Various wireless synchronization schemes using for example, Golay Codes or other super orthogonal codes could be implemented. This will be very useful in outdoor measurements as well as where the TX is located at higher altitudes. The comparison of results for different antenna element spacing or geometries would also be useful to further evaluate the impact on the antenna with regards to capacity and spatial power profiles. Further analysis at a lower center frequency like 800 MHz could be useful and of other indoor type environments so as to have a more comprehensive comparative analysis that would provide a useful database for the network planner when making appropriate space-time coding choices.

- Maximum entropy based modelling

  The new modelling approach presented shows potential and has opened up new possibilities for further investigation and analysis. One of the simpler approaches of using linear programming was chosen in order to find the initial guess and then the gradient descent method was used to find optimum values for the system of non-linear equations. Other methods should be investigated to determine the relative accuracies achievable. One could also compare this model to other models such as the Weichselberger [102] and the virtual channel representation [106], both for the capacity predictions and the spatial power representation for this measured environment, as well as other environments, with and without perfect CSI.

REFERENCES

[1] W. C. Jakes Jr, *Multipath interference in microwave mobile communications*. New York: Wiley, 1974.

[2] V. Tarokh, N. Seshadri, and A. R. Calderbank, "Space-time codes for high data rate wireless communication: performance criterion and code construction," *IEEE Trans. Information Theory*, vol. 44, pp. 744–765, March 1998.

[3] D. Bevan and R. Tanner, "Performance comparison of space-time coding techniques," *Electronics Letters*, vol. 35, pp. 1707–1708, Oct. 1999.

[4] G. Foschini, "Layered space-time architecture for wireless communication in fading environment when using multiple antennas," *Bell Labs Tech. J.*, vol. 1, pp. 41–59, Autumn 1996.

[5] G. D. Golden, C. J. Foschini, R. A. Valenzuela, and P. W. Wolniansky, "Detection algorithm and initial laboratory results using V-BLAST space-time communication architecture," *Electronics Letters*, vol. 35, pp. 14–16, Jan. 1999.

[6] H. Bölcskei, A. J. Paulraj, K. V. S. Hari, and R. U. Nabar, "Fixed broadband wireless access: State of the art, chalenges and future directions," *IEEE Communications Magazine*, pp. 100–108, Jan. 2001.

[7] B. Clerckx, C. Oestges, D. Vanhoenacker-Janvier, and L. Vandendorpe, "Robustness of space-time coding in spatially correlated fast-fading MIMO channels," in *Proc. 2005 IEEE 62nd Veh. Technology Conf.*, vol. 4, Dallas, TX, Sep. 25-28 2005, pp. 2413–2417.

[8] G. Ginis and J. Cioffi, "Vectored transmission for digital subscriber line systems," *IEEE J. Selected Areas in Communications*, vol. 20, pp. 1085–1104, June 2002.

[9] I. Telatar, "Capacity of multi-antenna gaussian channels," AT&T Bell Laboratories, Tech. Report #BL0112170-950615-07TM, 1995.

[10] A. Goldsmith, S. A. Jafar, N. Jindal, and S. Vishwanath, "Capacity limits of MIMO channels," *IEEE Trans. Information Theory*, vol. 21, pp. 684–702, June 2003.

[11] T. Yoo and A. Goldsmith, "Capacity of fading MIMO channels with channel estimation error," in *Proc. 2004 IEEE Intl. Conf. Communications*, vol. 2, Paris, France, June 20-24 2004, pp. 808–813.

[12] M. Herdin, "Non-stationary indoor MIMO radio channels," Ph.D. dissertation, Technische Universität Wien, August 2004.

[13] M. Ivrlač, T. Kurpjuhn, C. Brunner, and W. Utschick, "Efficient use of fading correlation in mimo systems," in *Proc. 2001 IEEE 54th Veh. Technology Conf.*, vol. 4, Atlantic City, NJ, Oct. 7-11, 2001, pp. 2763–2767.

[14] J. W. Wallace, M. A. Jensen, A. L. Swindlehurst, and B. D. Jeffs, "Experimental characterization of the MIMO wireless channel: Data acquisition and analysis," *IEEE Trans. Wireless Communications*, vol. 2, pp. 335–343, March 2003.

[15] G. J. Foschini and M. J. Gans, "On limits of wireless communications in a fading environment when using multiple antennas," *Wireless Personal Commun.*, vol. 6, pp. 311–335, March 1998.

[16] A. Burr, "Evaluation of capacity of indoor wireless MIMO channel using ray tracing," in *Proc. of the 2002 Intl. Zurich Seminar on Access, Transmission, and Networking*, Zurich, Switzerland, Feb. 19-21, 2002, pp. 28–1–28–6.

[17] M. Steinbauer, A. F. Molisch, and E. Bonek, "The double-directional radio channel," *IEEE Antennas and Propag. Mag.*, vol. 43, pp. 51–63, Aug. 2001.

[18] K. Yu, M. Bengtsson, B. Ottersten, D. McNamara, P. Karlsson, and M. Beach, "A wideband statistical model for NLOS indoor MIMO channels," in *Proc. 2002 IEEE 55th Veh. Technology Conf.*, vol. 1, Birmingham, AL, May 6-9, 2002, pp. 370–374.

[19] M. A. Jensen and J. W. Wallace, "A review of antennas and propagation for MIMO wireless communications," *IEEE Trans. Antennas Propagation*, pp. 2810–2824, Nov. 2004.

[20] T. M. Cover and J. A. Thomas, *Elements of Information Theory*. John Wiley and Sons, 1991.

[21] J. G. Proakis, *Digital Communications*. McGraw-Hill, 1995.

[22] M.-S. Alouini and A. Goldsmith, "Capacity of nakagami multipath fading channels," in *Proc. 1997 IEEE Spring Veh. Technology Conf.*, vol. 1, 1997, pp. 358–362.

[23] J. B. Anderson, "Antenna arrays in mobile communications: Gain, diversity, and channel capacity," *IEEE Antennas and Propagation Magazine*, vol. 42, pp. 12–16, April 2000.

[24] B. T. Maharaj, L. P. Linde, J. W. Wallace, and M. Jensen, "Co-located indoor 2.4 and 5.2 GHz MIMO channel measurements: frequency scaling of capacity and correlation," in *Proc. 2005 IEEE Intl. Conf. on Telecommunications*, vol. 1, Cape Town, South Africa, May 18-23, CDROM 2005.

[25] J. B. Andersen and R. G. Vaughan, "Transmitting, receiving, and scattering properties of antennas," *IEEE Antennas Propag. Magazine*, vol. 45, Aug. 2003.

[26] G. G. Raleigh and J. M. Cioffi, "Spatio-temporal coding for wireless communication," *IEEE Trans. Selected Areas in Communications*, vol. 46, pp. 357–366, March 1998.

[27] T. K. Moon and W. C. Stirling, *Mathematical Methods and Algorithms for Signal Processing*. Prentice-Hall, 2000.

[28] M. A. Khalighi, J. Brossier, G. Jourdain, and K. Raoof, "Water filling capacity of Rayleigh MIMO channels," in *Proc. 2001 IEEE 12th Intl. Symp. on Personal, Indoor and Mobile Radio Comm.*, vol. 1, San Diego, CA, Sep. 30 - Oct 3, 2001, pp. 155–158.

[29] J. B. Andersen, "Array gain and capacity for known random channels with multiple element arrays at both ends," *IEEE J. Selected Areas in Communications*, vol. 18, pp. 2172–2178, Nov. 2000.

[30] L. Zheng and D. Tse, "Diversity and multiplexing: A fundamental tradeoff in multiple antenna channels," *IEEE Trans. Information Theory*, vol. 49, pp. 1073–1096, May 2003.

[31] M. Herdin, H. Özcelik, H. Hofstetter, and E. Bonek, "Variation of measured indoor MIMO capacity with receive direction and position at 5.2 GHz," *Electronics Letters*, vol. 38, pp. 1283–1285, Oct. 10, 2002.

[32] D. Chizhik, G. J. Foschini, M. J. Gans, and R. A. Valenzuela, "Propagation and capacities of multi-element transmit and receive antennas," in *Proc. 2001 IEEE Antennas and Propag. Society Intl. Symp.*, vol. 1, Boston, MA, July 8-13 2001, pp. 438–441.

[33] D. Gesbert, H. Bölcskei, D. A. Gore, and A. J. Paulraj, "Outdoor MIMO wireless channels: Models and performance prediction," *IEEE Trans. Selected Areas in Communications*, vol. 50, pp. 1926–1934, Dec. 2002.

[34] D. Chizhik, G. J. Foschini, M. J. Gans, and R. A. Valenzuela, "Keyholes, correlations, and capacities of multielement transmit and receive antennas," *IEEE Trans. Wireless Communications*, vol. 2, pp. 361–368, April 2002.

[35] P. Almers, F. Tufvesson, and A. F. Molisch, "Measurement of keyhole effect in a wireless multiple-input multiple-output (MIMO) channel," *IEEE Communication Letters*, vol. 7, pp. 373–375, Aug. 2003.

[36] D. P. McNamara, M. A. Beach, P. N. Fletcher, and P. Karlsson, "Capacity variation of indoor multiple-input multiple-output channels," *Electronics Letters*, vol. 36, pp. 2037–2038, Nov. 2000.

[37] D. Shiu, G. J. Foschini, M. J. Gans, and J. M. Kahn, "Fading correlation and its effect on the capacity of multielement antenna systems," *IEEE Trans. Selected Areas in Communications*, vol. 48, pp. 502–513, March 2000.

[38] D. Chizhik, F. Rashid-Farrokhi, J. Ling, and A. Lozano, "Effect of antenna separation on the capacity of BLAST in correlated channels," *IEEE Communication Letters*, vol. 4, pp. 337–339, Nov. 2000.

[39] N. Chiurtu, B. Rimoldi, and E. Telatar, "Dense multiple antenna systems," in *Proc. IEEE 2001 Information Theory Workshop*, Cairns, Australia, Sep. 2-7 2001, pp. 108–109.

[40] C. N. Chuah, D. N. C. Tse, J. M. Kahn, and R. A. Valenzuela, "Capacity scaling in MIMO wireless systems under correlated fading," *IEEE Trans. Information Theory*, vol. 48, pp. 637–650, March 2002.

[41] S. Q. Wei, D. Goeckel, and R. Janaswamy, "On the asymptotic capacity of MIMO systems with fixed length linear antenna arrays," in *Proc. 2003 IEEE Intl. Conf. Communications*, vol. 4, Anchorage, AK, May 11-15 2003, pp. 2633–2637.

[42] H. Krim and M. Viberg, "Two decades of array signal processing research: The parametric approach," *IEEE Signal Processing Magazine*, vol. 13, pp. 67–94, July 1996.

[43] M. Bartlett, "Smoothing periodograms from time series with continuous spectra," *Nature*, vol. 161, pp. 686–687, May 1948.

[44] J. Capon, "High-resolution frequency-wavenumber spectrum analysis," *IEEE Proceedings*, vol. 57, pp. 1408–1418, Aug. 1969.

[45] M. Steinbauer, "A comphrensive transmission and channel model for directional radio channels," COST259, Tech. Rep. No. TD(98)027, Bern, Switzerland, Feb. 1998.

[46] M. Steinbauer, "The radio propagation channel: A non-directional, directional and double directional point-of-view," Ph.D. dissertation, Technische Universität Wien, November 2001.

[47] Q. H. Spencer, B. D. Jeffs, M. A. Jensen, and A. L. Swindlehurst, "Modeling the statistical time and angle of arrival characteristics of an indoor multipath channel," *IEEE J. Selected Areas in Communications*, vol. 18, pp. 347–360, March 2000.

[48] J. Fuhl, J. P. Rossi, and E. Bonek, "High-resolution 3-D direction-of-arrival determination for urban mobile radio," *IEEE Trans. Antennas Propagation*, vol. 45, pp. 672–682, April 1997.

[49] A. Richter, D. Hampicke, G. Sommerkorn, and R. S. Thoma, "Joint estimation of DoD, time-delay, and DoA for high-resolution channel sounding," in *Proc. 2000 IEEE 51st Veh. Technology Conf.*, vol. 2, Tokyo, Japan, May 15-18, 2000, pp. 1045–1049.

[50] S. Y. Seidel and T. S. Rappaport, "Site-specific propagation prediction for wireless in-building personal communication system design," *IEEE Trans. Vehicular Technology*, vol. 43, pp. 879–891, Nov. 1994.

[51] D. J. Cichon and T. Kurner, "Propagation prediction models," in *COST 231 Final Rep.*, 1995, available online at http://www.lx.it.pt/cost231/.

[52] G. E. Athanasiadou, A. R. Nix, and J. P. McGeehan, "A microcellular ray-tracing propagation model and evaluation of its narrow-band and wide-band predictions," *IEEE J. Selected Areas in Communications*, vol. 18, pp. 322–335, March 2000.

[53] M. F. Iskander and Z. Yun, "Propagation prediction models for wireless communication systems," *IEEE Trans. Microwave Theory Techniques*, vol. 50, pp. 662–673, March 2002.

[54] A. L. Swindlehurst, G. German, J. Wallace, and M. Jensen, "Experimental measurements of capacity for MIMO indoor wireless channels," in *IEEE Third Workshop on Signal Processing Advances in Wireless Communications, 2001. (SPAWC '01)*, March 2001, pp. 30–33.

[55] C. Takahashi, Z. Yun, M. F. Iskander, G. Poilasne, V. Pathak, and J. Fabrega, "Propagation-prediction software and site-planning software for wireless communication systems," *IEEE Antennas and Propagation Magazine*, vol. 49, pp. 52–60, September 2007.

[56] R. A. Valenzuela, "Ray tracing prediction of indoor radio propagation," in *Proc. 1994 IEEE 5th Intl. Symp. on Personal, Indoor and Mobile Radio Comm.*, vol. 1, The Hague, The Netherlands, Sep. 18-23, 1994, pp. 140–144.

[57] P. Marques, J. Fernandes, and J. Neves, "Complex impulse response modeling for wideband channels," in *Proc. 1998 IEEE Spring Veh. Technology Conf.*, vol. 2, Ottawa, Ontario, Canada, May 18-21, 1998, pp. 702–706.

[58] Z. Yun, M. F. Iskander, and Z. Zhang, "Complex-wall effect on propagation characteristics and mimo capacities for a indoor wireless communication environment," *IEEE Trans. Antennas Propagation*, vol. 52, pp. 914–922, April 2004.

[59] Z. Zhang, R. Sorensen, Z. Yun, M. F. Iskander, and J. F. Harvey, "A ray-tracing approach for indoor/outdoor propagation through window structures," *IEEE Trans. Antennas Propagation*, vol. 50, pp. 742–748, May 2002.

[60] F. Tila, P. R. Shepherd, and S. R. Pennock, "Theoretical capacity evaluation of indoor micro- and macro-MIMO systems at 5 GHz using site specific ray tracing," *Electronics Letters*, vol. 39, pp. 471–472, March 6 2003.

[61] K. R. Dandekar, A. Arredondo, G. Xu, and H. Ling, "Using ray tracing to study urban vector channel propagation characteristics," in *Proc. 1999 IEEE Spring Veh. Technology Conf.*, vol. 1, Houston, TX, May 16-20, 1999, pp. 381–385.

[62] R. B. Ertel, P. Cardieri, K. W. Sowerby, T. S. Rappaport, and J. H. Reed, "Overview of spatial channel models for antenna array communication systems," *IEEE Pers. Commun.*, pp. 10–21, Feb. 1998.

[63] D.-S. Shiu, *Wireless communication using dual antenna arrays*. Kluwer Academic Publishers, 2000.

[64] A. Abdi and M. Kaveh, "A space-time correlation model for multielement antenna systems in mobile fading channels," *IEEE J. Selected Areas in Communications*, vol. 20, pp. 550–560, April 2002.

[65] A. Abdi and M. Kaveh, "Space-time correlation modelling of multielement antenna systems in mobile fading channels," in *Proc. 2001 IEEE Intl. Conf. Acoustics, Speech, and Signal Processing*, Salt Lake City, UT, May 7-11, 2001, pp. 2505–2508.

[66] A. Abdi and M. Kaveh, "A versatile spatio-temporal correlation function for mobile fading channels with non-isotropic scattering," in *IEEE Workshop on Statistical Signal and Array Processing*, Pocono Manor, PA, Aug. 14-16 2000, pp. 58–62.

[67] D. Gesbert, D. Bölcskei, D. Gore, and A. Paulraj, "Mimo wireless channels: capacity and performance," in *Proc. 2000 IEEE Global Telecomm. Conf.*, vol. 2, Nov. 2000, pp. 1083–1088.

[68] A. A. M. Saleh and R. A. Valenzuela, "A statistical model for indoor multipath propagation," *IEEE J. Selected Areas in Communications*, vol. SAC-5, pp. 128–137, Feb. 1987.

[69] J. W. Wallace and M. A. Jensen, "Statistical characteristics of measured MIMO wireless channel data and comparison to conventional models," in *Proc. 2001 IEEE 54th Veh. Technology Conf.*, vol. 2, Atlantic City, NJ, Oct. 7-11 2001, pp. 1078–1082.

[70] J. W. Wallace and M. A. Jensen, "Measured characteristics of the MIMO wireless channel," in *Proc. 2001 IEEE 54th Veh. Technology Conf.*, vol. 4, Atlantic City, NJ, Oct. 7-11 2001, pp. 2038–2042.

[71] J. W. Wallace and M. A. Jensen, "Modeling the indoor MIMO wireless channel," *IEEE Trans. Antennas Propagation*, vol. 50, pp. 591–599, May 2002.

[72] L. M. Correia, *Wireless Flexible Personalised Communications*. John Wiley & Sons, 2001.

[73] M. Stege, J. Jelitto, M. Bronzel, and G. Fettweis, "A multiple input-multiple output channel model for simulation of Tx- and Rx-diversity wireless systems," in *Proc. 2000 IEEE 52nd Veh. Technology Conf.*, vol. 2, Boston, MA, Sep. 24-28, 2000, pp. 833–839.

[74] T. Svantesson, "A physical MIMO radio channel model for multi-element multi-polarized antenna systems," in *Proc. 2001 IEEE 54th Veh. Technology Conf.*, vol. 2, Atlantic City, NJ, Oct. 7-11, 2001, pp. 1083–1087.

[75] T. Svantesson, "On capacity and correlation of multi-antenna systems employing multiple polarizations," in *Proc. 2002 IEEE Antennas and Propag. Society Intl. Symp.*, vol. 3, San Antonio, TX, June 16-21, 2002, pp. 202–205.

[76] T. Svantesson, "A double-bounce channel model for multi-polarized MIMO systems," in *Proc. 2002 IEEE 56th Veh. Technology Conf.*, vol. 2, Vancouver, BC, Sep. 24-28, 2002, pp. 691–695.

[77] L. Hanlen and M. Fu, "Multiple antenna wireless communication systems: limits to capacity growth," in *Proc. 2002 IEEE Wireless Comm. and Networking Conf.*, vol. 1, March 17-21, 2002, pp. 172–176.

[78] R. Tingley and K. Bahlavan, "A statistical model of space-time radio propagation in indoor environments," in *Proc. 2000 IEEE-APS Conf. on Antennas and Propagation for Wireless Comm.*, Waltham, MA, Nov., 6-8 2000, pp. 61–64.

[79] A. F. Molisch, "A generic model for MIMO wireless propagation channels," in *Proc. 2002 IEEE Intl. Conf. Communications*, vol. 1, New York, NY, April 28 - May 2, 2002, pp. 277–282.

[80] R. J. Piechocki, J. P. McGeehan, and G. Tsoulos, "A new stochastic spatio-temporal propagation model (SSTPM) for mobile communications with antenna arrays," *IEEE Trans. Selected Areas in Communications*, vol. 49, pp. 855–862, May 2001.

[81] J. D. Parsons, *The Mobile Radio Propagation Channel*. Halsted Press, 1992.

[82] D. Gesbert, M. Shafi, D.-S. Shiu, P. J. Smith, and A. Naguib, "From theory to practice: an overview of MIMO space-time coded wireless systems," *IEEE J. Selected Areas in Communications*, vol. 21, pp. 281–302, April 2003.

[83] C. Xiao, J. Wu, S. Y. Leong, Y. R. Zheng, and K. B. Letaief, "A discrete-time model for spatio-temporally correlated MIMO WSSUS multipath channels," in *Proc. 2003 IEEE Wireless Comm. and Networking Conf.*, vol. 1, New Orleans, LA, March 16-20, 2003, pp. 354–358.

[84] G. Byers and F. Takawira, "The influence of spatial and temporal correlation on the capacity of MIMO channels," in *Proc. 2003 IEEE Wireless Comm. and Networking Conf.*, vol. 1, New Orleans, LA, March 16-20, 2003, pp. 359–364.

[85] B. Maharaj and L. Linde, "Capacity for spatial-temporal correlated MIMO fading channel," in *Proc. 2004 IEEE Africon Conf.*, vol. 1, Gaborone, Botswana, Sep. 15-17 2004, pp. 269–274.

[86] J. Fuhl, A. F. Molisch, and E. Bonek, "Unified channel model for mobile radio systems with smart antennas," *IEE Proc. Radar, Sonar and Navigation*, vol. 145, pp. 32–41, Feb. 1998.

[87] I. S. Gradshteyn and I. M. Ryzhik, *Table of Intergrals, Series, and Products*. Academic Press, 6th edition, ISBN 0-12-294757-6, 2000.

[88] B. T. Maharaj, J. W. Wallace, L. P. Linde, and M. A. Jensen, "A low cost open-hardware wideband MIMO wireless channel sounder," *IEEE Trans. Instrumentation and Measurement*, first review completed, July 2007.

[89] B. T. Maharaj, J. W. Wallace, L. P. Linde, and M. A. Jensen, "Frequency scaling of spatial correlation from co-located 2.4 and 5.2 GHz wideband indoor MIMO channel measurements," *Electronics Letters*, vol. 41, pp. 336–337, 17 March 2005.

[90] B. T. Maharaj and L. P. Linde, "Geometric modelling of a spatially correlated MIMO fading channel," *SAIEE Africa Research Journal*, vol. 97, no. 2, pp. 191–197, June 2006.

[91] B. B. Varghese and B. T. Maharaj, "A spatially correlated model for mimo fading channels," in *Proc. 2005 IEEE Intl. Conf. on Telecommunications*, vol. 1, Cape Town, South Africa, May 18-23, CDROM 2005.

[92] Q. H. Spencer, C. B. Peel, A. L. Swindlehurst, and M. Haardt, "An introduction to the multi-user MIMO downlink," *IEEE Communications Magazine*, vol. 42, pp. 60–67, Oct. 2004.

[93] R. S. Thoma, D. Hampicke, A. Richter, G. Sommerkorn, A. Schneider, U. Trautwein, and W. Wirnitzer, "Identification of time-variant directional mobile radio channels," *IEEE Trans. Instrumentation and Measurement*, vol. 49, pp. 357–364, Apr. 2000.

[94] J. W. Wallace, "BYU wideband MIMO channel sounder:technical reference," Brigham Young University, Tech. Rep. DSpace 1877/538, 2006. [Online]. Available: http://hdl.handle.net/1877/538

[95] B. T. Maharaj, L. P. Linde, J. W. Wallace, and M. Jensen, "A cost-effective wideband MIMO channel sounder and initial co-located 2.4 GHz and 5.2 GHz measurements," in *Proc. 2005 IEEE Intl. Conf. Acoustics, Speech, and Signal Processing*, vol. 3, Philadelphia, PA, March 18-23 2005, pp. 981–984.

[96] J. W. Wallace, "Modeling electromagnetic wave propagation in electrically large structures," Ph.D. dissertation, Brigham Young University, 2002, available on the Internet at http://www.ycomm.org.

[97] H. Özcelik, M. Herdin, W. Weichselberger, J. Wallace, and E. Bonek, "Deficiencies of 'Kronecker' MIMO radio channel model," *Electronics Letters*, vol. 39, pp. 1209–1210, Aug. 7 2003.

[98] C. Xiao, J. Wu, and S. Y. Leong, "A discrete-time model for spatio-temporally correlated MIMO WSSUS multipath channels," *IEEE Trans. Wireless Communications*, vol. Sept., pp. 1678–1688, Sept. 2004.

[99] A. F. Molisch, M. Steinbauer, M. Toeltsch, E. Bonek, and R. S. Thoma, "Capacity of MIMO systems based on measured wireless channels," *IEEE J. Selected Areas in Communications*, vol. 20, pp. 561–569, April 2002.

[100] D. P. McNamara, M. A. Beach, and P. N. Fletcher, "Spatial correlation in indoor MIMO channels," in *Proc. 2002 IEEE 13th Intl. Symp. on Personal, Indoor and Mobile Radio Comm.*, vol. 1, Lisboa, Portugal, Sep. 15-18, 2002, pp. 290–294.

[101] D. Chizhik, J. Ling, P. W. Wolniansky, R. A. Valenzuela, N. Costa, and K. Huber, "Multiple-input-multiple-output measurements and modeling in Manhattan," *IEEE J. Selected Areas in Communications*, vol. 21, pp. 321–331, April 2003.

[102] W. Weichselberger, M. Herdin, H. Özcelik, and E. Bonek, "A stochastic MIMO channel model with joint correlation of both link ends," *IEEE Trans. Wireless Communications*, vol. 5, pp. 90–100, Jan. 2006.

[103] M. Debbah and R. Muller, "MIMO channel modelling and the principle of maximum entropy," *IEEE Transactions on Information Theory*, vol. 51, no. 5, pp. 1667–1690, May 2005.

[104] A. Zajič and G. Strüber, "Space-time correlated mimo mobile-to-mobile channels," in *Proc. 2006 IEEE Intl. Symp. on Personal, Indoor and Mobile Radio Comm.*, vol. CDROM, Finland, September 2006.

[105] A. Zajič and G. Strüber, "A three-dimensional mimo mobile-to-mobile channel model," in *Proc. 2007 IEEE Wireless Comm. and Networking Conf.*, vol. CDROM, Hong Kong, PRC, 18-23 March 2007.

[106] A. M. Sayeed, "Deconstructing multiantenna fading channels," *IEEE Trans. on Signal Processing*, vol. 50, pp. 2563–2579, Oct. 2002.

MIMO Channel Modelling for Indoor Wireless Communications

BTJ Maharaj

sunil.maharaj@up.ac.za

February 2008

UNIVERSITEIT VAN PRETORIA
UNIVERSITY OF PRETORIA
YUNIBESITHI YA PRETORIA

SENTECH
connecting You

Sentech Chair in Broadband Wireless Multimedia Communications (BWMC)
Department of Electrical, Electronic and Computer Engineering

Presentation Outline

1. Introduction
2. Geometric Modelling
3. WB MIMO Measurement System
4. Model Assessment
   - Capacity
   - Spatial Correlation
   - Double Directional Channel
5. Maximum Entropy Approach to Channel Modelling
6. What has been Achieved?
7. Outputs

What is a MIMO System?

- Given an arbitrary wireless communication system, one considers a link for which the TX end and as well the RX end is equipped with multiple antenna elements.

- TX antenna signal and RX antennas at the other end are ‘combined’ in such a way that the BER or data rate(bps) of the communication for each MIMO user will be improved.

Traditional SISO System

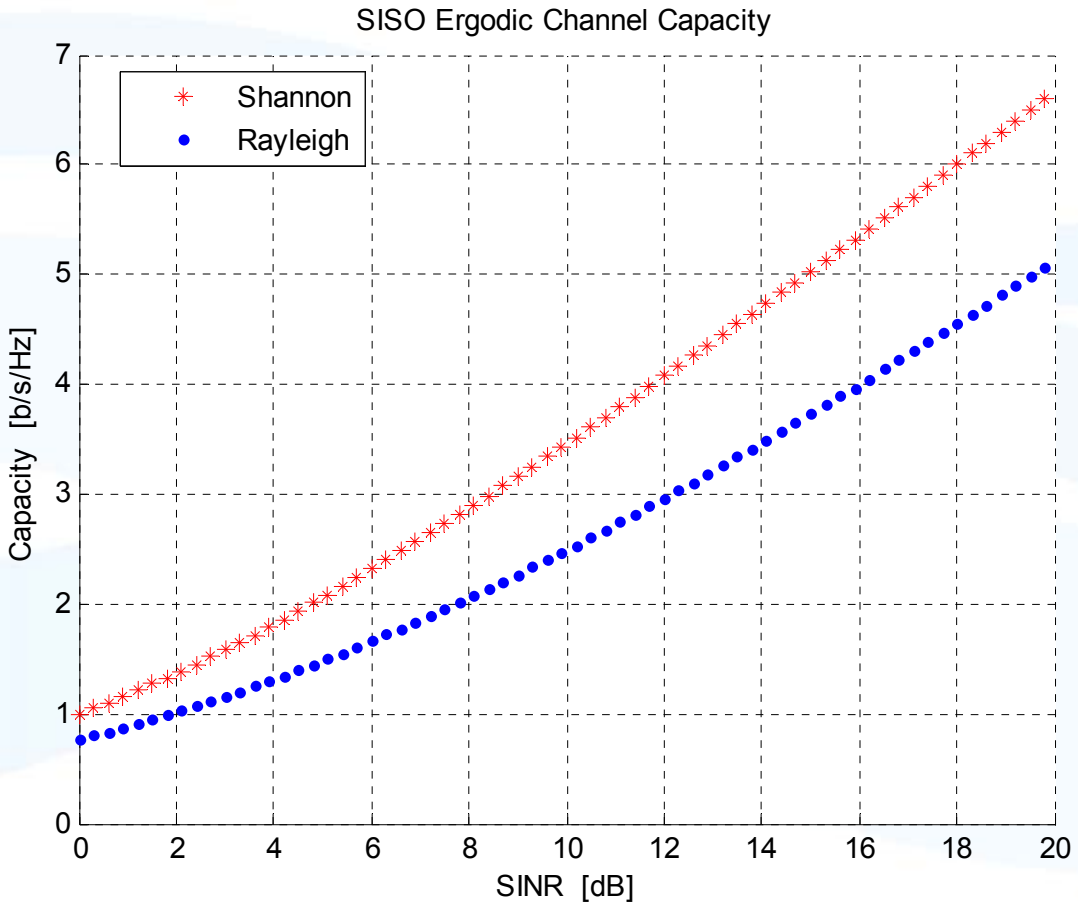

Opportunities for MIMO Technology – "Beyond the Shannon Bound"

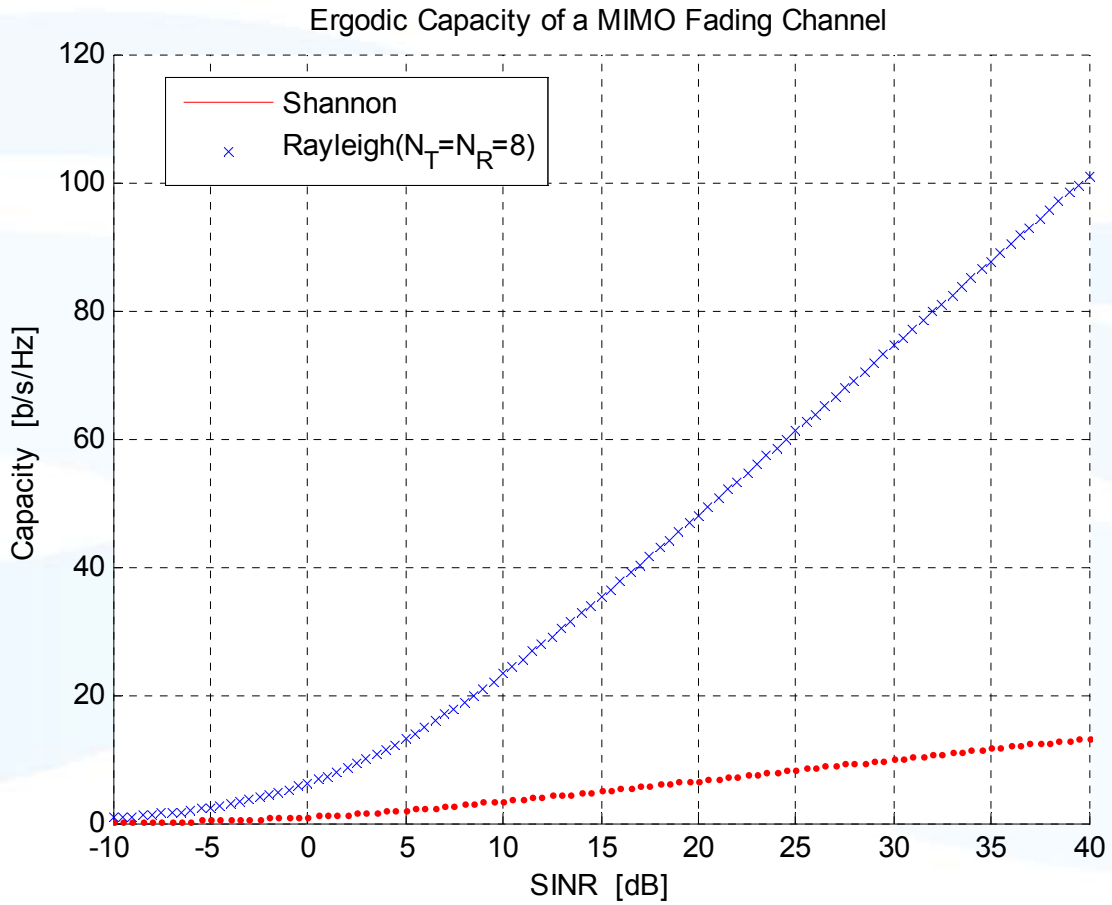

Block Diagram of a MIMO Wireless System

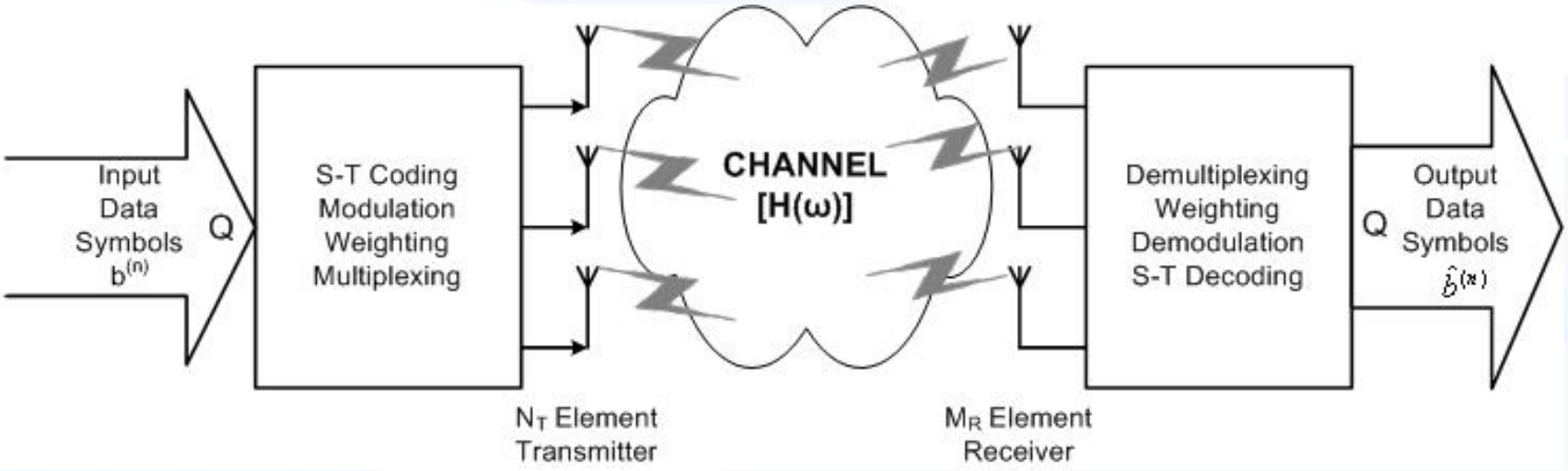

Benefits of MIMO Systems

- Spectral efficiency improvement
- Increases network's quality (QoS)
- Data rate increases substantially
- Operator's revenue increases
- Meet needs for future applications and services in 3G, 4G and NGN…

MIMO Channel Modelling

- MIMO systems increase capacity of wireless channel without increasing system BW in a rich scattering environment
- Space-time coding is informed by channel behaviour
- Various approaches to channel modelling:
  - Ray tracing
  - Geometric modelling
  - Channel sounding
- Channel sounding arguably most accurate representation of real world channels – ‘At a cost!!’

Geometric Modelling: System Description

- Fixed wireless scenario at 2.4 GHz
- Uniform scattering at TX
- Von Mises pdf of scatterers at RX with varying degrees of isotropic scattering
- Derive ST Model
- Present a ST correlation function with some key elements such as antenna element spacing, degree of scattering, AoA at user and antenna array configuration

Geometric Model for a 2x2 MIMO Channel

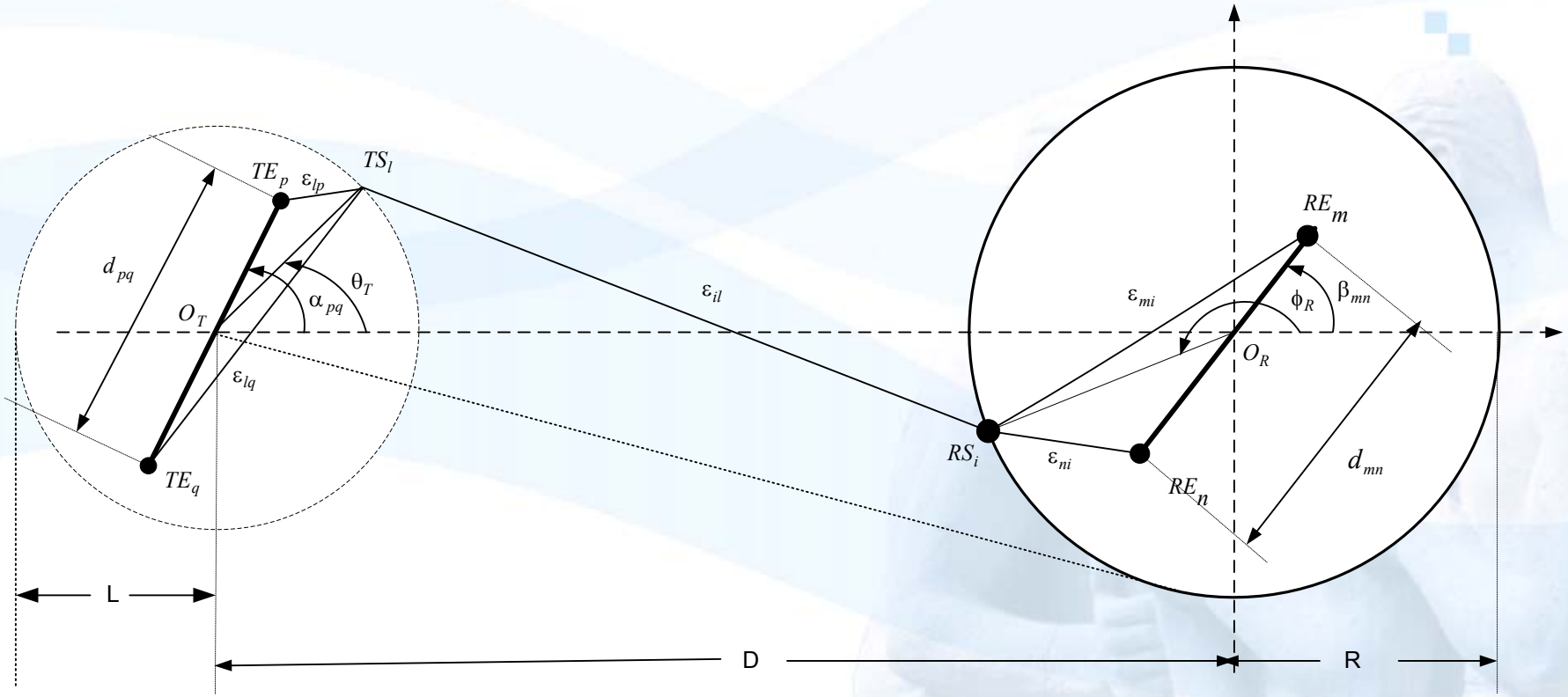

Mathematical Equation

This MIMO system can be written using the complex baseband notation as:

$$\bar{y}(t) = \overline{H}(t)\bar{x}(t) + \bar{n}(t)$$

$\overline{H}(t)$ is the channel matrix of complex path gains $h_{ij}(t)$ between TX_j and RX_i.

$\bar{n}(t)$ is the complex envelope of the AWGN with zero mean from each receive element,

$\bar{x}(t)$ is the transmit vector made up of the signal transmitted from each TX n_tx1 antenna element,

$\bar{y}(t)$ is the receive vector made up of the signal from each point RS_i.

The channel gain, $h_{mp}(t)$, for the link TE_p - RE_m as shown in Fig. 1, can be written as:

$$h_{mp}(t) = \sqrt{\Omega_{mp}} \lim_{L,N \to \infty} \frac{1}{\sqrt{LN}} \sum_{l=1}^{L} \sum_{i=1}^{N} g_{il} \times \exp\left\{ j\psi_{il} - \frac{2\pi j}{\lambda} \left[\varepsilon_{lp} + \varepsilon_{il} + \varepsilon_{mi} \right] \right\}$$

The Cross Correlation Function

The space-time correlation between two links, TE_p – RE_m and TE_q - RE_n as shown in Figure can be defined as:

$$\rho_{mp,nq}(\tau,t) = E[h_{mp}(t).h^{*}_{nq}(t+\tau)/\sqrt{\Omega_{mp}\Omega_{nq}}]$$

One can write:

$$h_{mp}(t) = \sqrt{\Omega_{mp}} \lim_{L,N\to\infty} \frac{1}{\sqrt{LN}} \sum_{l=1}^{L}\sum_{i=1}^{N} g_{il} \times \exp\left\{ j\psi_{il} - \frac{2\pi j}{\lambda}\left[\varepsilon_{lp} + \varepsilon_{il} + \varepsilon_{mi}\right]\right\}$$

$$h^{*}_{nq}(t) = \sqrt{\Omega_{nq}} \lim_{L,N\to\infty} \frac{1}{\sqrt{LN}} \sum_{l=1}^{L}\sum_{i=1}^{N} g_{il} \times \exp\left\{ -j\psi_{il} + \frac{2\pi j}{\lambda}\left[\varepsilon_{lq} + \varepsilon_{il} + \varepsilon_{ni}\right]\right\}$$

Making the respective substitutions gives:

$$\rho_{mp,nq} = \int_{-\pi}^{\pi}\int_{-\pi}^{\pi} \exp\left\{\frac{-2\pi j}{\lambda}\left[\varepsilon_{\theta p} - \varepsilon_{\theta q} + \varepsilon_{m\phi} - \varepsilon_{n\phi}\right]\right\}.p(\theta_T)p(\theta_R)d\theta_T d\theta_R$$

Joint Antenna Correlation Function

One can write the JACF [7, 11, 13] as:

$$\rho_{mp,nq} \cong \rho_{pq}^{TX} \cdot \rho_{mn}^{RX}$$

If the pdf of scatterers at the TX is:

$$p(\theta) = 1/2\pi$$

And at the RX the scattering distribution can be described by the von Mises PDF as

$$p(\phi) = \frac{\exp[k\cos(\phi - \mu)]}{2\pi I_0(k)}$$

where:

$$\mu \in [-\pi, \pi]$$

k is the isotropic scattering parameter
Φ is the mean direction of the AOA seen by the user

I_o is the zero order modified Bessel function

Antenna Correlation Functions

Simplifying the equations, one gets closed form expressions:

$$\rho_{pq}^{TX} = I_0[jc_{pq}] \qquad where; c_{pq} = \frac{2\pi d_{pq}}{\lambda}$$

$$\rho_{mn}^{RX} = \frac{1}{I_0(k)} I_0\left[k^2 - b_{mn}^2 + j2kb_{mn}\cos(\mu - \beta_{mn})\right]^{1/2} \qquad where; b_{mn} = \frac{2\pi d_{mn}}{\lambda}$$

Using:

$$\overline{X} = \overline{U}\sqrt{\overline{R_T}}; \qquad \overline{R_T} \text{ is the } n_T \times n_T \text{ matrix of the TX antenna correlation}$$

$$C = \log_2 \det\left(I_{n_R} + \frac{\rho}{n_T}\mathbf{H}\mathbf{H}^H\right)$$

RESULTS

Figure 2. ccdf vs Capacity for varying antennas

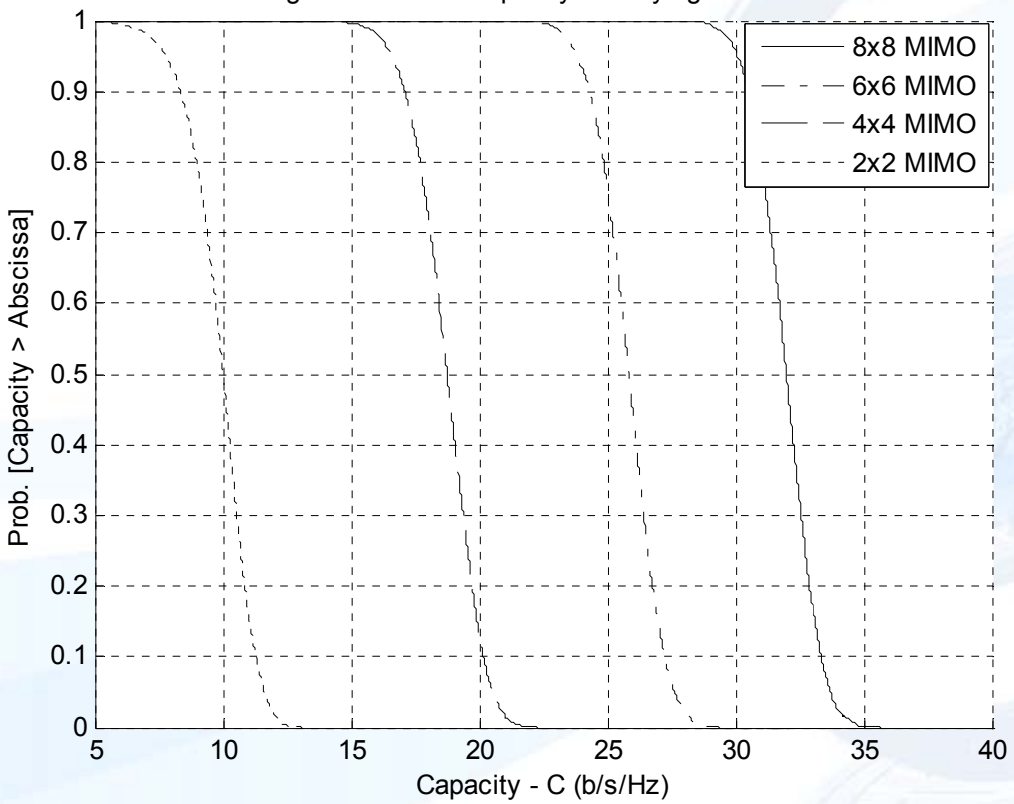

RESULTS

Figure 3 ccdf vs Capacity for varying antennas element spacing at RX

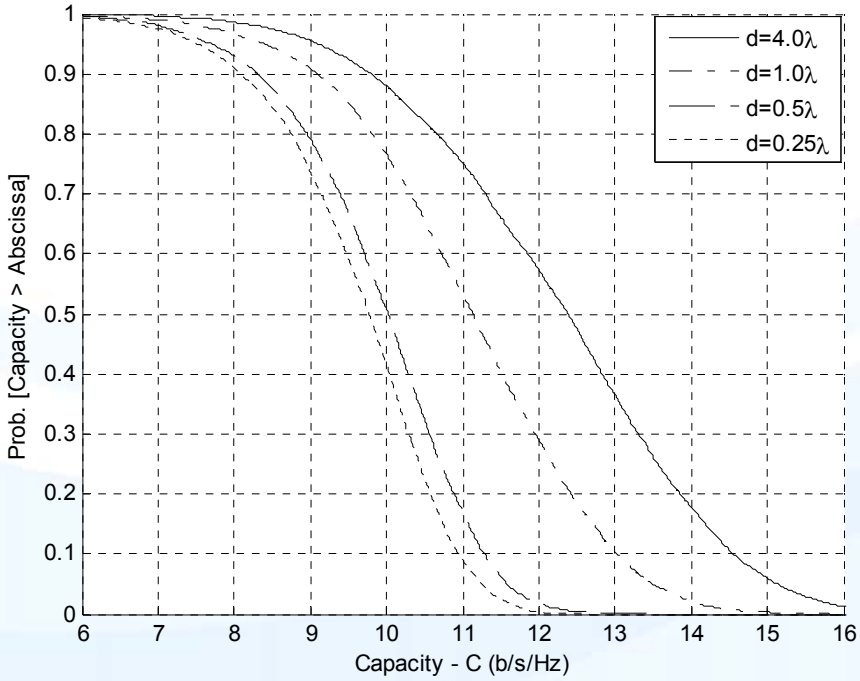

Figure 4 ccdf vs Capacity for varying scattering, k

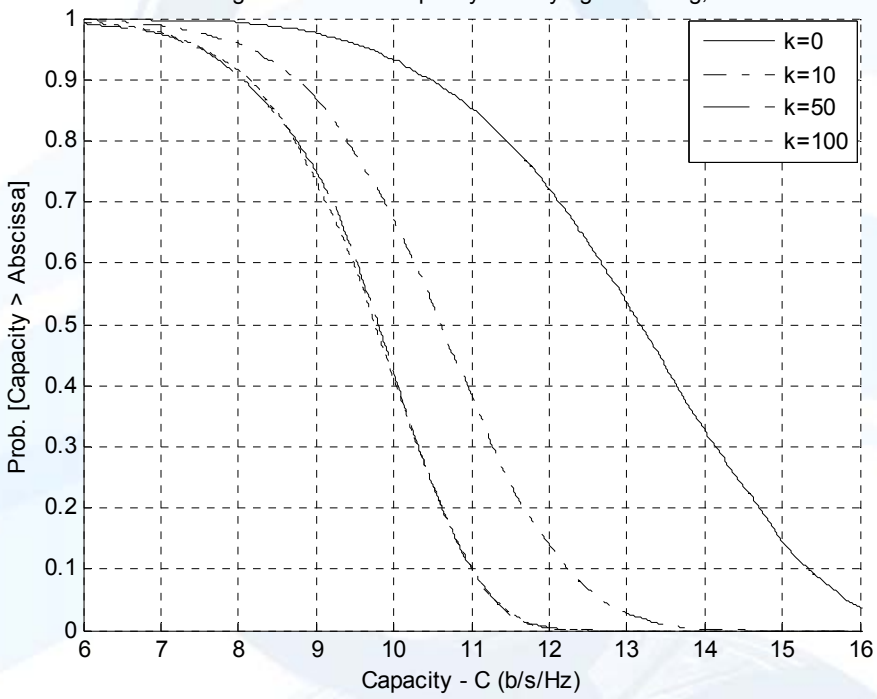

UNIVERSITEIT VAN PRETORIA
UNIVERSITY OF PRETORIA
YUNIBESITHI YA PRETORIA

RESULTS

Figure 6 ccdf vs Capacity for varying SNR

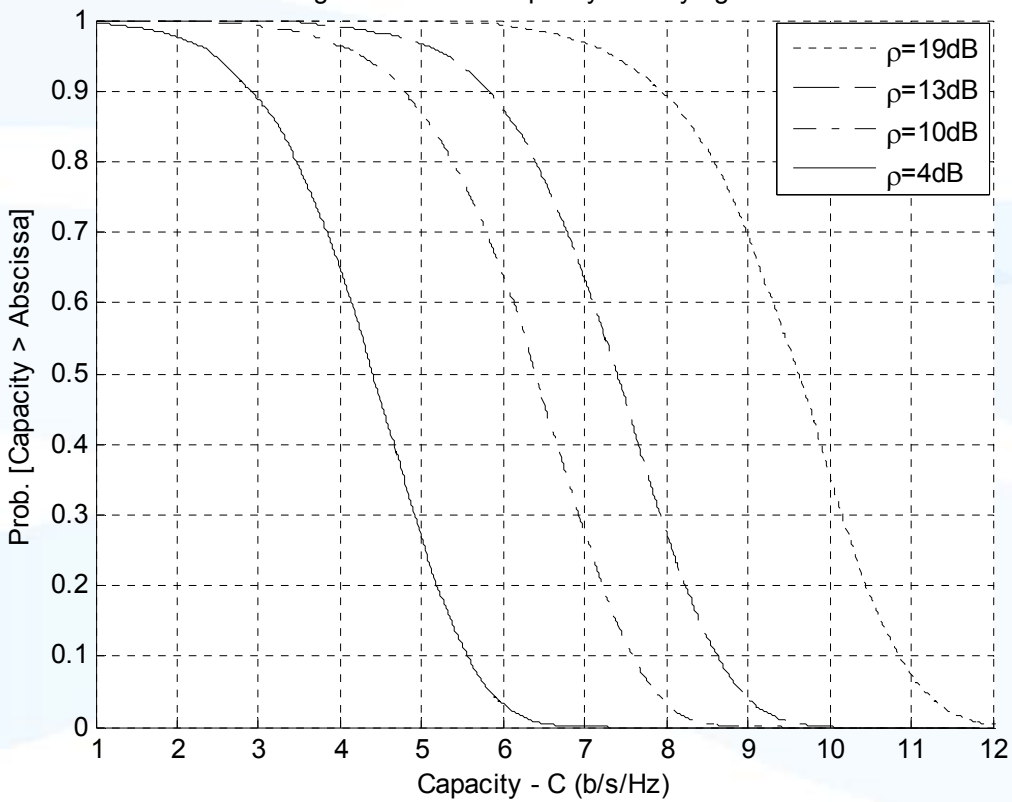

Geometric Modelling Conclusions

1. This model gives an indication of the theoretical performance gains of a MIMO system

2. From a geometric based model a joint correlation function and TX and RX correlation functions were derived in a neat, compact and closed form

3. Model incorporates the key parameters such as configuration of antenna array, number of antenna elements, antenna spacing, antenna orientation and degree of scattering at RX.

4. Shown that number of antenna elements has greatest impact on channel capacity.

5. Could be a simplification of real environment!

WB MIMO Measurement System

WB MIMO Channel Sounder

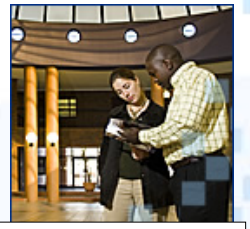

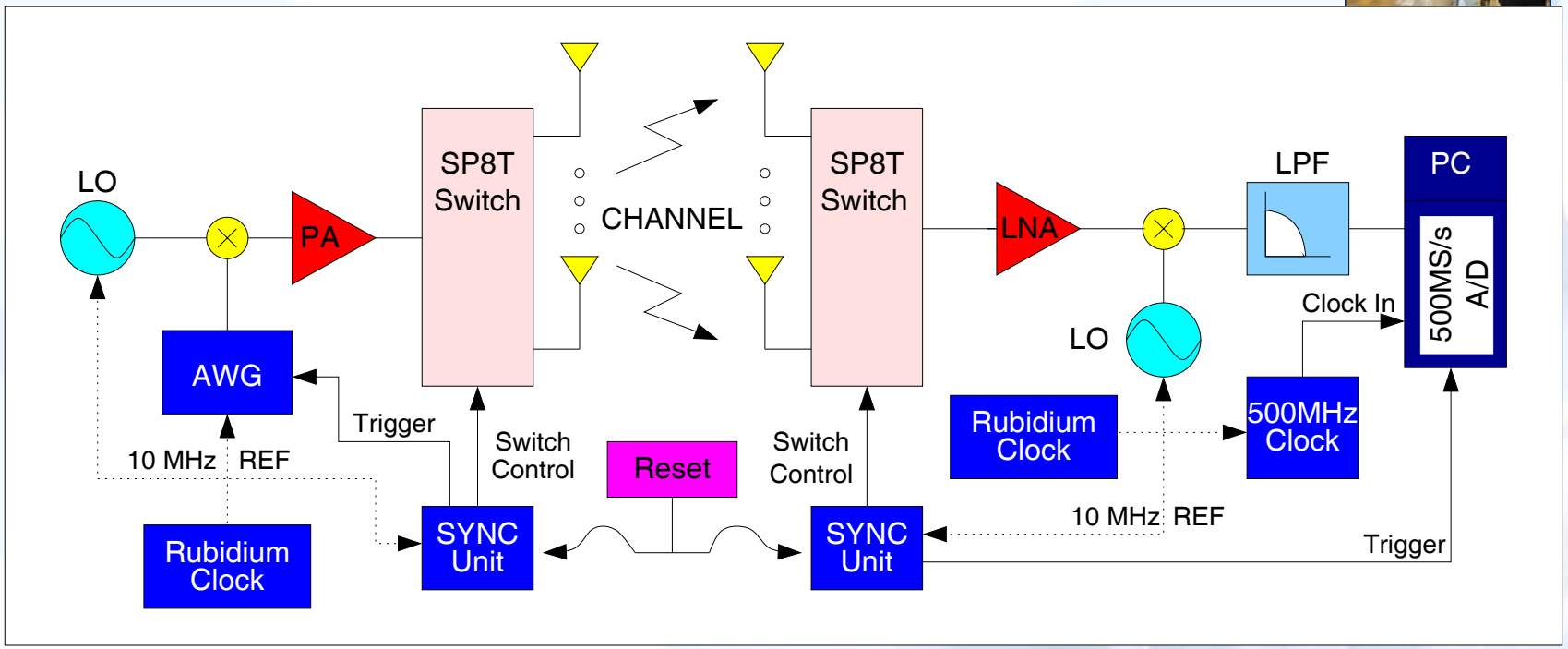

- **Low Cost 8x8 Architecture: switched array, COTS components/instruments**
- **PC-based A/D simplifies data processing (MATLAB)**
- **Up to 100 MHz instantaneous bandwidth**
- **2-6 GHz center frequency**

System Implementation - TX

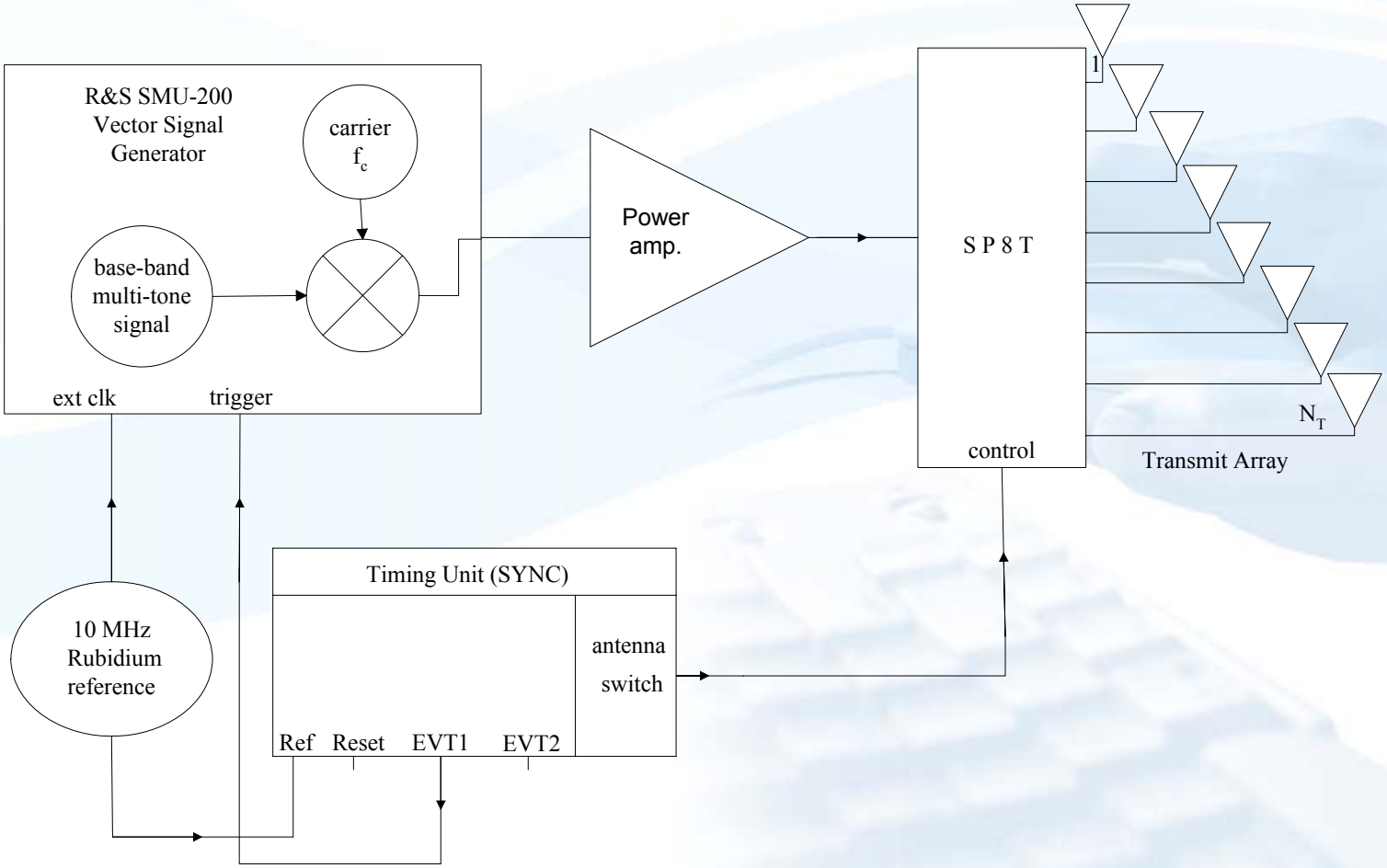

System Implementation - RX

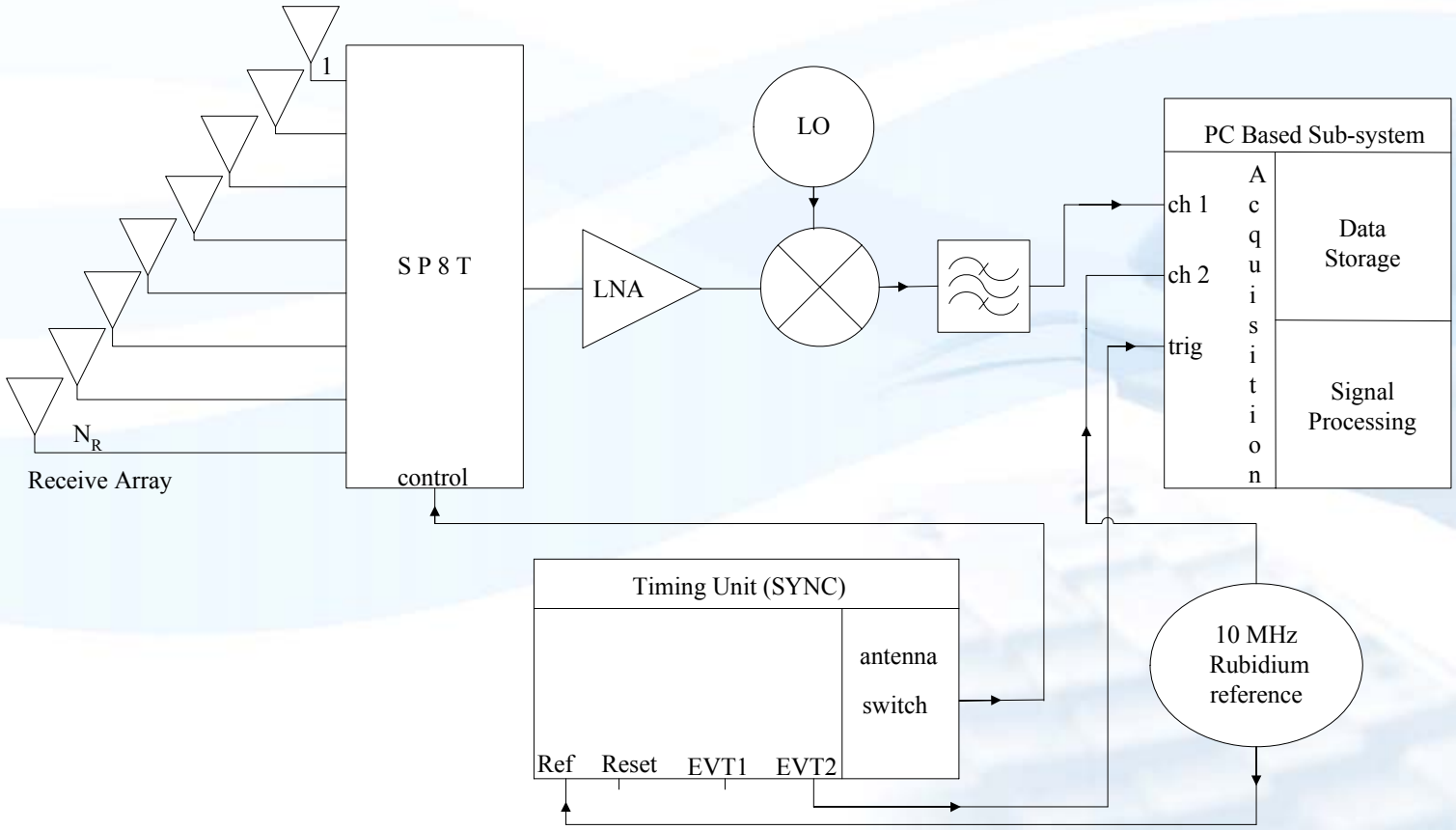

Measurement Method – UP System

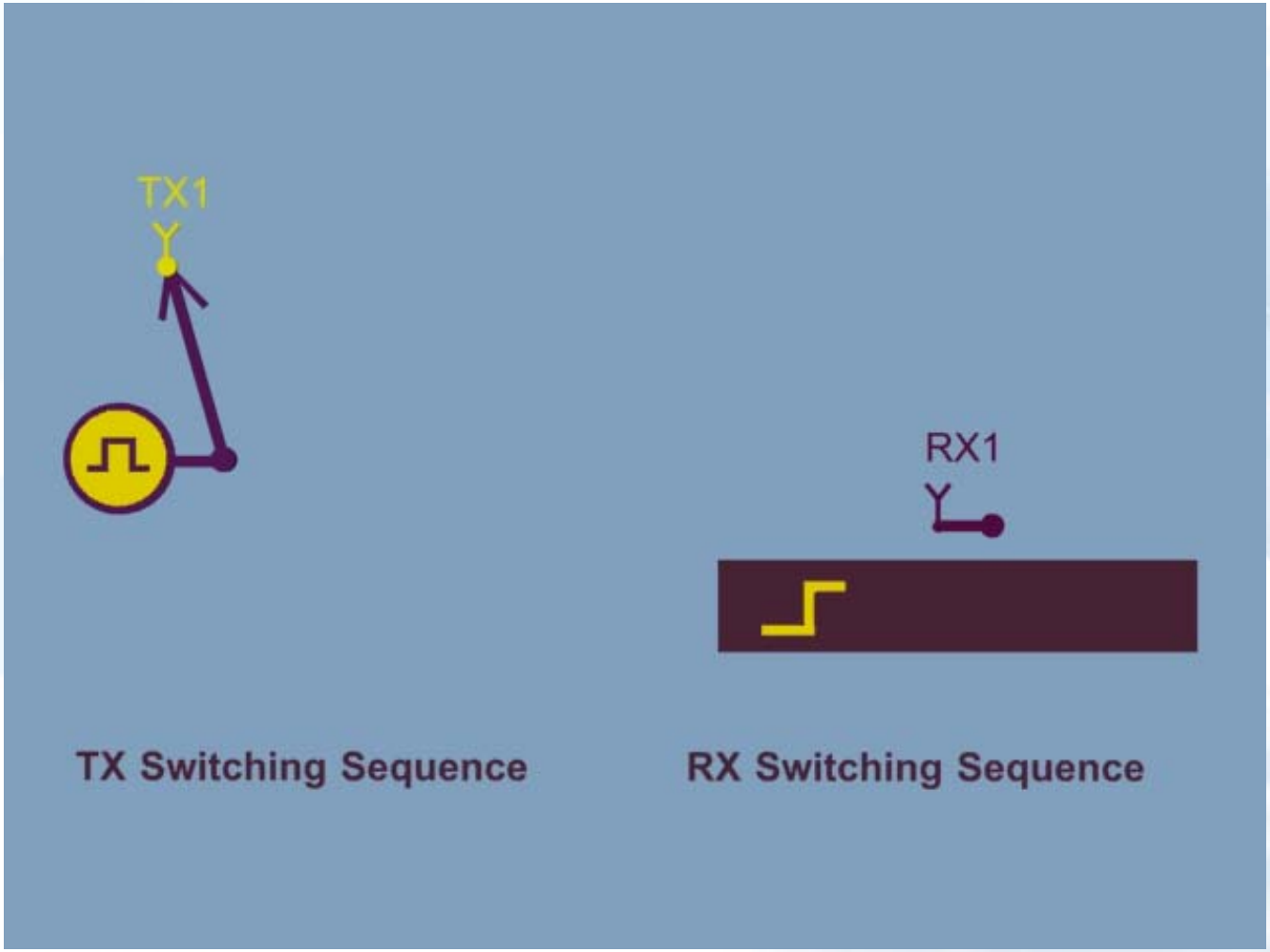

Synchronization Sequences

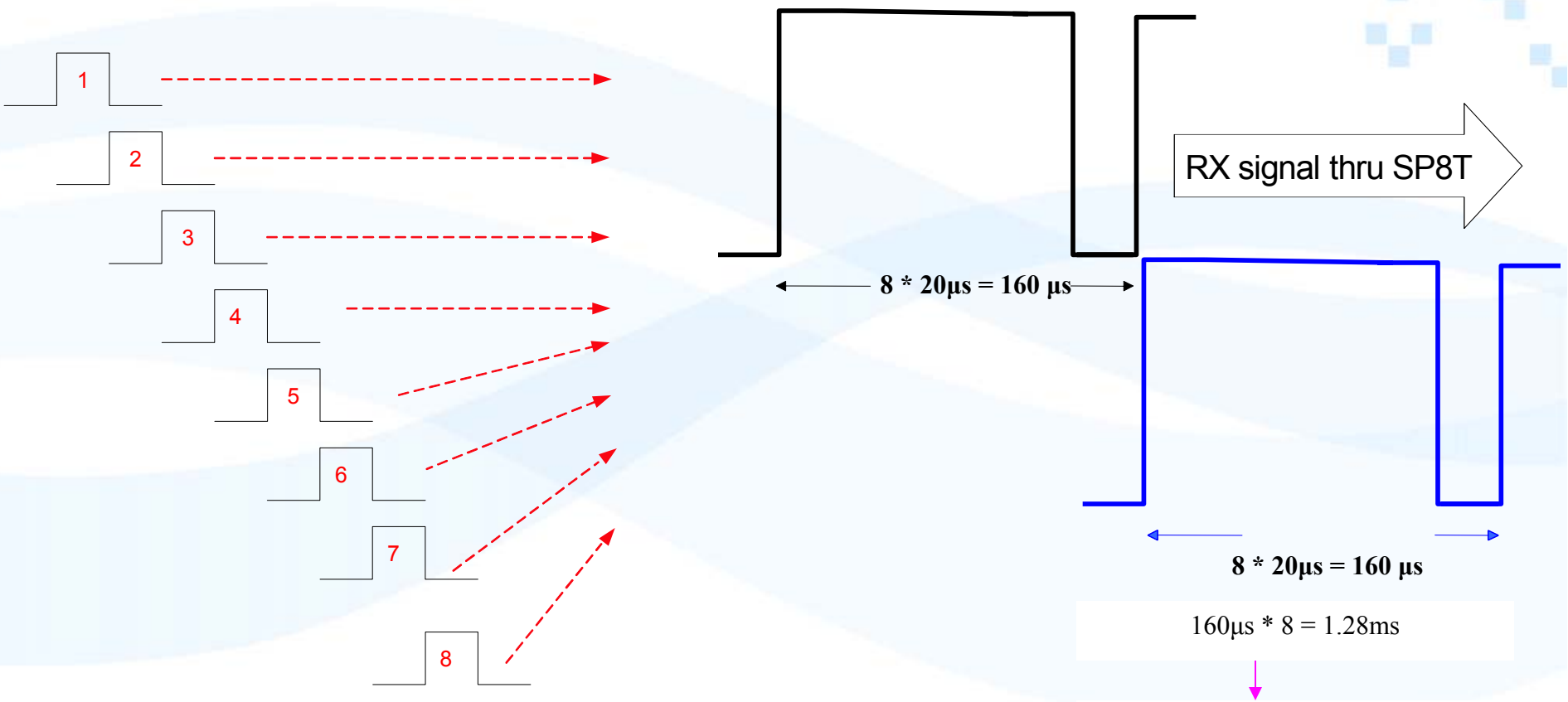

TX signal from SP8T

160µs * 8 = 1.28ms

1.28ms + 198.72ms = 200ms

200ms * 20snapshots = 4s

4s * 2sequences = 8s

UNIVERSITEIT VAN PRETORIA
UNIVERSITY OF PRETORIA
YUNIBESITHI YA PRETORIA

Synchronization Unit (SYNC)

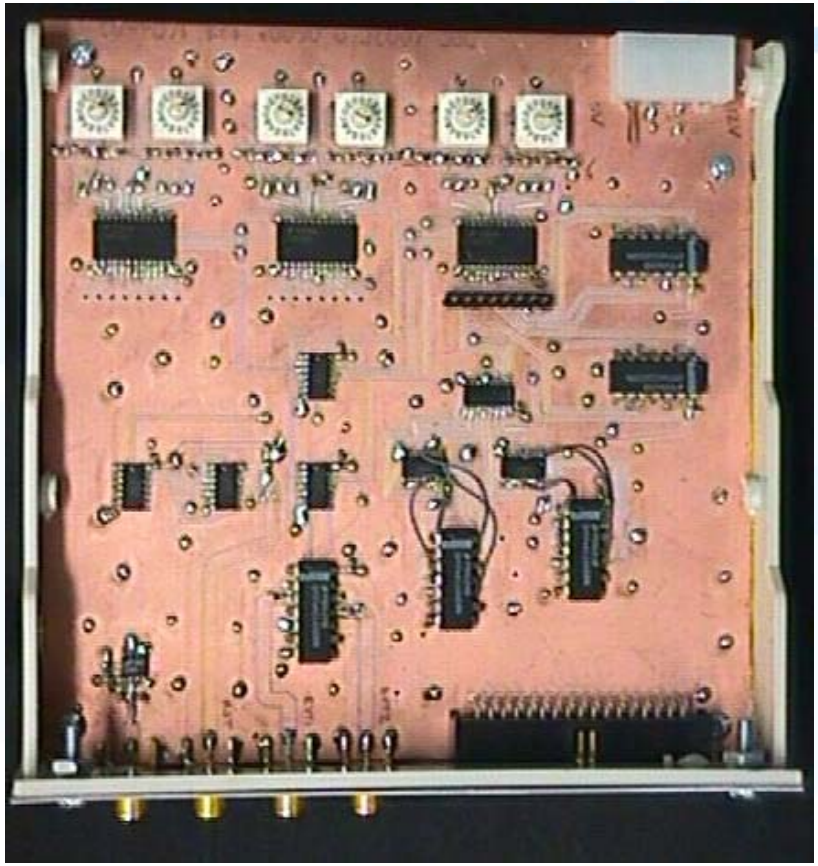

Measurement System

The multi-tone signal is of the form:

$$x(t) = \sum_{i=0}^{N} \cos(2\pi f_i t + \varphi_i)$$

$f_i = (0.5 + i)MHz$

$i = 0,1,...,39$

$\varphi_i = \{0, \pi\}$; is random (but fixed) phase shift for each tone that spreads the signal energy in time

To avoid artifacts associated with turning the signal on and off abruptly, the multitone signal of length T is multiplied by a Gaussian windowing function of the form

$$w(t) = \begin{cases} e^{-(T_1 - t)^2 / 2\sigma^2}, & 0 \le t < T_1 \\ e^{-(T_2 - t)^2 / 2\sigma^2}, & T_2 < t \le T \\ 1, & Otherwise \end{cases}$$

where:

T_1 and T_2 are the limits of the window

σ standard deviation controls the rise and fall time of the window

Hence:

$$Y(f) = X(f) * W(f)$$

Monopole Antennas

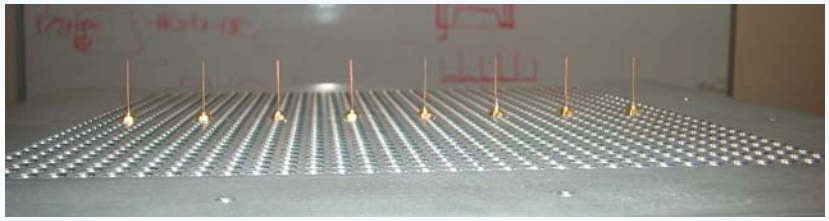

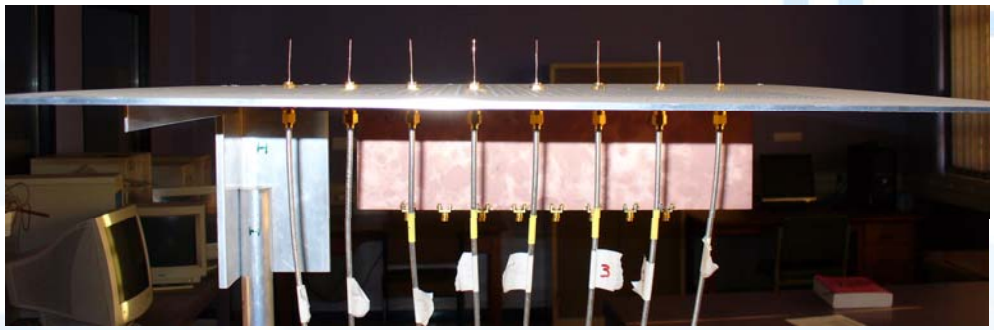

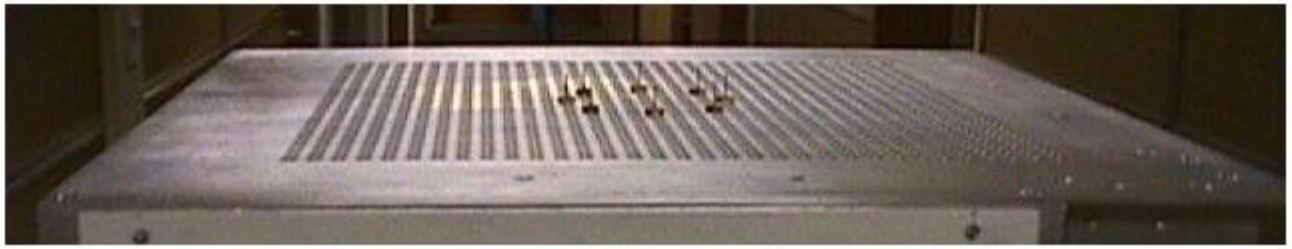

System developed and deployed at UP

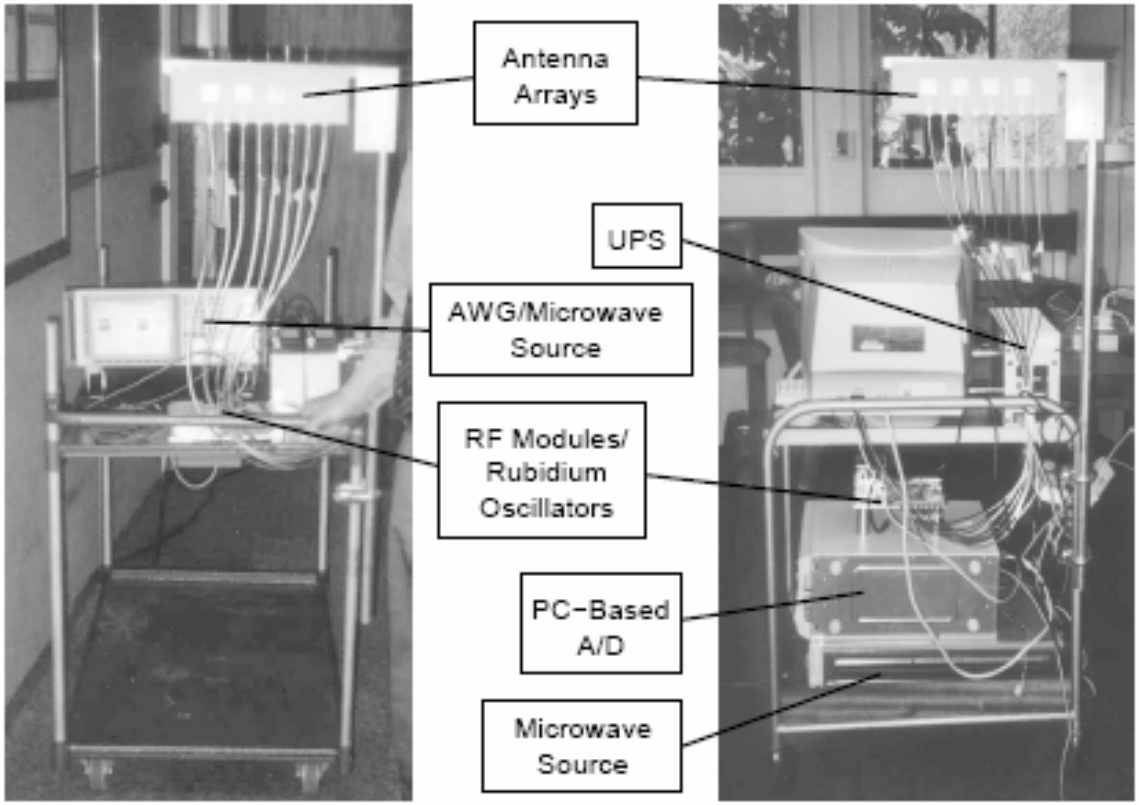

(a) Transmit (b) Receive

TX Hardware – 5.2 GHz

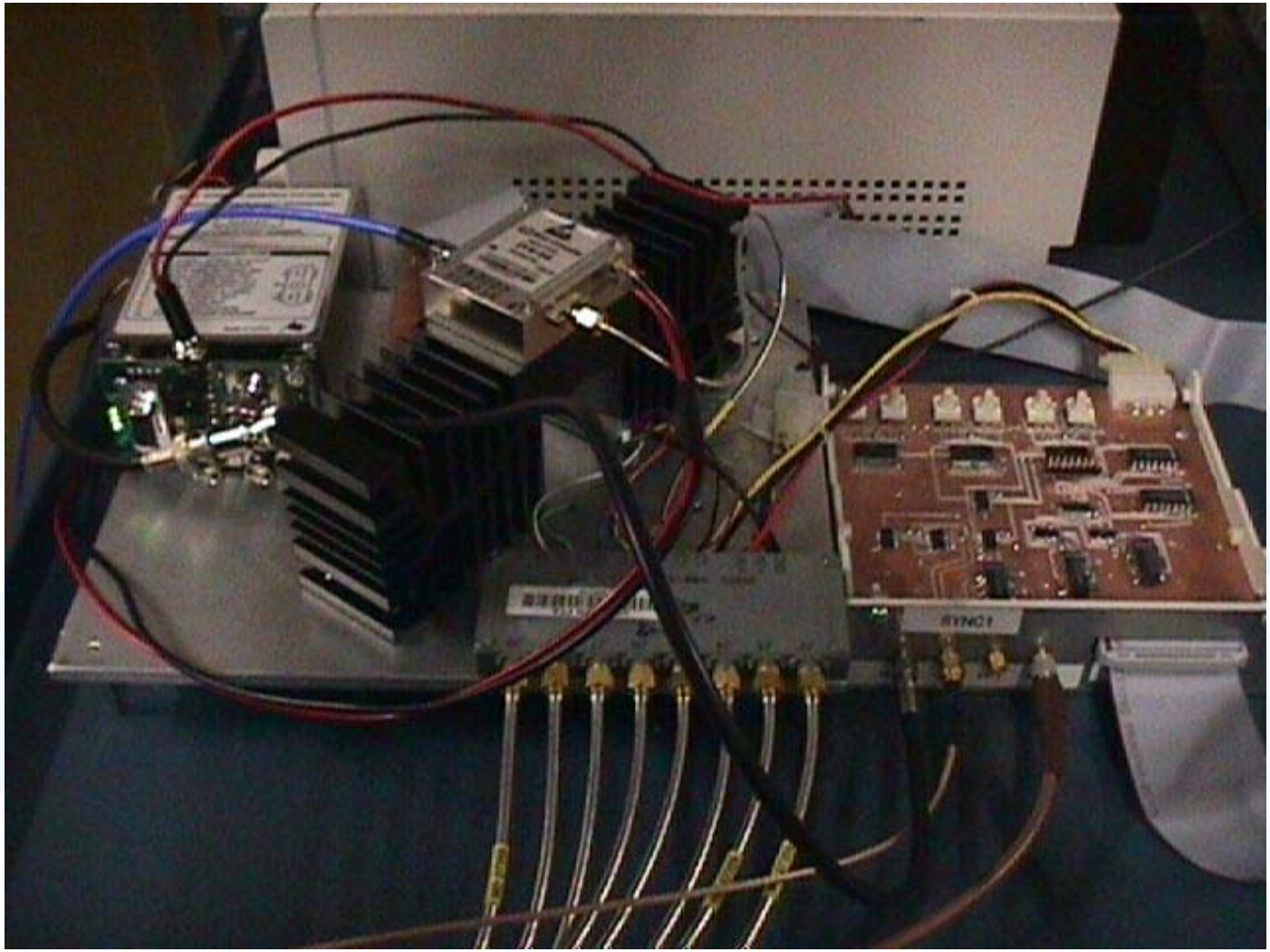

RX Indoor Measurement Locations

Measurement Environment – 2nd floor CEFIM

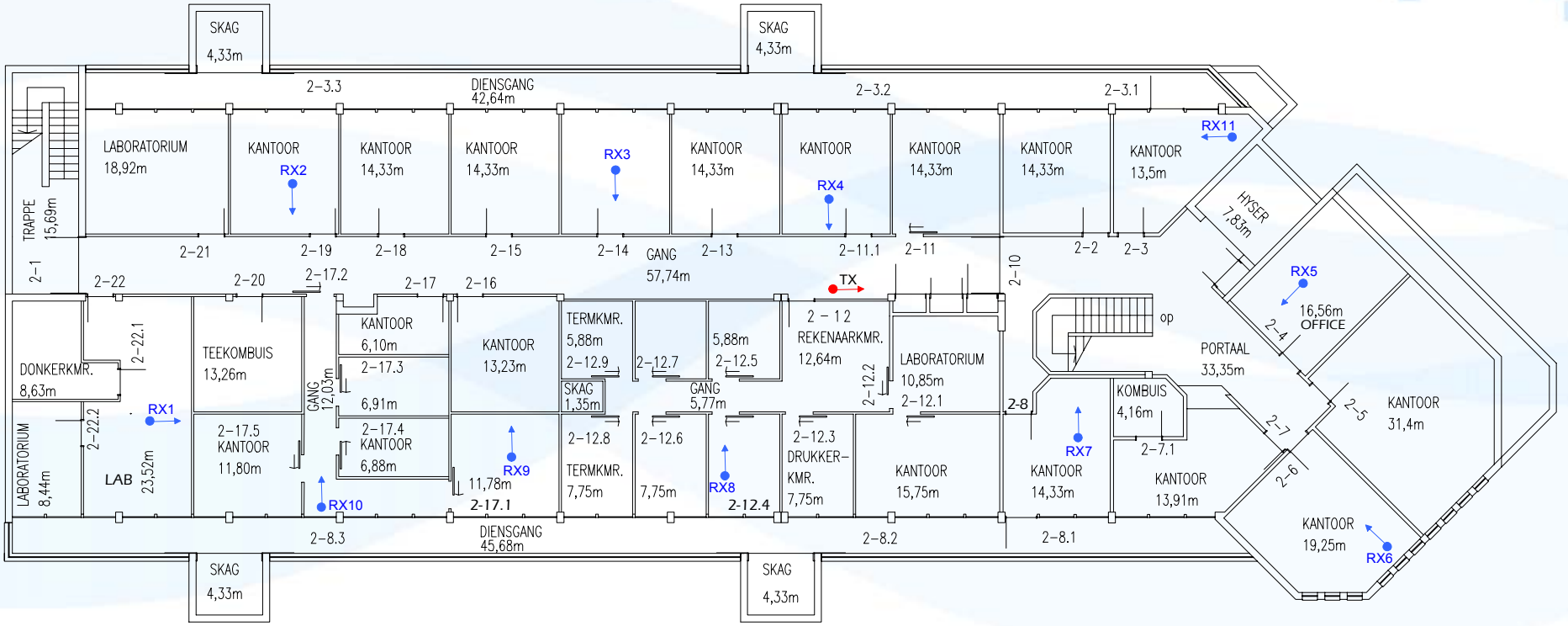

Data Processing

The Channel Matrix, H is represented in the ff form:

H(f,rx,tx,s,ss):

(Freq. bins,

RX antennas,

TX antennas,

sequence no,

snapshots)

Channel Matrix Normalization: remove effect of path loss

$$\tilde{\mathbf{H}}^{(n)} = \left(\frac{1}{N_R N_T N_S} \sum_{m=1}^{N_S} \left\| \mathbf{H}^{(m)} \right\|_F^2 \right)^{-1/2} \mathbf{H}^{(n)}$$

$\tilde{\mathbf{H}}^{(n)}$ = n^{th} normalized channel matrix

$\mathbf{H}^{(n)}$ = n^{th} non-normalized channel matrix

$\|\cdot\|_F$ = Frobenius norm

$N_R = N_T = 8$

N_S = no. of channel measurements (snapshots and freq. bins)

$(.)^H$ = the conjugate matrix transpose

WB MIMO Channel Sounder System Conclusion

- True channel behavior requires a system capable of direct channel measurement.
- Presented a successfully deployed ‘switched array’ system capable of probing from 2-6 GHz with a channel BW of 100MHz.
- Capable of having up to 8 TX and 8 RX antennas in an indoor environment.
- Reliable and repeatable measurements were taken in 3 different indoor environments at 2.4GHz and 5.2GHz.

Data Analysis and Model Assessment

- Capacity Modelling
- Spatial Correlation
- Double Directional Channel

Capacity for a 8x8 MIMO employing UCA

Channel capacity with no CSI

$$C = \log_2 \det(\mathbf{I} + \frac{\rho}{N_T} \tilde{\mathbf{H}} \tilde{\mathbf{H}}^H),$$

Average Channel Capacity cross BW

$$\overline{C}_{loc} = \left(\sum_{k=1}^{K} C_k \right) \Big/ K$$

K = no. of frequency bins

RESULTS

Channel eigenvalue cdfs for circular arrays at 2.4GHz and 5.2GHz

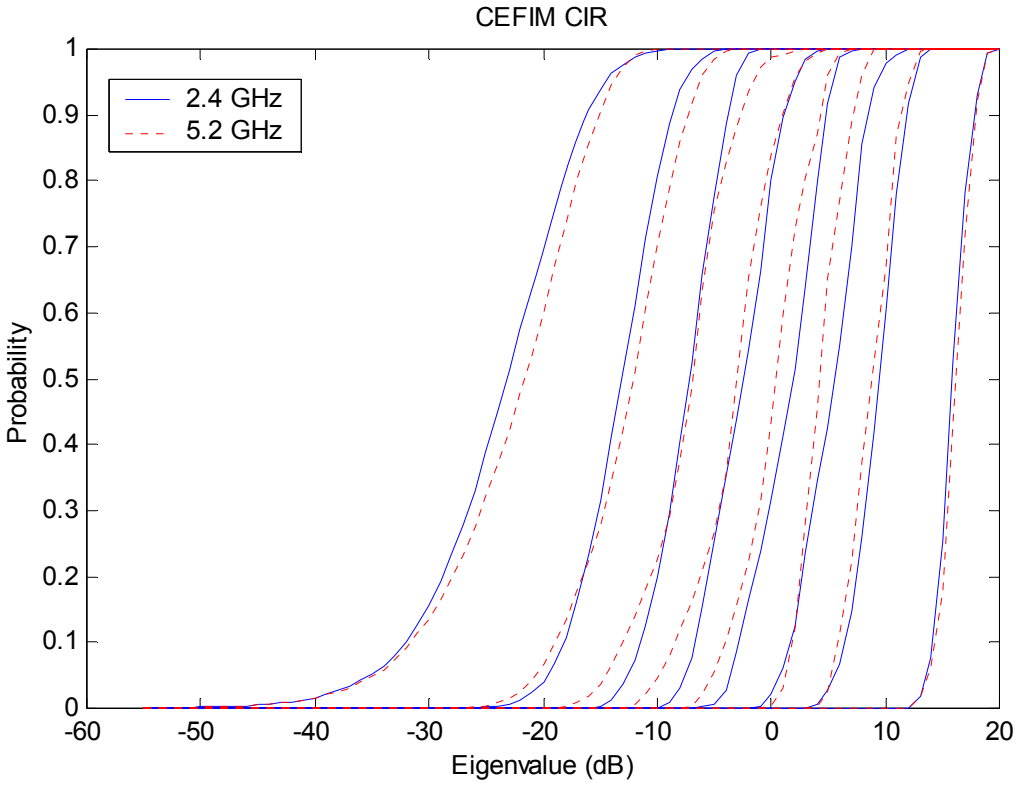

Results
Capacity vs excitation BW at location 9

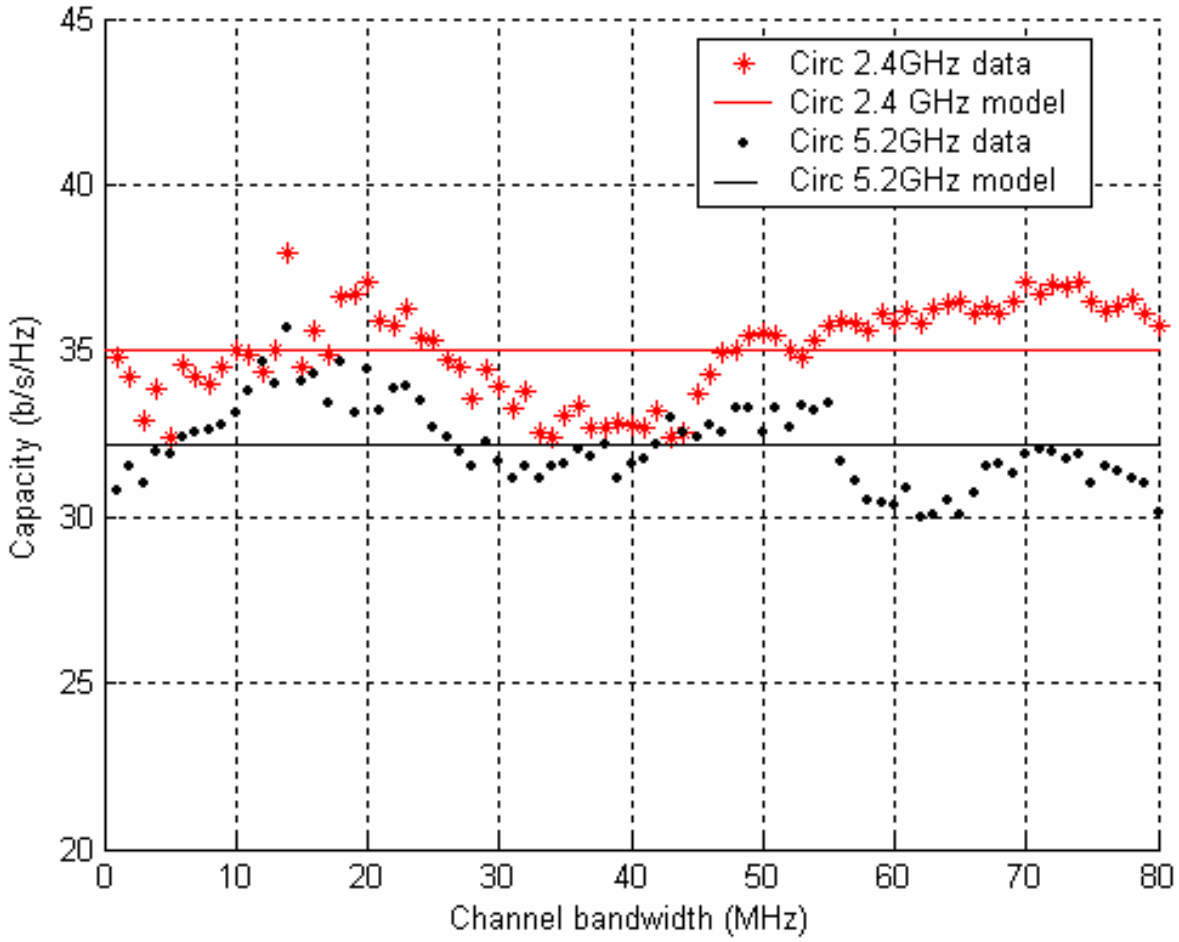

Circular Array Average Capacity

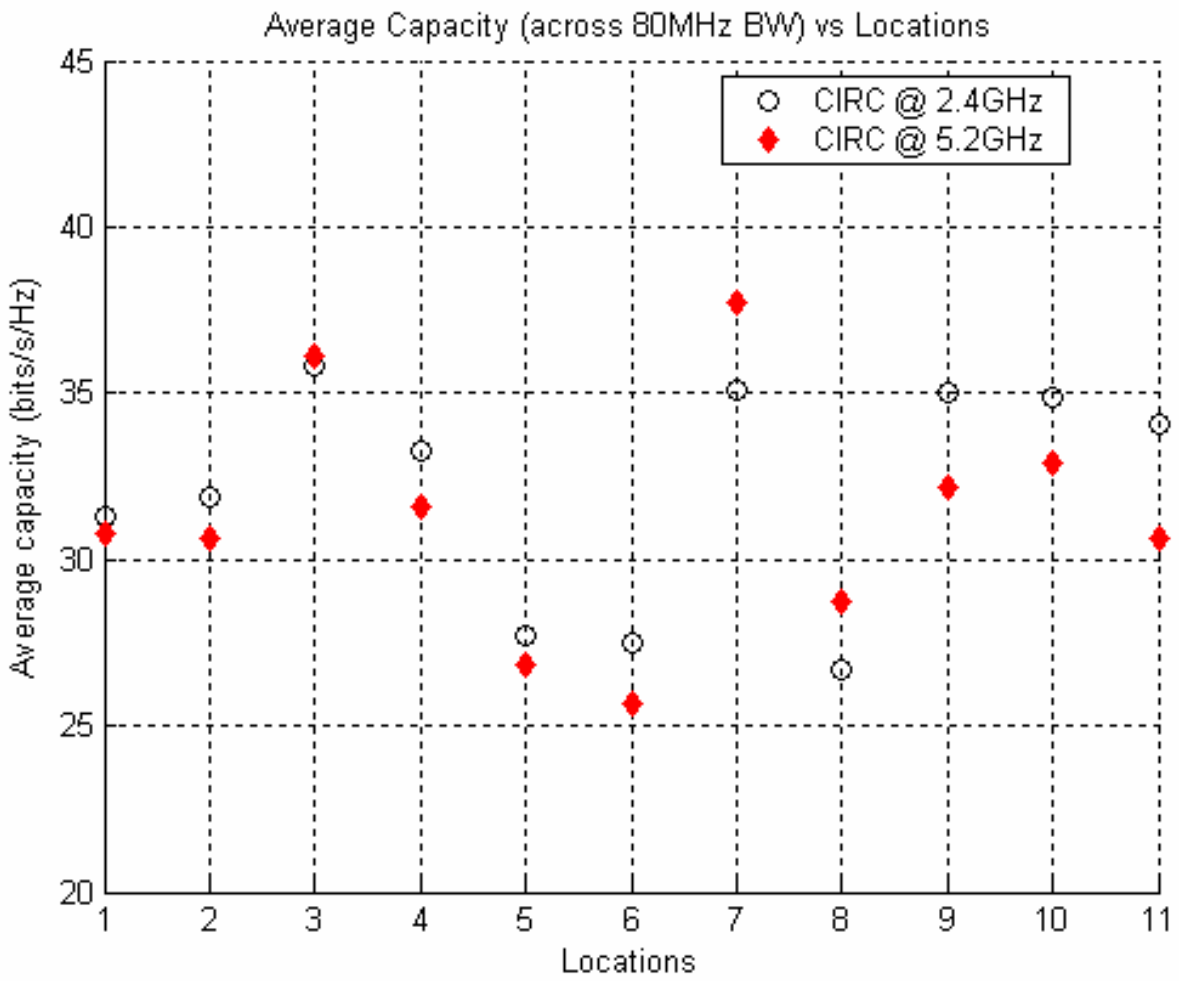

Results
Modelling freq scaling of capacity for UCA

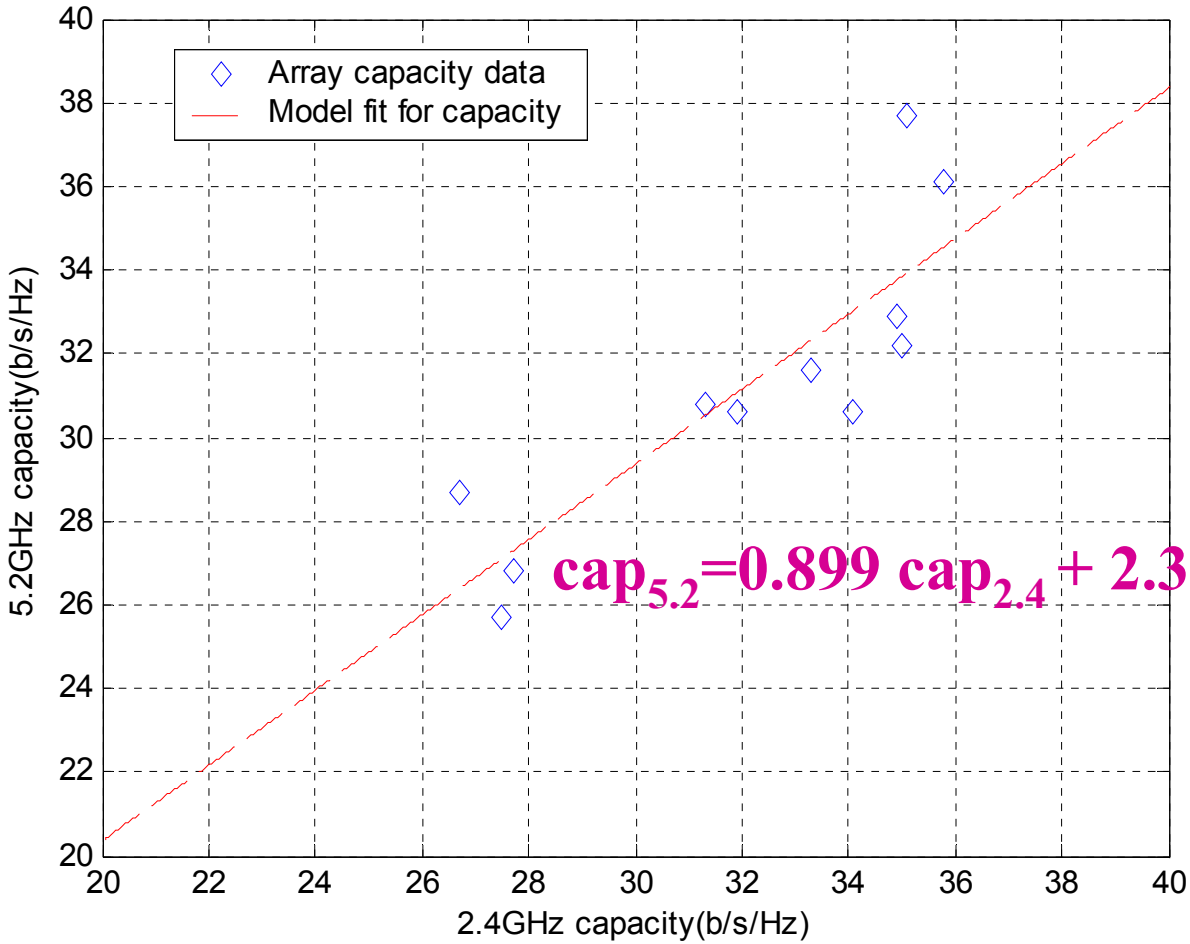

$$cap_{5.2} = 0.899\ cap_{2.4} + 2.367$$

Spatial Correlation:
Shift Invariant Correlation - ULA

The correlation coefficient at the RX for element displacement ℓ:

$$\rho_\ell = \frac{\left[\sum_{k=1}^{N_S}\sum_{j=1}^{N_T}\sum_{i=1}^{N_R-\ell} H_{i,j}^{(k)} H_{i+\ell,j}^{(k)*}\right]}{\left[\left(\sum_{k=1}^{N_S}\sum_{j=1}^{N_T}\sum_{i=1}^{N_R-\ell}\left|H_{i,j}^{(k)}\right|^2\right)\left(\sum_{k=1}^{N_S}\sum_{j=1}^{N_T}\sum_{i=1}^{N_R-\ell}\left|H_{i+\ell,j}^{(k)}\right|^2\right)\right]^{1/2}}$$

$H_{i,j}^{(k)}$ is the k^{th} channel snapshot from the j^{th} TX to the i^{th} RX antenna

$\mathbf{N_s}$= 20*80; is the number of snapshots taken across all freq. bins and observations

$\mathbf{N_T} = \mathbf{N_R} = 8;$ is number of TX and RX antennas respectively

Modelling of Correlation

Magnitude of correlation coefficient, ρ_ℓ could be modelled as:

$$y_\ell = e^{-b\ell\Delta x}$$

where:

Δx is the element separation in wavelengths

b is the estimated decorrelation parameter

Average mean square error (MSE) at {TX,RX}:

$$\bar{d} = \frac{1}{\{N_T, N_R\}} \sum_{\ell=0}^{\{N_T, N_R\}-1} (|\rho_\ell| - y_\ell)^2$$

Frequency scaling analysis through linear regression of decorrelation or capacity by:

$$q_{5.2} = a_1 + a_2 q_{2.4}$$

where: $q_{\{5.2,2.4\}}$ is either the capacity or decorrelation at 5.2 GHz and 2.4 GHz, respectively, and a_1 and a_2 are obtained with a minimum MSE fit

Results:

Calculated relative correlation coefficients with curve fit for RX location 4

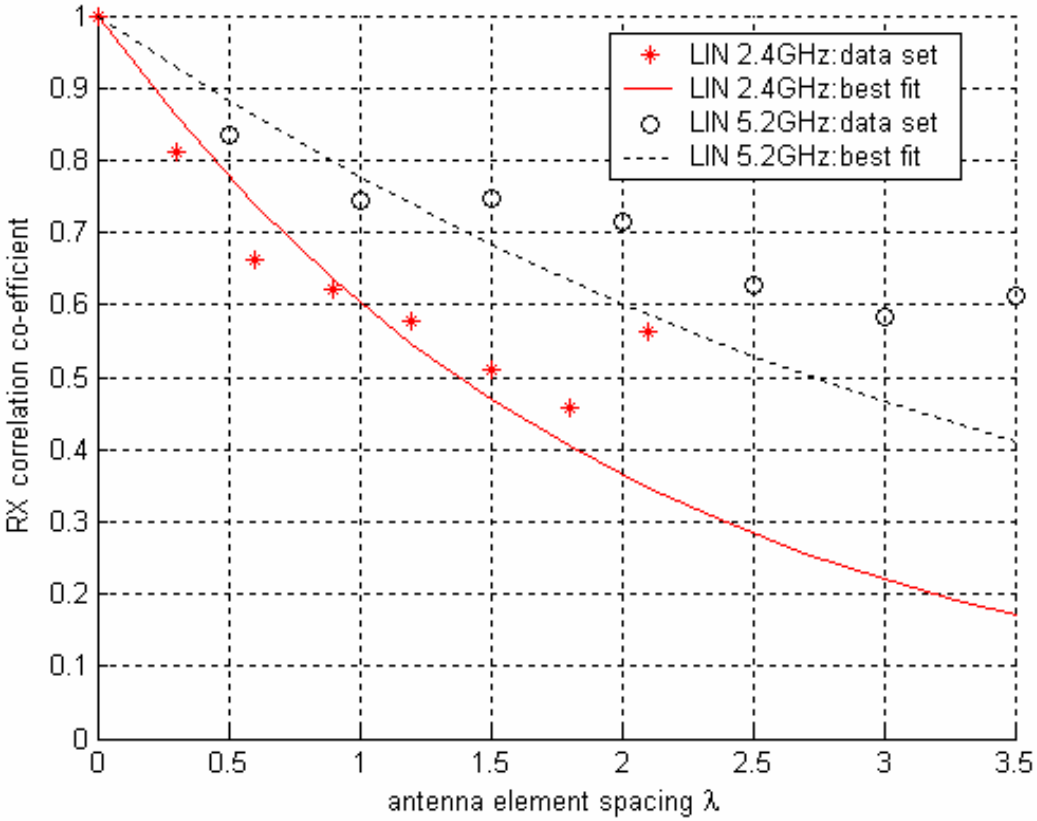

Results:

Calculated relative correlation coefficients with curve fit for TX location 8

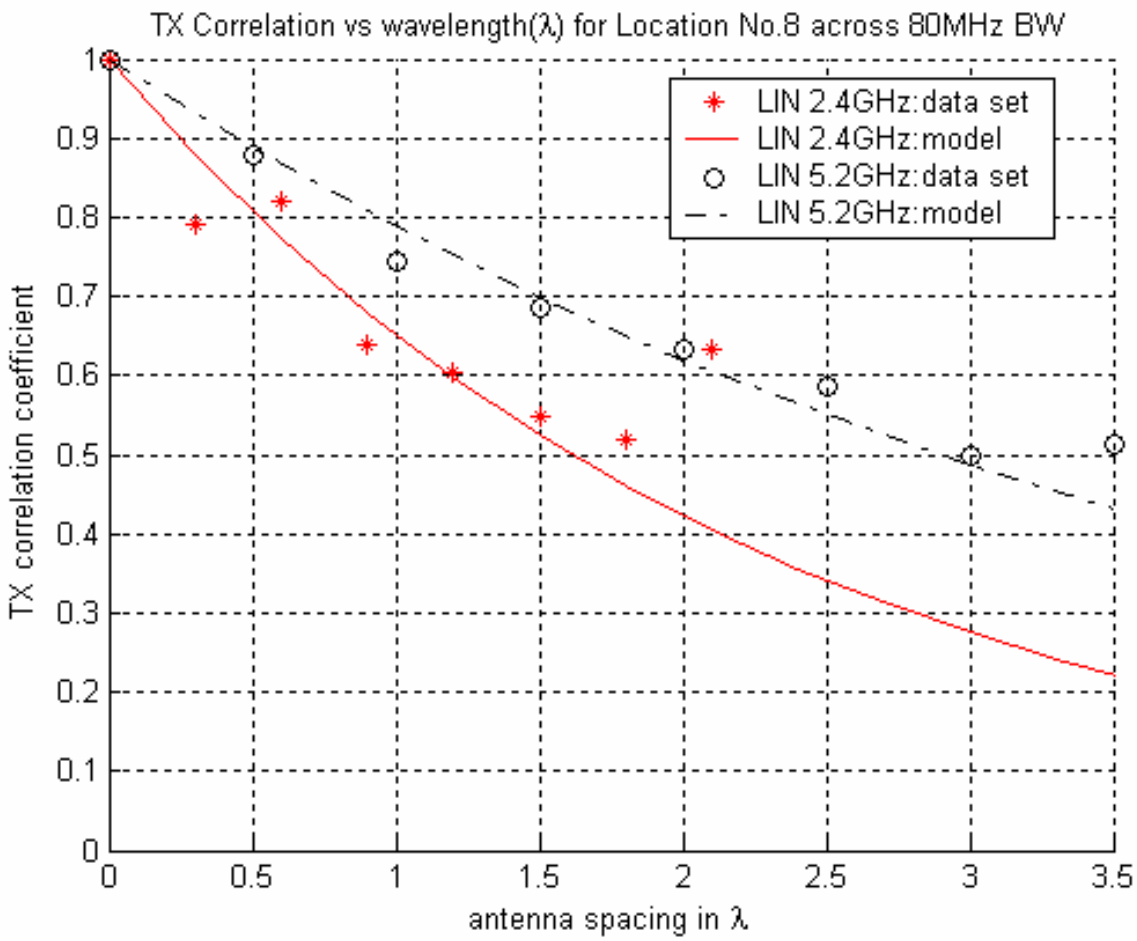

Results:

Relationship of decorrelation with respect to frequency scaling

RX

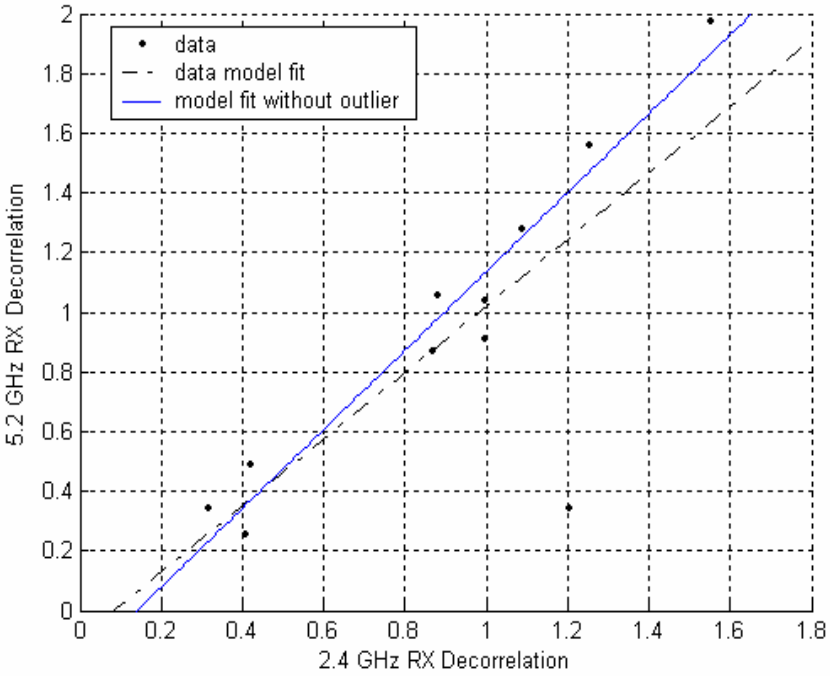

TX

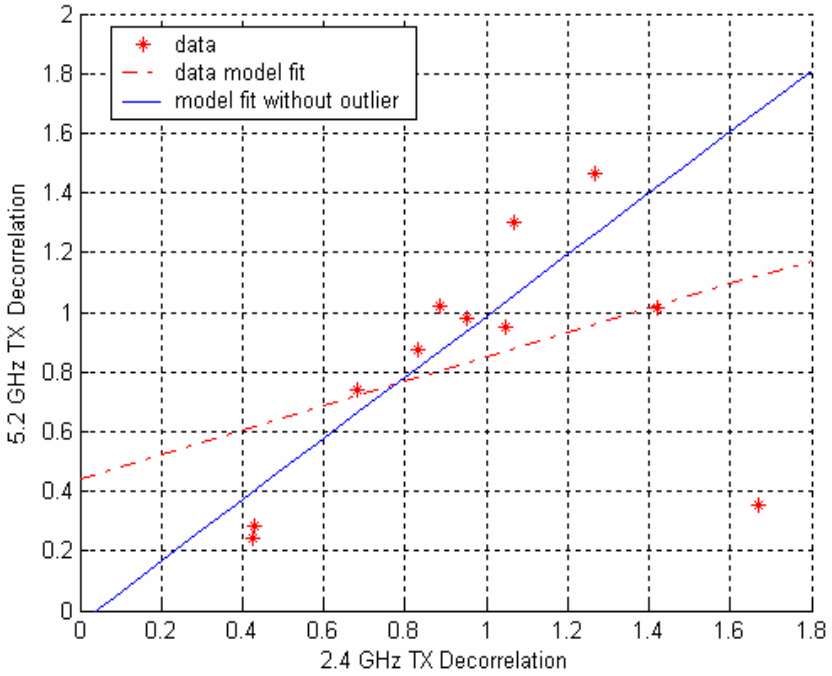

Results

TABLE I

DECORRELATION PARAMETER (b) AND ERROR wrt WAVELENGTH (λ) AT RX

Locations	5.2 GHz		2.4 GHz	
	b	error (%)	b	error (%)
1	0.8702	3.27	0.8690	4.76
2	1.2795	1.76	1.0903	4.48
3	1.5591	5.64	1.2546	2.00
4	0.2550	1.06	0.4080	0.75
5	1.0536	2.57	0.8799	3.49
6	0.3432	0.98	0.3182	1.15
7	0.9071	0.72	0.9978	0.17
8	0.4883	1.46	0.4190	0.35
9	0.3442	0.45	1.2042	1.18
10	1.0403	2.40	0.9980	2.90
11	1.9721	5.41	1.5548	3.65

Results

TABLE II
DECORRELATION PARAMETER (b) AND ERROR wrt WAVELENGTH (λ) AT TX

Locations	5.2 GHz		2.4 GHz	
	b	error (%)	b	error (%)
1	0.9769	1.54	0.9511	0.18
2	1.0189	2.66	0.8849	1.69
3	1.2988	1.68	1.0666	2.34
4	0.2400	2.96	0.4270	2.90
5	0.8746	2.08	0.8325	0.06
6	0.7402	5.84	0.6833	0.56
7	1.4634	1.13	1.2678	1.38
8	0.2845	0.51	0.4302	0.84
9	0.3530	1.03	1.6701	0.96
10	1.0134	0.75	1.4210	3.15
11	0.9514	0.49	1.0462	0.76

Data Analysis and Model Assessment: Conclusion

Capacity for UCA wrt frequency scaling:

- **Observed a linear model fit**
- **Variance of 1.91**
- **High degree of correlation of capacities**
- **Hence capacity at different centre freq can be reliably predicted**

Model for Spatial correlation of ULA at a location

- **RX**
  - **exponential model fit gives typical MSE of 0.2% and 3.3% at two carrier freq's**
  - **only 20% of locations gave MSE of 4%-5.5%(max)**
  - **average error at 5.2GHz = 2.34%**
  - **average error at 2.4 GHz = 2.26%**
- **TX**
  - **Similar to RX**
  - **average error at 5.2GHz = 1.9%**
  - **average error at 2.4 GHz = 1.4%**

Conclusion wrt Spatial Correlation

- Spatial correlation wrt frequency scaling
  - decorrelation parameter shows high dependence
  - linear model gives MSE of 0.012 at RX
  - linear model gives MSE of 0.034 at TX
  - strong dependence of correlation at two centre frequency's implies:
    - high correlation in directional signature of multi-path propagation
    - level of multi-path may be very similar
- Results useful for ST coding, MIMO system development, network planning, channel measurement campaigns

Double Directional Channel Modelling for indoor co-located WB MIMO measurements

Double Directional Channel

• Previous modelling efforts [Steinbauer, et al] have defined the double directional channel in terms of a paired discrete plane-wave departures and arrivals at the TX and RX

• Indoor environments have much more severe multipath, hence extracting individual plane-wave arrivals can be very difficult

• Hence the new approach we proposed is to define the double directional response in terms of spatial power spectra obtained from the joint TX/RX Bartlett or Capon beamformers

Double directional channel: Capon beamformer

$$P_{CAP}(\nu_T,\nu_R)=\frac{1}{\mathbf{a}(\nu_T,\nu_R)^H\hat{\mathbf{R}}^{-1}\mathbf{a}(\nu_T,\nu_R)}$$

$\{\cdot\}^H$ denotes the complex conjugate transpose

ν_T and ν_R are the azimuth angles at the TX and RX respectively

$\hat{\mathbf{R}}$ is the sample covariance matrix

$\mathbf{a}(\nu_T,\nu_R)$ Joint steering vector is defined as:

$$\mathbf{a}(\nu_T,\nu_R)=\mathbf{a}_T(\nu_T)\otimes\mathbf{a}_R(\nu_R)$$

Double directional channel: Bartlett beamformer

Sample covariance matrix is computed as:

$$\hat{\mathbf{R}} = \frac{1}{K}\sum_{k}\mathbf{h}^{(k)}\mathbf{h}^{(k)H}$$

K is the total number of frequency bins

$\mathbf{h}^{(k)} = \mathrm{Vec}\{\mathbf{H}^{(k)}\}$ $\mathrm{Vec}\{\cdot\}$ - vector operation to stack a matrix into a vector

$\mathbf{a}_{\{T,R\}}$ are the separate array steering vectors for the TX and RX

Similary the joint Bartlett Beamformer is defined as:

$$P_{BAR}(\nu_T,\nu_R) = \frac{\mathbf{a}(\nu_T,\nu_R)^H \hat{\mathbf{R}}\mathbf{a}(\nu_T,\nu_R)}{\mathbf{a}(\nu_T,\nu_R)^H \mathbf{a}(\nu_T,\nu_R)}$$

Correlation coefficient (Metric) – DDC Spectra

Similarly of spectra is evaluated through correlation coefficient as

$$\rho = \frac{\sum_{i=1}^{N}\sum_{j=1}^{N}(P_{2.4,ij} - \overline{P}_{2.4})(P_{5.2,ij} - \overline{P}_{5.2})}{\sqrt{\left[\sum_{i=1}^{N}\sum_{j=1}^{N}(P_{2.4,ij} - \overline{P}_{2.4})^2\right]\left[\sum_{i=1}^{N}\sum_{j=1}^{N}(P_{5.2,ij} - \overline{P}_{5.2})^2\right]}}$$

N no. of discretization points; f = 2.4 GHz or 5.2 GHz

$$P_{f,ij} = P_{\{CAP,BAR\}}(\nu_{T,i}, \nu_{R,j})$$

$$\nu_{T,i} = \nu_{R,i} = \frac{2\pi(i-1)}{N}$$

$$\overline{P}_f = \frac{1}{N^2}\sum_i\sum_j P_{f,ij}$$

UNIVERSITEIT VAN PRETORIA
UNIVERSITY OF PRETORIA
YUNIBESITHI YA PRETORIA

Results
Measured spatial power spectra at RX location 4: Bartlett beamformer

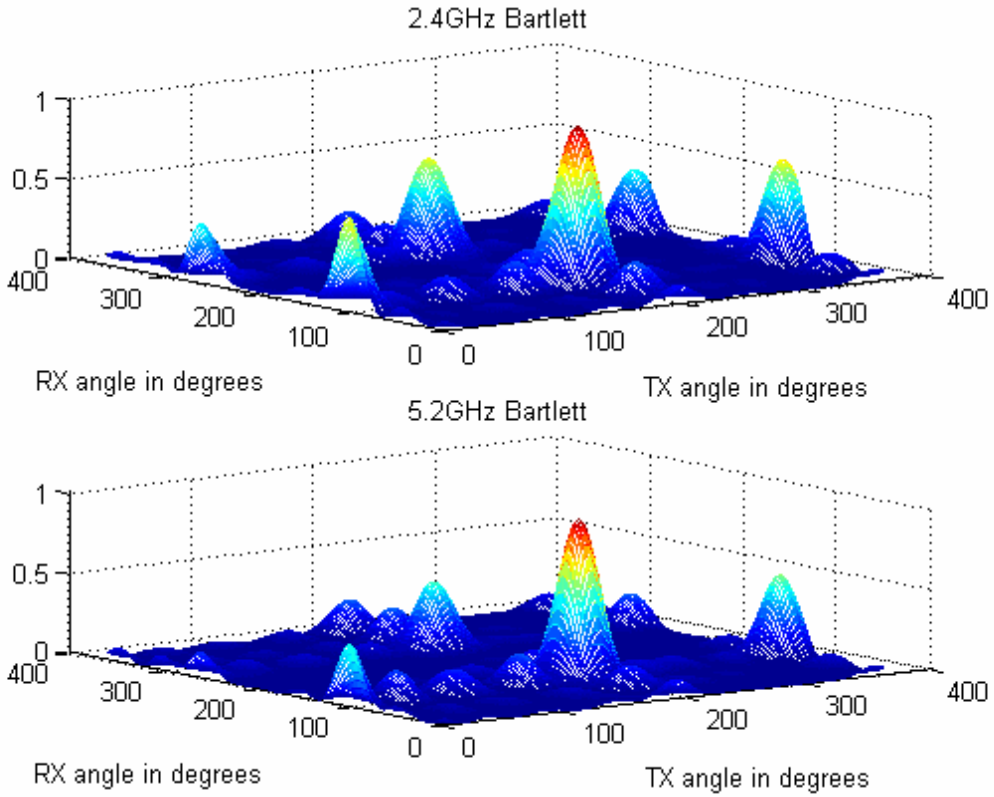

Results
Capon at Location 4

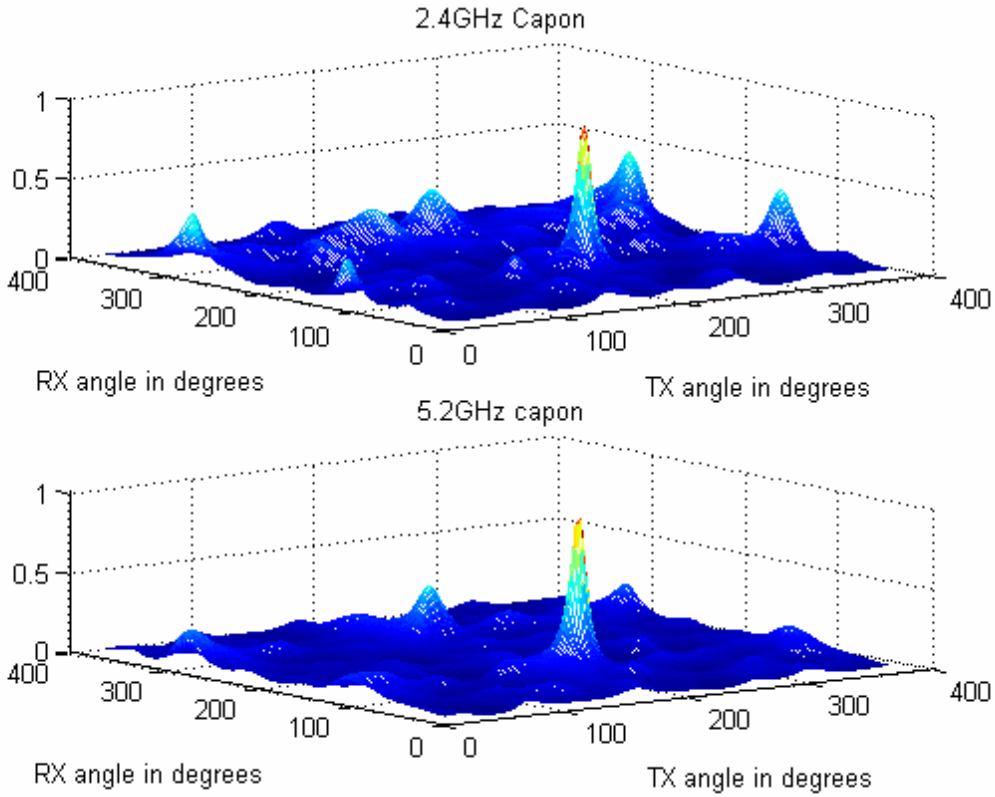

Results
Measured spatial power spectra at RX location 11

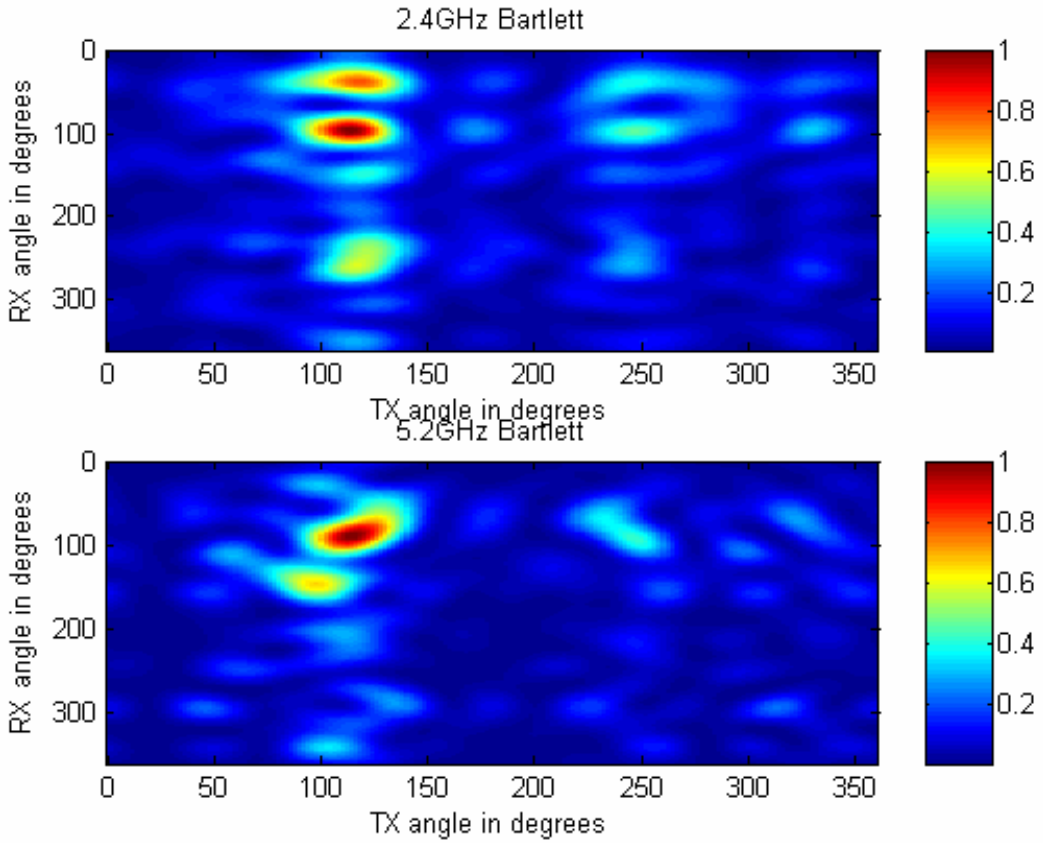

Results
Capon at Location 11

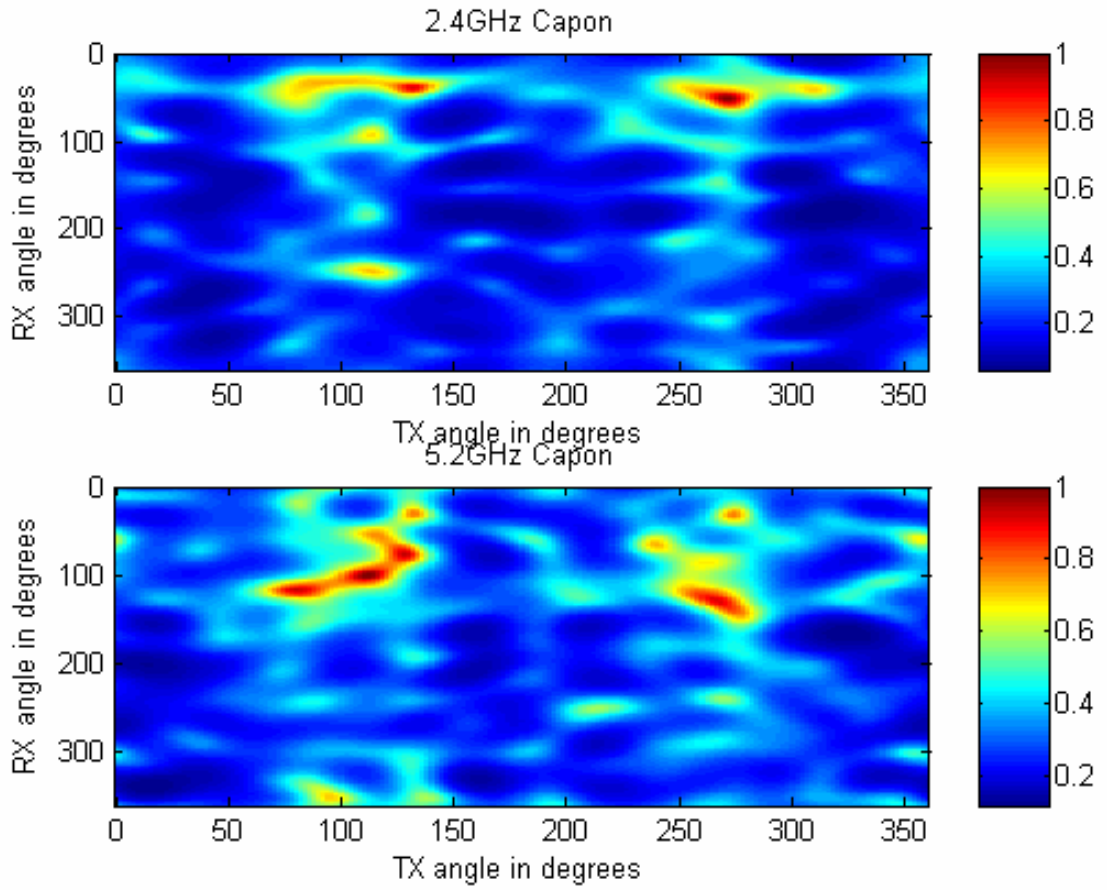

Results
Spectral Correlation at 2.4- & 5.2 GHz

Physical Location	1	2	3	4	5	6	7	8	9	10	11
Bartlett Beamformer	0.37	0.56	0.43	0.56	0.62	0.59	0.35	0.51	0.33	0.25	0.41
Capon Beamformer	0.73	0.77	0.72	0.94	0.59	0.46	0.56	0.76	0.56	0.16	0.63

DDC: Conclusion

- Presented frequency scaling in DD Channel
- High degree of similarity
  - Implies MPP at two frequencies is mainly due to specular reflections
  - Good correlation of power spectra
- Suggests scaling of channel behaviour prediction
- Frequency scaling could save time and cost ito network planning if used properly

MIMO Channel Modelling:

Maximum Entropy Approach

Introduction

- Modeling using Kronecker Model – [Kai Yu, et. al.]

$$R_H = R_T \otimes R_R$$

  - allows one to compute the full joint covariance matrix from the separate Rx and Tx covariance matrices

- Discrepancies in results from above for capacity (eigenvalues) and joint spatial spectra – [Özcelik, et. al.]
  - especially for larger arrays with higher correlation

- Use of partial information from full covariance in separate TX / RX covariance information - [Weichselberger, et. al.]

Maximum Entropy (ME) Approach

- Information theoretic approach proposed by [Debbah and Müller, TIF'05]
  - By not imposing any artificial structure on channel, ME principle should provide more accurate and consistent modeling
  - This is based only on channel knowledge at hand

Our New Approach

- Applying ME to derive the full joint covariance based on knowledge of only the separate TX and RX covariance
- Investigate that this ME approach offers any channel modeling improvement
- Compare the spatial power spectra:
  - using the double directional channel
  - to indoor WB measurement campaign
  - Kronecker Model

Model Description (ME1)

Suppose we know the TX and RX covariance as $\mathbf{R}_T$ and $\mathbf{R}_R$, respectively and stats of channel constrained by:

$$\mathrm{E}\left\{\mathbf{H}\mathbf{H}^H\right\} = \mathbf{R}_R \qquad \mathrm{E}\left\{\sum_k H_{ik}H_{jk}^*\right\} = R_{R,ij} \qquad (1)$$

$$\mathrm{E}\left\{\mathbf{H}^H\mathbf{H}\right\} = \mathbf{R}_T^T \qquad \mathrm{E}\left\{\sum_k H_{ki}H_{kj}^*\right\} = R_{T,ij} \qquad (2)$$

$$p(\mathbf{H}) \geq 0 \qquad (3)$$

$$\int p(\mathbf{H})d\mathbf{H} = 1, \qquad (4)$$

To maximize the entropy wrt above constraints;

$$\int p(\mathbf{H}) \log p(\mathbf{H})d\mathbf{H}$$

p(**H**) is the joint pdf of the elements of channel matrix **H**

ME Model (ME2)

We can write the Lagrangian L[p(**H**)], and set its derivate equal to zero (ie. *d*L/*d*p =0), giving

$$p(\mathbf{H}) = \exp\left[\lambda_0 + \sum_{ij}\mu_{R,ij}\sum_{k}H_{ik}H^*_{jk} + \sum_{ij}\mu_{T,ij}\sum_{k}H_{ki}H^*_{kj}\right]$$

$$= c_0\exp\left(\sum_{ijk\ell}\mu_{R,ik}H_{ij}H^*_{k\ell}\delta_{j\ell} + \sum_{ijk\ell}\mu_{T,j\ell}H_{ij}H^*_{k\ell}\delta_{ik}\right)$$

writing $c_0=\exp(\lambda_0)$, gives

$$p(\mathbf{H}) = c_0\exp\left[\sum_{ijkl}H_{ij}H^*_{k\ell}\underbrace{(\mu_{R,ik}\delta_{j\ell} + \mu_{T,j\ell}\delta_{ik})}_{-R^{-1}_{ij,k\ell}}\right]$$

this is the form of standard MCN pdf

ME Model (3)

This can be expressed with the Kronecker Product as

$$\mathbf{R} = -(\underbrace{\mathbf{I}_T \otimes \boldsymbol{\mu}_R + \boldsymbol{\mu}_T \otimes \mathbf{I}_R}_{\mathbf{A}})^{-1}.$$

Which is different from the Kronecker Model [Yu, et. al.]

$$\mathbf{R} = \mathbf{R}_T \otimes \mathbf{R}_R.$$

The eigenvalue decomposition (EVD) of $\mu_{T,R}$:

$$\boldsymbol{\mu}_T = \boldsymbol{\xi}_T \boldsymbol{\Lambda}_T \boldsymbol{\xi}_T^H, \qquad \boldsymbol{\mu}_R = \boldsymbol{\xi}_R \boldsymbol{\Lambda}_R \boldsymbol{\xi}_R^H,$$

Hence we can write:

$$\mathbf{R}^{-1} = -\underbrace{(\boldsymbol{\xi}_T \otimes \boldsymbol{\xi}_R)}_{\boldsymbol{\xi}} \underbrace{(\mathbf{I}_T \otimes \boldsymbol{\Lambda}_R + \boldsymbol{\Lambda}_T \otimes \mathbf{I}_R)}_{\boldsymbol{\Lambda}} \underbrace{(\boldsymbol{\xi}_T \otimes \boldsymbol{\xi}_R)^H}_{\boldsymbol{\xi}^H},$$

ME (4)

- The eigenvectors are just the Kronecker product of the separate TX and RX eigenvectors
- The eigenvalues can be found by substituting **R** into the original constraints

Hence we can re-write the TX or RX covariance, eg

$$R_{R,ik} = \sum_j R_{ij,kj},$$

With the RX covariance constraint as:

$$\{-\mathbf{R}_R\}_{ik} = \sum_m \xi_{R,im}\xi^*_{R,km} \underbrace{\sum_n \Lambda^{-1}_{mn,mn}}_{-D_{R,mm}}.$$

simply the EVD of RX covariance

$$\mathbf{R}_R = \boldsymbol{\xi}_R \mathbf{D}_R \boldsymbol{\xi}_R^H.$$

ME (5)

To solve for **R** (full) we need to solve

$$D_{R,mm} = d_{R,m} = -\sum_n \frac{1}{\lambda_{R,m} + \lambda_{T,n}}$$

$$D_{T,nn} = d_{T,n} = -\sum_m \frac{1}{\lambda_{R,m} + \lambda_{T,n}}$$

One method to solve is by indirect approach since **H** is a Gaussian process,

ME maximizes det(**R**)

Need to find **Λ**, such that det(- **Λ**$^{-1}$) is maximized, ie if:

$$f_{mn} = -\Lambda^{-1}_{mn,mn},$$

Maximize $\det(\mathbf{R}) = \prod_{ij} f_{ij}$ subject to ff constraints:

$$d_{T,j} = \sum_i f_{ij} \qquad d_{R,i} = \sum_j f_{ij} \qquad f_{ij} \geq 0.$$

ME (6)

Since constraints are linear and $-\Pi_{ij} f_{ij}$ is convex

⇒ can use linear programming to find initial guess for f_{ij}

⇒ use gradient descent method to find minimum of function

Data Processing

- Since multipath path scattering in indoors is severe, we define the double directional response in terms of spatial power spectra for joint RX/TX Bartlett beamformers as

$$P(\nu_T, \nu_R) = \frac{\mathbf{a}(\nu_T, \nu_R)^H \hat{\mathbf{R}} \mathbf{a}(\nu_T, \nu_R)}{\mathbf{a}(\nu_T, \nu_R)^H \mathbf{a}(\nu_T, \nu_R)}.$$

$\upsilon_{T,R}$ = azimuth angle at TX or RX

$\hat{R}$ = sample covariance matrix

The joint steering vector is defined as:

$$\mathbf{a}(\nu_T, \nu_R) = \mathbf{a}_T(\nu_T) \otimes \mathbf{a}_R(\nu_R)$$

Sample covariance matrix $\hat{\mathbf{R}} = \frac{1}{K} \sum_k \mathbf{h}^{(k)} \mathbf{h}^{(k)H}$

$h^{(k)} = \mathrm{Vec}\{H^{(k)}\}$

Results – Location 3

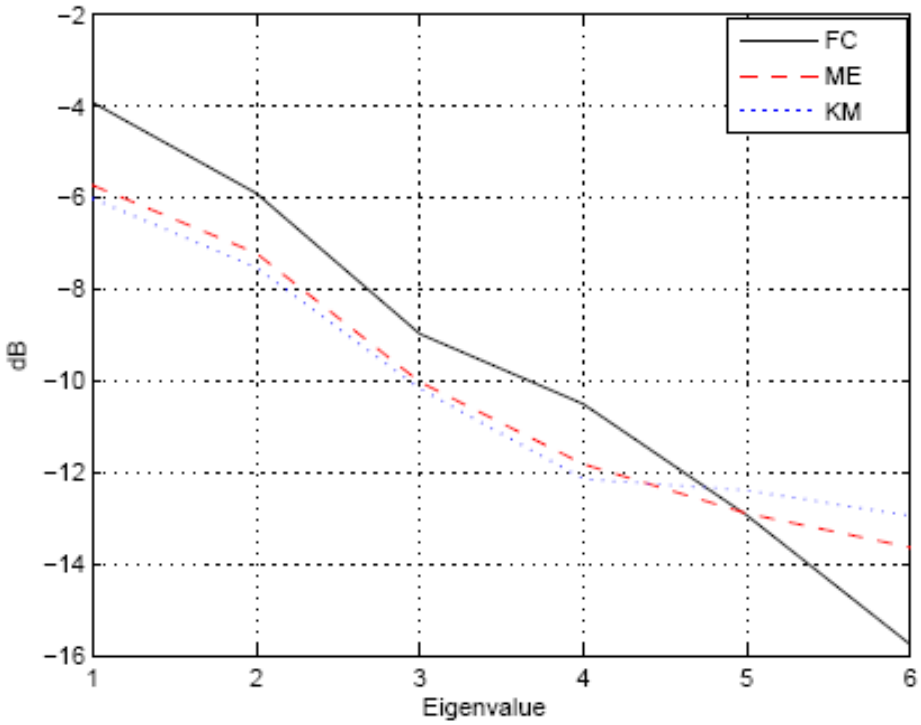

Results – Location 9

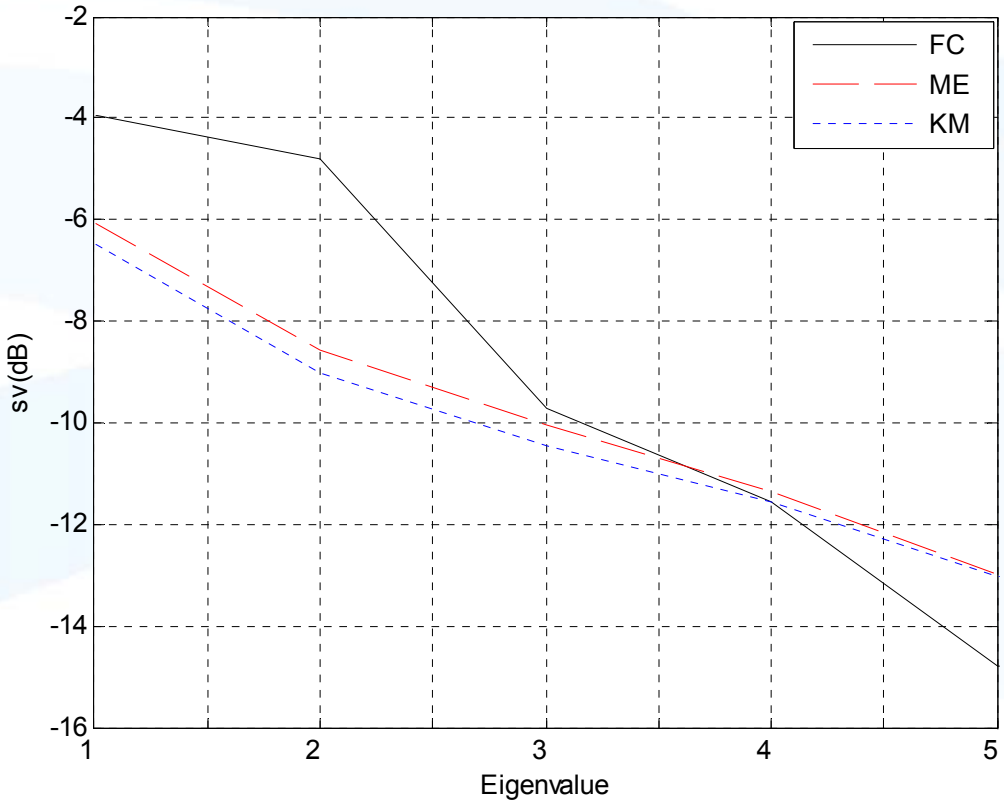

Results – Location3

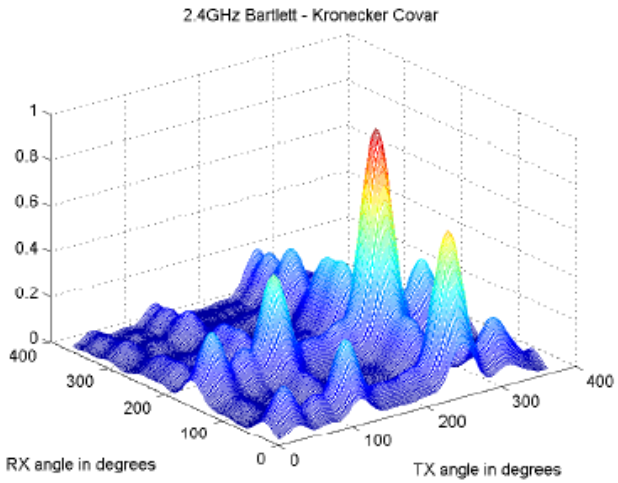

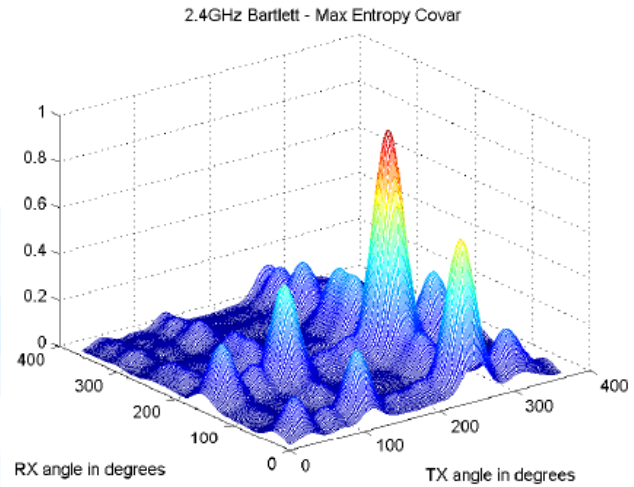

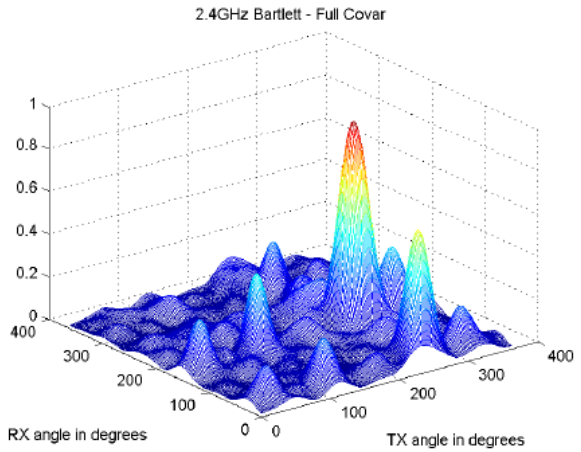

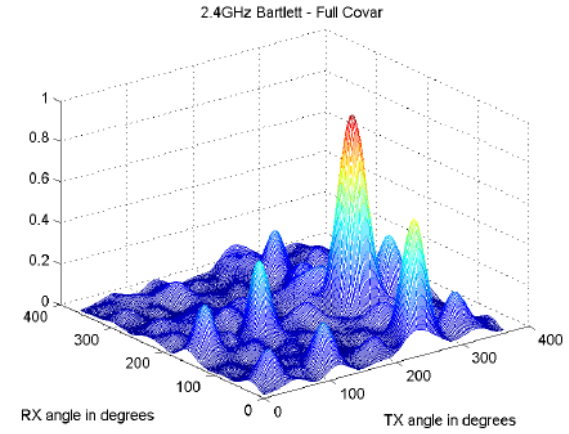

Results
Joint correlation of spatial power spectra

CORRELATION COEFFICIENT OF SPATIAL POWER SPECTRA

Locations	Bartlett beamforming at 2.4 GHz	
	$\rho_{FC,ME}$	$\rho_{FC,KM}$
1	0.9387	0.9377
2	0.9258	0.9088
3	0.9470	0.99264
4	0.9927	0.9887
5	0.9716	0.9615
6	0.9818	0.9798
7	0.8850	0.8889
8	0.9872	0.9845
9	0.9028	0.8966
10	0.9007	0.8985
11	0.9261	0.9229

ME Approach to Channel Modelling: Conclusion

- Presented a ME approach for obtaining full covariance when only separate covariances are known
- The eigenvalues are different from the Kronecker Model
- For this indoor environment at 2.4GHz, KM and ME Model gave very similar double directional power spectra results but different metric
- This means that the modeled channels attain ME bound
- This suggests that the KM model represents a fundamental limit
- Opportunity for further testing of model

What has been achieved? (1)

1. Presented a Geometric Model for flat fading wireless indoor environment with scattering at both the TX and RX which have some of key components that affect the channel behavior.

2. Developed a unique WB MIMO Channel Sounder capable of operating in the 2- 6 GHz range with an excitation BW of 100MHz.

3. Developed and presented the concept of ‘frequency scaling’ in describing MIMO channel behavior.

What has been achieved? (2)

4. Modelled capacity for a UCA
5. Modelled spatial correlation for a ULA
6. Extended the Double Directional Channel Model to include spatial power spectra through joint beamforming.
7. Developed the new MIMO Channel Model (MWL Model) based on the maximum entropy approach.
8. Established an agenda for further research and MIMO channel characterization

Outputs

- Artifact (WB MIMO Channel Sounder)

- Currently have 10 publications
  - 4 Journal publications
    - 3 Published
    - 1 Accepted for Publication
  - 5 Peer reviewed International Conference Publications
  - 1 Invited Paper: International Conference Publication

Thank You

for

attending

UNIVERSITEIT VAN PRETORIA
UNIVERSITY OF PRETORIA
YUNIBESITHI YA PRETORIA

UNIVERSITEIT VAN PRETORIA
UNIVERSITY OF PRETORIA
YUNIBESITHI YA PRETORIA

UNIVERSITEIT VAN PRETORIA
UNIVERSITY OF PRETORIA
YUNIBESITHI YA PRETORIA

UNIVERSITEIT VAN PRETORIA
UNIVERSITY OF PRETORIA
YUNIBESITHI YA PRETORIA

UNIVERSITEIT VAN PRETORIA
UNIVERSITY OF PRETORIA
YUNIBESITHI YA PRETORIA